SELF POWERED SENSING BY COMBINING NOVEL SENSOR ARCHITECTURES WITH ENERGY HARVESTING

by

VISHWAS NARAYAN BEDEKAR

Presented to the Faculty of the Graduate School of
The University of Texas at Arlington in Partial Fulfillment
of the Requirements
for the Degree of

DOCTOR OF PHILOSOPHY

THE UNIVERSITY OF TEXAS AT ARLINGTON
December 2009

Dedicated to my parents

Narayan Vishwanath Bedekar and Smita Narayan Bedekar

ACKNOWLEDGEMENTS

I would like to express my deepest appreciation and gratitude for my supervising professor, Dr. Shashank Priya, Materials Science and Engineering Department, Virginia Tech, Blacksburg, VA. I was very fortunate to have found a great mentor and advisor like him. I would like to thank him for his constant support and guidance for carrying out this research and also for his limitless help in writing several technical documents including this thesis.

I would also like to thank Dr. Pranesh Aswath for his valuable suggestions and motivation during my academic career. I am grateful to Dr. Choong-un Kim for his inspiration and help during this research. I am also grateful to my committee members Dr. Ping Liu and Dr. Wen Chan for their valuable time and suggestions to improve this research. I am grateful to Dr. Gurpreet Singh for his help and encouragement in this research. I am also thankful to Dr. Mirza Bichurin for his help in the research. I would like to thank the staff and faculty of Nanoscale Characterization and Fabrication Laboratory (NCFL), Virginia Tech, Blacksburg, VA for their help in this research. I would like to thank my former colleague Dr. Rashed Islam for passing on his knowledge and experience and helping me in research. Thanks to the former group members Makarand, Robert and HyunUk for encouraging and helping me. I am grateful to my present group members Dr. Ahn, Dr. Park, Yonas, Alex, Deepam, Nick, Scott and Su Chul for their continuous support throughout this research. Special thanks are due to Josiah, Mana and Keyur for their help in this research. I am also thankful to my other colleagues Arunya, Hande, Eray, Mihir, Bo Hoon, Emil,

Poonnapob, Kevin for their support and encouragement. I would like to acknowledge all the faculty and staff members of Materials Science and Engineering Department for sharing knowledge and offering generous help. I am especially grateful to Jennifer Standlee and Libia Cuauhtli for taking care of my paperwork and other formalities.

I would like to thank my parents for their limitless love and support throughout my life and family members for their support and encouragement.

Finally, I express my sincere gratitude to Lord Ganesha and Lord Dattatreya for giving me the ability to be where I am today.

November 25, 2009

ABSTRACT

SELF POWERED SENSING BY COMBINING NOVEL SENSOR ARCHITECTURES WITH ENERGY HARVESTING

Vishwas Narayan Bedekar, PhD

The University of Texas at Arlington, 2009

Supervising Professor: Shashank Priya

Recent advancements in the field of wireless sensor networks have resulted in increasing demand for self-powering techniques that reduces the dependence on batteries. In order to address this problem, there has been significant effort on generating small electrical power locally by harvesting energy from freely available environmental sources such as mechanical vibrations, wind, and stray magnetic field. Further, there is need for inventing new sensing techniques to reduce the overall power consumption. The road for reaching the destination of self-powered sensor networks requires cooperative progress in reduction in sensor power consumption by developing new sensing mechanisms and local generation of power by developing high efficiency energy harvesters.

The sensing techniques investigated in this thesis utilize piezoelectric materials, piezoresistive materials, and magnetoelectric composites. Prior studies on structural health monitoring have demonstrated the use and promise of piezoelectric sensors. In this research, impedance spectroscopy based sensing technique was investigated with respect to two

parameters (i) effect of the piezoelectric vibration mode on damage index metric, and (ii) selection of frequency band through manipulation of the electrode size and shape. These results were then used to determine sensor geometry and dimensions for detecting surface defects, fatigue and corrosion. Based upon these results, power requirement for structural health monitoring sensors was determined. Next, piezoelectric materials were coupled with magnetostrictive material for novel magnetic field gradient sensing. Novel ME composite materials were synthesized to achieve passive sensing of magnetic field. ME particulate composites in system $[Pb(Zr_{0.52}Ti_{0.48})O_3]$ - $0.2[Pb(Zn_{1/3}Nb_{2/3})O_3]$ (PZT) – $NiFe_2O_4$ (NFO) were synthesized using (i) core-shell particles followed by high pressure compaction sintering, (ii) organic slurry in a sacrificial matrix followed by high temperature annealing, and (iii) co-firing. A pressure assisted co-firing technique was developed to achieve 3D pillar composite structure.

The ceramic – ceramic (CC) gradiometer resembles in functionality a magnetoelectric transformer. It measures the magnetic field gradient and sensitivity with respect to a reference value. The CC gradiometer designed in this study was based upon the magnetoelectric (ME) composites and utilizes the ring-dot piezoelectric transformer structure working near resonance as the basis. This study investigated the gradiometer design and characterized the performance of gradiometer based upon Terfenol–D – PZT composites. The generated magnetic field due to converse ME effect interacts with the external applied magnetic field producing flux gradient which is detected through the frequency shift and output voltage change of the gradiometer structure. The performed measurements of voltage dependence on applied magnetic field clearly illustrate that the proposed design has extremely high level of magnetic field sensitivity and it can be used for measurement of magnetic field gradient.

Based upon these results, next a metal – ceramic gradiometer consisting of PZT and nickel was designed and characterized. In this thesis, two different designs of gradiometer with nickel and PZT laminate composites were fabricated. Nickel was chosen over other materials considering its co-firing ability with PZT. It can give a better control over dimensional parameters of the gradiometer sample and further size reduction is possible with tape casting technique. Detailed theoretical analysis was conducted in order to understand the experimental results. The fabricated metal – ceramic gradiometer showed high sensitivity for a wide range of frequency (247 – 251 kHz for gradiometer design A and 234 – 239 kHz for gradiometer design B) and can be utilized for broadband magnetic field gradient sensing. Power analysis was conducted for the magnetic field gradient sensors based on the performance curves.

In order to significantly reduce the power consumption of health monitoring and magnetic field sensors, bottom – up design of structural health monitoring and magnetic field sensors was investigated. A MWCNT/SiCN nanotube template was developed that exhibits piezoresistive effect. Next, a novel nanotube morphology "nanoNecklace" was synthesized that consists of $BaTiO_3$ (BTO) nanoparticles decorated along the surface of SiCN. Monolayer coating of SiCN on MWCNT serves two purposes: (i) modifies the surface wetting characteristics, and (ii) enhances the piezoresistive effect. Investigation of the mechanisms that provide periodic arrangement of BTO on nanotube surface was conducted using HRTEM and contact angle measurements. Next, we tried to modify the surface wetting characteristics of MWCNTs in order to get a full coating of BTO nanoparticles. We synthesized acid treated functionalized MWCNTs and coated them with BTO. Acid concentration, coating temperature and coating time were optimized in order to obtain fully coated MWCNTs with BTO. Microstructural characterization was performed using various techniques such as Scanning Electron Microscopy (SEM), Transmission Electron Microscopy (TEM), and Energy Dispersive Spectrum (EDS). Coating thickness of 5-15 nm was confirmed with High Resolution – TEM imaging. X-ray Photoelectron Spectroscopy was performed to confirm perovskite phase of BTO. The average BTO nanoparticle size was found to be 4-8 nm. Contact angle measurements were carried out and were correlated with the percentage of coating on the surfaces of nanotubes. The SiCN/MWCNT approach was further extended to fabricate magnetoelectric nanowire based sensors designs. In this approach a SiCN-NT template was coated with BTO and $CoFe_2O_4$ (CFO) nanoparticles. Microstructural studies indicated the presence of piezoelectric (BTO) as well as magnetic (CFO) material on the nanotube surface.

In order to power the sensors from mechanical vibrations, we investigated two different techniques, (i) piezoelectric and (ii) inductive. For piezoelectric energy harvesting, high energy density piezoelectric compositions corresponding to $0.9Pb(Zr_{0.56}Ti_{0.44})O_3$ – $0.1Pb[(Zn_{0.8/3}Ni_{0.2/3})Nb_{2/3}]O_3$ + 2 mol% MnO_2 (PZTZNN) and $0.8[Pb(Zr_{0.52}Ti_{0.48})O_3]$–$0.2[Pb(Zn_{1/3}Nb_{2/3})O_3]$ (PZTPZN) were synthesized by conventional ceramic processing technique using different sintering profiles. Plates of the sintered samples were used to fabricate the piezoelectric bimorphs with optimized dimensions to exhibit resonance in the loaded condition in the range of ~200 Hz. An analytical model for energy harvesting from bimorph transducer was developed which was confirmed by experimental measurements. The results show that power density of bimorph transducer can be enhanced by increasing the magnitude of product (d.g), where d is the piezoelectric strain constant and g is the piezoelectric voltage constant.

Under inductive energy harvesting, we designed and fabricated a small scale harvester that was integrated inside a pen commonly carried by humans to harvest vibration energy. Inductive energy harvesting was selected in order to achieve high power at lower frequencies. The prototype cylindrical harvester was found to generate 3mW at 5 Hz and 1mW at 3.5 Hz operating under displacement amplitude of 16mm (corresponding to an acceleration of approximately 1.14 g_{rms} at 5Hz and 0.56 g_{rms} at 3.5 Hz, respectively). A comprehensive mathematical modeling and simulations were performed in order to optimize the performance of the vibration energy harvester. The integrated cylindrical harvester prototype was found to generate continuous power of 0.46–0.66mW under normal human actions such as jogging and jumping which is enough for a small scale sensor.

TABLE OF CONTENTS

APPENDIX

LIST OF ILLUSTRATIONS

LIST OF TABLES

CHAPTER 1

INTRODUCTION

1.1 Background of Pressure Sensors

Pressure sensors typically measure force using functional materials and are widely deployed in process control and feedback systems. Pressure sensors convert the pressure or force into current or voltage signals. There are several ways to detect the pressure (i) deformation of the diaphragm (capacitance change, optical detection, change of current in tunneling tip), (ii) strain measurement (piezoresistance), (iii) charge generation, and (iv) resonance shift. Capacitive sensors detect pressure as a capacitance associated with the distance between two (or more) diaphragms, which changes in response to a change in pressure. In resistive sensors, pressure changes the resistance by mechanically deforming the sensor, enabling the resistors in a bridge circuit to detect pressure as a proportional voltage across the bridge. Conventional resistive pressure measurement devices include films resistors, strain gauges, metal alloys, and polycrystalline semiconductors.

1.1.1 Piezoelectric sensors

Piezoelectric sensors use direct or converse “piezoelectric effect”. A direct piezoelectric effect can be defined as induction of charge due to application of mechanical stress whereas a converse piezoelectric effect can be defined as generation of stress due to applied electric field. Figure 1.1 shows the schematic of direct piezoelectric effect.

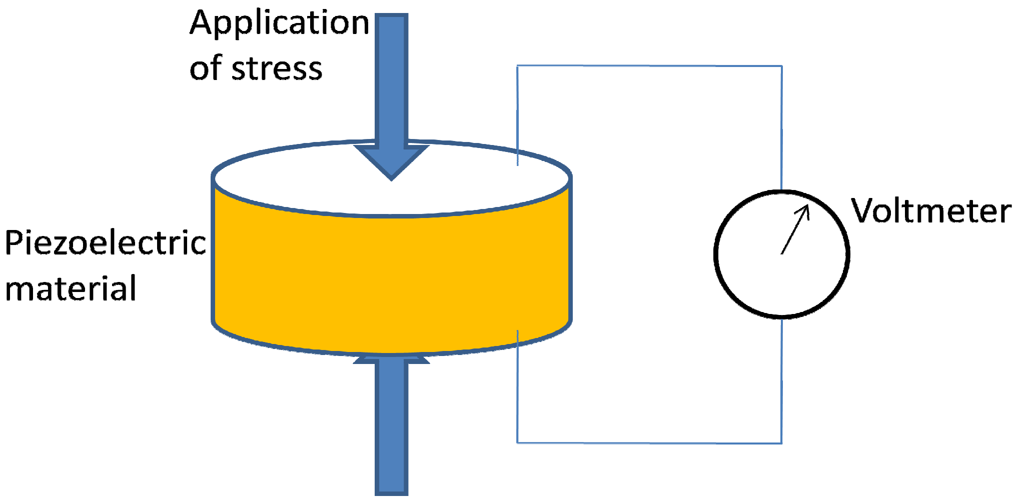

Figure 1.1 Direct Piezoelectric Effect

Piezoelectric sensors have become of particular interest due to their versatility, low power consumption and higher bandwidth.

Piezoelectric transducers provide the interface between the mechanical and electrical systems with an efficiency of around 50% (the conversion from mechanical stress to electric field is proportional to square of the electromechanical coupling factor, k^2 and the magnitude of k_{33} for commonly used piezoelectric ceramics is of the order of 0.7). It has been shown that thin-film unimorph type PZT based transducer can supply 20 nW/mm^2 (3 nW with 150 mm^2 area) when external mechanical vibrations are imposed upon the PZT. Recently, there has been success in synthesizing high performance single crystals with better k and energy density. However, implementation of the single crystal piezoelectrics is challenging on the micro/nano platform. Textured thin films of these compositions can be grown but the coefficients are compromised and the device fabrication requires multiple steps. At this juncture, the best power density reported for the piezoelectric energy harvesting devices is in the range of 0.3 – 0.5 $\mu W/mm^3$. Further improvements in this magnitude requires discovery of materials and mechanisms. Thus in this thesis, we focused our attention on synthesis and characterization of the multifunctional magnetoelectric material that complements the piezoelectric scheme and offers multimodality. High aspect ratio magnetoelectric nano-wires synthesized in this program will provide ability to capture the vibration energy more effectively. This energy can be supplemented by capturing the stray magnetic field which is always present in the buildings and other industrial environment. Further, the nanotube-based building blocks developed in this program can be used to develop large scale energy harvesting systems.

1.1.2 Structural Health Monitoring

Structural health monitoring (SHM) in aerospace, civil and mechanical engineering infrastructure implies continuous monitoring of defect progression using periodically sampled dynamic response measurements from an array of sensors, understanding and extracting damage sensitive parameters and analyzing these parameters in order to predict the structural health. There are various types of non-destructive examination techniques used for structural health monitoring such as liquid penetrant test (LPT), radiographic inspection, ultrasonic testing (UT), eddy currents testing, magnetic particles and magnaflux, lamb wave detection etc. Most of these techniques involve acquisition of the electrical signature from the material and conduct online analysis to facilitate life-cycle management decisions. [1] Piezoelectric sensors are commonly deployed for structural health monitoring of elastic materials using variety of techniques such as impedance spectroscopy, rayleigh waves and lamb waves [1].

1.1.3 Types of Damages

Various types of damages can be exemplified as cracks, delaminations, fatigue, corrosion etc. Figure 1.2 shows most common damages observed in structures. Damage prognosis and diagnosis becomes very critical in structures like pipeline joints, aircraft wings, marine vehicles, engines running in adverse environments.

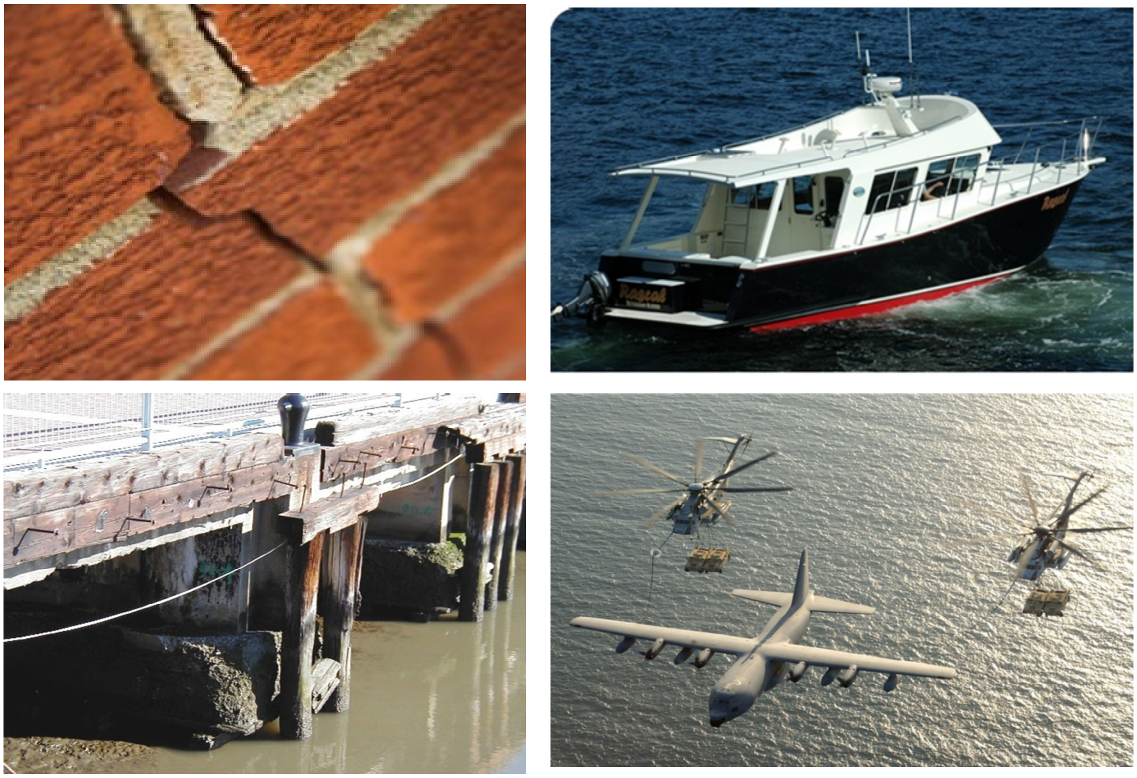

Figure 1.2 Types of damages (i) Cracks, (ii) Ship Joints (iii) Corrosion (iv) Aircraft wings

The three stages of condition-based maintenance (CBM) are diagnostics, prognostics, and maintenance scheduling. The diagnostics involve real time fault monitoring and diagnosis, background studies, and fault analysis. Figure 1.3 shows the systems approach to the design of the CBM that includes failure identification and its criticality, failure analysis and decision making, failure classification, prediction of failure evolution, scheduling of required maintenance, and collaboration with the logistics. [2-4]

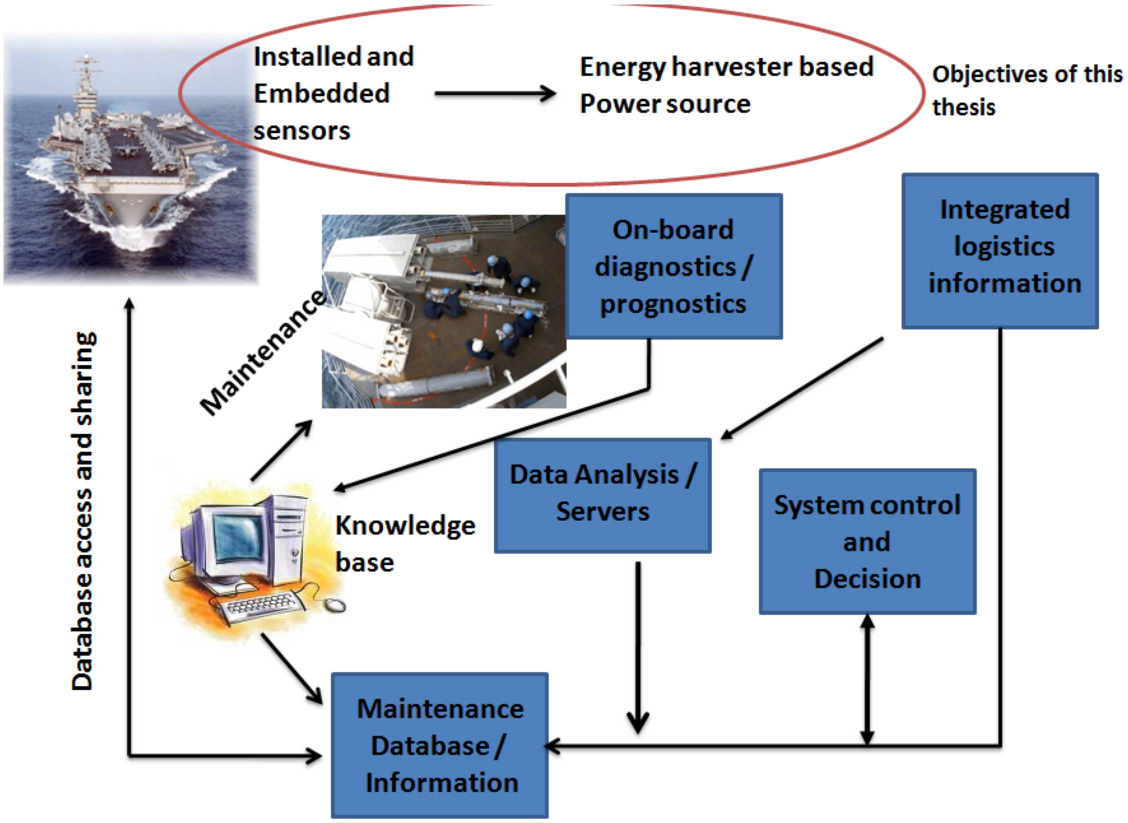

Figure 1.3 Real time condition-based maintenance system with integrated management. As an example, Navy ship platform is shown in this figure that illustrates the system architecture.

1.1.4 Damage detection using Impedance Spectroscopy

Inman et. al. have applied the impedance spectroscopy method on variety of structures to detect minute changes in the integrity [5]. Several advantages have been listed for this method which includes: (i) applicable on complex structures to monitor damages in non-accessible locations, (ii) involves self-sensing actuators which have excellent reliability, wide frequency range and fatigue characteristics, and (iii) low power requirement.

Theoretical modeling of impedance based health monitoring sensors has been extensively discussed in literature [6-21]. Liang et al. [6] have shown that electrical admittance $Y(\omega)$ of the system consisting of a piezoelectric actuator bonded to structure is combined function of the mechanical impedance of the PZT actuator $Z_a(\omega)$ and that of the host structure Z_s, given as:

$$Y(\omega) = i\omega a\left(\bar{\varepsilon}_{33}^{T}(1 - i\delta) - \frac{Z_s(\omega)}{Z_s(\omega) + Z_a(\omega)} d_{3x}{}^{2}\bar{Y}_{xx}^{E}\right) \tag{1}$$

where a is the geometry constant of PZT, d_{3x} is the piezoelectric constant in arbitrary x direction at zero stress, $\bar{Y}_{xx}$ is the complex Young's modulus of PZT at zero electric field, and $\varepsilon_{33}{}^{T}$ is the dielectric constant of PZT at zero stress. Hence, the mechanical impedance of structure is related to the impedance of PZT actuator. Thus, by monitoring the change in electrical impedance of PZT useful information about the structure can be obtained. If the structure is damaged then parameters such as mass, stiffness or damping would be changed and the mechanical impedance of the structure would be modified. Assuming all other PZT properties remain constant, it is the external structure's impedance that uniquely determines the overall electrical impedances [14] Figure 1.4 shows a schematic of impedance based SHM technique.

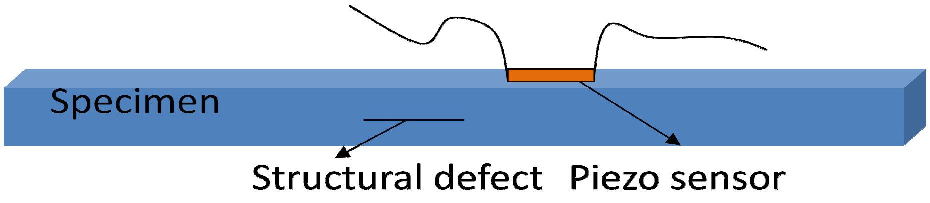

Figure 1.4 Impedance based Structural Health Monitoring.

Impedance spectroscopy based health monitoring technique have been previously demonstrated on several systems including aging aircraft panels, pipeline joints, and civil structures such as concrete, bridges, beams and plates to detect various kinds of defects. [7, 14, 17, 21] In this thesis, we have implemented this technique for monitoring the health of rocket motors. Several defense related applications utilize solid rocket motors composed of a metallic casing and solid rocket composite chemical fuel along with detonating charge. It is of significant interest to the manufacturers to monitor the changes in the rocket motor occurring during transportation, handling, storage, and loading conditions. One of the effective ways to achieve this is by attaching an external sensor that provides information about delamination between casing and fuel, microcracks occurring in the composite fuel, and deformation of the casing. External sensors are preferred over the embedded sensors as they do not interfere with the operating mechanism of the motor. Further, the sensor in this application should have high reliability for long shelf life, consume low power for long operation, and should not interfere with the electronics or signals of the rocket motor. Impedance based health monitoring sensors satisfy most of these criterions and hence are preferred choice for rocket motors.

1.2 Background of Nanotechnology

Recent developments in the field of nanoscience and nanotechnology have brought us to the point where it’s now possible to realize practical nanodevices. Examples include – molecular switches that work at room temperature, scanning probe microscopy, microfluidic systems, and molecular tags. It is known that the physical properties of materials with reduced characteristic dimensions (<100nm) can be radically different from their bulk counterparts and, as such, present an excellent opportunity to develop a broad class of new materials. Traditional manufacturing techniques have been successfully applied in the past in a top-down approach to fabricate components and devices down to the micron scale region. However, such manufacturing practices are merely impossible to apply to the nanoscale regime, since entirely different phenomena dominate the behavior of the materials in that domain. Thus, at present, novel manufacturing approaches are needed in order to take advantage of the enormous potential of nanoscale structures.

Research thrusts in today’s environment are on discovering multifunctional material (MFM) systems, ones that have at least two desired functions for a given set of conditions. The multiple functions in the material can be invoked individually or collectively by modulating external controllable parameters such as load, temperature, current, electric field, magnetic field, and etc. To exemplify, research is in progress on load bearing energy generating materials which not only protect against impact but also generate electric charge under stress. Discovery of novel MFMs is critical to the advancement of electromechanical systems which heavily rely on material properties. Nanoscience, combined with the appropriate synthesis technique, could open the possibility of realizing a new generation of MFMs.

1.2.1 Introduction to carbon nanotubes

Since the discovery [22], Carbon nanotubes have been utilized in many fields such as electronics, chemical sensing biological sensing, reinforced composite materials, etc. [23-26] Figure shows single walled carbon nanotube (SWCNT) and multi walled carbon nanotube.

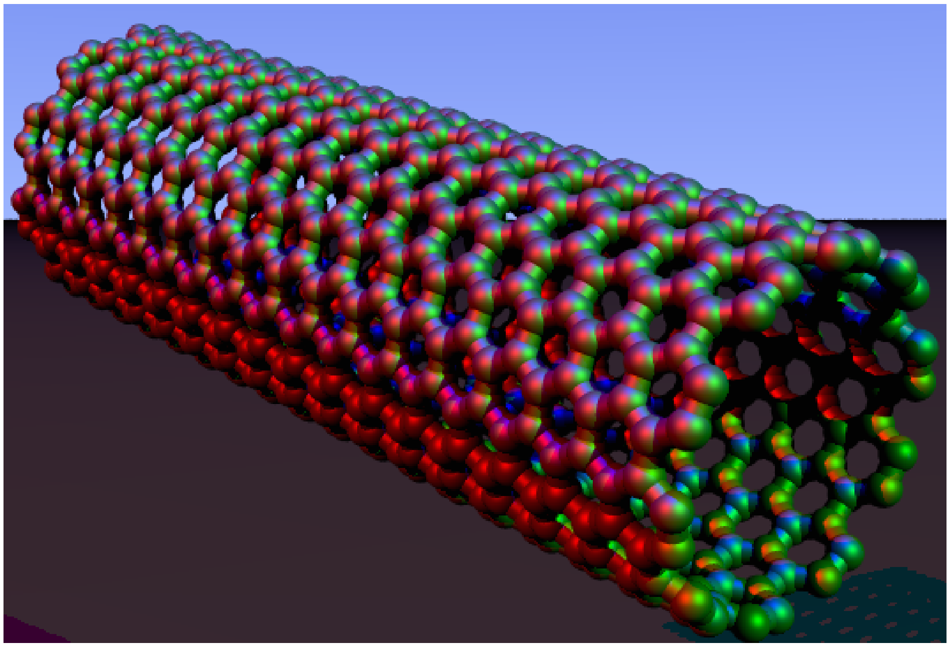

Figure 1.5 Schematic of single walled carbon nanotube (Ref: 27 http://en.wikipedia.org/wiki/Carbon_nanotube#Single-walled)

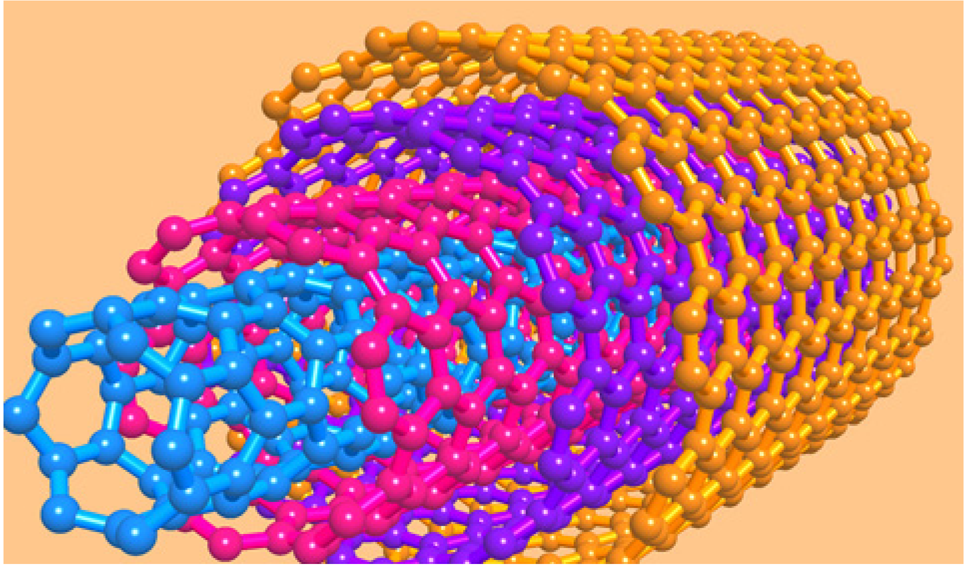

Figure 1.6 Schematic of Multi walled carbon nanotube (Ref: 28 http://www.crystalsoftcorp.com/Gallery/mwcnt3.jpg.html)

Commonly used CNT synthesis methods are arc plasma discharge, CVD and laser ablation. Owing to their unique geometry and bonding structure, CNTs have interesting thermal, mechanical, and electrical properties. Chemical bonding in nanotubes is composed of sp^2 bonds like graphite and both SWNT and MWNT's are found resilient to chemical or thermal decomposition. Manipulation of single CNT is difficult and hence their use as conducting paths for large scale chip manufacturing has not yet been realized. In the present study, CNT's were used as a template to deposit the coating of SiCN and form an surface that can be used to coat both piezoelectric and magnetic materials.

1.2.2 Literature review of carbon nanotube based nano-structures

In order to utilize carbon nanotubes in sensing applications, several studies have been conducted to modify the nanotube surface and utilize it as an template. Optimization of surface characteristics of nanotubes would lead to more advanced template materials with superior characteristics. There have been several studies showing attachment of foreign materials on the nanotube surfaces in order to modify and improve its structural and functional characteristics. For example, attachment of polymers, inorganic and organic compounds have been already published in literatures. [29-34]

1.3 Piezoresistive sensors

The discovery of piezoresistivity in silicon and germanium in 1954 launched the production of semiconductor based sensors. [35] Four years later in 1958, silicon strain-gauge, metal-diaphragm sensors were introduced in commercial market. [36] Micromachined pressure sensors became available in year 1963, [37] bulk-micromachined sensors in 1980's, and surface micromachined pressure sensors in 1990's. [38-40] The resistance change in a monocrystalline semiconductor (a piezoelectric effect) is substantially higher than that in standard strain gauges, whose resistance changes with geometrical changes in the structure. Figure 1.7 shows the data on the current state-of-the-art micro pressure sensor (CNM, www.cnm.es). Pressure ranges are from 0-35 mbar up to 0-1.5 bar and the corresponding sensitivities range from 325 mV/V/bar to 6 mV/V/bar. MAXIM's (www.maxim-ic.com/an871) low profile pressure sensor offers the sensitivity of 0.50 mV/mbar in the pressure of 0 – 100 mbar. The chip size is of the order of 3 x 3 x 1 mm^3 having the piezoresistive diaphragm of the size 2 x 2 mm^2. More recently, carbon nanotubes have generated a lot of interest because of their unique mechanical and electrical properties.

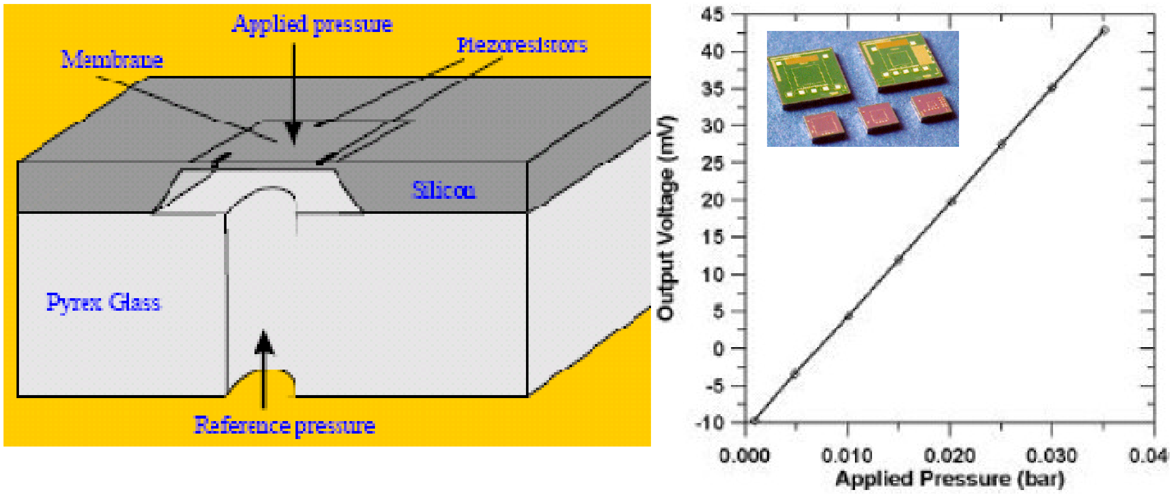

Figure 1.7 Picture of the commercial micro pressure sensor from (CNM, www.cnm.es) and its characteristics elaborating the limit of the present generation pressure sensors. The pressures at the lower end scale are offset by the limit of the sensitivity of poly-Si diaphragm.

Mathematically, piezoresistivity can be described as the linear coupling between mechanical stress and electrical resistivity. The piezoresistivity coefficient (π_{ijkl}) is a fourth rank tensor, and is defined by the relation between stress (σ_{kl}) and the electrical resistivity (ρ_{ij}) as:

$$\left(\frac{\Delta\rho_{ij}}{\rho_o}\right) = \pi_{ijkl}\sigma_{kl} \qquad (1)$$

Where stress and resistivity are second rank tensors, $\Delta\rho_{ij}$ is the change in resistivity, and ρ_o is the resistivity in unstressed state. The index in the piezoresistivity tensor defined by the above equation, π_{ijkl} cannot be interchanged implying, $\pi_{ijkl} \neq \pi_{klij}$. In triclinic crystals there are 36 non-zero coefficients for the piezoresitivity tensor but the number of components can be greatly reduced for the other point groups. Rewriting the above equation in Voigt or the matrix notation: [41,42]

$$\left(\frac{\Delta\rho_i}{\rho_o}\right) = \pi_{ij}\sigma_j \qquad (2)$$

The factors of 2 appear in the conversion whenever i = 1-6 and j = 4-6, such as $\pi_{11}=\pi_{1111}$, $\pi_{12}=\pi_{1122}$, $\pi_{16}=2\pi_{1112}$, $\pi_{44}=2\pi_{2323}$ etc.

The coefficients commonly of interest are longitudinal π_{11}, transversal π_{12}, and hydrostatic π_h. For a cubic material, these coefficients can be determined using relations:

(i) Uniaxial stress, current, and voltage measured in the same direction:

$$\pi_{11} = \Pi_{11} - (s_{11} - 2s_{12}) \qquad (3)$$

(ii) Uniaxial stress measured perpendicular to the direction of current and voltage:

$$\pi_{12} = \Pi_{12} + s_{11} \qquad (4)$$

(iii) Hydrostatic pressure, p corresponds to the case when $\sigma_1 = \sigma_2 = \sigma_3 = -p$ and $\sigma_4 = \sigma_5 = \sigma_6 = 0$:

$$\pi_h = \Pi_h - (s_{11} + 2s_{12}) \qquad (5)$$

where, s_{ij} are the elastic compliances and $\Pi = \Delta R/R_o$ corresponds to measured change in resistance.

The hydrostatic tensor coefficient π_h is related to π_{11} and π_{12} as:

$$\pi_h = -(\pi_{11} + 2\pi_{12}) \qquad (6)$$

A more common and widely used term in sensor terminology is the gauge factor or strain coefficient of piezoresistivity. It is denoted by ‘m’ and is described as:

$$\left(\frac{\Delta\rho_i}{\rho_o}\right) = \pi_{ij}\sigma_j \Rightarrow \left(\frac{\Delta\rho_i}{\rho_o}\right) = \pi_{ij}c_{jk}\varepsilon_k \Rightarrow \left(\frac{\Delta\rho_i}{\rho_o}\right) = m_{ik}\varepsilon_k \qquad (7)$$

1.4 Magnetic field sensors

Magnetoelectric composite sensors work on the following principle: An external AC magnetic field creates strain in the magnetostrictive layer which is elastically transferred to the piezoelectric layer which produces electric charge. The sensitivity of such sensor is proportional to the permeability and permittivity of the composite material. A large permeability material such as Metglas and a large permittivity material such as PZN – PT single crystal provide high magnitude of ME coefficient.

Table 1.1 List of current magnetic field sensing technologies

Magnetic sensor Type	**Detection principle**	**Sensitivity (G)**	**Frequency limits**	**Power**	**Size**	**T (℃)**
Search coil	Faraday’s law	10^{-6}-10^{-10}	1Hz-1MHz	1-10mW	2”-5”	
Flux gate magnetometer	magnetic induction and ferromagnetic hysteresis	10^{-6}-10^{2}	Max 10 KHz	5-50mW	1” or less	
Optically pumped Magnetometer	Zeeman effect	10^{-8}-1		~10W	12-20”	
Nuclear precession magnetometer	Gyro magnetic resonance	10^{-7}-1		0.5W	12-20”	
SQUID Magnetometer		10^{-10}-10^{-4}		~		-273 to 200
Hall effect sensor	Lorentz force	10-10^{3}	1MHz	0.2W		-273 to 200
Magneto resistive magnetometer	Magneto-resistive effect	10^{-2}-50	1GHz	0.1-0.5mW		-55 to 200
Magneto diode		10^{-1}-10^{4}			0.25”	-100 to 100

Table 1.1 continued.

Magneto transistor	Hall and Suhl effect	10^{-2}-10^{4}				
Fiber optic magnetometer	Magnetostriction and optical interference	10^{-7}-10	Below 60 Hz		4''	~
Magneto optical sensor	Faraday polarization effect	10-10^{8}			~	~
Magnetoelectric detector	Magnetoelectric effect	10^{-3}-10^{3}	10^{5}Hz- 10^{-2}Hz		~	-75 to 70

As seen from the table above, SQUID has highest sensitivity but they need coolant to keep the super conducting material operating in its superconducting phase hence are quite expensive. ME sensors are relatively new entry in the magnetic sensing materials and have moderate to high sensitivity. Figure 1.8 summarizes the detection range of various magnetic field sensors (taken from http://www.misl-usa.com/articles.html)

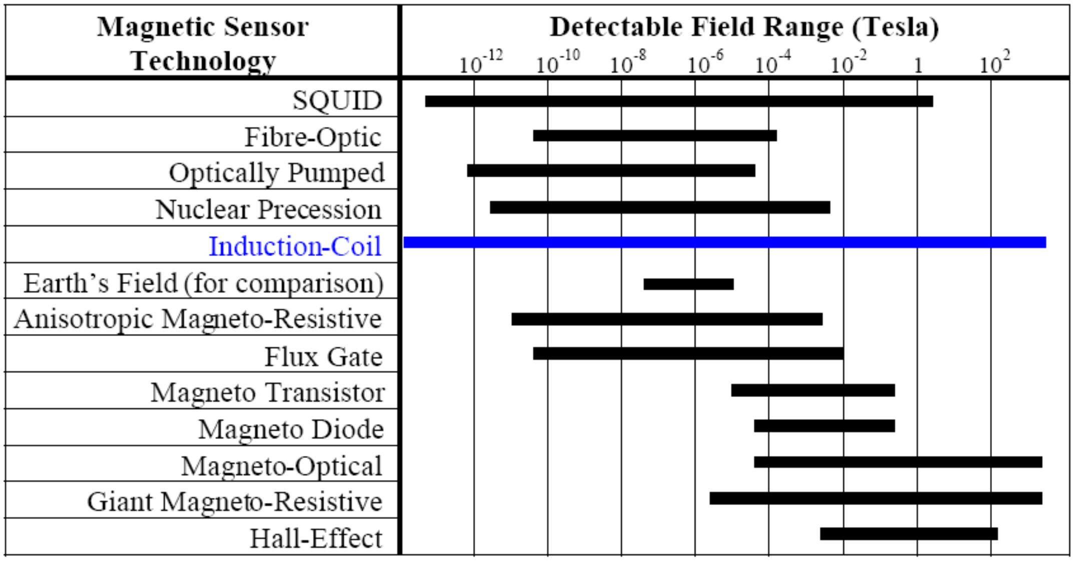

Figure 1.8 Detection range of various magnetic field sensors (taken from http://www.misl-usa.com/articles.html)

1.5 Energy Harvesting technologies

1.5.1 What is high energy density material?

The primary factor for the selection of a piezoelectric material for an energy harvesting device and for sensor applications is the transduction rate. *The magnitude of the transduction is governed by the effective piezoelectric stress constant, d, and the effective piezoelectric voltage constant, g*. Using linear constitutive piezoelectric equations, a relation between the energy density of the piezoelectric material and the transduction coefficient (d.g) under an applied stress *X* can be derived. Under an applied force ($F = X \cdot A$, where *A* is the area), the open circuit output voltage (*V*) of the ceramic is given as:

$$V = E \cdot t = -g \cdot X \cdot t = -\frac{g \cdot F \cdot t}{A} \qquad (1)$$

where t is the thickness of the ceramic, *E* is the electric field, and g is the piezoelectric voltage coefficient. At low frequencies (far from resonance), a piezoelectric plate can be assumed to behave like a parallel plate capacitor (*C*). Hence, electric energy available under an alternating stress excitation is given as: $U = \frac{1}{2}CV^2$ or energy per unit volume, $u = \frac{1}{2}(d.g) \cdot \left(\frac{F}{A}\right)^2$

(2)

Equations (1) and (2) show that under given experimental conditions, a material with high (d.g) product and high g constant will generate high voltage and power when the piezoceramic is directly employed for energy harvesting and sensing.

We have developed a complete analytical model relating the microstructural features to the magnitude of piezoelectric constant. The criterion for maximization of the product (d.g) with respect to the microstructure variable x (such as grain size) can be determined as following: [43, 44]

$$\left|d\right| = \varepsilon^{n} \tag{3}$$

where ε is dielectric constant and n is constant. Using Eq.(3) the maximum magnitude of the product (d.g) is given as:

$$\mathrm{Max}(d.g) = \varepsilon^{2n-1} \tag{4}$$

Our results indicate that all the materials follow the Eq.(3) and scale with the magnitude of n. Figure 1.9 shows the results on the PZT – PZN system illustrating the fact that as the magnitude of n decreases to unity the magnitude of g increases sharply (min(n) = 0.5). [45-46] We have conducted preliminary research on fabrication of the polycrystalline ceramic composition with desired microstructure (such as grain size and shape) for the PZT-based compositions. Using modified sintering process, we were able to obtain a ceramic composition exhibiting the magnitude of g_{33} and d_{33} as 55.56 x 10^{-3} m^2/C and 291 x 10^{-12} C/N respectively, yielding the magnitude product $d_{33}.g_{33}$ as ~16168 x 10^{-15} m^2/N which is significantly higher than the reported values in literature. In this program we propose to investigate the synthesis process and fundamental studies on microstructure design that can yield high energy density along with high fracture toughness.

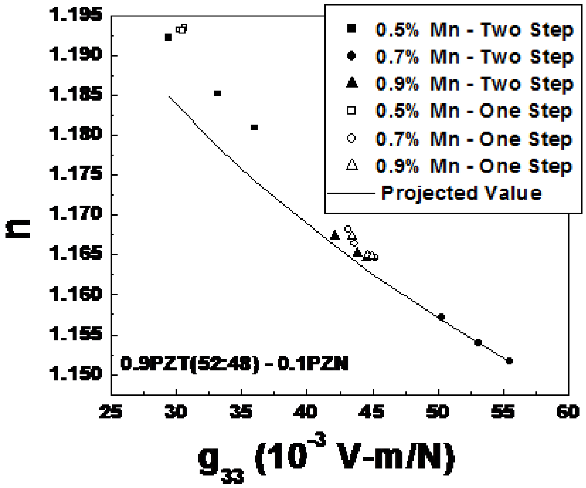

Figure 1.9 Variation of material constant, n, as a function of piezoelectric voltage coefficient, g_{33} for the composition 0.9PZT (52: 48) – 0.1 PZN + y wt% $MnCO_3$. Two step sintering refers to the process where the ceramic is held at high temperature for few minutes and then quenched to a lower temperature and held for long time period. One step refers to conventional sintering.

There are two extreme cases to the high energy density material, PVDF piezoelectric polymer (d_{33} = 33 pC/N, $\varepsilon_{33}/\varepsilon_o$ = 13, g_{33} = 286.7 x10^{-3} m^2/C) and relaxor piezoelectric single crystals such as PZN – 7%PT (d_{33} = 2500 pC/N, $\varepsilon_{33}/\varepsilon_o$ = 6700, g_{33} = 42.1 x10^{-3} m^2/C). It can be seen from this data that piezoelectric polymer has the highest piezoelectric voltage constant, g_{33}, of 286.7 x10^{-3} m^2/C and relaxor-based single crystals have the highest product ($d_{33}.g_{33}$) of the order of 105250 x 10^{-15} m^2/N.

1.5.2 What other material parameters are important?

Recently, a quantitative model was reported describing the efficiency (η) of the mechanical to electric conversion process as: [47]

$$\eta = \left(\frac{1}{2}\right)\frac{k^2}{1-k^2} \Bigg/ \left(\frac{1}{Q_m} + \frac{1}{2}\frac{k^2}{1-k^2}\right) \tag{5}$$

where k is the coupling factor and Q_m is the mechanical quality factor of the material. Consequently, designing a high energy density material for harvesting involves the realization of “hard” and “soft” properties at the same time. In order to develop such a ceramic the most critical component in addition to proper composition is microstructure. Based on a simple damped spring-mass model it can be shown that the maximum generated power from the energy harvester is given as:

$$P_{\max} = \frac{mY_o^2 \omega_n^3}{4\varsigma} \qquad (6)$$

where $\omega_n^2 = k/m$ is the system resonant frequency, $\varsigma = d \big/ 2\sqrt{mk}$ is the damping ratio, m is the seismic mass (electrical analog inductance, L), d is the damping constant (electrical analog resistance, R), k is the spring constant (electrical analog inverse capacitance, 1/C), and Y_o is the maximum amplitude of the vibration. A high magnitude of the spring constant requires high elastic modulus in the material.

In this thesis, we propose to implement piezoelectric energy harvesters using high energy density materials. Piezoelectric generator consists of three energy transformation steps and three kinds of losses. In the first step, the ambient energy is transformed in to the mechanical vibration energy of the piezoelectric transducer using simple mechanical structure which could be directly incorporated in the transducer assembly. In this step, there is mechanical loss related to the mechanical impedance such as damping factor and reflection ratio. In the second step, the mechanical vibration energy is transformed into electrical energy through direct piezoelectric effect. Energy transduction rate depends on electromechanical coupling factor and piezoelectric constant of the material. In the third step, the generated electrical energy is transferred to the sensor. Generally, electrical impedance matching methods are required to enhance the efficiency of transfer process. Piezoelectric harvester can be easily modified to interact with any stray magnetic field in the surrounding and capture magnetic energy. [48]

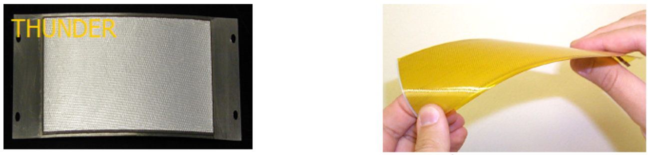

THin layer **UN**imorph **Driv**ER

Active **F**iber **C**omposite

Macro**F**iber **C**omposite

Radial **F**ield
Diaphragm

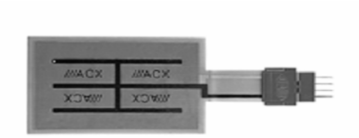

Figure 1.10 Pictures of the commercially available low-profile commercial flexible piezoelectric transducers. Most commonly, MacroFiber composites (MFCs) operating in d_{31} mode are utilized. MFCs have been extensively modeled and characterized for performance. Life-time testing on MFC's shows no changes in output power up to 1.4 million cycles.

The maximum power from the piezoelectric transducers is obtained by operating at the resonance frequency which is dependent upon the configuration, size, and loading conditions. MFCs can be easily tailored to match the resonance conditions. MFCs are available from the company Smart Materials Inc., Florida. There are several structural modifications that can be done to MFCs to couple with the strain effectively.

CHAPTER 2

MOTIVATION AND RESEARCH OBJECTIVES

2.1 Motivation of Research

Recent advancements in sensor networks have resulted in increased power demands for continuous functioning of the sensor networks. These sensors include pressure sensors, chemical sensors, optical sensors, temperature sensors, magnetic field sensors etc. all these sensors are provided with power using various techniques, primarily through batteries. Batteries need recharging, periodic replacement and it is a hazardous waste. The sensors used in data acquisition systems in remote networks require a centralized energy source for continuous operation and thus need continuous maintenance which is expensive and may delay the operation. In addition to power source, there are several issues regarding the performance of the sensors that needs to be addressed including sensitivity of the sensor, reduction of power consumption, and multifunctionality which can reduce the number of sensors. There is a strong need to develop self powered sensor networks which utilize available energy sources for harvesting and supplying continuous power to the sensors.

2.2 Objectives of Research

Motivated by the problems mentioned in the previous section, this thesis tries to address these limitations by reducing the power consumption of these sensors and development of mechanisms to generate electrical power on demand.

The primary goals of this thesis are:

1. Design new architectures for sensing pressure and magnetic field and analyze the fundamental mechanism using theory and experiments.

2. Synthesize advanced nanomaterials to implement the novel sensing techniques.

3. Develop understanding of mechanical energy harvesting to derive the function for power density and efficiency. Apply this understanding to design, fabricate and characterize energy harvesters.

CHAPTER 3

EXPERIMENTAL APPROACH AND TECHNIQUES

3.1 Powder Synthesis

Conventional mixed oxide ceramic processing route was followed to synthesize all the bulk ceramic compositions used in this thesis. Figure 3.1 shows a schematic of process flow for ceramic powder synthesis.

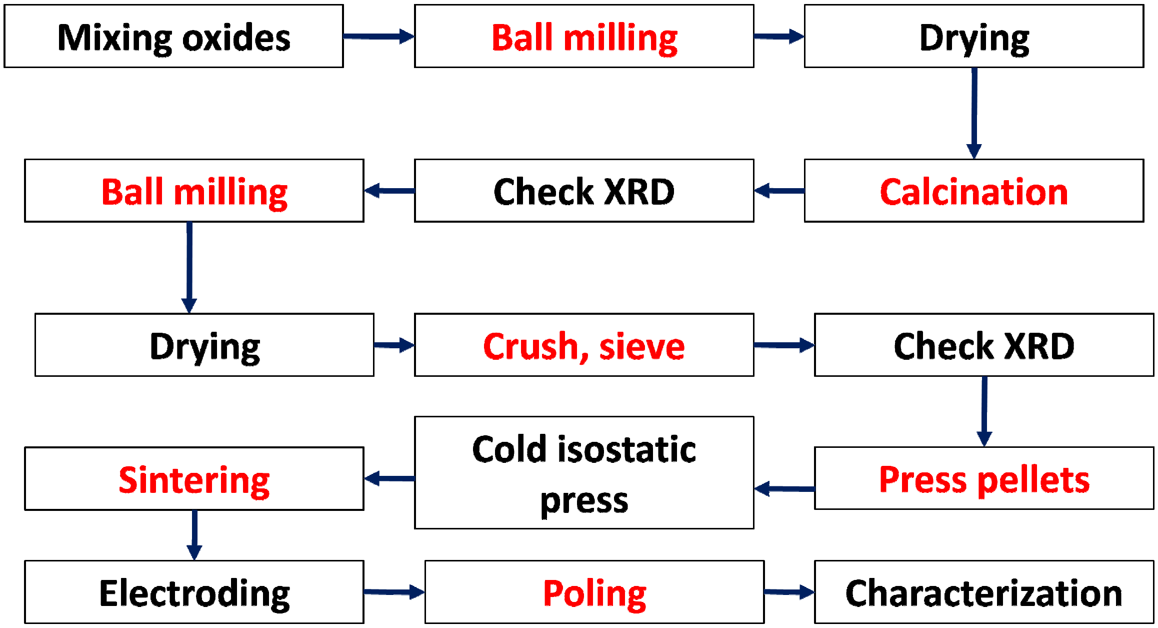

Figure 3.1 Conventional ceramic processing route.

Synthesis of hard piezoelectric composition is described below. Reagent-grade powders of PbO, ZrO_2, ZnO, NiO, Nb_2O_5, MnO_2, and TiO_2 were obtained from Alfa Aesar Co. (Ward Hill, MA). Stoichiometric ratios of powders corresponding to the composition $0.9Pb(Zr_{0.56}Ti_{0.44})O_3$ – $0.1Pb[(Zn_{0.8/3}Ni_{0.2/3})Nb_{2/3}]O_3$ + 2 mol% MnO_2 (PZTZNN) were ball milled with ethyl alcohol and YSZ grinding media (5 mm diameter, Tosoh Co. Tokyo, Japan) in a polyethylene jar for 24 h.

After drying, the PZTZNN powder was calcined at 800℃ for 3 h. Calcined powder was crushed, sieved and then ball milled separately with alcohol and grinding media for 30 ~ 48 h. After ball milling, the powders were dried at 80℃ and sieved. Sieved powders were pressed in to discs of dimension 12.7 mm x 1 mm using a hardened steel die and hydraulic press under a pressure of 1.5 ksi. The green body was next pressed in cold isostatic press (CIP) operating at 20 ksi for 10 min in order to improve the density of the green body. After CIP, the samples were sintered in air atmosphere using a Sentrotech furnace at 1050℃ for 2 h. The sintered samples were then polished and electroded using Ag-Pd electrode with firing temperature of 650℃. The samples were poled at 3-4 kV/mm using a high voltage supply in an oil bath maintained at 120℃.

3.2 Structural Characterization: Phase and Crystal Structure

X-ray Diffraction (XRD) was used in order to confirm the phase of the synthesized powder. (Siemens Krystalloflex 810 D500 and Xpert – PRO X-ray Diffractometer from PANalytical, Inc.) Fine powder of PZT composition after calcination was pressed in a sample holder of the X-ray diffractometer using a glass slide. A typical XRD pattern of as synthesized powder of PZTZNN is shown in following figure where a single phase perovskite structure can be seen.

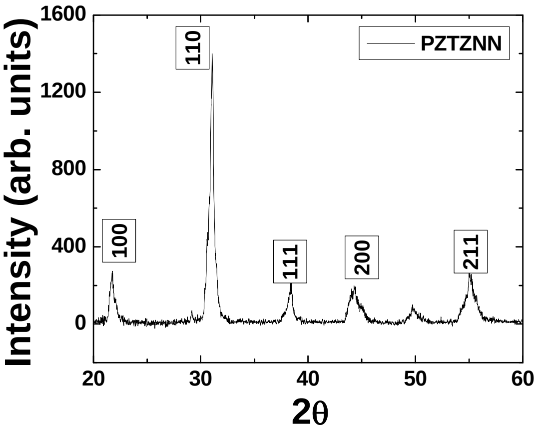

Figure 3.2 XRD pattern of PZTZNN calcined powder.

3.3 Microstructural Characterization

3.3.1 Optical Microscopy

Optical microscopy was used to observe the surface of the samples after sintering and any other heat treatment. Optical microscopy was also used to confirm the soldering and bonding joints on the bimorph transducers.

3.3.2 Scanning Electron Microscopy

Scanning electron microscopy was performed using LEO (Carl Zeiss SMT, Inc.) 1550 high-performance Schottky field-emission SEM. Before SEM, ceramic samples were annealed at a temperature 100 ℃ below the sintering temperatur e and held for 30 mt and then cooled down to room temperature at the rate of 3^oC/min. Nanowires distribution and aspect ratio was determined by SEM under high magnification. Cross-sectional SEM was performed to confirm the grain morphology and packing.

3.3.3 X-ray Energy Dispersive spectrum (EDS)

Elemental analysis was performed using Oxford INCA Energy E2H X-ray Energy Dispersive Spectrometer (EDS) system with silicon drifted detector to identify the concentration and distribution of elements. Spot EDS and area EDS are most commonly used for determination of elements based on the X-ray energy dispersive spectrum. Elemental mapping option available in the EDS was used to study the interface characteristics in composite and layered materials.

3.3.4 Transmission Electron Microscopy (TEM)

Philips 420 TEM was used in order to observe microstructure of PZT samples as well as nanoparticles and nanotubes. High resolution Transmission Electron Microscopy was performed using FEI Titan 300, with acceleration voltage of 200 KeV in order to study interfacial characteristics of nanotube samples. The stoichiometric composition and chemical information of the sintered ceramics and nanotubes was studied using a high performance multi-technique surface analysis. Cross-sectional and plan-view TEM sample preparation was performed in our laboratory using a well-established method. Selected-area electron diffraction, bright-field and dark field imaging was used to examine the quality and crystallographic structure of the composites, morphology and distribution of nanotubes boundaries, and misfit dislocations at the inter phase interface as well as other microstructural features. In conjunction with the TEM, nano-beam electron diffraction and X-ray energy-dispersive spectroscopy (EDAX) with a probe size down to a few nanometers, was employed to investigate the crystallographic structure and stoichiometric composition across the interface boundaries. Combined, all these experimental results were used to establish the structure – property relationship for composites.

3.3.4.1 Bulk Ceramic TEM Sample Preparation

TEM sample preparation consisted of cutting the ceramic bulk sample in to small pieces of less than 2x2 mm^2 area. The sample was then polished on both sides until surface became optically clean. This mirror-like polished sample was then glued on a Copper TEM grit by using a M-BOND epoxy on opposite side of the sample. This grit was then mounted on a transparent stub and further polished up to the sample thickness of 50 ~ 75 µm. Next, sample was mounted on a dimple grinder to further grind and polish it with copper with constant rotation of the stage until sample turns slightly transparent in the middle. Next,high energy ions were bombarded at the center of the sample using a ion milling machine.

3.3.4.2 Nanotubes and nanoparticles sample preparation

Nanotubes were first dispersed in propanol or isopropyl alcohol and then ultrasonicated for 5 – 10 minutes for homogeneous mixing. Next, a dropper was used to disperse a small drop of this solution on a Lacie carbon Copper TEM grit. Samples were then dried overnight at room temperature and sealed in a box for TEM characterization.

3.4 Surface Characterization

3.4.1 X-ray Photoelectron Spectroscopy

The PHI Quantera SXM Scanning Photoelectron Spectrometer Microprobe (XPS) was used for quantitative analysis of the chemical elements and chemical states within the top few nanometers of a surface. The XPS consists of a focused, monochromatic X-ray source for small-spot analysis, and it was automated for high sample throughput. Depth profiling was accomplished with automated ion milling. A general spectrum of SiCN MWNTs is shown in the following figure consisting of peak intensity for different binding energy (BE) of the elements.

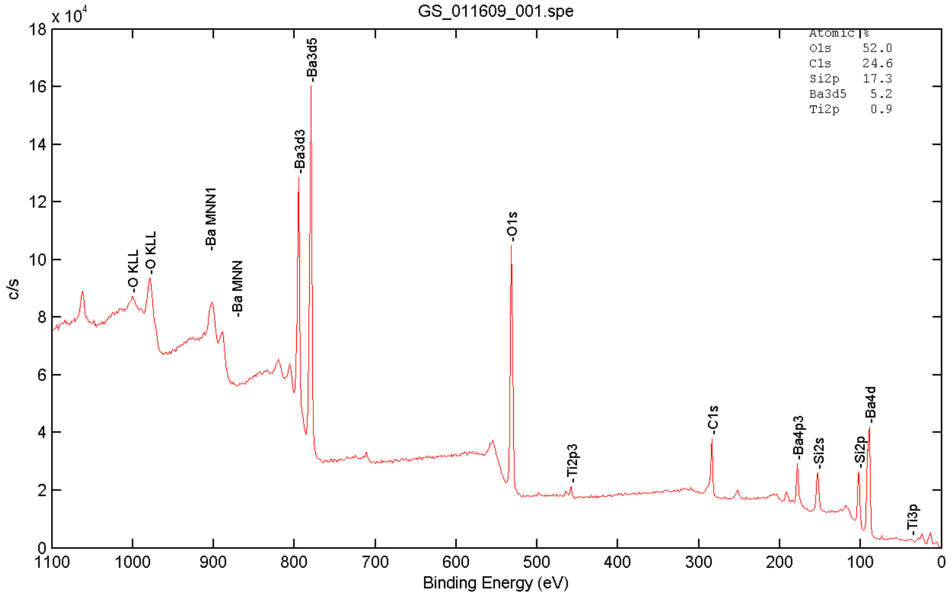

Figure 3.3 A typical XPS survey spectrum

3.4.2 Contact angle measurement

A thin layer of MWCNTs was deposited on the Si/SiO2/Ti/Pt wafers using spin coating with a recipe of 1000 rpm for 10 seconds. The samples were dried in air atmosphere. Contact angle measurements were performed using FTA 200 Dynamic Contact Angle Analyzer (First Ten Angstroms, Inc.). The system consisted of a moving stage and a Sanyo Navitar high resolution camera with zoom microscope. The live image was captured with the help of computer software for further analysis. A water drop was pushed out of a computer controlled syringe pump on the surface under investigation which then settled down on the surface. The drop was then focused on the screen with the help of microscope and contact angle was measured by drawing the sharp edges of the baseline and the drop. Measurements were repeated 3 – 4 times and then averaged to arrive at final angle.

3.5 Electrical Characterization

3.5.1 Dielectric and Piezoelectric measurements

Electromechanical properties and resonance characteristics were determined by HP 4194A impedance analyzer (Hewlett Packard Co. USA). The capacitance (C_p) and dielectric loss (tanδ) were measured using a HP 4274 LCR meter. The piezoelectric charge constant of the samples was measured by Berlincourt APC YE 2730A d_{33} meter. The coupling coefficient (k_p) mechanical quality factor (Q_m), piezoelectric voltage constant (g_{33}) and elastic stiffness were determined from these measured properties by following IEEE standard: [49]

For a radial mode disk, s_{11}^{p} can be calculated as following:

$$s_{11}^{p} = \frac{\eta_1^2}{\rho(2\pi f_s a)^2[1-(\sigma^p)^2]} \qquad (3)$$

where η_1 is the frequency constant, σ^p is the planar Poison’s ratio, f_s is the resonance frequency, a is the radius and ρ is the density. The coefficients η_1 and σ^p can be found by measuring ratio of 1st overtone to fundamental resonance frequency (258 kHz). For example, for the ratio of 2.602 η_1 and σ^p values can be found to be 2.074 and 0.341 respectively from IEEE standards. Using these values s_{11}^p can be calculated. The transverse mode coupling constant k_{31} can be calculated by using the following expression [49]:

$$k_{31}^2 = k_p^2 \frac{(1-\sigma_p)}{2} \qquad (4)$$

If k_{31} and s_{11}^E are known, than d_{31} can be calculated as following:

$$k_{31}^2 = \frac{d_{31}^2}{(s_{11}^E \varepsilon_{33}^T)} \qquad (5)$$

The magnitude of s_{12}^E can be found by using the following expression [49]:

$$k_p^2 = \frac{2d_{31}^2}{[(s_{11}^E + s_{12}^E)\varepsilon_{33}^T]} \qquad (6)$$

3.5.2 Siglab Analyzer (Ref: www.mathworks.com)

Siglab analyzer (Mathworks, Inc.) integrated with Matlab for digital signal processing was used to characterize the energy harvesters. The system had 4 input channels and 2 output channels. SigLab performs various measurements including transfer function magnitude, phase, and coherence using broad band FFT techniques or swept sine, auto and cross correlation, and impulse response for non-stationary spectrum analysis. These measurements were all performed directly in the MATLAB environment, making them available for custom post-processing using MATLAB and Simulink, or comparison with theoretical performance. Samples were mounted on a Ling Dynamic shaker using a home built clamp. Acceleration measurements were taken on the base of the structure and tip mass by using a shear accelerometer (Piezotronics, Inc.), PDV 100 Laser vibrometer (Polytech, Inc.) and a spectral analyzer (Siglab

Model 20-42). The output from the accelerometer was sent through a sensor signal conditioner (Piezotronics Inc. Series 481). The output from laser vibrometer was recorded using Siglab. A small breadboard was used to vary the load resistors across the output of bimorph electrical terminals. The Siglab analyzer was used for collecting the time traces, power spectrums of acceleration and output voltage, and the transfer function from base acceleration to tip mass acceleration.

3.6 Mechanical Testing

Mechanical testing was performed using a 810 Materials Testing Machine (MTS corp.) for load controlled fatigue testing. For a load controlled fatigue test, the load limits were kept within 300 – 130 lbs and number of cycles were fixed at 20000 with a frequency of 20 Hz (i.e. 20 cycles/sec).

3.7 Magnetic Characterization

3.7.1 Vibrating Sample Magnetometer (VSM)

Typical setup of VSM involves mounting the sample at the end of a rigid rod attached to a mechanical resonator which oscillates the sample, usually in a vertical direction, at a fixed frequency (ω). Surrounding nearby the sample is a set of pick-up coils. As the sample moves, its magnetic field which is proportional to its magnetic moment, M, alters the magnetic flux through the coils, dM/dt. This induces a current directly proportional to dM/dt, which can be amplified and detected using lock-in amplifiers. The external magnetizing field is provided by a horizontal electromagnet. The magnetic moment can be converted into Magnetization (Ms) dividing by sample weight. A typical VSM measurement can be shown by Figure 3.4.

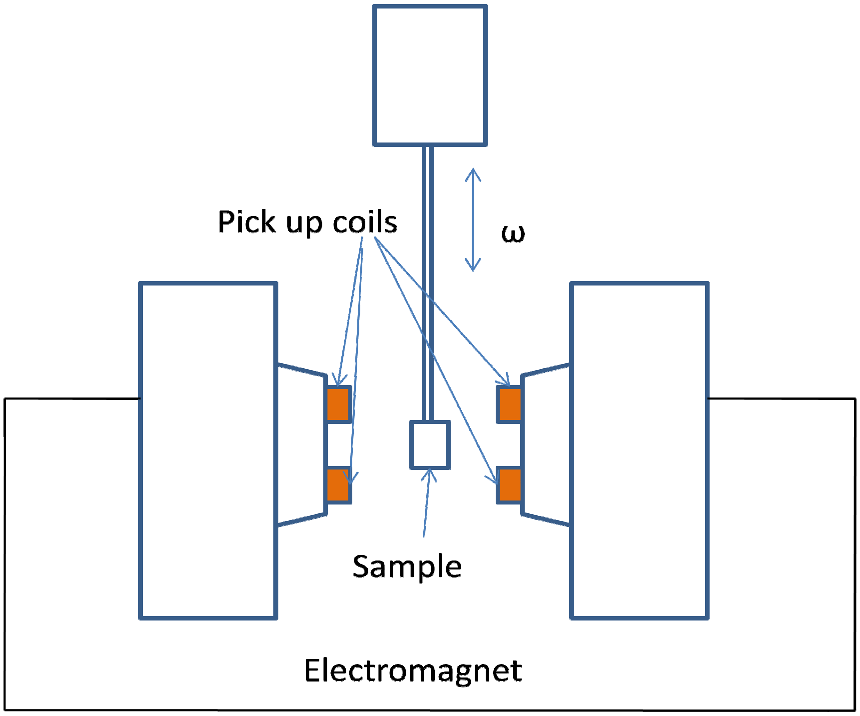

Figure 3.4 Vibrating Sample Magnetometer setup

3.8 Magnetoelectric Characterization

The magnetoelectric (ME) measurement consists of a DC bias field along with an AC magnetic field. The AC magnetic field was generated by a Helmholtz coil with calculated number of turns and geometry and powered by function generator. The output voltage generated from the composite was measured using a SR850 DSP lock-in amplifier (Stanford Research Systems. Inc.). Magnetoelectric coefficient (dE/dH) was measured by applying an A.C. magnetic field at 1 kHz and 1Oe amplitude (H) under varying DC magnetic bias. The ME coefficient (mV/cm.Oe) can be calculated by dividing the output voltage by the thickness of the sample and applied AC magnetic field. A typical ME measurement system is shown in the Figure 3.5.

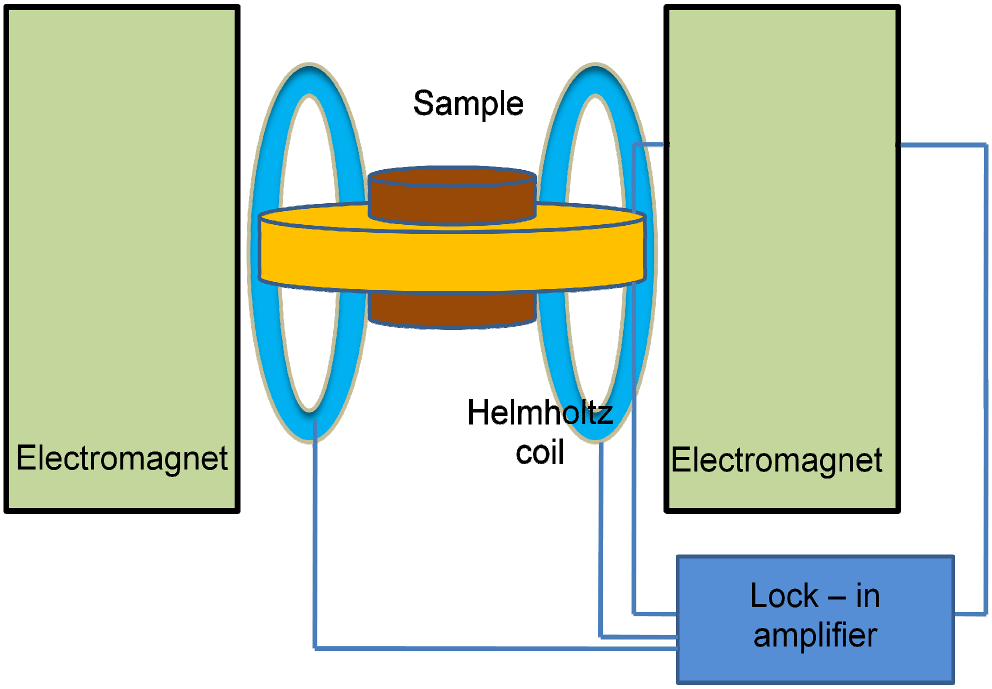

Figure 3.5 ME measurement system

CHAPTER 4

STRUCTURAL HEALTH MONITORING AND POWER ANALYSIS

4.1 Fatigue damage detection using Impedance Spectroscopy

4.1.1 Introduction

From chapter one the admittance signature of PZT sensor bonded to a structure can be written as:

$$Y(\omega) = i\omega a\left(\bar{\varepsilon}_{33}^{T}(1 - i\delta) - \frac{Z_s(\omega)}{Z_s(\omega) + Z_a(\omega)} d_{3x}{}^{2}\bar{Y}_{xx}^{E}\right) \qquad (1)$$

Here, the Za is the actuator impedance and Zs is the structural impedance. As discussed in chapter 1, any change in the structure will cause the change in the impedance response from the sensor attached to the structure.

In this chapter, we address the design issues of impedance based health monitoring sensors and investigate the response on a prototype rocket motor whose external casing was made of aluminum. [50] We further investigate corrosion detection using the optimized sensor design. Different sensor designs were fabricated for understanding the effect of excitation modes which are explained further in the experimental. From equation (1) it is clear that the imaginary part of the impedance/admittance is dependent on dielectric constant ε_{33}^{T}. Since ε_{33}^{T} is sensitive to temperature it affects the imaginary part of the impedance to a greater extent. Real part (R) of impedance is used for our analysis, therefore, it may be assumed to have no effects from temperature variations. To detect incipient damage with high sensitivity, electrical impedance is measured at high frequencies in the range of 50 kHz – 150 kHz. For this frequency range, wavelength of excitation is small and can easily detect defects like cracks and delaminations. [14, 51] The detection frequency band for the sensor is preferred to be far away from the PZT resonance frequency since the amplitude of the impedance peak corresponding to piezoelectric resonance response is much higher than the peaks corresponding to coupling between the structure and PZT. Several advantages of impedance spectroscopy technique can be summarized as follows: [52]

1. The technique can be easily applied to any complex structures since it is not based on any model.
2. The Piezoelectric material based sensors exhibit fast response, high conversion efficiency, light weight, higher range of linearity and long term stability.
3. High frequency range can detect very small local defects due to the very short wavelengths on the order of the micro-crack lengths.
4. Easy interpretation of the data using conventional techniques.
5. Implementation in non-accessible areas and provision of online damage detection.

4.1.2 Experimental procedure

Hard PZT composition $0.9Pb(Zr_{0.56}Ti_{0.44})O_3 - 0.1Pb[(Zn_{0.8/3}Ni_{0.2/3})Nb_{2/3}]O_3$ + 2 mol% MnO_2 (PZTZNN) was synthesized using a typical mixed oxide ceramic processing route. Two different sensor geometries were fabricated such as round and square. The dimensions of fabricated round shaped sensor were Φ10.4 x 0.5 mm3 whereas the final dimensions of the fabricated square sensor were 10.4 x 10.4 x 0.5 mm3. A square notch was created in order to initiate crack adjacent to the sensor location. Fabricated round and square sensors are shown in fig. 4.1.

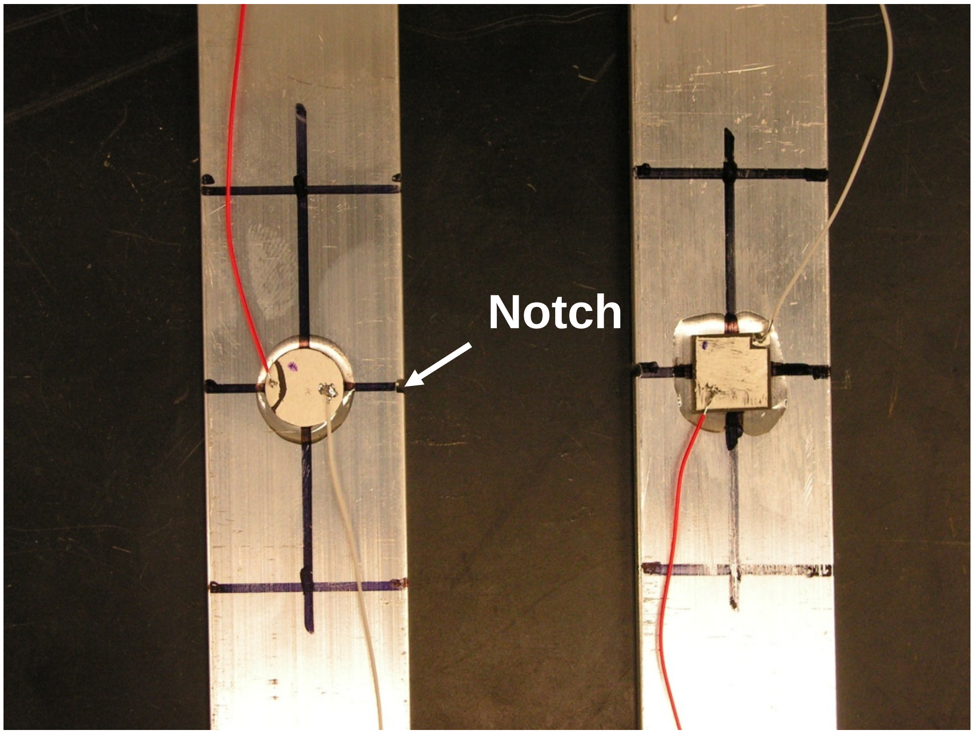

Figure 4.1 Fabricated PZTZNN round and square sensor designs

The impedance responses of round and squares sensors in the Free State can be summarized in Figure 4.32:

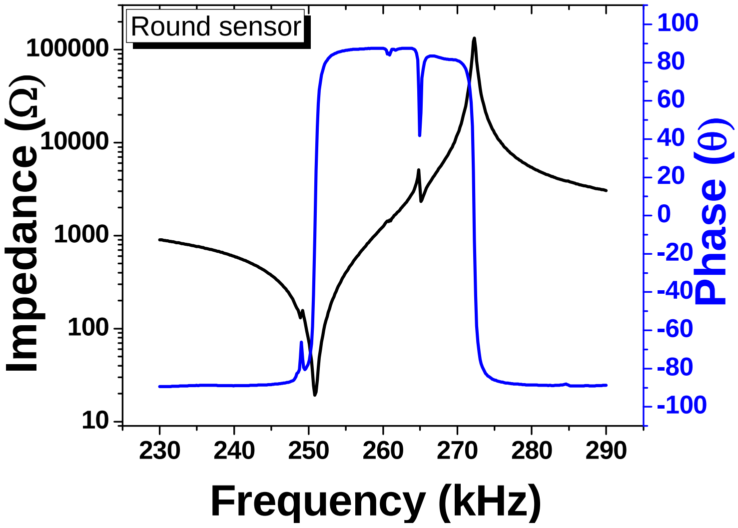

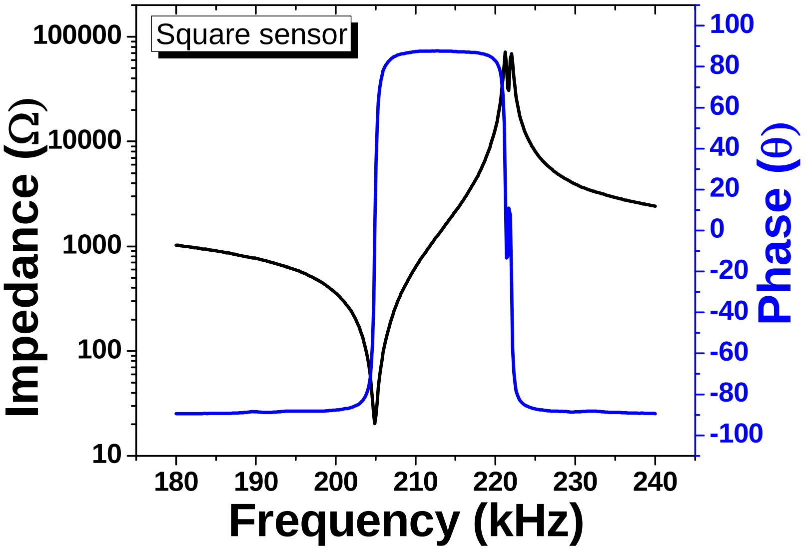

Figure 4.2 Free impedance responses of the round and square sensors fabricated with PZTZNN composition

The sensors were then bonded on the aluminum plate of dimensions 12 x 1 x 1/8 inches^3 as shown in Figure 4.1. Sensors were validated for structural bonding after every set of data. This can be done by simply monitoring the complex impedance and phase response of the sensor. It has been shown by Park et al. that during self diagnostics of piezoelectric active sensors the impedance signature approaches free state impedance signature if the sensor was debonded from the structure. Both the samples were subjected to load controlled fatigue test. Load was varied from 300 to 1300 lbs at a frequency of 20 cycles per sec. Impedance response was recorded after every 20000 cycles up to 100000 cycles which indicates crack initiation. The physical and mechanical properties of the aluminum used in this test are listed in Table 4.1 (www.matweb.com). [53]

Table 4.1 Mechanical properties of Al used for fatigue test (www.matweb.com)

Tensile Strength	310 MPa
Yield strength	275 MPa
Modulus of elasticity	69GPa
Density	2.7 gm/cc
Poisson’s ratio	0.33
Fatigue Strength	95 MPa
Fracture Toughness	29 MPa-m$^{1/2}$
Shear Modulus	26 GPa

4.1.3 Comparison of square and round sensor geometry

R-X responses for the entire fatigue tests for round and square samples can be shown in following figures.

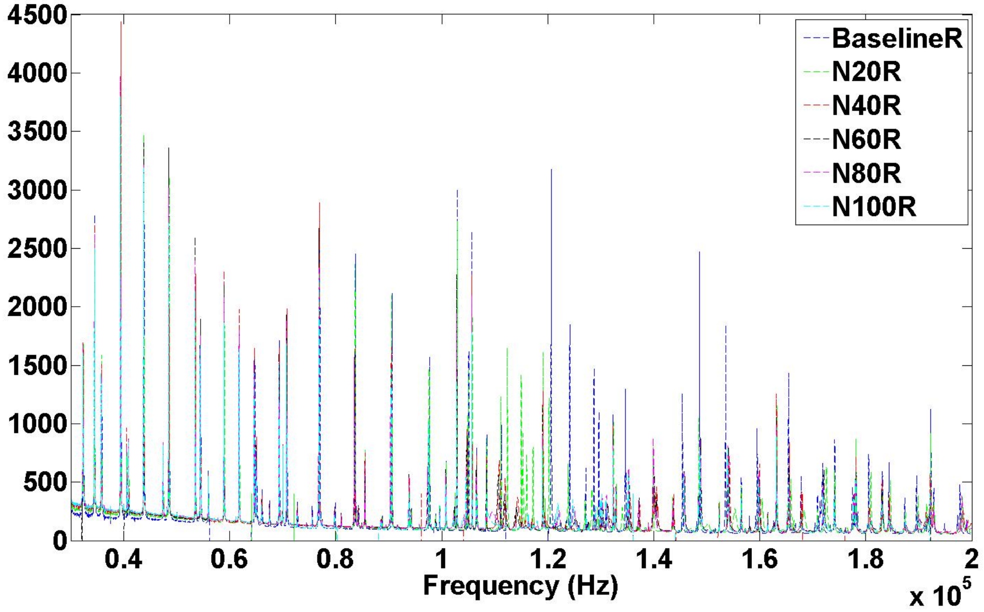

Figure 4.3 R-X response of round Sensor for the entire fatigue test (freq: 50 kHz – 150 kHz)

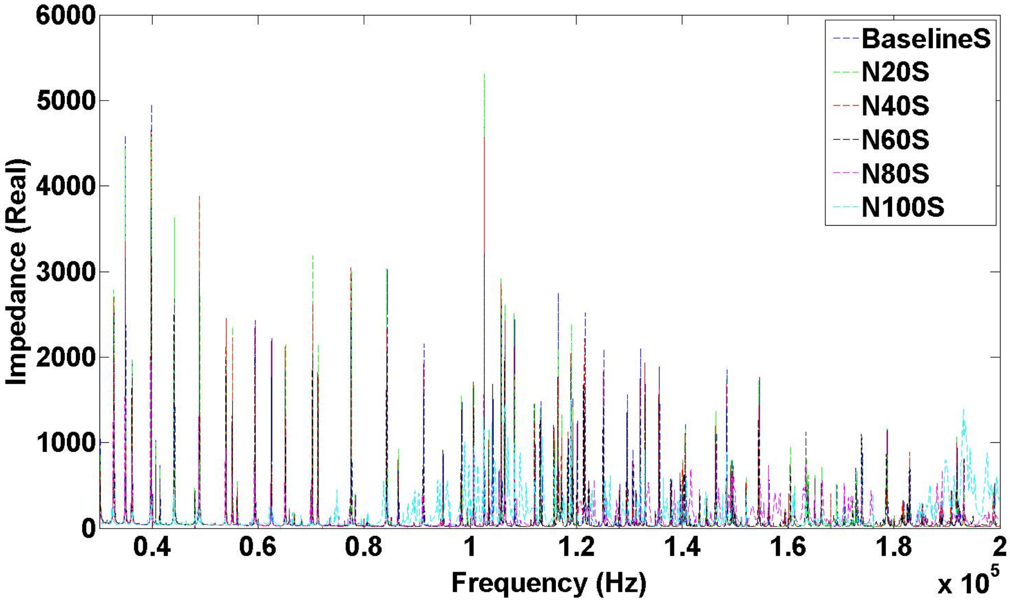

Figure 4.4 R-X response of square Sensor for the entire fatigue test (freq: 50 kHz – 150 kHz)

For quantification of damage a scalar metric was obtained using a root mean square deviation (RMSD) formula. Thus, the damage index metric can be represented by Eq. (2):

$$\text{Damage index} = \sqrt{\sum (R_1 - R_0)^2 \Big/ \sum R_0^2} \qquad (2)$$

where R corresponds to real part of impedance. The subscripts “1” and “0” correspond to the test id under consideration and baseline state respectively. The aluminum sample of same dimension and machined from same piece was used for all the fatigue tests. The impedance response after making the square notch was considered as a baseline measurement.

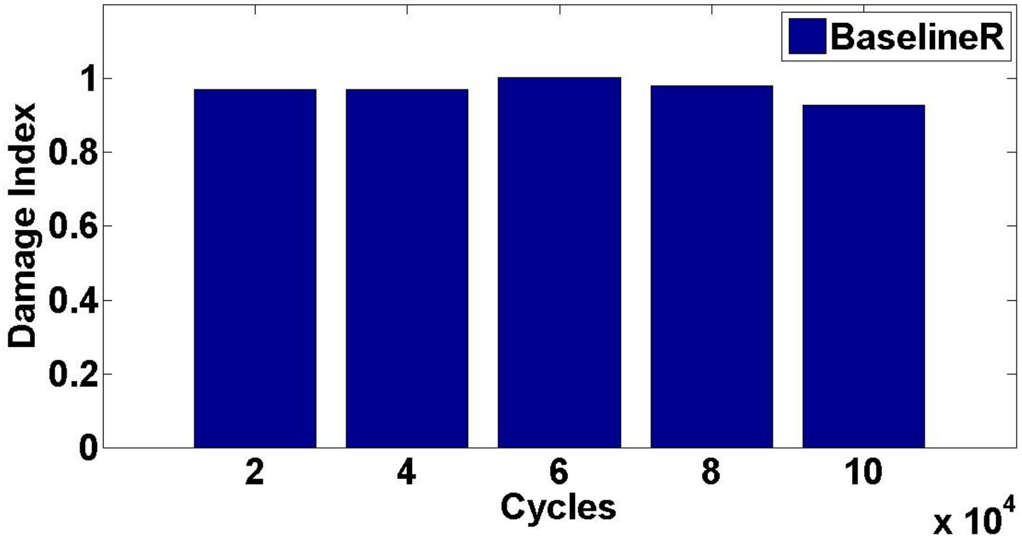

Figure 4.5 Damage index as a function of no. of cycles for round sensor (freq range: 50 kHz – 150 kHz)

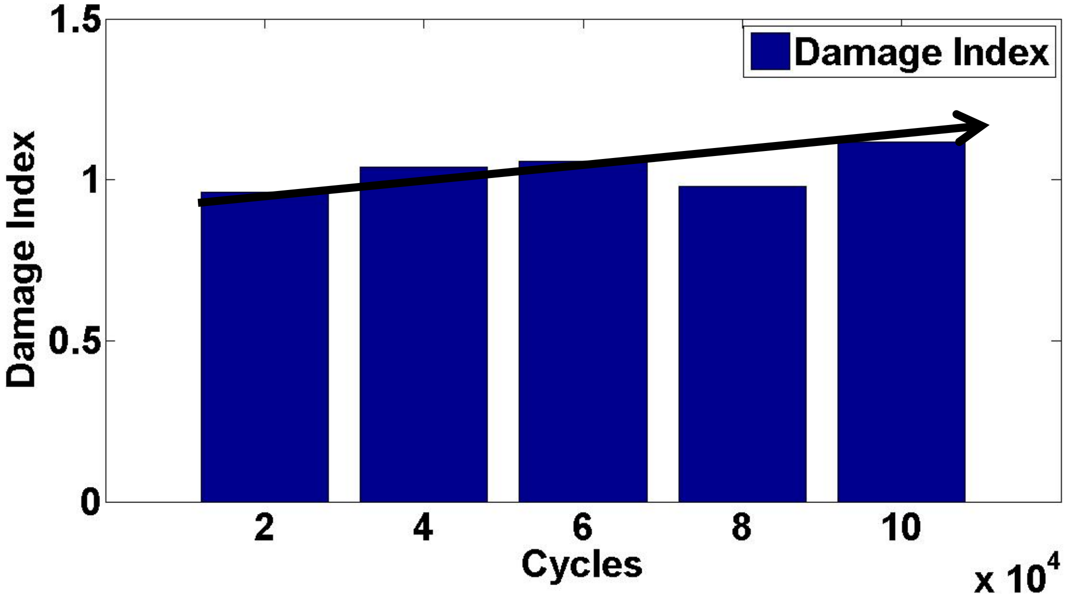

Figure 4.6 Damage index as a function of no. of cycles for square sensor (freq range: 50 kHz – 150 kHz)

The damage index metric for round sensor first increases up to 60K cycles and then decreases with increasing number of cycles, thus indicating reduction of the sensitivity after 60K cycles. The change in the magnitude of damage index was found to be small. This can be addressed by the effect of loading conditions used in the fatigue test. The load cycles of 300 – 1300 lbs is considerably smaller range for an aluminum beam of given dimensions. The quantified damage is small compared to a specimen with an induced visible crack. The square sensor showed consistently increasing trend of damage index metric for the entire fatigue test. Thus, square sensor was found to be more sensitive than the round sensor for the given conditions of the fatigue test. Based upon the analysis of damage index for the entire range we selected square sensor design as the sensor for damage detection of rocket motor and corrosion.

4.1.4 Selection of frequency band and sensitivity of the sensor

In order to investigate the effect of frequency band on the sensitivity of the sensor, three sensor designs were fabricated as follows. A soft PZT composition of $0.8[Pb(Zr_{0.52}Ti_{0.48})O_3]$–$0.2[Pb(Zn_{1/3}Nb_{2/3})O_3]$ (PZTPZN) having square geometry (10 x 10 sq. mm) with three different electrode areas (4, 6 and 9.6 sq.mm) were fabricated. Thus, the selected electrode areas of the sensors were 4 mm^2, 6 mm^2 and 9.6 mm^2. The sensors were subjected to identical fatigue testing conditions as explained earlier for the round and square shaped sensors and impedance response was recorded after every 20K cycles for the entire fatigue test. Broad frequency range was chosen in order to investigate the effect of frequency range on the damage detection for a particular electrode area of the sensor. The impedance response after making a notch was considered as baseline measurement.

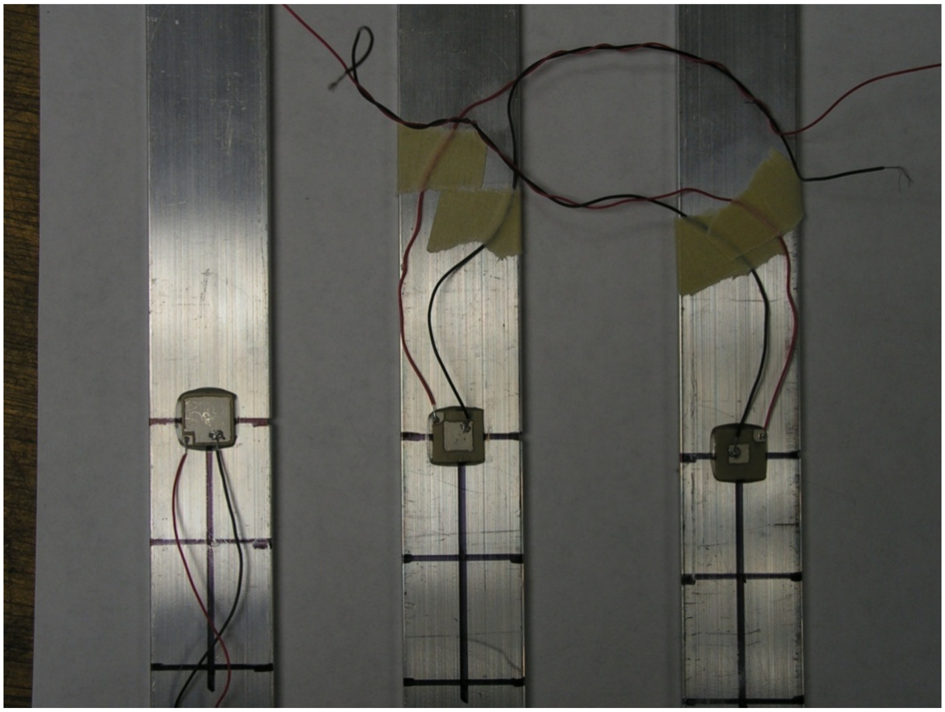

Figure 4.7 Fabricated sensors with different electrode area

The impedance responses of all the samples in the free state can be summarized in Figure 4.8. R-X responses for the entire fatigue tests are shown in Figure 4.9 - 4.11. While the impedance responses for the entire test gives qualitative approach to the damage, we propose a new strategy based on the number of peaks and magnitude of the real part of impedance monitored over the entire fatigue test in order to quantify the damage occurring to the aluminum specimen. The number of peaks above certain threshold (100Ω) are plotted for different frequency ranges to identify the optimum frequency range to be analyzed based on electrode area design.

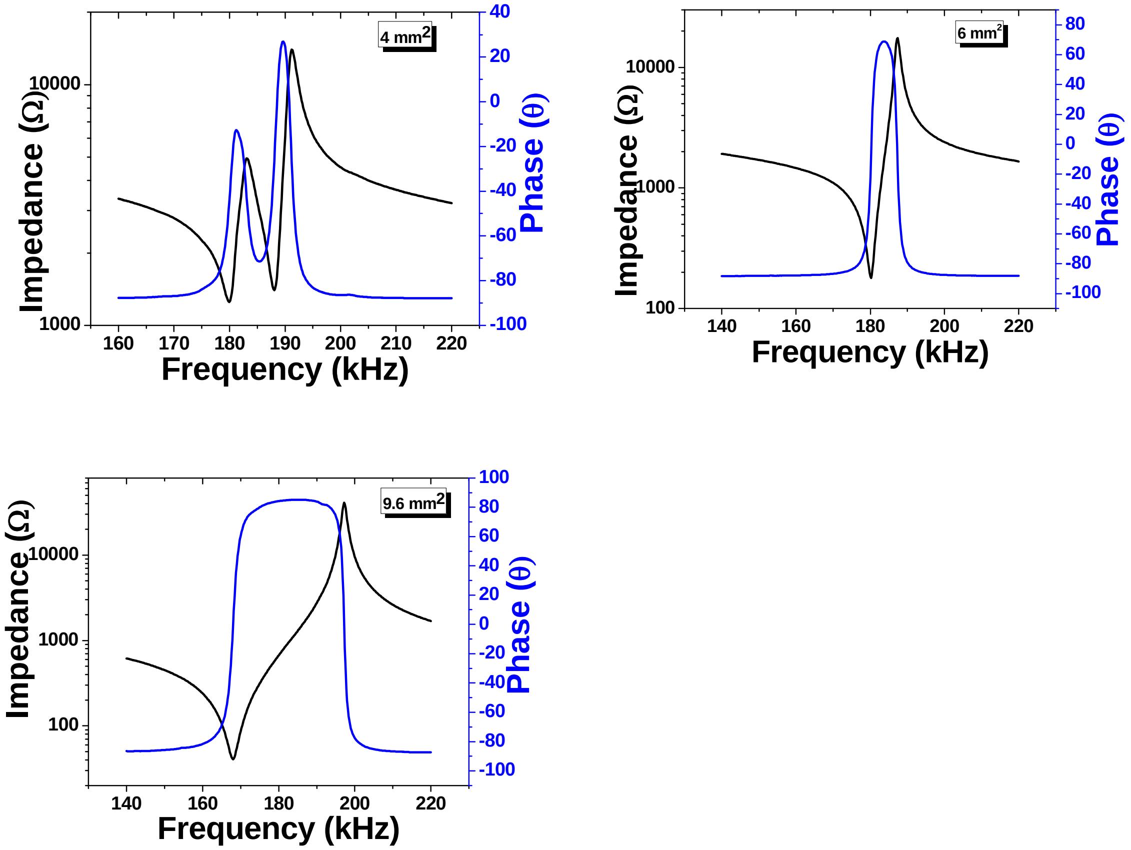

Figure 4.8 Free impedance responses of the 3 samples fabricated with PZTPZN material R-X responses for the entire fatigue tests can be shown in following figures.

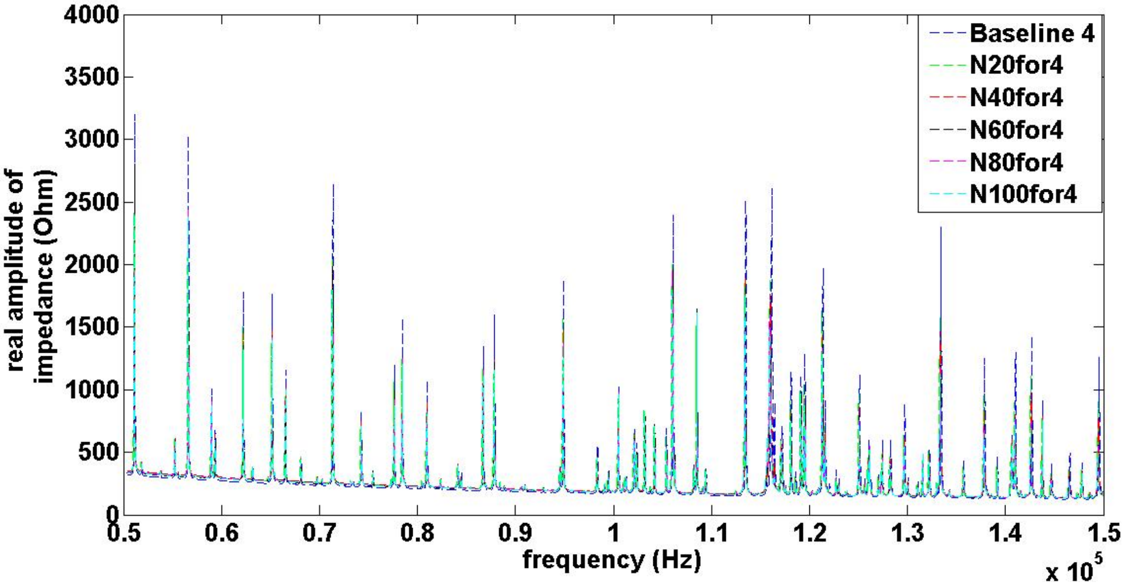

Figure 4.9 R-X response of Sensor with 4 mm^2 electrode area for the entire fatigue test (freq: 50 kHz – 150 kHz)

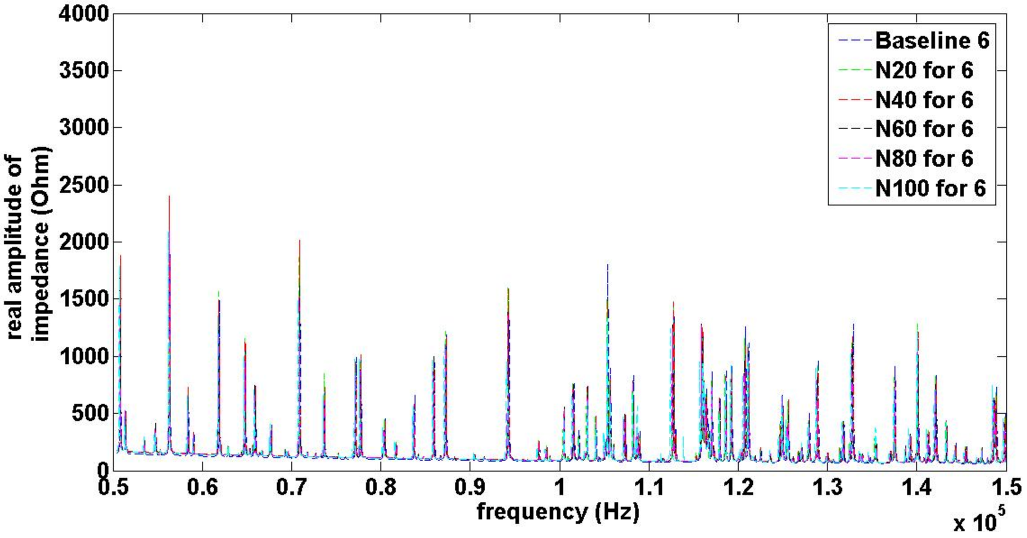

Figure 4.10 R-X response of Sensor with 6 mm^2 electrode area for the entire fatigue test (freq: 50 kHz – 150 kHz)

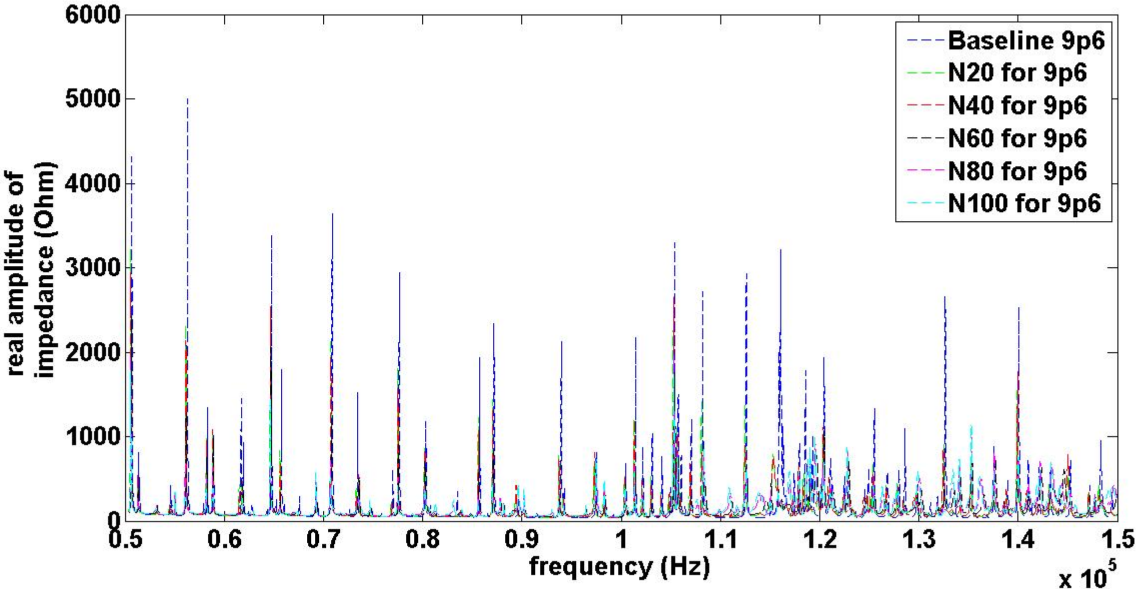

Figure 4.11 R-X response of Sensor with 9.6 mm^2 electrode area for the entire fatigue test (freq: 50 kHz – 150 kHz)

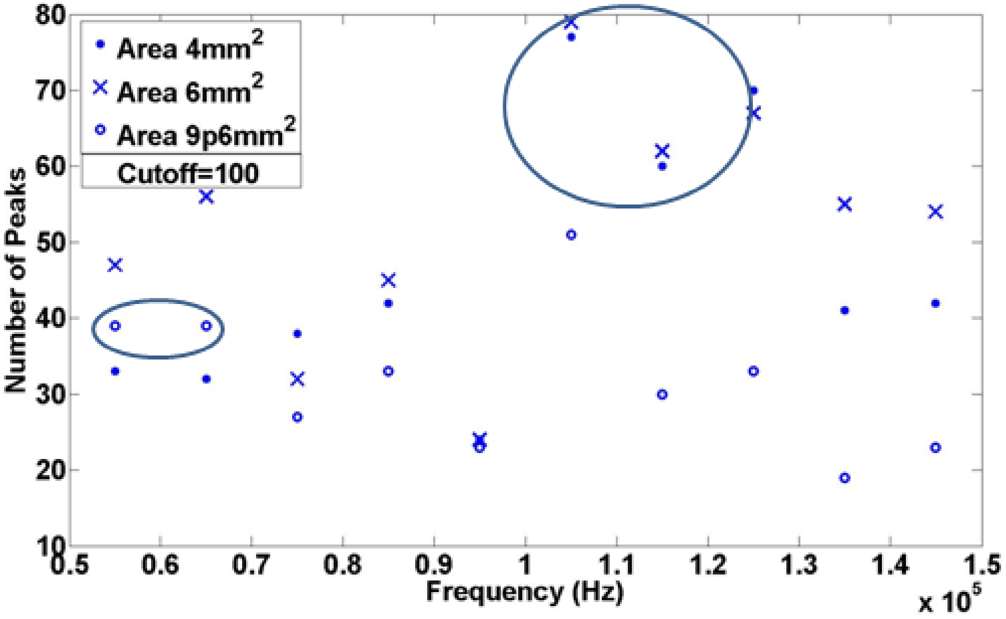

Figure 4.12 Number of peaks over entire range (50kHz – 150kHz) for all 3 sensors with cutoff = 100

Based on the results of Figure 4.12, we find that the range 100 kHz – 130 kHz shows high number of peaks consistently for the 4 and 6 mm^2 electrode areas. For 9.6 mm^2 electrode area, the frequency range of 50 kHz – 70 kHz was selected. Next, we focus on analyzing these frequency ranges further. The cutoff magnitude of real part of impedance was set at 1000 Ω and number of peaks for different frequency ranges namely, 100 kHz – 110 kHz, 110 kHz – 120 kHz and 120 kHz – 130 kHz were plotted and counted for baseline case, 20k cycles, 40k cycles, 60k cycles, 80kcycles and 100k cycles. Similar analysis was performed for sensor with area 9.6 mm^2 for frequency band of 50 kHz – 70 kHz and the results are summarized in Table 4.2 - 4.4.

Table 4.2 can be graphically represented by Figure 4.13. From Figure 4.13, one can observe that at certain frequencies the magnitude of impedance decreases with number of cycles, however, not all frequency peaks show this trend. Table 4.3 is graphically represented by plot shown in Figure 4.14. From Figure 4.14, it can be seen that peak intensity at the chosen frequencies show a decreasing trend over the entire fatigue test. Compared to the similar results for sensor with 4 mm^2 electrode area, the number of frequencies at which the impedance value decreases is higher. Thus, this sensor shows higher sensitivity compared to the sensor with electrode area of 4 mm^2. Further, it can be noticed that some frequencies shift towards lower values as the damage is induced in the specimen.

Table 4.2 Identification of peaks for sensor area 4 sq.mm

FreqPeaks	Baseline4	N204	N404	N604	N804	N1004
106040	2396.47	2002.96	1883.42	1971.46	1950.13	1794.87
108520	1582.12	1514.14	1516.8	1644.04	1527.78	1615.1
113440	2513.42	1852.77	1901.58	1782.72	1766.12	1745.7
115960	2605.26	1888.38	1764.51	1645.87	1599.4	1477.69
121340	1970.24	1630.31	1431.37	1363.62	1327.02	1279.29

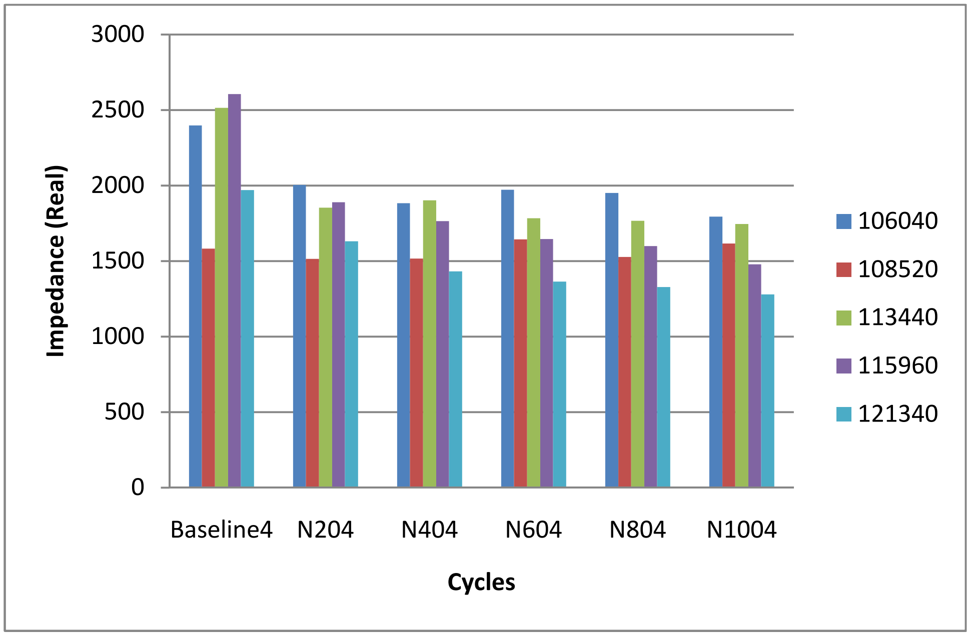

Figure 4.13 Identified peak intensity as a function of no. of cycles for 4 sq.mm area

Table 4.3 Identification of peaks for sensor area 6 sq.mm

FreqPeaks	Baseline6	N206	N406	N606	N806	N1006
105400	1801.11	1511.65	1481.51	1324.77	1249.81	1329.76
112720	1348.96	1495.9	1469.83	1274.48	1239.34	1246.34
115920	1178.48	1204.79	1263.83	1282.81	1270.12	950.949
116080	1178.48	1204.79	1263.83	822.825	886.94	931.066
119220	922.249	899.317	845.278	827.075	832.377	922.633
121120	1116.47	1077.7	1075.59	1013.12	989.383	1102.21

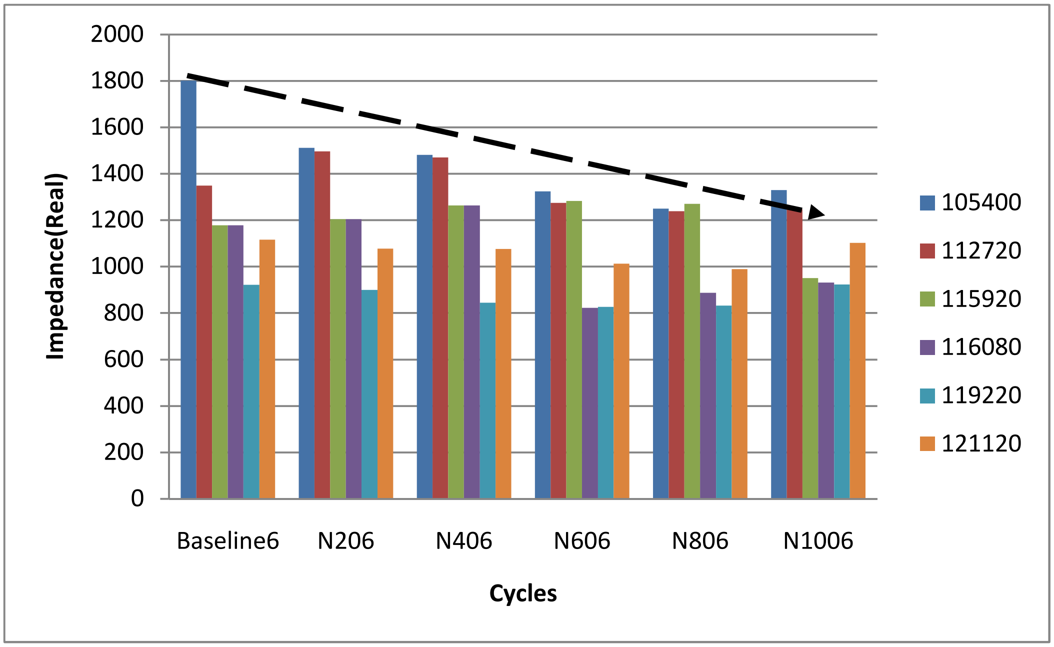

Figure 4.14 Identified peak intensity as a function of no. of cycles for 6 sq.mm area

Table 4.4 Identification of peaks for sensor area 9.6 sq.mm

FreqPeaks	Baseline9p6	N209p6	N409p6	N609p6	N809p6	N1009p6
50600	4311.61	3222.87	2942.91	2417.48	1933.47	1778.71
64660	3386.55	2538.03	2538.88	2055.84	1375.52	1453

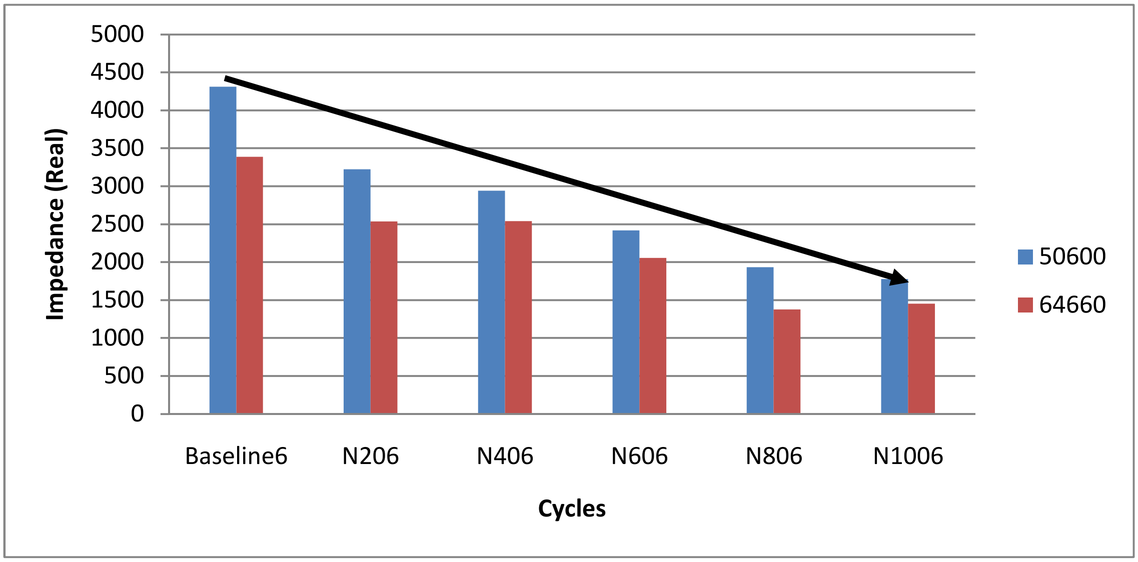

Figure 4.15 Identified peak intensity as a function of no. of cycles for 9.6 sq.mm area

Table 4.5 can be graphically represented by Figure 4.15. Figure 4.15 indicates a clear decrease in the intensity of the chosen peaks over the entire fatigue test. Peak broadening was also observed during the change in intensity and frequency shift calculations. Thus for 9.6 mm^2 electrode area, the peak intensity of the real part of impedance decreases almost linearly which enables one to quantify the fatigue damage occurring in the specimen. Also, change in the peak intensities are higher compared to that for the 6 mm^2 electrode area. Thus based upon the changes in the peak intensity and frequency shift we can summarize following observations:

1. The sensor with 9.6 mm^2 electrode area shows highest sensitivity for the fatigue damage induced in the aluminum specimen.
2. Higher frequency band (100 – 130 kHz) gives better sensitivity for smaller electrode areas.
3. Linear change was observed in the peak intensity over the entire test.
4. Higher coupling coefficient of sensor with 9.6 mm^2 electrode area provides high sensitivity in relatively lower frequency band (50 – 70 kHz).

4.2 Damage detection of rocket motor

The prototype rocket motor was purchased from DiscountRocketry.com and is manufactured by Rouse Tech Monster Motors. The model for the motor was Rouse-Tech 38/120 Reloadable Rocket Motor System (Dia. 38 mm and 97.282 mm long without aft closure). This reloadable rocket motor system consists of motor casing, forward and aft closures (the top and bottom grip). All these components were assembled together along with motor reloads to make the rocket motor system. The separation gap between top grip and o-ring in contact with the fuel chamber was used as an induced defect in rocket motor. Figure 5(a) shows the rocket motor with square piezo sensor attached to it. Damage was induced by loosening the upper grip which creates separation between fuel and top section. This damage can be considered as delamination type. Figure 5(b) shows the variation of damage metric as delamination was increased. X-ray radiographs are also provided in the same figure for different response ids which clearly show the increasing separation between fuel and mounting section (HP-cabinet X-ray system-Faxitron series, Tube Voltage = 30 KVp, Time of exposure = 7 mins). The separation for different response id’s as determined from radiographs was 1, 2, 3 and 5mm (response id 1, 2, 3 and 4). The damage index flattens after response id 3 because it reaches the limit of expansion of inner component of rocket motor and any further loosening of grip does not increase the damage.

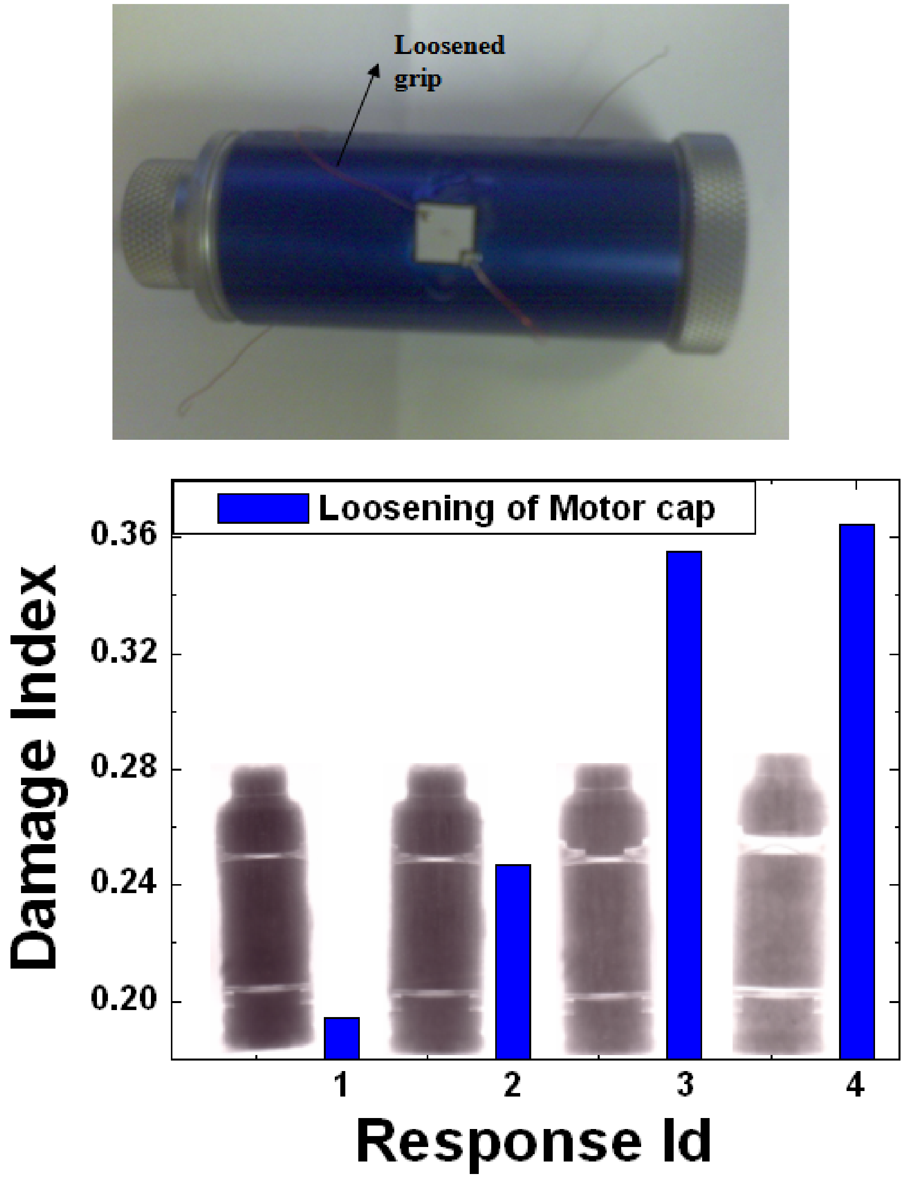

Figure 4.16 (a) Picture of the rocket motor with attached square piezo sensor
(b) Damage index metric along with X-ray radiographs for various response ids indicating the change with degree of delamination.

The results of Figure 4.16 clearly demonstrate the ability of square sensor in capturing the internal defects of rocket motor. Further, from results of Figure 4.4, it can be interpreted that the square sensor can detect deformation occurring in the casing of the rocket motor due to handling or any other accidental failure. Thus, an externally mounted sensor is able to provide information about both external and internal defects.

4.3 Corrosion Detection Using Impedance Spectroscopy

Corrosion is a significant type of structural damage that threatens the structural integrity and is major cause of failure in metals. Macroscopic manifestations of corrosion are the advanced stages of a complex and dynamic processes that begin at the microscopic level. The need to quantify the initial stages of corrosion has spurred the development of a multitude of analytical techniques.[54] Corrosion is often not expressed in terms of a design property magnitude like other properties but rather in more qualitative terms such as material is immune, resistant, susceptible or very susceptible to corrosion.[55] In this study we investigate the applicability of impedance spectroscopy technique for monitoring the cumulative corrosion damage in Al specimen and evaluate the sensor sensitivity.

It is known that corrosion resistance of aluminum is dependent upon the formation of the protective oxide film. [56] Oxide films formed in air at room temperature are 2-3 nm thick on pure aluminum. [57] This film is stable in aqueous media when the pH is between about 4.0 and 8.5, and is naturally self-renewing. Any accidental abrasion or mechanical damage of the surface film is rapidly repaired. The conditions that promote corrosion of aluminum and its alloys are directly correlated to the degradation of the oxide film. Prolonged occurrence of corrosion will require local degradation of the protective oxide film and minimize the availability of oxygen to rebuild it.

4.3.1 Experimental Procedure

An Al specimen of dimension 76.2 x 19.05 x 2.54 mm3 was diced out of Al-6061 grade block (contains Si, Cu, Mg, Cr, and few others). Aluminum 6061 is a high to medium strength alloy which offers a range of good mechanical properties, machinability, excellent joining characteristics, and good corrosion resistance. For this reason it is suitable for applications such as impact stock for low pressure ammunitions, aerospace connectors, aircraft fittings, brake pistons, and valves. The alloy is also suitable for the hardware used in marine environments. Thus, we select this grade for the evaluation of the corrosion behavior and attempt to design a sensor that can detect the earliest change in characteristics.

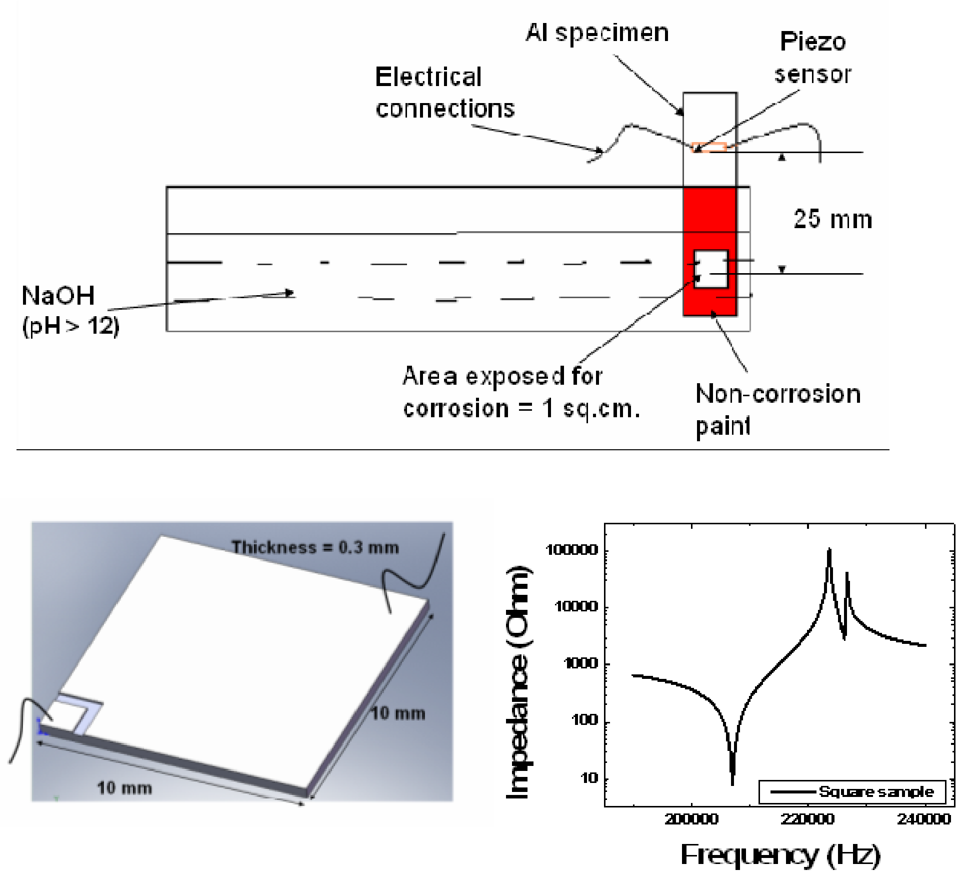

Figure 4.17 (a) Experimental setup of corrosion detection, and (b) Sensor design and impedance response in the un-bonded state.

The setup for the induction of corrosion consists of an acid/base bath with Al plates submerged at specific depths. No counter electrode was used in this setup. A non-corrosive coating was applied on the specimen so as to isolate a 1cm^2 area in the submerged section of Al which is exposed to the bath as shown in Figure 4.17(a). A piezoelectric sensor was synthesized from hard PZT composition and was bonded to the Al piece by using non-conductive epoxy. Figure 1(b) shows the dimension of the piezoelectric sensor and planar mode impedance response. The longitudinal piezoelectric constant (d33) for the poled sample was found to be as 190 pC/N. Electrodes were attached to the PZT and connected to an HP 4194A impedance analyzer.

An off resonance frequency range of 75 kHz – 90 kHz was chosen to study the R-X signature response of the piezoelectric sensor.[9, 58] The work distance (the distance between sensor and area under corrosion) was reduced in steps. For all the experiments, four different sets of data collections done corresponding to measurement of impedance response every 30 s, 5 mts, 15 mts, and 30 mts. All this data was combined together and the damage index metric was plotted as a function of time on the same graph so as to get a correlation between the damage index and the actual damage occurring in the specimen.

4.3.2 Results and Discussion

4.3.2.1 Damage Index Monitoring

The impedance signature immediately after the gripping was used as the baseline analysis. The analysis of the R-X results for the sensor was based on the damage index metric which is given as follows: [16, 59]

$$\text{Damage index} = \sqrt{\sum (R_1 - R_0)^2 \Big/ \sum R_0^2} \qquad (1)$$

where R corresponds to real part of impedance. The subscripts “1” and “0” correspond to the test id under consideration and initial state respectively.

The Al samples were polished totally to mirror like finish and then exposed to corrosion in acid and base media. Both acid (HNO3) and base (NaOH) are used for inducing corrosion on Al specimen. The rate of corrosion in Al is dependent upon the pH of the environment. It is known that oxide films formed on the surface is not stable in acidic (pH<4) and alkaline (pH>9) environments. [56] Aluminum shows stable corrosion behavior in the HNO3 environment but abrades in the alkaline media. Thus, the prediction of the damage in the alkaline media was pursued in this study. One molar solution of NaOH was prepared using standard procedure. The pH of this solution was always maintained above 12 for the entire test.

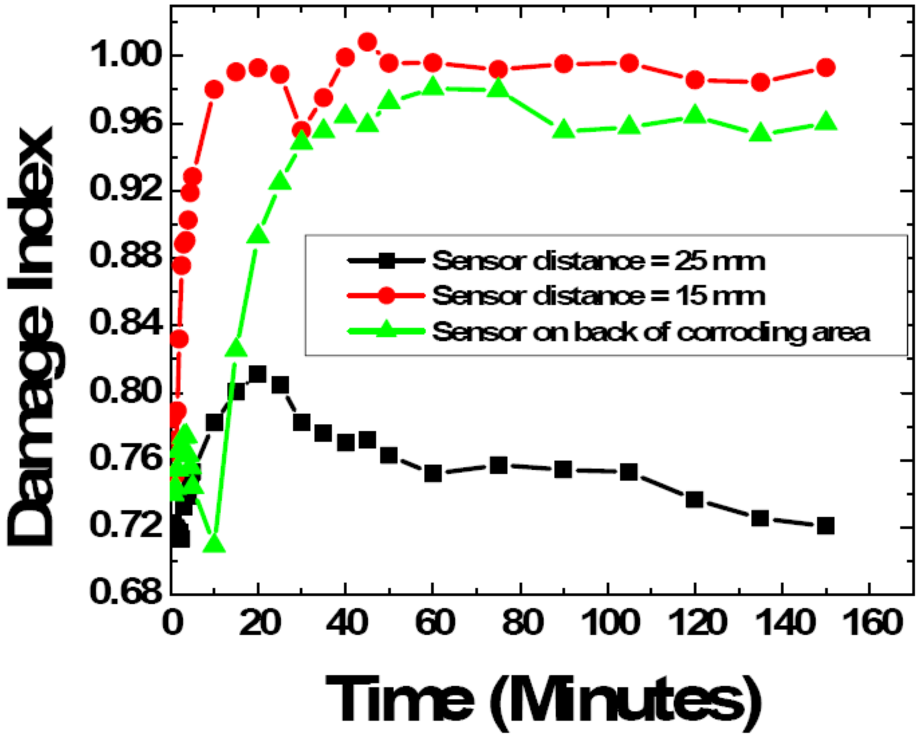

Figure 4.18 Damage index metric as a function of time and location for the entire test.

The damage index metric as a function of time for the entire test is shown in Fig. 2. The distance between the sensor and the area under corrosion was varied from 25 mm to 15 mm. The magnitude of damage index increases as we decrease the distance between the sensor and the area where damage is occurring. The sensitivity of the sensor was found to be maximum at 15mm from the corrosion area. Another point that can be noted from Figure 4.18 is that the damage index reaches its maximum magnitude at about 20 mts of the test after which it saturates or becomes insensitive to further corrosion.

4.3.2.2 Microstructural Characterization

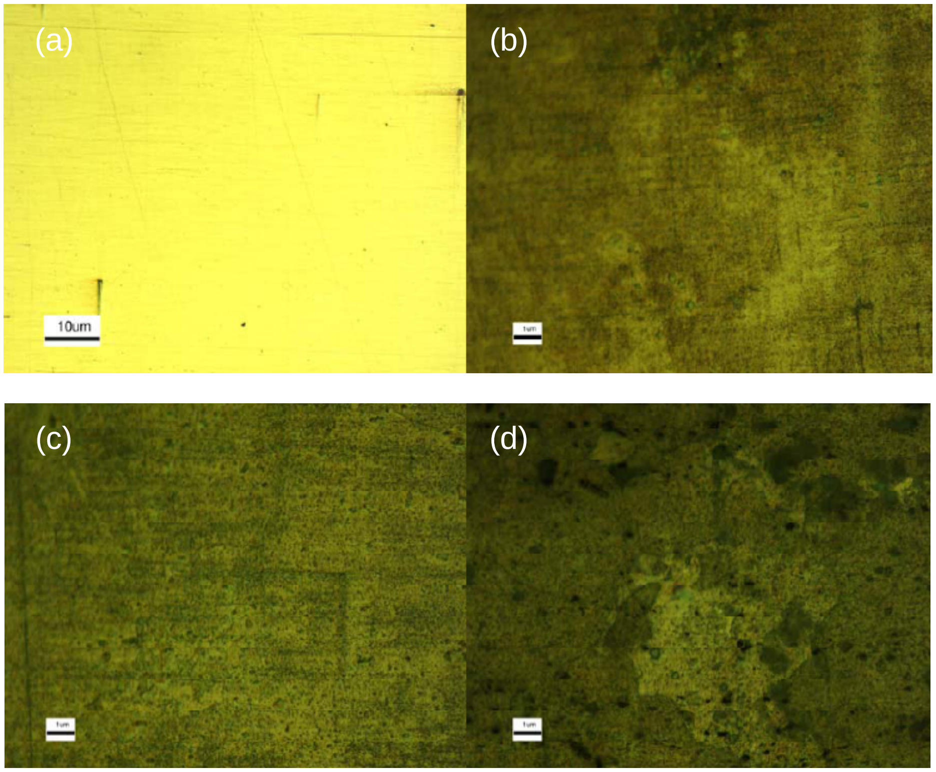

Figure 4.19 (a) Polished Al sample, (b) Etched Al-sample, (c) Corroded Al sample, time of exposure = 1 min (d) Corroded Al sample, time of exposure = 15 min

Figure 4.19 (a) and (b) shows polished Al piece under optical microscope. Figure 4.19 (c) and (d) shows the Al sample exposed to corrosion in NaOH for 1 and 15 mts. It can be seen from this figure that the surface oxide starts to form as the specimen is corroding. Further, degradation can be found to occur on the surface which is very common phenomenon in Al corrosion and can be associated to the microgalvanic process between the intermetallic phases and the matrix alloy. [60] The phases often act as the local cathodes because of their Fe content, and surrounding matrix undergoes localized attack. No particular grain structure was seen which matches with the reported micrographs (Atlas Microstructure for Al 6061 grade) [61]. As the time increases, more degradation occurs by formation of the corrosion product.

In order to understand the nature of the corrosion products further analysis was conducted using SEM.

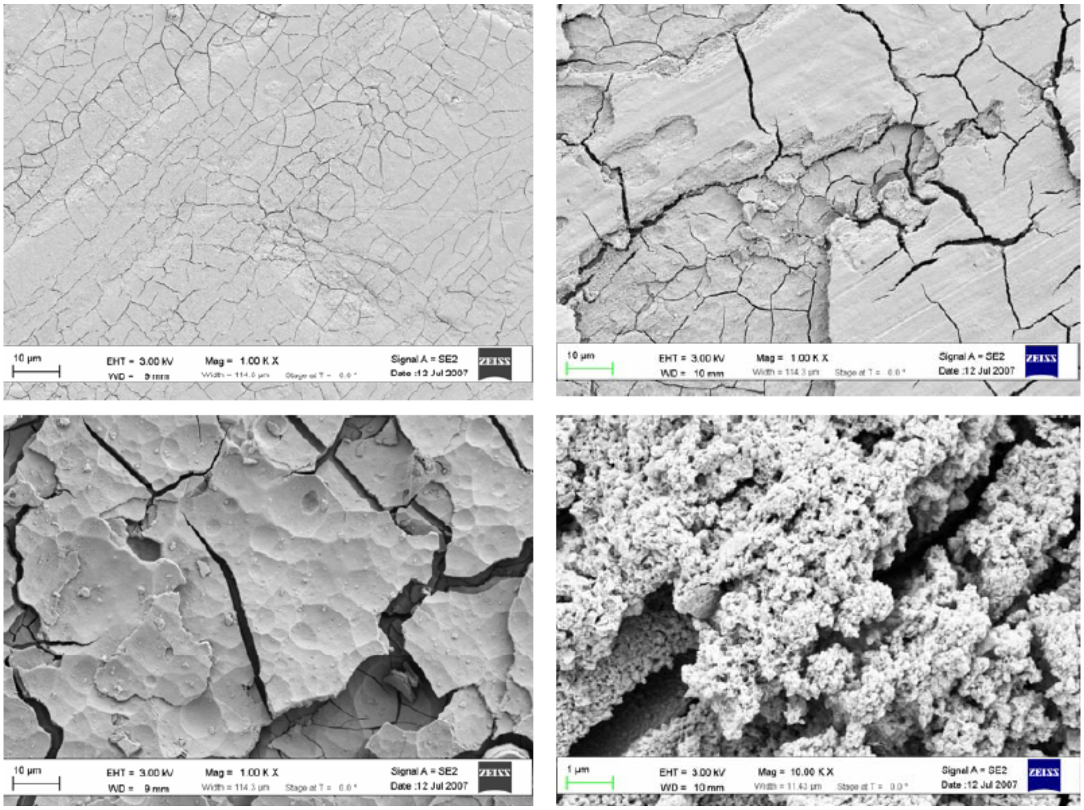

Figure 4.20 SEM micrographs of the corroded sample as a function of time of exposure in NaOH (a) 1 minute (b) 15 minutes, (c) 60 minutes, and (d) corrosion products under high magnification.

For SEM, corroded samples after 1, 15 and 60 mts were chosen to map the increase and saturation in impedance response. Figure 4.20 (a)-(c) shows the surface structure of Al after 1, 15, and 60 mt of exposure to NaOH. Figure 4.20 (d) shows corrosion product under high magnification which is large quantity of oxides as confirmed by high percentage of oxygen in the

EDX analysis. These images indicate that the number of micro-cracks are increasing with time while an oxide layer is being formed on the freshly exposed surface. Thus, the damage occurs by finding the new surface and is dependent upon its availability. The thickness of this oxide layer increases with time and for the sample held for 60 mts in the bath, a thick layer of oxide along with large cracks along the depth were found to be formed. After 15 mts of exposure time, the cracks are still being formed but at the same time the availability of fresh alloy area is being reduced. After the 60 mts the oxide layer formed is getting abraded however, the intensity of corrosion is decreasing as there is further less availability of fresh area. This analysis was supported by the EDAX ZAF standard less quantification method in SEM as shown in Figure 4.21 which indicates the increasing oxygen percentage on the surface.

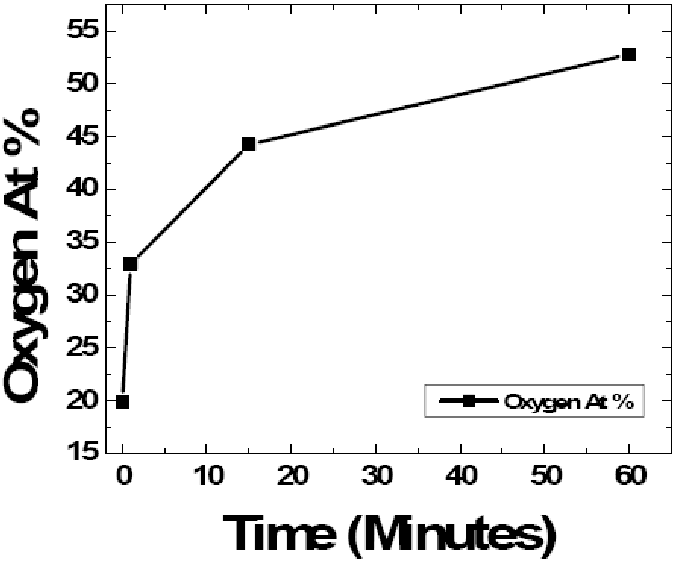

Figure 4.21 EDX analysis of the oxygen content at the surface as a function of time.

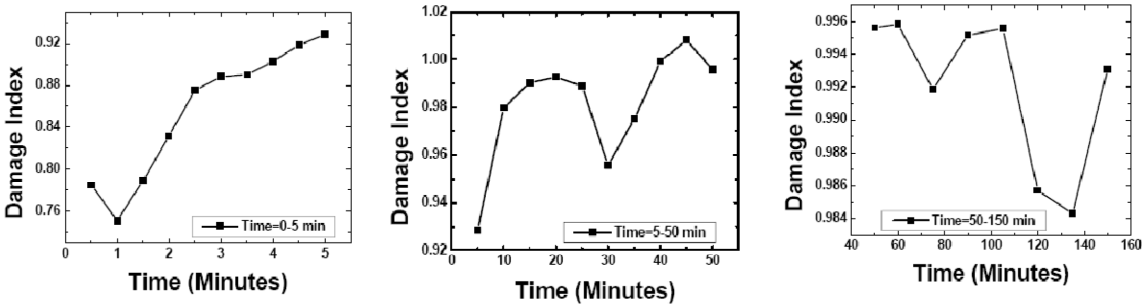

Figure 4.22 Damage index metric as a function of time for the sensor located at 15 mm from the area under corrosion. (a) 0 – 5 mts, (b) 5 – 50 mts, and (c) 50 – 150 mts.

Figure 4.21 (a), (b), and (c) shows the data for the sensor at 15 mm distance from the corrosion area as a function of time interval. It can be seen from Figure 4.21 (a) that there is sharp rise in the index within 5 mts of the test after which it starts to saturate. For the time interval of 5 – 15mts there is still increase in the index after which it starts to saturate. These results are consistent with the SEM observation. For the time interval of 15 – 150 mts the corrosion is basically driven by the availability of the fresh surface. Combining the results from Figure 4.19Figure 4.20, Figure 4.21 it can be summarized that impedance spectroscopy is able to predict the dynamic nature of the Al-alloy corrosion in the early periods (< 15 mts) which is related to formation of the microcracks and surface oxide. Once a thicker layer of oxide has been formed the sensitivity of the sensor saturates.

4.4 Power analysis

The voltage applied from the impedance analyzer was fixed at 0.5V. Real part of the impedance was used as the magnitude of the resistance in the power calculations. At the resistance magnitude of 1 kΩ, the power requirement of the sensor are given by:

$P = V^2/R = 1^2/ (1e3) = 0.5$ mW

4.5 Chapter Summary

Structural health monitoring sensors have been utilized for detection of damage types such as delamination and corrosion. Effect of electrode area on the selection of frequency band for fatigue damage detection were studied. Corrosion damage can be effectively quantified and detected in its early stages for Al-6061 alloy which was the desired goal of this study. The damage caused in the basic environment was studied by the impedance spectroscopy based piezoelectric wafer sensor. There is an optimum distance for detection of corrosion (15 mm between sensor and area under investigation in this study).

CHAPTER 5

CERAMIC – CERAMIC MAGENTOELECTRIC COMPOSITE GRADIOMETER

5.1 Introduction

Magnetoelectric composite materials consisting of piezoelectric and magnetostrictive phases respond to both electric and magnetic field. The composites exploit product property and various synthesis techniques can be adopted to combine two different phases depending upon the crystal symmetry, lattice parameters and physical state. The presence of piezoelectric and magnetostrictive phases in the same material provides the opportunity to develop a voltage gain device operating on the following principle. An applied AC magnetic field induces strain in the magnetostrictive phase which is transferred onto the piezoelectric phase in an elastically coupled system. The piezoelectric phase produces the electric charge in proportion to the applied strain. Previously, Ryu et al., Srinivasan et al., and Dong et al. have reported such a device utilizing the trilayer and multilayer composite structures as Terfenol-D/PZT/Terfenol-D and obtained high voltage gain [62-66]. These devices have shown significantly large magnitude of ME coefficients as compared to that of particulate sintered composites.

Recently, we have reported a magnetic field sensor based on piezoelectric transformer with ring-dot electrode pattern [67, 68]. A piezoelectric transformer is a two port device, where on one port the applied input voltage is converted into stress through converse piezoelectric effect, and on the other port this generated stress is converted back into voltage through direct piezoelectric effect [69]. In this prior design, a voltage was applied to the ring section at resonance frequency which induces a magnetic field in the dot section. If an external magnetic object is then brought in the vicinity of the dot section, the change in magnetic field will induce a change in the voltage gain of the transformer via the magnetoelectric (ME) effect. Here, we have combined our prior magnetic field sensor design with a new laminate geometry to achieve ME gradiometer. Our findings demonstrate enhanced sensitivity to small changes in magnetic field using the multilayer PZT ring and Terfenol-D disk. In addition, we propose a theoretical model describing the low frequency response of sensor and resonance response of the proposed ME gradiometer. A very good agreement was obtained between the experiment and theory.

5.2 Experimental Procedure

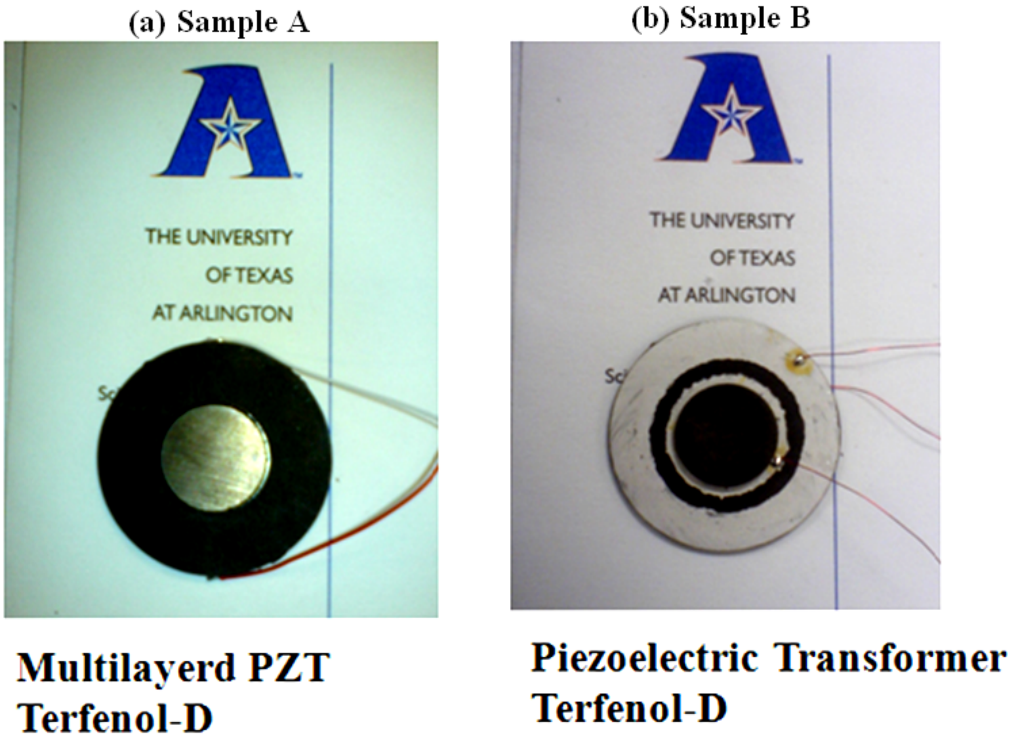

Figure 5.1 Picture of the fabricated magnetoelectric gradiometer. (a) Sample A: Sensor design, multilayered PZT ring (diameter = 29 mm) bonded with co-centric Terfenol-D (diameter = 13 mm). The co-fired PZT element had 10-layer of 100 μm thickness with dimensions of 29 mm diameter and 1mm thickness; and (b) Sample B: Ring-dot structure of the magnetoelectric gradiometer fabricated by bonding PZT (APC 841) disc and Terfenol-D (13 mm) bonded in the center. The ring and dot are separated by a thin insulation gap. The ground electrode is at the bottom side of the PZT.

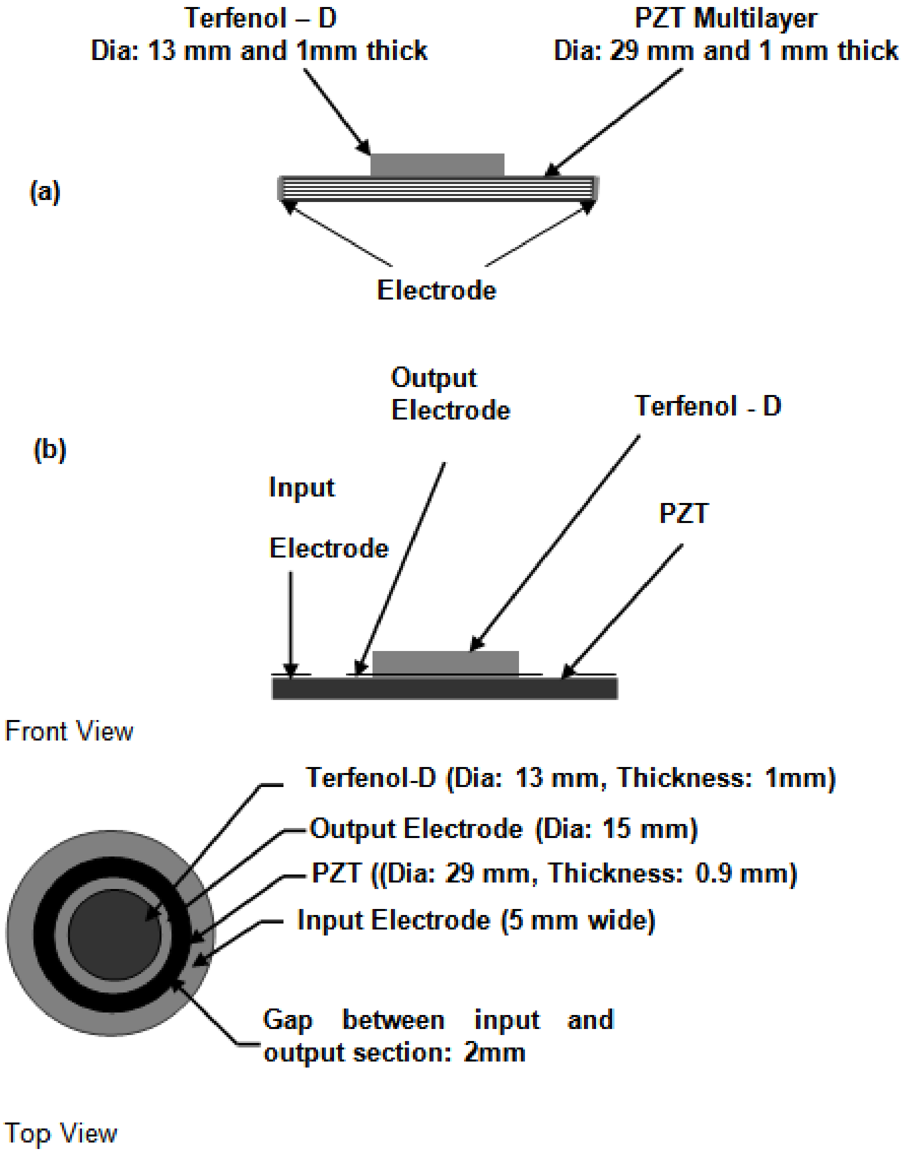

Figure 5.2 (a) Schematic diagram of the sensor illustrating the dimensions and layout of various elements**,** (b) Schematic diagram of the ring-dot structure illustrating the dimensions and layout of various elements.

Multilayer PZT disks were synthesized by tape casting technique using Ag-Pt electrodes (Dongil Tech., Korea, composition D210). The co-fired PZT element had 10-layer of 100 μm thickness with dimensions of 29 mm diameter and 1 mm thickness. Sample A was fabricated by bonding the multilayer PZT disc with co-centric Terfenol-D (diameter = 13 mm) using a Loctite E – 30CL Hysol epoxy adhesive as shown in Figure 5.1 (a).

Curing was done in temperature range of 60 – 75 ^{o}C for one hr. Sample B (gradiometer) had ring dot electrode pattern printed on top surface of PZT (APC 841), where ring acts as the input while dot acts as the output. The output section had a diameter of 15 mm and the input section had a width of 5 mm. There was an insulation gap between input and output section of 2 mm. The ground electrode was at the bottom of PZT. Terfenol – D disc with diameter of 13 mm was bonded on the output section as shown in Figure 5.1(b) and Figure 5.2(a) and Figure 5.2(b). Table 5.1 shows the relevant piezoelectric properties of ceramics.

Table 5.1 Piezoelectric properties of the D210 composition used for fabricating the multilayer disks.

	High g (D210)	Hard (APC 841)
ε_r	681	1350
k_p (%)	0.58	0.60
d_{31} (10^{-12} C/N)	120	109
g_{31} (10^{-3} Vm/N)	20	10.5
Q_m	89.7	1400
T_c (ºC)	340	320
$d_{31} \cdot g_{31}$	2.4E-12	0.99E-12

The piezoelectric constant of synthesized composite was measured by APC YE 2730A d_{33} meter. Resonance characteristics were determined by HP 4194A impedance analyzer (Hewlett Packard Co. USA). For sample A, the voltage output was measured by applying an AC magnetic field at low frequency (5 – 10 Hz) with 2Oe amplitude (H) under varying DC magnetic bias. The AC magnetic field was generated by a Helmholtz coil powered by Agilent 3320 function generator and NF high speed bipolar power amplifier (HAS 4052). DC magnetic bias was generated by using solenoid coil set powered by Kepco DC power supply. The output voltage generated from the composite was measured by using SRS DSP lock-in amplifier (model SR 830).

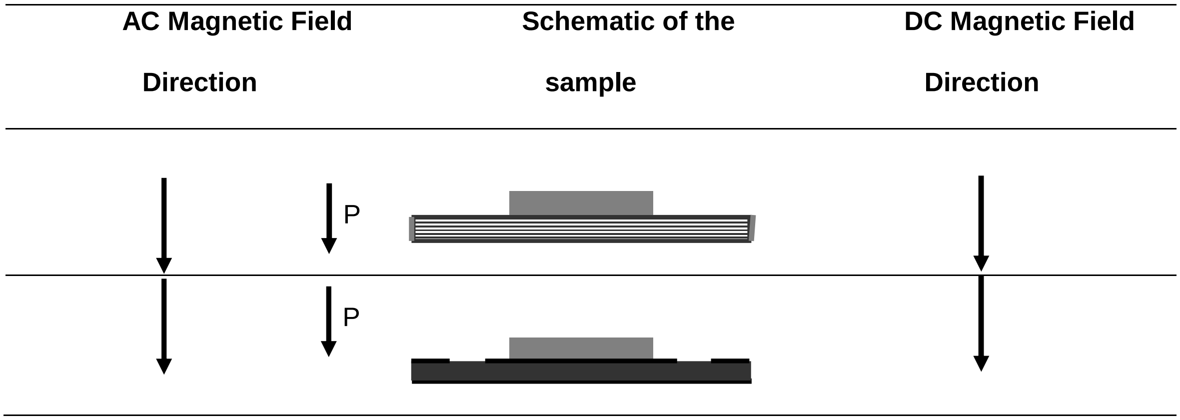

Figure 5.3 AC and DC magnetic field directions used in the measurements, where P is the polarization of PZT.

For the gradiometer design, Sample B, a input voltage of 1 V_{p-p} was applied on the ring section and output voltage was measured from dot section using a Tektronix TDS 420A four channel digital oscilloscope with varying DC magnetic bias field. Figure 5.3 shows the direction of applied AC and DC magnetic field during the measurement. The frequency range was chosen near resonance frequency (90.6 kHz) of the transformer as determined from the impedance curves shown in Figure 5.4. The magnetic field generated in the dot-section was measured by using the magnetic field sensor (AC/DC magnetometer from Alphalab Inc.). All the measurements were repeated to check the consistency of results.

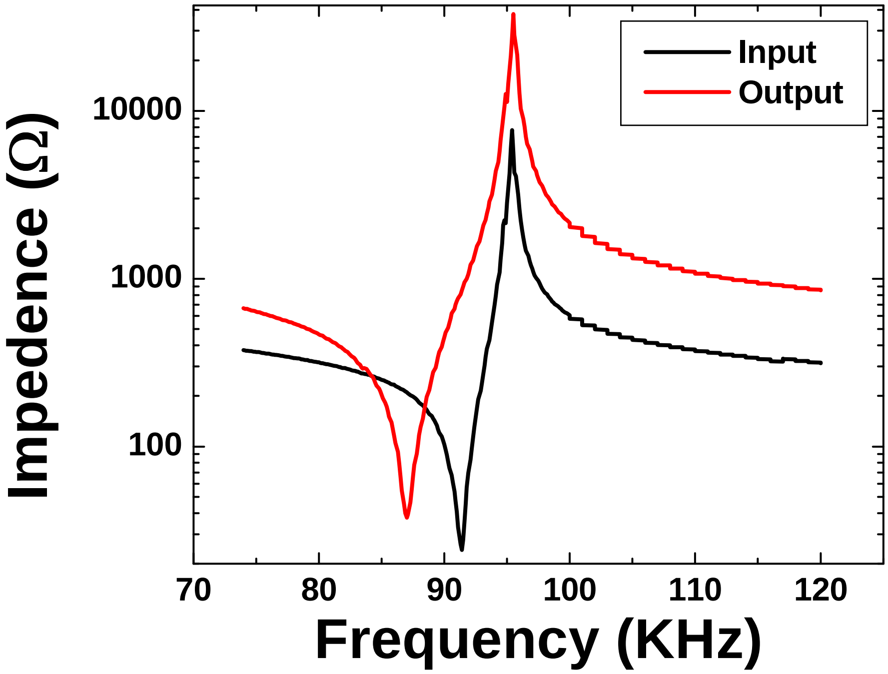

Figure 5.4 Impedance spectrum of the input and output section. The output was under open circuit condition when measuring the input spectrum and vice-versa.

5.3 Results and Discussion

A piezoelectric transformer operating near resonance point can be represented by the equivalent circuit shown in Table 5.2.

Table 5.2 Equivalent circuit parameter of the input and output sections at resonance – antiresonance frequency range.

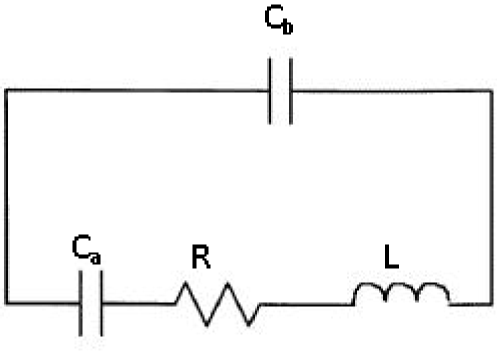

	Input Section **(88 – 98 kHz)**	**Output Section** **(84 – 97 kHz)**
R (Ω)	**24.79**	**33.64**
L (mH)	**8.12**	**8.94**
C_a (pF)	**373.92**	**374.01**
C_b (nF)	**4.20**	**1.84**

In this circuit R, L, C_a are the motional resistance, inductance and capacitance, and C_b is the damped capacitance. Figure 5.4 shows the impedance spectrum of input and output section (Sample B shown in Figure 5.1(b)). Using this spectrum the magnitude of equivalent circuit parameters was calculated for both input and output. Unipoled transformers were fabricated by designing the input and output electrodes on the same side of disk, as shown in Figure 5.1(b) and Figure 5.2 (a). The bottom electrode of the disk was common ground to both input and output sections. Applying the electrical excitation to the external ring (input), radial extensional vibration is generated in the ring which then propagates to the center dot (output). At the center electrode, mechanical vibrations are again converted into electrical voltage. The connecting wires should be soldered at the nodal points of the input and output sections. For input section, the nodal point lies at one-fourth distance from the edge of transformer while for the output section, nodal point lies at the center. Simplistically, the gain of transformer is given by:

$$\mathrm{Gain} = \sqrt{\frac{\mathrm{C_a(input)}}{\mathrm{C_a(output)}}} \tag{1}$$

and efficiency of transformer is given by:

$$\mathrm{Efficiency} = \frac{1}{1+4\pi f_{r,in} C_{a,in} R_{in} (\frac{C_{b,out}}{C_{a,out}})} \tag{2}$$

where in and out stand for the input and output respectively. The transformer is always operated between the frequency limits given by:

$$\omega_{\mathrm{SC}} = \frac{1}{\sqrt{LC}} \tag{3}$$

and

$$\omega_{\mathrm{OC}} = \frac{1}{\sqrt{L(C^{-1}+{C_{d2}}^{-1})^{-1}}} \tag{4}$$

where ω refers to the angular frequency and subscripts “SC” and “OC” refer to short circuit and open circuit conditions. The symbols L and C are the motional inductance and capacitance of transformer while C_{d2} is the damped capacitance of the output section. These frequencies can be easily determined from the impedance curves.

5.3.1 Theory of low frequency magnetoelectric magnetic field sensor (Sample A)

Working principle of ME sensor shown in Figure 5.1(a) is based on measuring the variation in ME voltage coefficient due to changes in applied magnetic field. The response of sample to the external magnetic field is related to the magnitude of ME voltage coefficient. For a given orientation of the fields as shown in Figure 5.3, the ME voltage coefficient can be expressed as [66]:

$$\alpha_E = 2\frac{\mu_0 kv(1-v)\,{}^{p}d_{31}q_{31}}{\{2\,{}^{p}d^{2}{}_{31}(1-v)+{}^{p}\varepsilon_{33}[({}^{p}s_{11}+{}^{p}s_{12})(v-1)-v({}^{m}s_{11}+{}^{m}s_{12})]\}} \tag{5}$$

$$X\frac{[({}^{p}s_{11}+{}^{p}s_{12})(v-1)-kv({}^{m}s_{11}+{}^{m}s_{12})]}{\{[\mu_0(1-v)-{}^{m}\mu_{33}v][kv({}^{m}s_{12}+{}^{m}s_{11})-\left({}^{p}s_{11}+{}^{p}s_{12}\right)(v-1)]+2\,{}^{m}q^{2}{}_{31}kv^{2}]\}},$$

where $v = {}^{p}v/({}^{p}v + {}^{m}v)$, k is the coupling factor, and ${}^{p}v$ and ${}^{m}v$ denote the volume of piezoelectric and magnetostrictive phase, respectively. For this case, nonzero components of ${}^{p}s_{ij}$, ${}^{p}d_{ki}$, ${}^{m}s_{ij}$, ${}^{m}q_{ki}$ are provided by Table 5.3.

Table 5.3 Nonzero coefficients of piezoelectric and magnetostrictive phases and homogeneous material for longitudinal field orientation.

Piezoelectric phase	
Piezoelectric coefficients	Compliance coefficients
${}^{p}d_{15} = {}^{p}d_{24}$ ${}^{p}d_{31} = {}^{p}d_{32}$ ${}^{p}d_{33}$	${}^{p}s_{11} = {}^{p}s_{22}$ ${}^{p}s_{12} = {}^{p}s_{21}$ ${}^{p}s_{13} = {}^{p}s_{23} = {}^{p}s_{31} = {}^{p}s_{32}$ ${}^{p}s_{33}$ ${}^{p}s_{44} = {}^{p}s_{55}$ ${}^{p}s_{66} = 2({}^{p}s_{11} + {}^{p}s_{12})$
Magnetostrictive phase	
Piezomagnetic coefficients	Compliance coefficients
${}^{m}q_{15} = {}^{m}q_{24}$ ${}^{m}q_{31} = {}^{m}q_{32}$ ${}^{m}q_{33}$	${}^{m}s_{11} = {}^{m}s_{22} = {}^{m}s_{33}$ ${}^{m}s_{12} = {}^{m}s_{21} = {}^{m}s_{13} = {}^{m}s_{23} = {}^{m}s_{31} = {}^{m}s_{32}$ ${}^{m}s_{44} = {}^{m}s_{55} = {}^{m}s_{66}$

Voltage output is given as: $U_{out} = \alpha_E \cdot \delta H \cdot t$, where t is the piezoelectric phase thickness. Figure 5.5 shows the theoretical and measured values of output voltage as a function of DC magnetic field, indicating very good correspondence between the model and experiment. Variation of output voltage as a function of DC magnetic field was obtained by computing the magnetic field dependence of piezomagnetic coefficient q. It can be noted from Figure 5.5 that output voltage varies almost linearly with DC magnetic field at low frequencies and small AC magnetic field of 2Oe. This linear change allows us to use this design for DC magnetic field sensing with high precision.

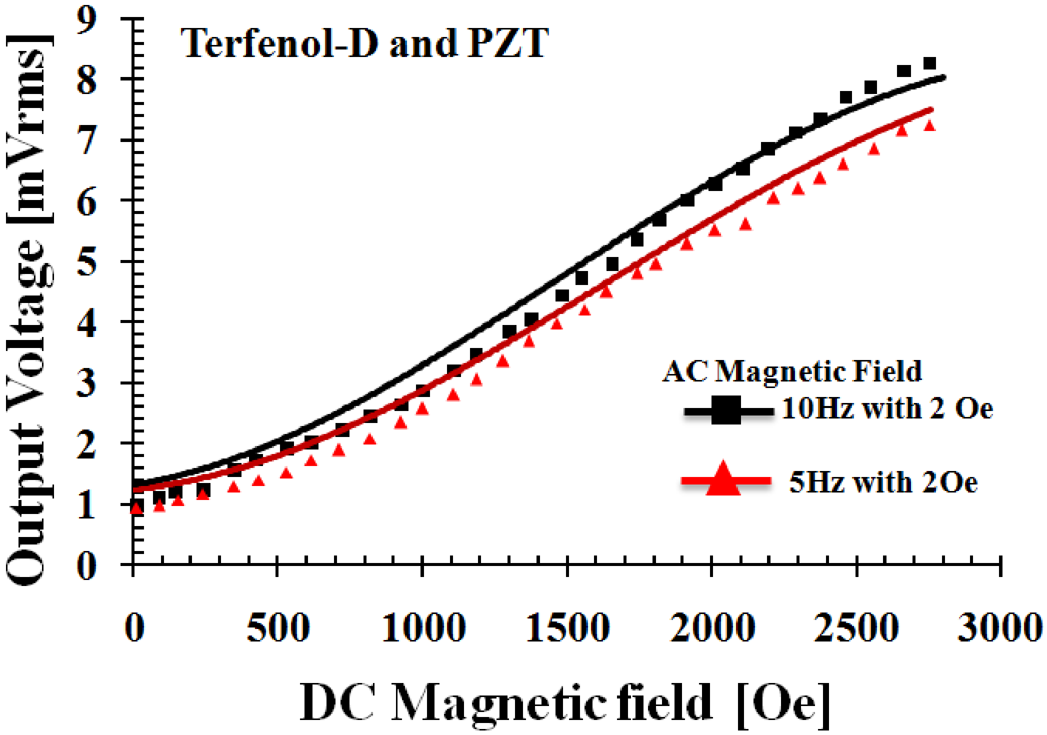

Figure 5.5 Solid line is theoretical dependence of output voltage from the first design (multilayered PZT bonded with Terfenol-D disc, Sample A) shown in Figure 5.1(a) at low frequency. Dot is output voltage at low frequency. The applied AC magnetic field was fixed at 2 Oe. A large output voltage can be noted at low frequencies.

5.3.2 Theory of magnetoelectric gradiometer (Sample B)

ME effect near electromechanical resonance (EMR) frequency for gradiometer shown in Figure 5.1(b) can be expressed as [70]:

$$\alpha_E = -\frac{1}{\Delta_a}\left[\frac{2d_{31}q_{31}}{\varepsilon_{33}s_{11}(1-v)}\left(\frac{(1+v)J_1(k)}{\Delta_r} - 1\right) + \frac{\alpha_{33}}{\varepsilon_{33}}\right], \qquad (6)$$

where q_{ij} and d_{ij} are piezomagnetic and piezoelectric coefficients, ε_{ij} is the permittivity matrix, $\alpha_{33}/\varepsilon_{33}$ is the value of low frequency ME coefficient. Further,

$\Delta_r = kJ_0(k) - (1-v)J_1(k)$,

$\Delta_a = 1 - K^2_p + K^2_p(1+v)\, J_1(kR)/\Delta_r + iG$, and

$K^2_p = 2d^2_{31}/\varepsilon_{33}\, \varepsilon_{33}(1-v)$ is the coefficient of electromechanical coupling for radial mode, and G is the loss factor. It can be noted that the magnitude of ME effect is dependent upon the material parameter $d_{31} \cdot q_{31}$.

The shift in EMR frequency range can be estimated as a function of magnetic field, H [71]. This shift is due to change in Young's modulus (E) caused by the applied magnetic field: namely the ΔE effect. The shift δfr in the EMR frequency range can be estimated as a function of bias magnetic field as follows:

$$\delta f_r = \frac{\Delta E f_r}{2E(1+v)z}\,\frac{(3+v)z^2J_0^2(z) - 8zJ_0(z)J_1(z) + [(1+v)z^2 + 4(1-v)]J_1^2(z)}{z\left[J_0^2(z) + J_1^2(z)\right] - 2J_0(z)J_1(z)}. \qquad (7)$$

where

$$\frac{\Delta E}{E} = \frac{4}{27}E\Lambda t_2^2\,\frac{\left[\cosh(h) - \cosh\left(\frac{h}{3}\right)\right]\left[\cosh(h) - 9\cosh\left(\frac{h}{3}\right)\right]}{\left[\cosh(h) + 3\cosh\left(\frac{h}{3}\right)\right]^2},$$

where $h = 3\chi_0 H/Ms$ is a dimensionless parameter, χ_0 is the permeability at $H=0$, $\Lambda = 3\chi/Ms^2$, and $t_2 = -B_2\frac{1}{2c_{44}}$, Ms is the saturation magnetization, B_2 is the magnetoelastic constant, and c_{ij} is the stiffness coefficient, $z = kR$, $v = -s_{12}/s_{11}$ is Poisson's ratio, $k = \omega\sqrt{\rho s_{11}(1-v^2)}$, ρ is the density, ω is the angular frequency, and $J_0(k)$ and $J_1(k)$ are Bessel functions of the first kind. Figure 5.6 (a) and (b) show the calculated and measured results for the gradiometer design illustrated in Figure 5.1(b).

These results show the variation of output voltage from the dot-section with respect to applied DC magnetic field. The measured frequency was varied in the range of EMR of the gradiometer. It can be seen from Figure 5.6 (a) that there is change in slope on either side of the EMR. At the frequency of 91 and 91.2 kHz, the variation in output voltage becomes linear with increasing applied magnetic field. Figure 5.6 (b) shows the change in amplitude of output voltage with frequency for constant applied DC magnetic field. From Figure 5.6 (b), two regions can be clearly separated and the device can provide differential voltage as the magnetic field changes with respect to reference state as shown in Figure 5.7.

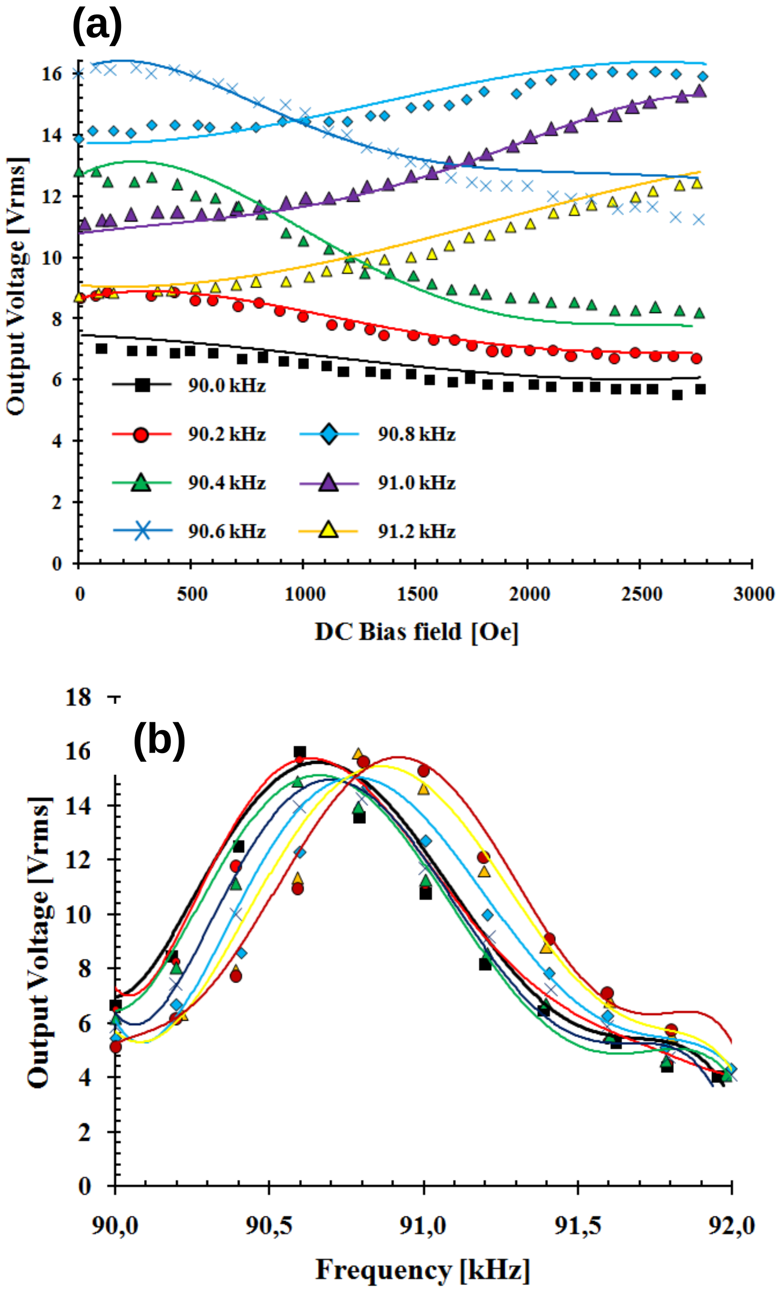

Figure 5.6 Ring-dot gradiometer. (a) Solid line is theoretical dependence of output voltage as a function of DC magnetic field at varying frequencies while symbols represent the experimental data, (b) Solid line is theoretical dependence of output voltage as a function of frequency at varying DC magnetic field while symbols represent the experimental data. The input voltage of gradiometer was fixed at 1V^{PP}.

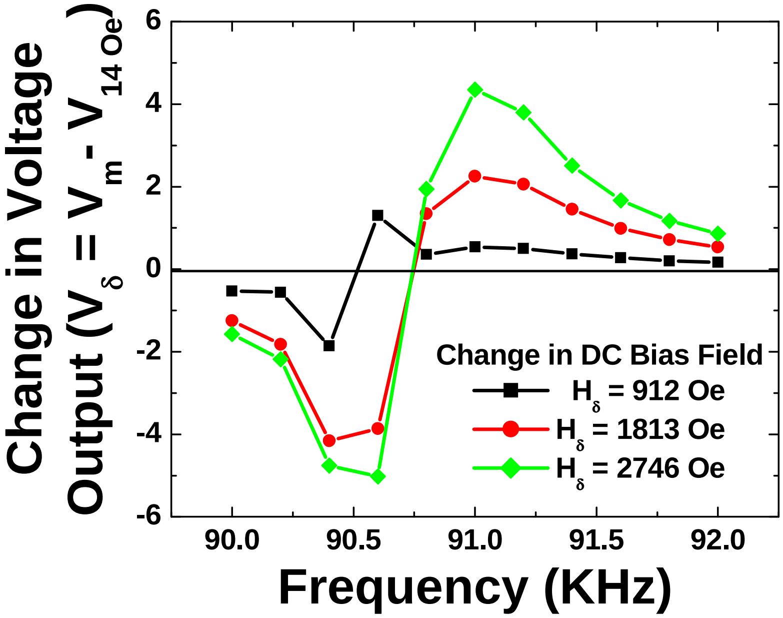

Figure 5.7 Change in output voltage with respect to change in DC magnetic field. A linear change was observed near the resonance frequency.

The mechanism for large differential change can be understood by measuring the generated magnetic field in the dot section as shown in Figure 5.8.

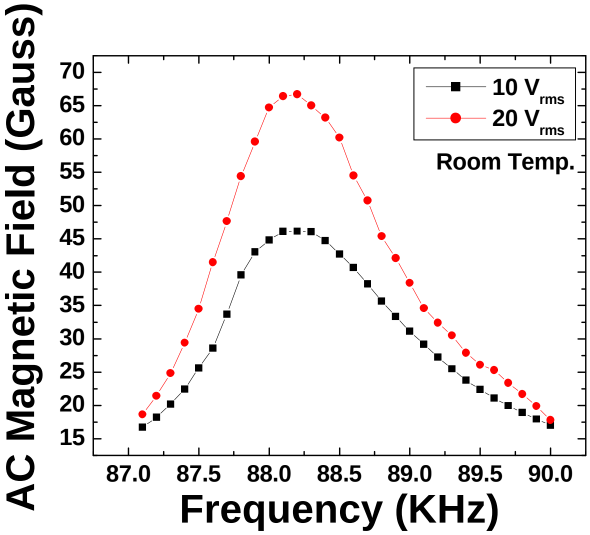

Figure 5.8 Magnetic field generated in the dot section with applied input voltage to the ring section.

Based on the results of Figure 5.8, the sensing mechanism can be proposed as following: A voltage is applied to the ring section at the resonance frequency which induces magnetic field in the dot section. If an external magnetic object is brought in the vicinity of the dot section than the resulting differential magnetic field will induce change in the voltage gain due to magnetoelectric effect. Figure 5.8 shows the plot of the generated AC magnetic field in the dot section as a function of frequency at constant input voltages. These measurements were in the vicinity of the EMR which is indicated by peak. It can be further seen in this figure that there is a significant change in magnitude of the generated AC magnetic field with applied input voltage to the ring section, which increases as the frequency approaches the resonance point. This generated AC magnetic field couples with the applied external magnetic field to provide differential change in the output voltage of dot section. The variation in the EMR frequency with increasing input voltage can be explained on the basis of reverse ME effect. Figure 5.9 summarizes the results on a 3D plot.

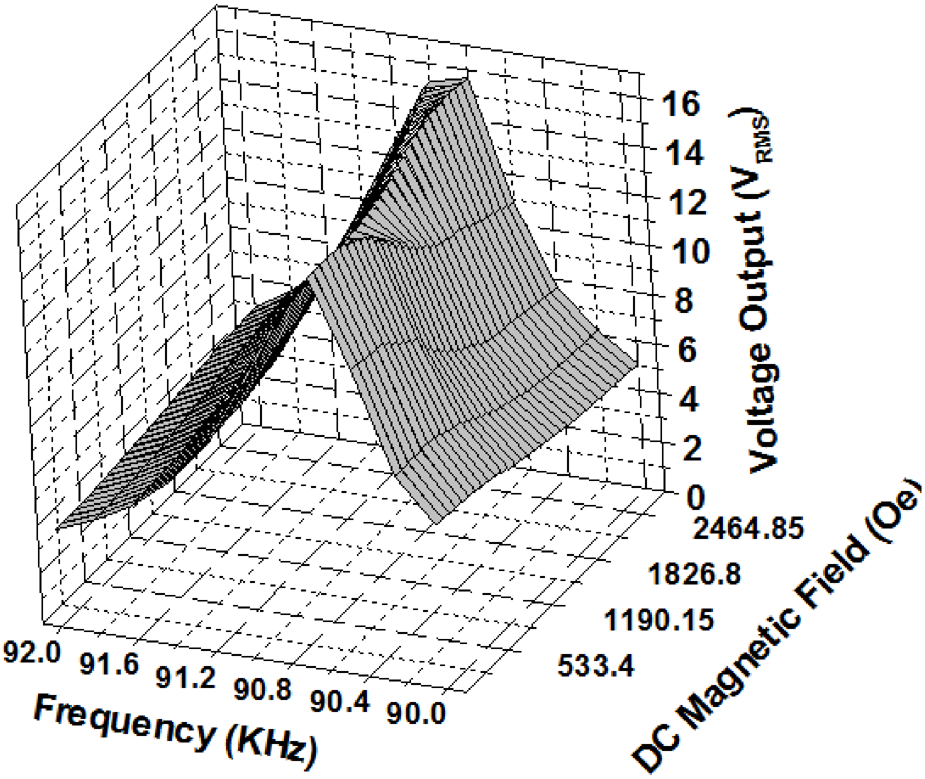

Figure 5.9 Voltage output from the ring-dot gradiometer [shown in Figure 5.1(b) and 5.2] in the vicinity of the resonance frequency with varying DC magnetic bias. The input voltage of the gradiometer was 1 $V^{PP.}$

Using the data in Figure 5.8, we can compute the converse magnetoelectric effect (CME) of composite which is defined as change in magnetization (or in our case magnetic field) with respect to applied electric field. The CME effect is given as, α_B = (dB/dV). At the resonance frequency, α_B can be calculated to be of the order of 3.4 G/V – 4.4 G/V. The range in the CME occurs due to the nonlinear response of the piezoelectric at higher applied voltages near resonance frequency.

5.4 Chapter Summary

In summary, large output voltage can be obtained from Sample A at low frequencies far from EMR, thereby allowing this design to be used as a magnetic field sensor. For Sample B, there was a significant change in resonance frequency and amplitude of output voltage with applied magnetic field. The results show that magnetoelectric gradiometer or Sample B can detect changes in DC magnetic field by measuring the differential output voltage change.

CHAPTER 6

METAL CERAMIC MAGNETOELECTRIC COMPOSITE GRADIOMETER AND POWER ANALYSIS

6.1 Introduction

Magnetoelectric (ME) composites use product property of magnetoelectric effect which involves induction of strain in the magnetostrictive material on application of magnetic field which is then transferred to piezoelectric material generating charge or voltage. The figure of merit of magnetoelectric effect can be given by magnetoelectric susceptibility α_{ij} which is a function of product of dielectric permittivity (ε) and magnetic permeability (μ). Hence, a ME composite consisting of a piezoelectric material with high dielectric constant and a magnetic material with high permeability will have high interaction between the two phases resulting from the high degree of stress transfer [72-74]. Magnetoelectric gradiometer detects gradient in magnetic field as a function of frequency near EMR. Previously, we have proposed a gradiometer design based upon $0.8Pb(Zr_{0.52}Ti_{0.48})O_3$-$0.2Pb(Zn_{1/3}Nb_{2/3})O_3$ (PZT) – Terfenol-D laminate composite structure with unipoled transformer architecture [75]. The fabricated gradiometer exhibited high sensitivity for detecting differential magnetic field near EMR. In this study, we fabricated two different designs of gradiometer with metal (nickel) and ceramic (PZT) as the material layers in the laminate composite. The dielectric permittivity (ε_r) of the PZT was calculated to be 1290. Nickel was selected over other materials considering its co-firing ability with PZT which will allow fabrication of multilayer structures using well established tape-casting technique. Nickel is widely used as conductive paste in multilayer chip capacitors owing to its high conductivity and low cost. It has been found that when nickel is fabricated into nano-sized powder, it forms chain-like structures due to its magnetic properties. The chain-form nickel powder based conductive paste has eight times higher conductivity than that fabricated from conventional powders [76]. Thus, it is possible to utilize both the characteristics of nickel at the same time, namely magnetostriction and electrical conductivity. Nickel and cobalt exhibit excellent magneto-strictive properties. The values of saturation magnetostriction, λ_s, for Ni and Co are lower than $CoFe_2O_4$, but are comparable to some common ferrites such as $NiFe_2O_4$ and $MnFe_2O_4$. The magnitude of the magnetostriction in rare-earth iron alloys is significantly higher, but they suffer from the drawback of poor electrical properties and complex synthesis. Ni exhibits anisotropic magnetostriction ($\lambda_{111} = -25 \times 10^{-6}$ and $\lambda_{100} = -46 \times 10^{-6}$) with an easy direction along <111>. The electrical resistivity of Ni ($\sim 6\times 10^{-6}\Omega^{-1}cm^{-1}$) is comparable with that of Co ($\sim 5.5\times 10^{-6}\Omega^{-1}cm^{-1}$), which allows both of them to be suitable for conductors [77]. Thus, the PZT – Ni magnetoelectric composite architecture provides a high ME figure of merit. It is possible to modify the magnetocrystalline properties of metal particles by processing conditions leading to changes in microstructure, morphology, surface chemistry and particle shape. Nickel is a magnetically soft material and has a saturation DC magnetic field on the order of few hundreds of Oe. Hence, in order to investigate the shift in resonance frequency of the gradiometer two different magnetic DC bias ranges were selected. The first magnetic DC bias range of 0 – 100 Oe was chosen to understand the effect of coercivity on the gradiometer characteristics and the second magnetic DC bias range of 0 – 1600 Oe was selected to evaluate the performance in the full range.

6.2 Experimental

The magnetoelectric gradiometer sample A (design 1) had the ring dot electrode pattern printed on top and the bottom surface of the PZT where ring acts as the input while dot acts as the output. The output section had a diameter of 4 mm and the input section has a width of 2.2 mm. There is an insulation gap between input and output section of 1.2 mm. Two nickel discs with diameter of 6.3 mm and thickness of 2 mm were bonded on the output section as shown in

Figure 6.1(a) Thus, the gradiometer has separated ground electrode. Inset shows picture of fabricated gradiometer. The gradiometer sample B (design 2) had the ring dot electrode pattern printed on the top surface of the PZT, where ring acts as the input while dot acts as the output. The output section has a diameter of 6.3 mm and the input section has a width of 2.2 mm. There is an insulation gap between input and output section of 1.2 mm. The ground electrode is at the bottom of the PZT. Inset shows picture of fabricated gradiometer. Nickel disc with diameter of 6.3 mm was bonded on the output section as shown in Figure 6.1(b). Thus, in this case the gradiometer has common ground electrode.

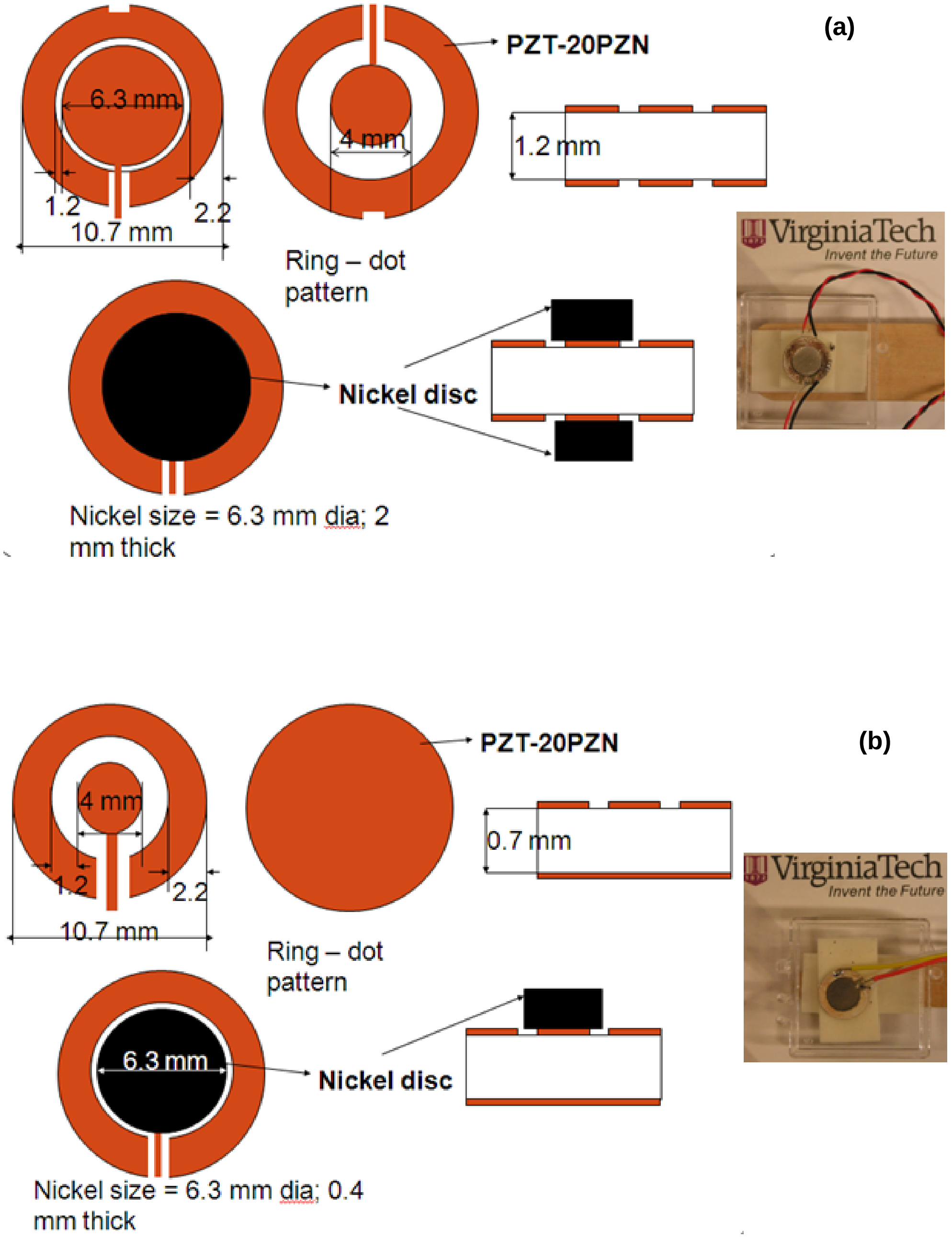

Figure 6.1 (a) Gradiometer design 1 (sample A): Fabrication of ring – dot electrodes with stripped electrode pattern and attachment of nickel disc on the output electrodes, Inset: picture of fabricated gradiometer (b) Gradiometer design 2 (sample B): Ring – dot electrode pattern with common ground electrode and attachment of nickel disc on the output electrode, Inset: picture of fabricated gradiometer

In both constructions ultra corrosion-resistant nickel (alloy 200/201) was used with the elemental composition shown in Table 6.1.

Table 6.1 Elemental composition of the nickel alloy used in the fabrication of the gradiometer.

Nickel 200 / 201 Chemical Composition, %							
	Ni	**Fe**	**Cu**	**C**	**Mn**	**S**	**Si**
Nickel 200	99.0 min	0.40 max	0.25 max	0.15 max	0.35 max	0.01 max	0.35 max
Nickel 201	99.0 min	0.40 max	0.25 max	0.02 max	0.35 max	0.01 max	0.35 max

The piezoelectric constant of the synthesized composite were measured by APC YE 2730A d_{33} meter. Resonance characteristics were determined by HP 4194A impedance analyzer (Hewlett Packard Co. USA). For the gradiometer samples A and B, the input voltage of 10 V_{p-p} was applied on the ring section and the output voltage was measured from dot section using a Tektronix TDS 420A four channel digital oscilloscope with varying DC magnetic bias field. The frequency range was chosen near resonance frequency of the transformer [78-80], i.e. 249 kHz for sample A and 235 kHz for sample B. The magnetic field generated in the dot-section was measured by using the magnetic field sensor (microprocessor controlled precision gauss meter from Walker LDJ scientific, Inc). All the measurements were repeated to check the consistency of results.

6.3 Results and discussion

For a piezoelectric transformer operating near resonance point, the equivalent circuit can be represented as shown in Table 6.2.

Table 6.2 Equivalent circuit parameter of the input and output sections at resonance – antiresonance frequency range.

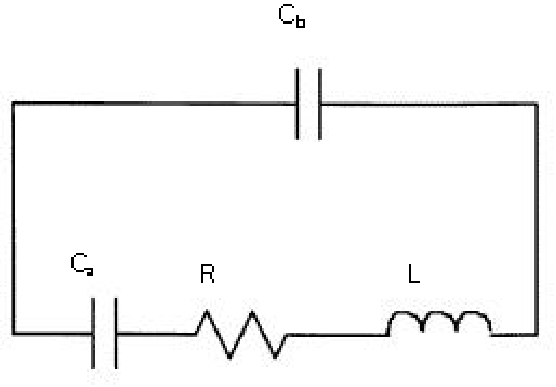

Sample A	Input section	Output section	Sample B	Input section	Output section
R(kΩ)	1.71	1.67	R(Ω)	337.94	669.56
L(mH)	23.085	48.97	L(mH)	7.31	14.37
Ca(pF)	16.785	8.392	Ca(pF)	62.75	32.485
Cb(pF)	467.235	315.06	Cb(pF)	719.39	307.49

In this circuit R, L, C_a are the motional resistance, inductance and capacitance, and C_b is the damped capacitance. Figure 6.2 (a) - (d) show the open circuit (OC) and short circuit (SC) impedance responses of samples A and sample B respectively.

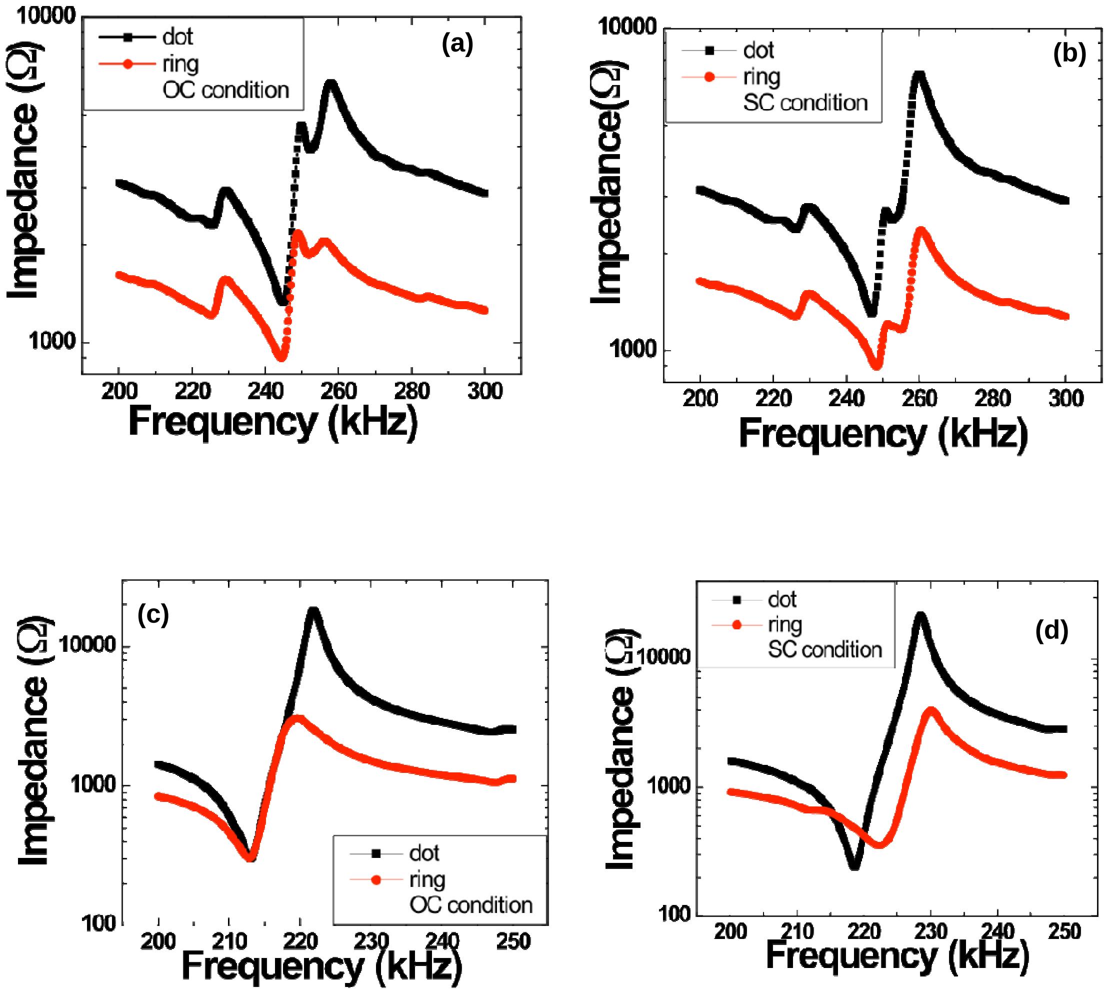

Figure 6.2 (a) Open circuit (OC) and (b) short circuit (SC) impedance response of sample A. (c) Open circuit (OC) and (d) short circuit (SC) impedance response of sample B.

Using these spectrums the magnitude of the equivalent circuit parameters was calculated for both input and output. Matching impedance of a piezoelectric transformer is given by:

$$Z_{match} = \frac{1}{2\pi f_r c_{b(output)}} \text{ (input short circuited)} \qquad (1)$$

where fr is the resonance frequency. Using the values listed in Table 6.2, the matching impedance was calculated to be 2028.75 Ω for Sample A and 2202.53 Ω for Sample B. Simplistically, the gain of the transformer is given by:

$$\mathrm{Gain} = \sqrt{\frac{\mathrm{C_a(input)}}{\mathrm{C_a(output)}}} \qquad (2)$$

Here, the transformer gains are 1.414 for sample A and 1.39 for sample B, and efficiency of the transformer is given by:

$$\mathrm{Efficiency} = \frac{1}{1+4\pi f_{r,in} C_{a,in} R_{in} (\frac{C_{b,out}}{C_{a,out}})} \qquad (3)$$

where in and out stand for the input and output, respectively. The expected efficiency of the transformer for Sample A was calculated to be 99.8% while that for Sample B was calculated to be 99.84%. The transformer is always operated between the frequency limits given by:

$$\omega_{SC} = \frac{1}{\sqrt{LC}} \qquad (4)$$

and

$$\omega_{OC} = \frac{1}{\sqrt{L(C^{-1}+C_{d2}{}^{-1})^{-1}}} \qquad (5)$$

where ω refers to the angular frequency and subscripts “SC” and “OC” refer to short circuit and open circuit conditions. The symbols L and C are the motional inductance and capacitance of the transformer while C_{d2} is the damped capacitance of the output section. The operating frequency range for sample A was calculated based on equations 4 and 5 as 248.27 kHz – 251.55 kHz and that for sample B was 232.94 kHz – 244.94 kHz.

The transformer characteristics for a unipoled transformer structure are directly related to the ratio of input/output area. Higher ratio means higher capacitance ratio of input and output section and vice versa. The transformer gain varies directly with area ratio. For high area ratio, large gain can be obtained. The working principle of gradiometer can be explained as follows: Gradiometer resembles in functionality a magnetic field sensor, where it measures the magnetic field gradient and sensitivity is determined the ability to quantify change with respect to a reference value. In order to increase the sensitivity of the gradiometer, higher voltage gain is essential which can be obtained with higher input – output area ratio of the transformer architecture. Higher gain will generate higher output voltage in the output section thereby increasing the ability of the magnetoelectric gradiometer to quantify magnetic field gradient near EMR range.

6.3.1 Theory of magnetoelectric gradiometer

Theoretical estimates of Ni-PZT gradiometer were similar to previously described taking into account the material parameters of nickel [75, 81-83]. Description of ME effect for ME gradiometer at the EMR frequency range is given by:

$$\alpha_E = -\frac{1}{\Delta_a}\left[\frac{2d_{31}q_{31}}{\varepsilon_{33}s_{11}(1-v)}\left(\frac{(1+v)J_1(k)}{\Delta_r} - 1\right) + \frac{\alpha_{33}}{\varepsilon_{33}}\right], \qquad (6)$$

where q_{ij} and d_{ij} are piezomagnetic and piezoelectric coefficients, ε_{ij} is the permittivity matrix, $\alpha_{33}/\varepsilon_{33}$ is the value of low frequency ME coefficient,

$\Delta_r = kJ_0(k) - (1-v)J_1(k)$,

$\Delta_a = 1 - K^2_p + K^2_p(1+v)\, J_1(kR)/\Delta_r + iG$,

$K^2_p = 2d^2_{31}/\varepsilon_{33}\ \varepsilon_{33}(1-v)$ is the coefficient of electromechanical coupling for radial mode, and G is the loss factor. It can be noted that the value of the ME effect is mainly determined by the product $d_{31}\cdot q_{31}$.

The shift in the EMR frequency range can be estimated as a function of H [75]. This shift is due to a change in Young’s modulus (E) caused by the magnetic field: namely, the ΔE effect. The shift δfr in the EMR frequency range can be estimated as a function of bias magnetic field based as follows:

$$\delta f_r = \frac{\Delta E f_r}{2E(1+v)z}\frac{(3+v)z^2J_0^2(z)-8zJ_0(z)J_1(z)+[(1+v)z^2+4(1-v)]J_1^2(z)}{z\left[J_0^2(z)+J_1^2(z)\right]-2J_0(z)J_1(z)}. \qquad (7)$$

where

$$\frac{\Delta E}{E} = \frac{4}{27}E\Lambda t_2^2\frac{\left[\cosh(h)-\cosh\left(\frac{h}{3}\right)\right]\left[\cosh(h)-9\cosh\left(\frac{h}{3}\right)\right]}{\left[\cosh(h)+3\cosh\left(\frac{h}{3}\right)\right]^2},$$

where $h = 3\chi_0 H/Ms$ is a dimensionless parameter, χ_0 is the permeability at $H=0$, $\Lambda = 3\chi/Ms^2$, and $t_2 = -B_2\frac{1}{2c_{44}}$, Ms is the saturation magnetization, B_2 is the magnetoelastic constant, and c_{ij} is the stiffness coefficient, $z = kR$, $v = -s_{12}/s_{11}$ is Poisson's ratio, $k = \omega\sqrt{\rho s_{11}(1-v^2)}$, ρ is the density, ω is the angular frequency, and $J_0(k)$ and $J_1(k)$ are Bessel functions of the first kind. Material parameters for nickel taken in the calculation are as following: ρ = 8900 kg/m^3; Young's modulus = $20\cdot10^{10}$ N/m^2; $\mu_{33}/\mu_0 = 20$; and q = $-3.1\cdot10^{-9}$ C/N. Material parameters for PZT were taken to be ρ = 7300 kg/m^3; Young's modulus = $0.7\cdot10^{11}$ N/m^2; $\varepsilon_{33}/\varepsilon_0 = 4100$; and d = $289\cdot10^{-12}$ C/N.

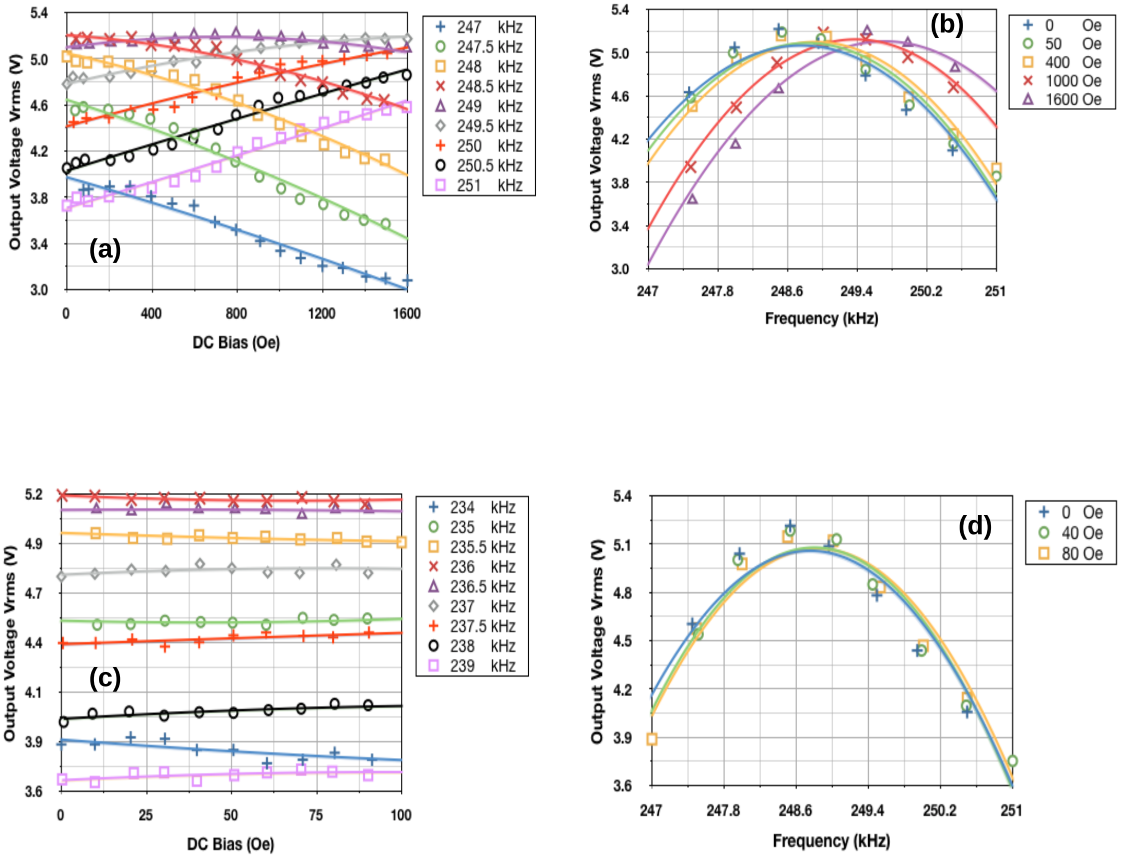

Figure 6.3 Theoretical dependence (solid line) and experimental results (dots) of ring-dot gradiometer design 1 (sample A) (a) Output voltage as a function of DC magnetic field (0 – 1600 Oe) at varying frequencies, and (b) Output voltage as a function of frequency at varying DC magnetic field (0 – 1600 Oe). (c) Output voltage as a function of DC magnetic field (0 – 100 Oe) at varying frequencies, and (d) Output voltage as a function of frequency at varying DC magnetic field (0 – 100 Oe). The input voltage of the gradiometer was fixed at $10V_{p\text{-}p}$.

Figure 6.3 (a) shows the dependence of voltage output in the dot section of sample A on DC bias field for various frequencies near EMR. Figure 6.3 (b) shows dependence of voltage output on frequency for different applied DC magnetic fields. Figure 6.3 (c) and (d) shows dependence of output voltage generated in the dot section on DC bias field and frequency within the range of 0 – 100 Oe DC bias field. InFigure 6.3, the solid line represents the theoretical values while the experimental data is shown by dots. The input voltage on the ring section was maintained at 10 $V_{p\text{-}p}$. It can be seen in Figure 6.3 (a) that there is change in slope on either side of the EMR. At the frequency of 250 and 250.5 kHz, the variation in output voltage is linear at higher applied magnetic field. In Figure 6.3 (b), two regions can be clearly separated and the device can provide differential voltage as the magnetic field changes with respect to reference state as shown in Figure 6.3 (b).

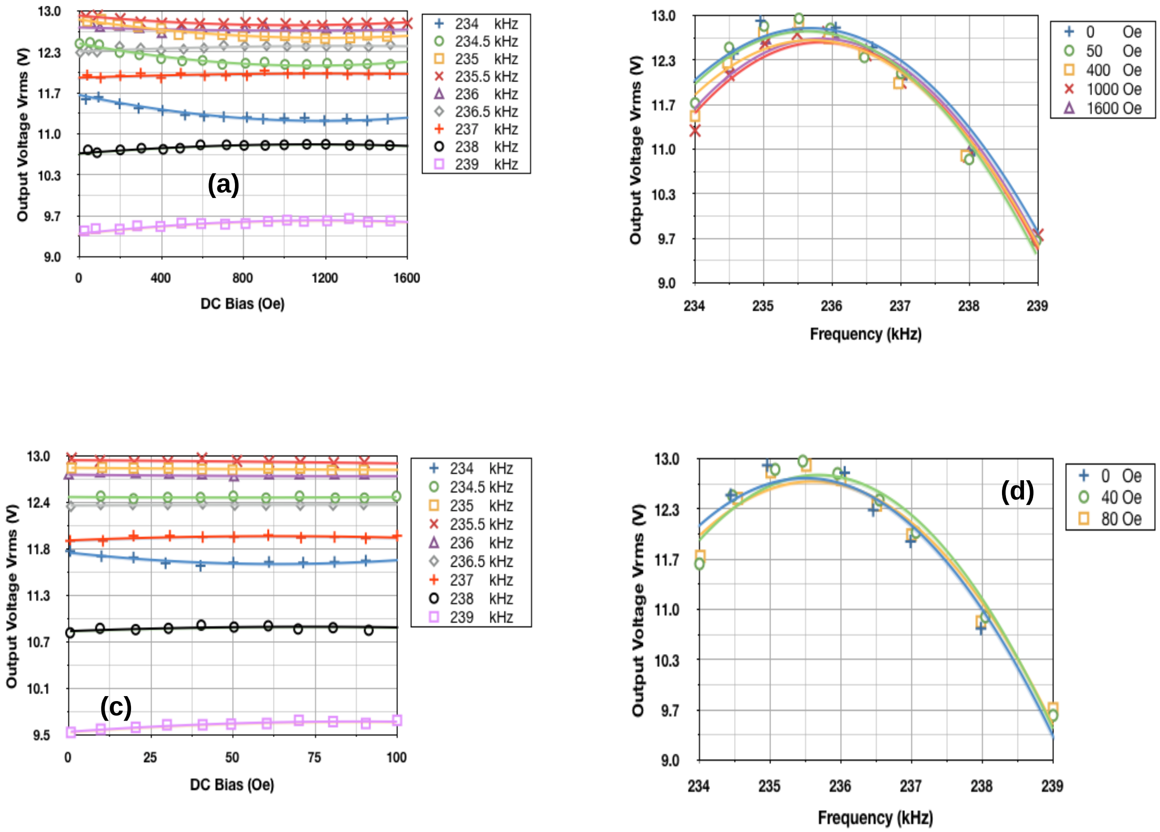

Figure 6.4 Ring-dot gradiometer design 1 (sample B) (a) Output voltage as a function of DC magnetic field (0 – 1600 Oe) at varying frequencies and (b) Output voltage as a function of frequency at varying DC magnetic field (0 – 1600 Oe). (c) Output voltage as a function of DC magnetic field (0 – 100 Oe) at varying frequencies, and (d) Output voltage as a function of frequency at varying DC magnetic field (0 – 100 Oe). The input voltage of the gradiometer was fixed at $10V_{p\text{-}p}$.

Figure 6.4 (a) shows the voltage output in the dot section of sample B as a function of DC bias field for various frequencies near EMR whereas; Figure 6.4 (b) shows voltage output as a function of frequency for different applied DC magnetic fields. Similarly, Figure 6.4 (c) and (d) shows the output voltage generated in the dot section of sample B as a function of DC bias field and frequency for the DC bias range of 0 – 100 Oe. The input voltage on the ring section was maintained at 10 $V_{p\text{-}p}$.

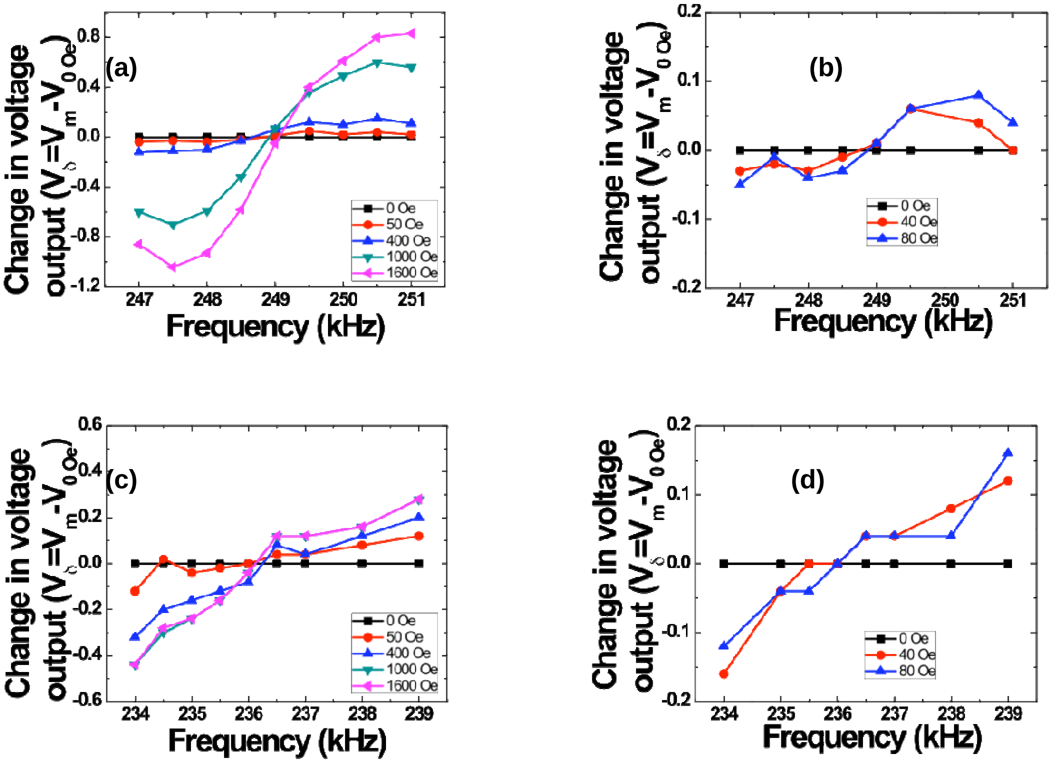

Figure 6.5 Change in output voltage with respect to change in the DC magnetic field, Input: 10 $V_{p\text{-}p}$ (sample A). Change in the output voltage doubled with increase in the input voltage; (a) DC Bias Range from 0 to 1600 Oe. (b) DC Bias Range from 0 to 100 Oe. Change in output voltage with respect to change in the DC magnetic field, Input: 10 $V_{p\text{-}p}$ (sample B); (c) DC Bias Range from 0 to 1600 Oe, (d) DC Bias Range from 0 to 100 Oe.

Figure 6.5 (a) - (d) shows differential voltage change as a function frequency at constant DC magnetic fields with respect to reference state. It can be noted in Figure 6.5 (a), that the change in the output voltage increases as DC bias field increases. Although for lower DC bias field the change is smaller and the change of slope is becomes significant at higher values of DC bias field.

6.4 Power analysis

Input voltage on the ring section of the Ni-PZT gradiometer = 10 $V_{p\text{-}p}$ = 3.54 V_{rms}

Resistance of the gradiometer near EMR can be given as:

$R >= 500\ \Omega$

Hence, required power for the gradiometer:

Power = $V^2/R = (3.54)^2 / 500 = 25.06 \times 10^{-3}$ W = 25.03 mW.

6.5 Chapter Summary

It can be noted that sample B generates higher output voltage in the dot section; however, sample A shows higher sensitivity for detecting gradient magnetic field. This can be explained by a simple fact that sample A has 2 input and 2 output sections, transferring stress on both sides of the PZT; thus, increasing the overall change in the differential magnetic field. Although, the differential output voltage of the gradiometers is smaller for 0 – 100 Oe DC Bias range, it shows significant change in the magnitude of output voltage for higher range of DC Bias field (0 – 1600 Oe). There is a clear change of slope on either side of the resonance frequency in the detection range of 0 – 1600 Oe DC bias and a linear change is observed near EMR. Also, the output voltage measured in the dot section of the gradiometer increases linearly with increasing input voltage to the ring section. It can also be noted that the Ni - PZT gradiometers work at higher frequency ranges (247 – 251 kHz for sample A and 234 – 239 kHz for sample B) maintaining the sensitivity of the gradiometer over a wide range of near EMR frequency range. Thus, this unipoled transformer structured Ni-PZT gradiometer can be a good candidate for detecting gradient magnetic field in a wide frequency range near EMR. Comparison of Terfenol-D/PZT structure with Ni-PZT one shows that Ni-PZT gradiometer requires the low bias fields for sensing magnetic field gradient and more technological and cheaper.

CHAPTER 7

BOTTOM – UP SENSOR DESIGNS FOR STRUCTURAL HEALTH MONITORING AND MAGNETIC FIELD GRADIENT SENSING

7.1 Synthesis and microstructural characterization of barium-titanate decorated SiCN-MWCNT nanotubes – “nanoNecklace”

7.1.1 Introduction

Barium titanate (BTO) is currently the material of choice in multilayer ceramic capacitors (MLCCs) that are finding application in a wide range of electronic devices such as cell phones, display devices, and computers. Polymer derived ceramic, SiCN, is a unique material, which depending upon the processing conditions, can posses electrical properties ranging from those of a complete insulator to a near electrical conductor. [84-85] This material has also been demonstrated as a heat dissipating material which could be an attractive property for capacitors driven at high electric fields.[86] Flexibility of SiCN-MWCNTs structure allows easy manipulation and positioning on a given substrate. In addition, SiCN layer modifies the surface wetting characteristics of MWCNTs thereby promoting the adhesion of BTO nanoparticles.

Size effect is an important consideration in ferroelectrics. Studies on BTO have shown that the minimum grain dimensions that maintain ferroelectricity are 50nm for pure ceramics and 110 nm for the doped case. [87] Theoretical models also predict the critical size for pure BTO [88] to be 44nm. Further it has been found that pure BTO has slightly smaller tetragonality in the powder form (as compared to single crystal) and the doped ceramics have much smaller tetragonality than of the pure ceramics. The reasons for these effects have been attributed to presence of intrinsic lattice stress.[89] SEM analysis combined with the surface tension measurements indicate that the surface bond contraction due to small size induces a compressive stress on the inner part of a grain. This effect plays an important role in ferroelectric materials in the nanometer size range. The induced stress causes decrease of Curie temperature and spontaneous polarization: with decreasing grain size, both of these effects get magnified. Another size- driven effect is the dielectric anomaly that arises due to the surface bond contraction. The domain wall contribution has an opposite effect compared to that with the surface bond contraction induced effect. When the grain size decreases to a value comparable to the width of domain walls, pinning points develop inside the grains and the domain wall motion is inhibited. The reduced wall mobility causes a decrease in the relative permittivity. The net effect depends on the relative play of the increase of relative permittivity by the surface bond contraction effect and its decrease by the domain wall pinning effect. These considerations are important for designing the nanostructures since if the grain size is smaller than the critical size, then the residual internal stress in the ceramic may lead to decrement in the permittivity. The decrement in permittivity is rapid beyond the critical size. Thus, our goal was to achieve BTO particle dimensions in range of 20 – 50 nm which is challenging as smaller sizes are preferable for coating.

7.1.2 Experimental Procedure

BTO- decorated SiCN nanotubes were synthesized by pyrolysis of polyurea (methylvinyl) silazane (Ceraset^{TM} Kion Specialty Polymers, Charlotte, NC) and barium titanium ethylhexano-isopropoxide metal-organic precursor on the surfaces of MWCNTs. Commercially available liquid Ceraset and barium titanium ethylhexano-isopropoxide (Alfa Aesar ^{TM}) were used as precursors for SiCN and barium titanate respectively. MWCNTs were used as a template material for SiCN monolayer coating. [90] The first step in synthesis was wetting of nanotubes with Ceraset by addition of 50 vol% of CNTs in a 5 vol% solution consisting of Ceraset and ethanol. This solution was ultra-sonicated for 30 min resulting in uniform coating of nanotubes with Ceraset. The second step consisted of adding 10vol% of BTO precursor to Ceraset-CNT solution followed by ultrasonication for 1 hr. The solution was then dried in air at ~80℃ under magnetic stirring to allow evaporation of ethanol. Dried powder was then cross-linked and pyrolyzed in an alumina tube furnace using two-step annealing profile under high purity nitrogen atmosphere. The annealing process consisted of heating the powder to 400℃ and holding for 2 hrs (for cross-linking of the Ceraset polymer), followed by heating at 900℃ for 4 hrs (to convert polymer into ceramic).

7.1.3 Results and Discussion

Figure 7.1 (a) and (b) show the microstructure of BTO coated on SiCN-MWCNTs. The nanotubes were found to have the diameter of 20 to 100 nm while BTO nanoparticles were found to be in the range of 10 ~ 40 nm in size.

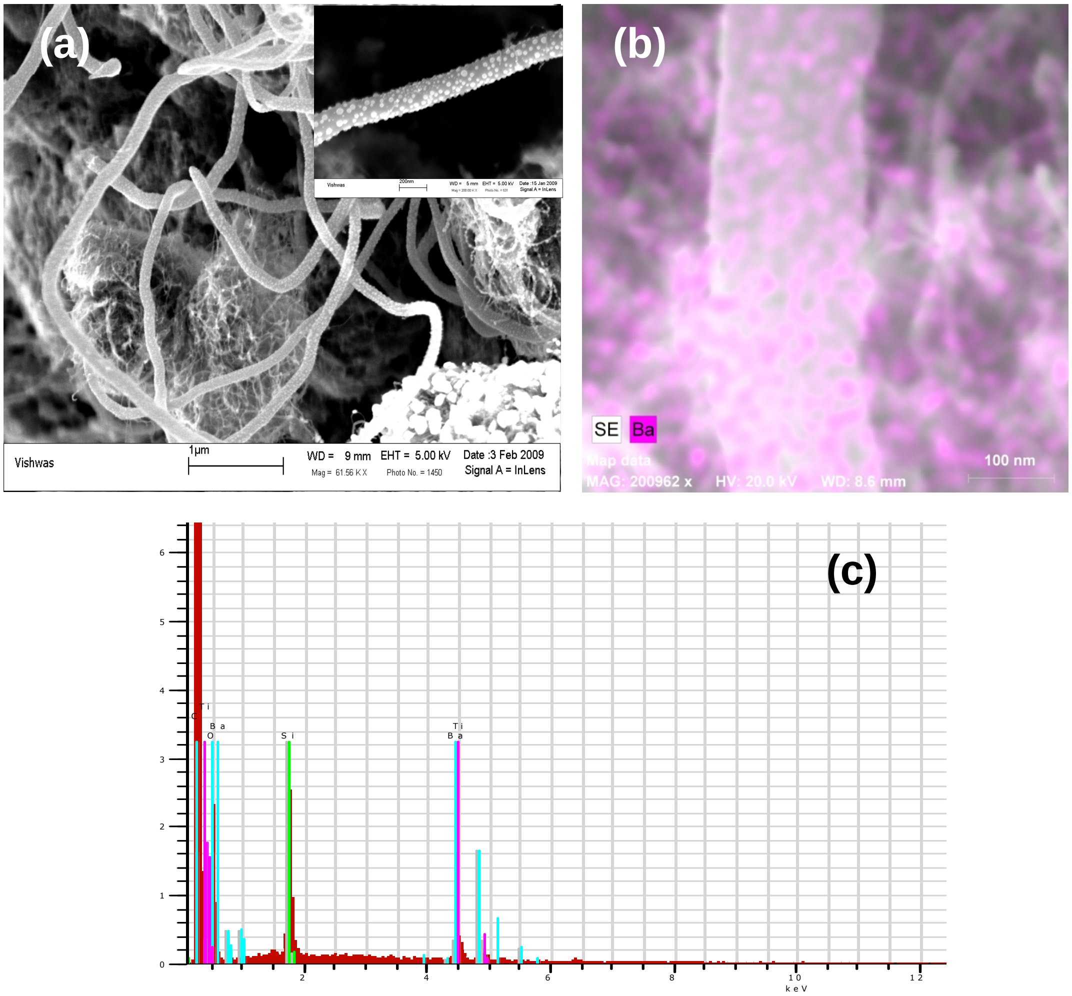

Figure 7.1 (a) FE-SEM image showing BTO nanoparticles covering the nanotube surface. Inset shows high magnification image of the area corresponding to nanotube surface; (b) EDS-elemental map corresponding to Ba element, showing the presence of barium in the nanoparticles and (c) EDS- spectra corresponding to Figure 7.1(b).

It was found that the nanotubes with larger diameter were fully coated with BTO nanoparticles while those with diameter in the range of 20 ~ 40 nm were only partially coated. This indicates that there is a specific size ratio (r_{MWCNT}/r_{BTO}) beyond which adhesion between the two phases (BTO and SiCN) becomes stronger due to increased surface area. We also expect that the wetting characteristics play an important role in achieving the adhesion between SiCN and BTO. Nanotubes with larger diameters contain higher number of surface defects providing smaller liquid contact angles as compared to thinner nanotubes. Barber et al. have experimentally shown that wetting properties are dependent upon the diameter (or curvature) of MWCNTs and the wetting properties are different for internal and external surfaces. [91] A monolayer coating of SiCN on the surface of MWCNTs increases the surface roughness and promotes wetting. SEM elemental mapping analysis (Bruker^{TM} EDX with a Silicon Drifted Detector) revealed presence of barium and titanium on the surface of the sample as shown in Figure 7.1(b). Corresponding elemental spectra are shown in Figure 7.1(c).

HRTEM analysis was conducted to confirm the presence of BTO nanoparticles (200 keV, FEI Company Titan 300). Figure 7.1(a) and (b) show the TEM images of synthesized nanoNecklace.

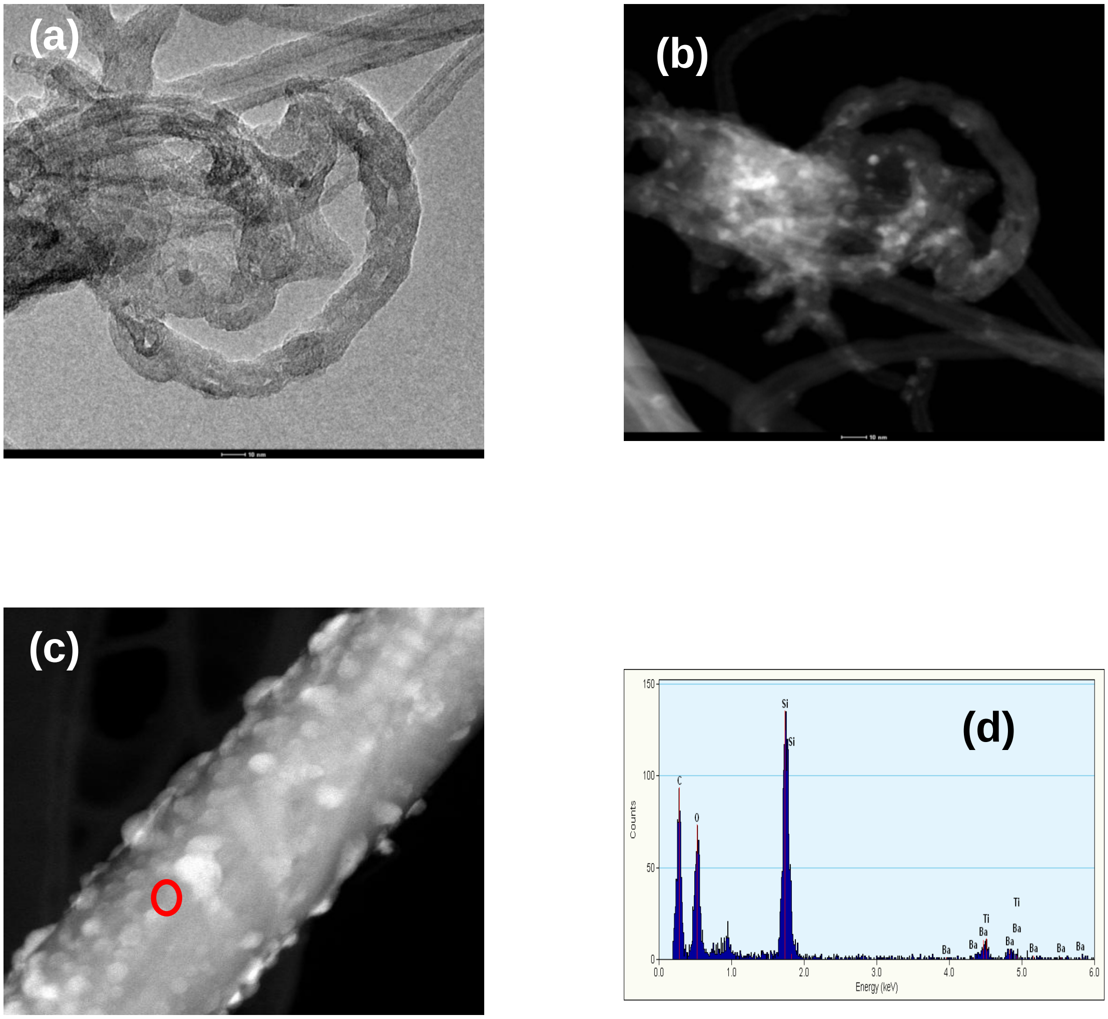

Figure 7.2 Scanning TEM images of NTs covered with BTO particles (a) Bright Field (BF) image (b) High Angle Annular Dark Field (HAADF) image (c) HAADF image of a single NT. Heavy elements such as Ba appear bright in HAADF mode, (d) X-EDS spectrum from red circle in Figure 7.1(c).

The bright field image shows the presence of BTO nanoparticles with a clear contrast in high angle annular dark field (HAADF) image indicating coating of BTO on larger diameter nanotubes. Figure 7.2 (c) and (d) show the HAADF high magnification micrographs of individual nanoNecklace with contrast in distribution of BTO phase and underlying SiCN phase. HAADF – EDS analysis confirmed the presence of Ba, Ti, Si, O and C elements as shown in the spectrum. X-ray photoelectron spectroscopy (XPS, PHI Quantera SXM with CasaXPS software) measurements were conducted in order to confirm the presence of Ba, Ti and O elements on the surface and investigate the nature of bonding.

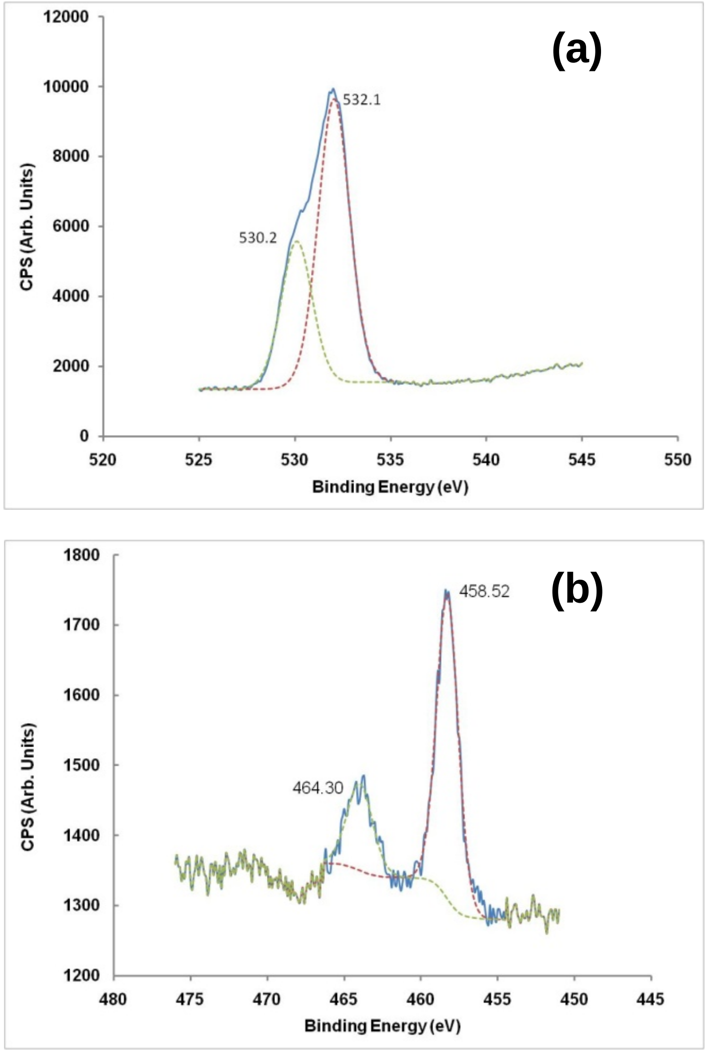

Figure 7.3 XPS spectra of (a) O-1s and (b) Ti-2p peaks, corresponding to $BaTiO_3$ and TiO_2 bonding type respectively (Dotted line is Gaussian-Lorentzian (30%) fitted XPS spectra).

The peaks at binding energy of 530.0 eV and 532.0 eV indicate the presence of TiO_2 and SiO_2 bonds respectively. High resolution (slow scan) XPS confirmed the presence of BTO bonding arrangement corresponding to binding energy of 458.52 eV as shown in Figure 7.3 (b) by Gaussian (70%)-Lorentzian (30%) fit (using the CasaXPS software). Combining the results of TEM and XPS analysis it can be summarized that nanoNecklace comprises of BTO nanoparticles arranged along the length of large diameter SiCN-MWCNT nanotubes. The morphology of nanoNecklace can be further improved by tailoring the wetting characteristics through surface functionalization and coatings. A change in wetting characteristics will allow more uniform coverage of BTO over the MWCNT template resulting in higher dielectric surface area and hence capacitance.

In order to get a full layer coating on the surfaces of the MWCNTs we propose functionalization treatment of the MWCNTs. in this approach, the MWCNTs are treated with acid which introduces carboxyl OH functional groups on the CNT surfaces. These groups become the defect sites for the BTO nanoparticles to get attached and form a full layer of coating.

7.2 Synthesis of fully coated barium titanate nanotubes: Nano-sensor

7.2.1 Experimental

60 mg of MWCNTs were immersed in 30 vol% nitric acid and kept at 120℃ for 12 hrs under constant stirring. Thus functionalized nanotubes were then rinsed with de-ionized water until the pH of the system became neutral and then dried in an oven at 80℃. In another experiment, the acid concentration was increased to 40 vol% and the procedure was repeated for functionalization of MWCNTs. Fourier Transform Infrared (FTIR) spectroscopy was performed in order to monitor the functionalization of the MWCNTs. For this purpose, 30 mg of functionalized MWCNTs were immersed in a mixture of 3 mL of barium titanium ethylhexano-isopropoxide (Alfa Aesar ^{TM}) and 5 mL of Isopropanol. The mixture was then stirred at various holding temperatures and times as summarized in Table 7.1. The powder was dried and then

annealed in a tube furnace at 700 ℃ for 2 hrs under high purity nitrogen atmosphere. The annealed powder was labeled and sealed in bottles for further characterization.

Table 7.1 Functionalization and coating parameters

HNO_3 conc.	30 vol %	40 vol %
BTO precursor concentration	3 mL	3 mL
Coating temperature	40, 60, 80 ℃	40, 60, 80 ℃
Coating time	1, 2, 3, 4 hours	1, 2, 3, 4 hours

7.2.2 Results and discussion:

7.2.2.1 Fourier Transform Infrared (FTIR) Spectroscopy

The surface of the MWCNTs can be chemically modified in order to induce certain properties. In this study, the MWCNTs were functionalized with 30% and 40% nitric acid in order to investigate effect of functionalization on the wetting characteristics of the carbon nanotubes.

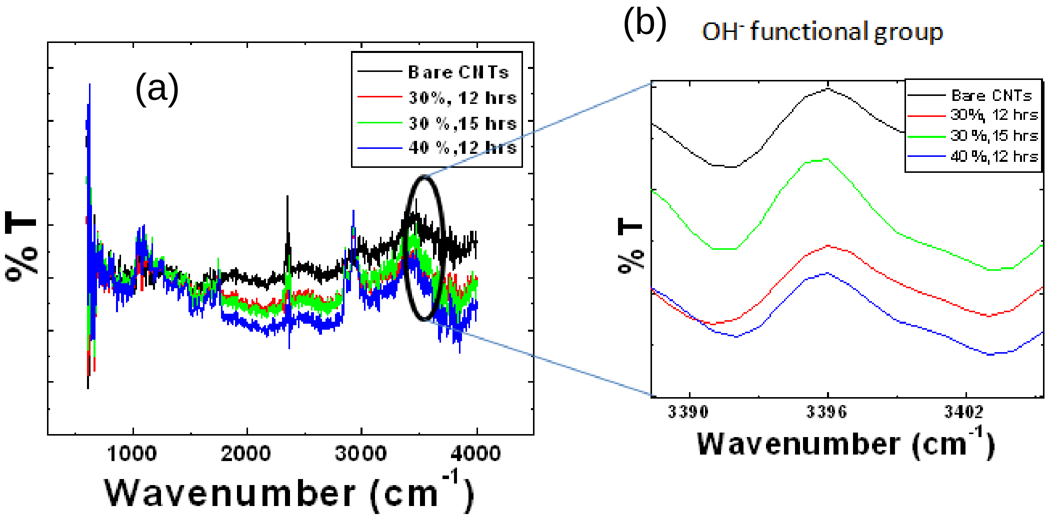

Figure 7.4 FTIR spectroscopy of functionalized MWCNTs (a) general transmittance spectrum (b) peaks showing presence of OH^- functional groups.

Figure 7.4 (a) shows the FTIR spectrum of MWCNTs functionalized with various acid concentrations and times. Functionalization of MWCNT can be defined as attachment of functional (OH-) groups. These functional groups act as defect sites for various compounds to get attracted. Contact angle of the surface of functionalized MWCNTs plays a very important role in determining the degree of coating on the surface. This has been explained in detail in section 7.2.2.3. From Figure 7.4 (b), the peak for OH^- functional group can be observed from the transmittance spectrum at a wavenumber of 3396 cm^{-1}. This peak is due to the vibrational modes of the OH- groups. Thus, the intensity of the peak is higher for functionalization time of 12 hrs with 30 vol% acid concentration. Also, the peak is broad indicating a large number of carboxyl groups are present on the surfaces of these MWCNTs. A peak observed at 1711 cm^{-1} corresponds to C=O stretching further indicating the introduction of carboxyl groups. [92-94]

7.2.2.2 Microstructural Characterization

Figure 7.5 shows the microstructure of BTO nanoparticles decorated functionalized MWCNT. The nanotubes were found to have diameters of 20 – 200 nm whereas the BTO nanoparicles size was found to be in the range of 5-25 nm. The coating thickness and coating yield depends on nanotube diameter and curvature of the surface. The coating temperature was varied from 40℃ to 80℃ and the coating time was varied from 1 hr to 4 hr while maintaining the BTO precursor concentration at 3 mL. From Figure 7.5 it can be clearly seen that the coating yield and coating thickness of BTO nanoparticles increases with increasing coating time. MWCNTs functionalized for 12 hrs in 30 vol% HNO_3 were found to be fully coated with BTO nanoparticles at coating temperature of 40℃ and and coating time of 3 hrs respectively. Figure 7.6 shows high magnification SEM image of fully coated carbon nanotubes with BTO nanoparticles. A thick layer can be revealed at places where the BTO layer is peeled off from the surface of the MWCNT.

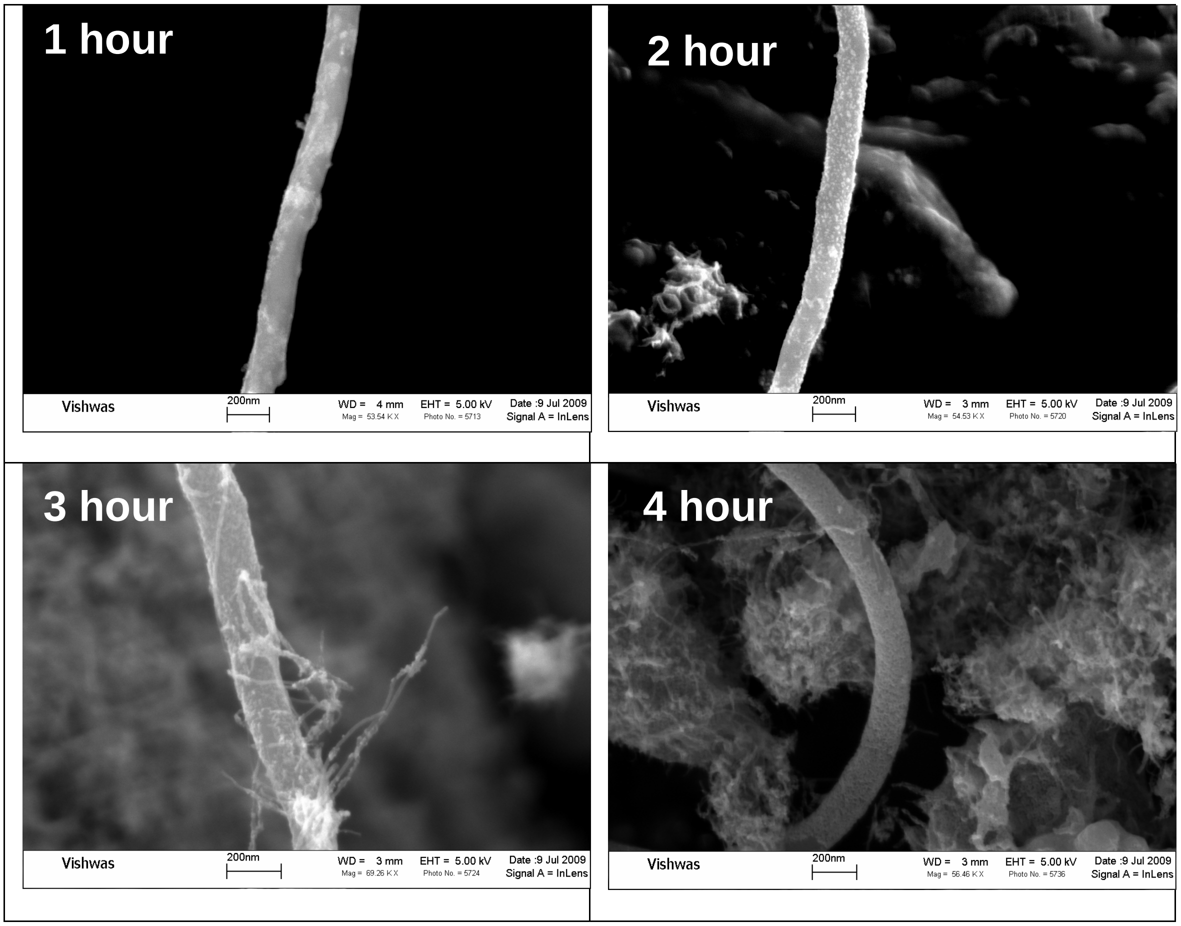

Figure 7.5 SEM micrographs of MWCNTs coated with BTO at coating temperature of 40℃ and coating time in the range of 1 – 4 hr.

Using high magnification SEM analysis, the coating thickness was observed to be 5 – 15 nm. Surface mapping revealed full coating of BTO nanoparticles on the nanotube surfaces. X-ray Energy Dispersive Spectrum (EDS) analysis was performed to confirm the presence of Ba, Ti and O on the surface of functionalized MWCNTs. TEM analysis shown in Figure 7.7 further confirms the presence of BTO nanolayer on the surface of the functionalized CNTs. The bright field (BF) and high angle annular dark field (HAADF) images revealed clear contrast between the CNTs and BTO nanoparticles as shown in Figure 7.8.

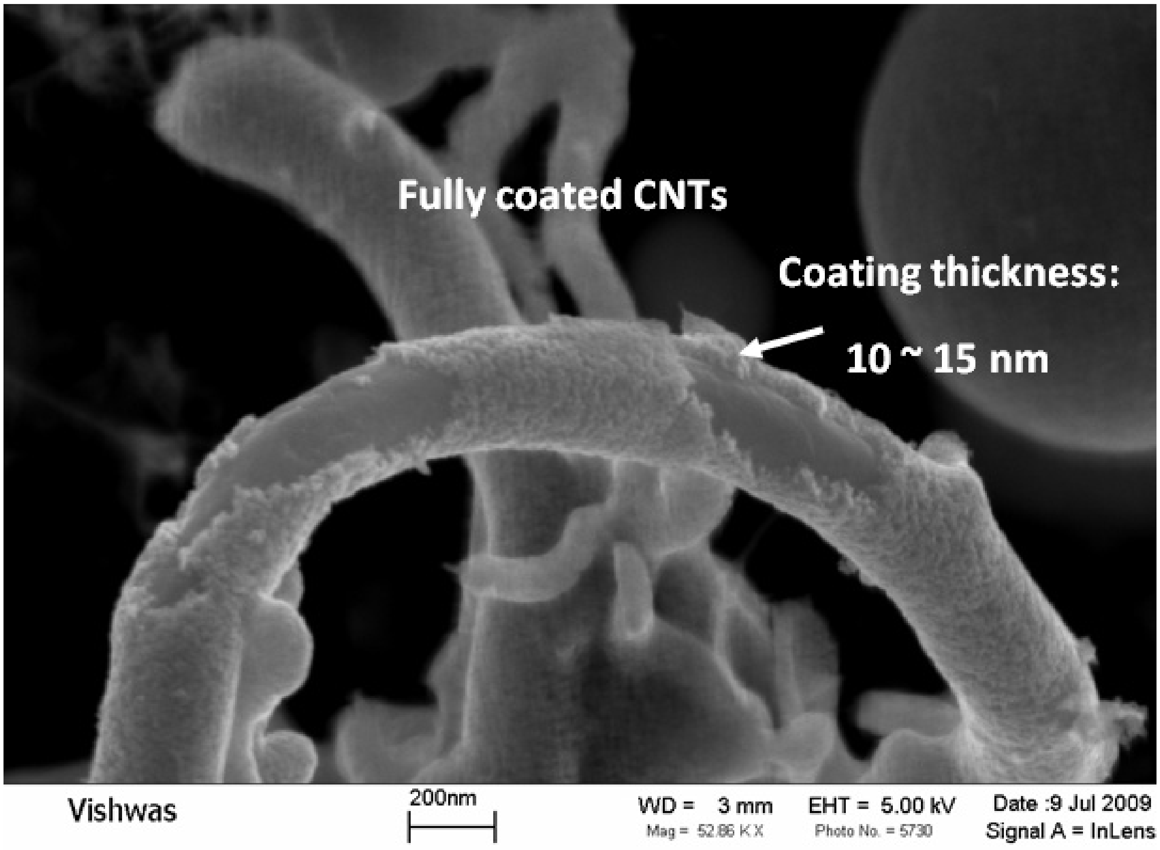

Figure 7.6 Microstructure of fully coated functionalized nanotubes.

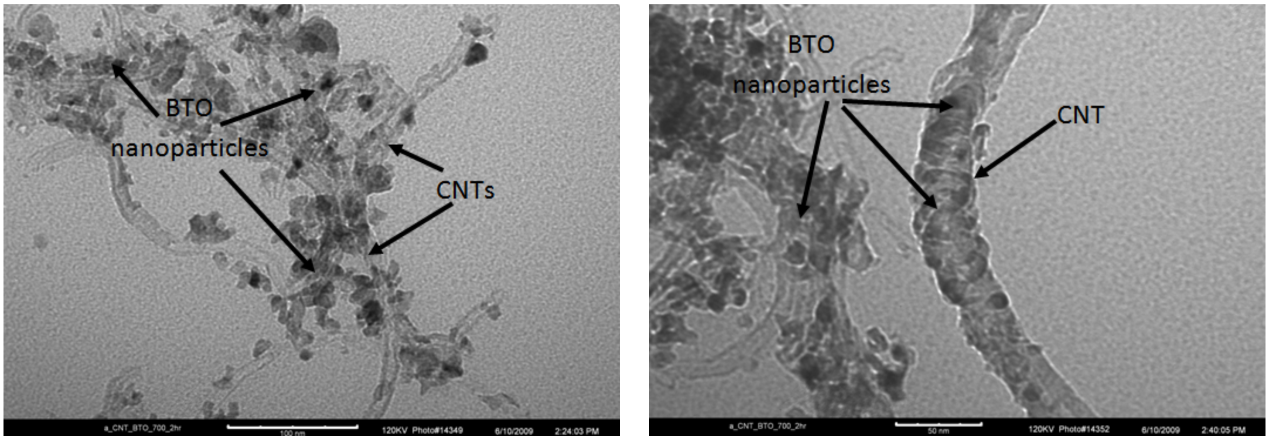

Figure 7.7 TEM images of partially coated MWCNTs with BTO nanoparticles.

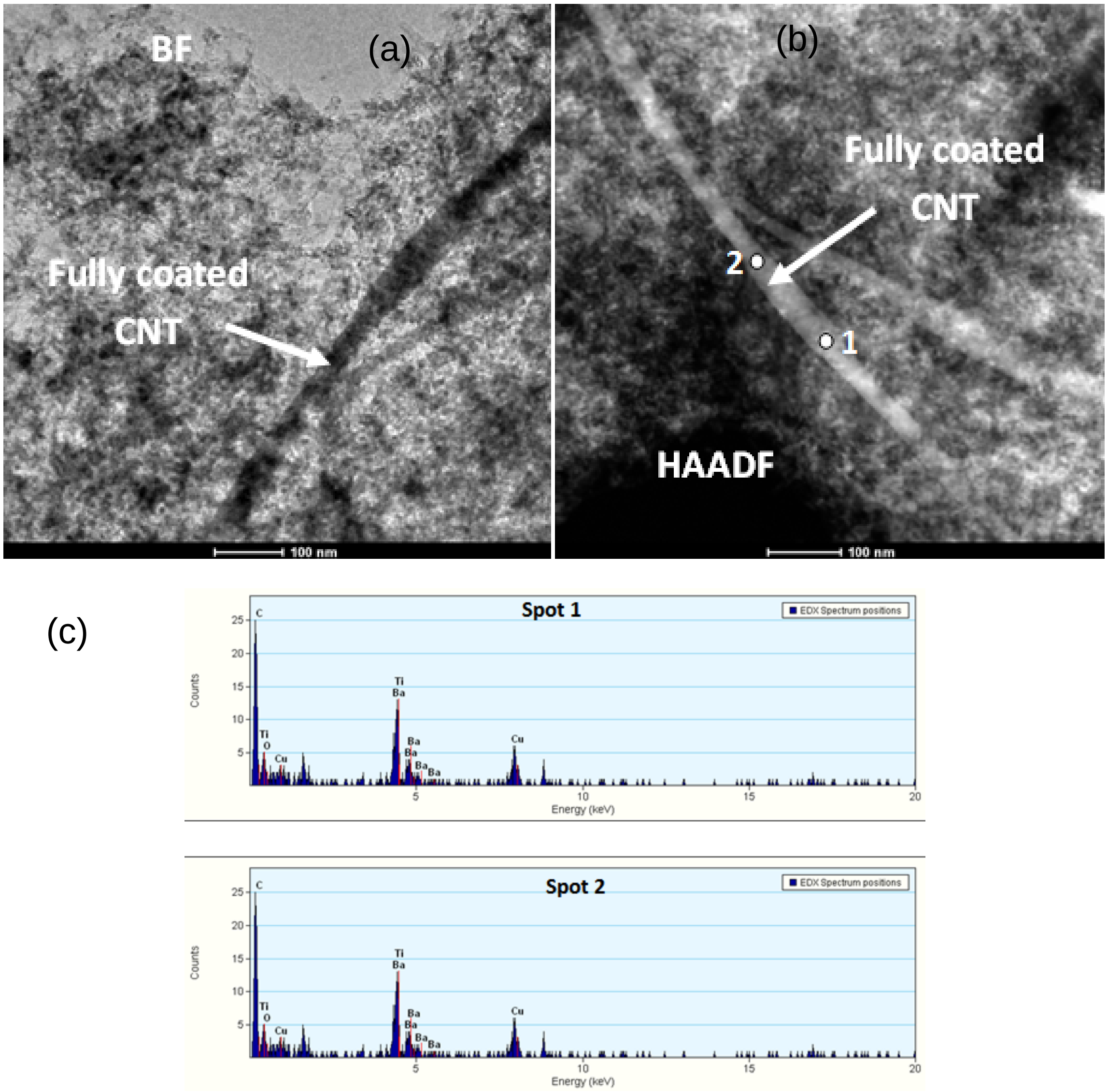

Figure 7.8 High magnification TEM images of fully coated nanotubes: (a) Bright Field (b) High angle annular dark field, and (c) EDS pattern of spots 1 and 2.

All the results from microscopy analysis showed that CNTs were fully coated with a thin layer of BTO. Depending upon the coating temperature and time, the thickness of BTO coating was found to vary. A line EDS scan was performed in order to quantify the coating thickness of

BTO on the CNT surface as shown in Figure 7.9 (a). EDS scans were performed across the entire diameter of the nanotube of diameter ~40nm, thus making each scan segment equal to 4 nm. At the beginning of the scan, intensity for C was highest indicating that the spot was just outside the CNT _BTO surface. The intensity for C reduced as a function of distance across EDS line scan up to 12 nm length and at the same time intensities for Ba and Ti increasd for scans at 8 and 12 nm respectively indicating the coating thickness of BTO. The C intensity increased in the middle range of the scans from 16 to 24nm indicating the middle portion of the CNT. At scan number 9 and 10 (i.e. distance 32 and 36nm on the EDS line scan) Ba and Ti concentration was higher.

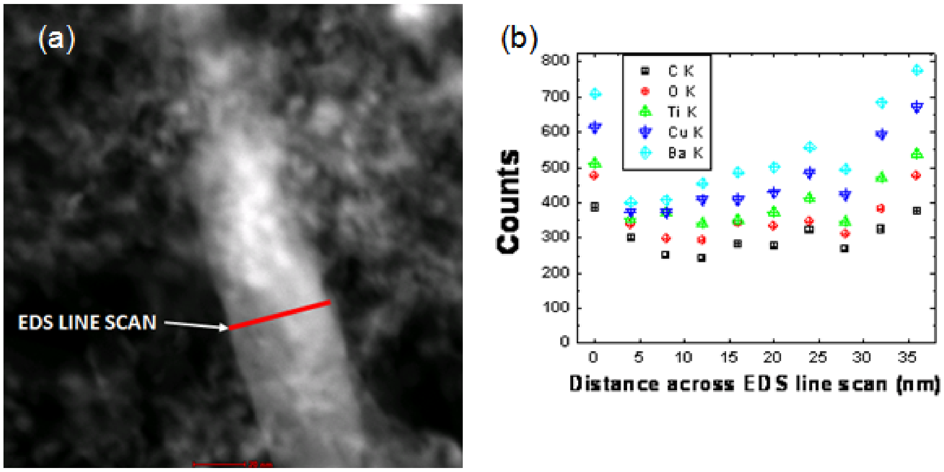

Figure 7.9 (a) Location of line EDS scan on a fully coated nanotubes (b) Intensity variation of various elements as a function of distance across the scan.

Figure 7.9(b) shows the variation of intensity in various elements across the EDS scan line. HR-TEM revealed the particle size of BTO to be in the range of 4-5 nm as shown in Figure 7.10(a). This supports our argument that there might be 2 to 3 layers of coating of BTO nanoparticles on the functionalized nanotube surface. Figure 7.10(b) shows the FFT from a selected area of the HRTEM image. Spot pattern in the FFT confirms crystalline state of BTO.

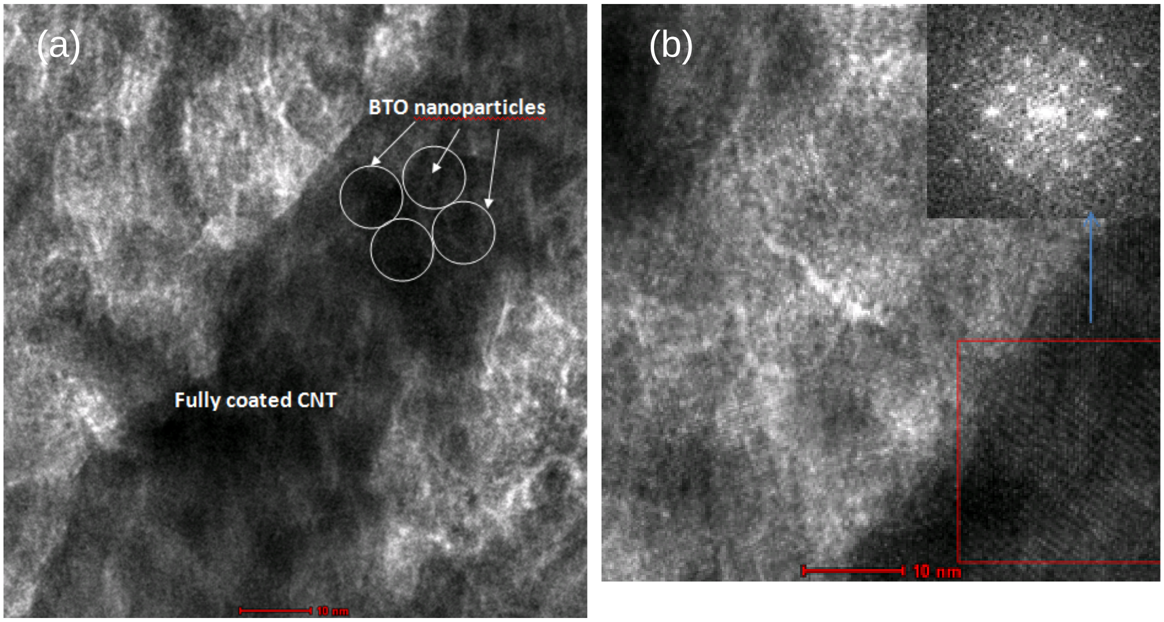

Figure 7.10 (a) HRTEM image of fully coated nanotube (b) FFT pattern from selected area of a HRTEM image.

X-ray photoelectron spectroscopy was performed in order to confirm the bonding states of $BaTiO_3$. The survey spectrum revealed peaks for Ba3d and Ti2p along with O1s peak. High resolution spectrum confirmed the binding energy of 458.52 eV which corresponds to $BaTiO_3$ type of bonding. A Gaussian (70%) – Lorentzian (30%) with Shirley background fit showed nice agreement with the expected nature of bonding.

7.2.2.3 Contact angle measurements

Thin layer of MWCNT samples was deposited on the Si/SiO2/Ti/Pt wafers using spin coating with an optimized recipe of 1000 rpm for 10 sec. The samples were than dried in inert atmosphere. Contact angle measurements were performed using FTA 200 Dynamic Contact Angle Analyzer (First Ten Angstroms, Inc). The system consisted of a moving stage and a Sanyo Navitar high resolution camera with zoom. Real-time images were captured with the help of computer software for further analysis. A water drop was pushed out of a computer controlled syringe pump on the surface under investigation which then settled on the nanotube surface. The drop was then focused on the screen with the help of microscope and contact angle was measured by drawing the sharp edges of the baseline and the drop. Measurements were repeated 3 – 4 times and then averaged.

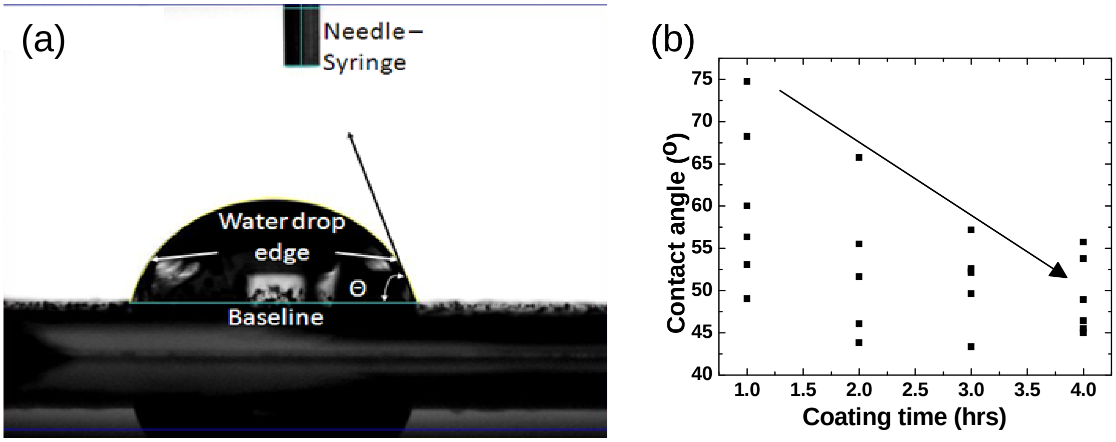

Figure 7.11 (a) Contact angle measurement setup (b) Contact angle vs. coating time for various recipes.

Table 7.2 Contact angle measurements

Conditions			**Contact angle (°)**	**Wetting tension (mN/m)**
Acid %	Coating Temp (℃)	Coating time (Hrs)		
30	40	1	68.24	26.97
		2	51.63	44.95
		3	52.30	43.56
		4	55.72	40.93

Table 7.2 – continued.

	60	1	60.00	35.63
		2	43.82	52.03
		3	43.35	52.82
		4	48.94	48.00
	80	1	56.35	40.21
		2	43.82	52.53
		3	49.61	49.50
		4	45.00	51.29
40	40	1	49.04	47.71
		2	55.50	41.22
		3	52.59	44.23
		4	53.77	43.04
	60	1	74.73	19.15
		2	65.73	29.89
		3	57.17	39.47
		4	45.49	50.75
	80	1	53.09	43.71
		2	46.06	50.52
		3	52.15	44.57
		4	46.42	51.08

Figure 7.11(a) shows a typical contact angle measurement setup. Table 7.2 summarizes contact angles for MWCNTs functionalized and coated at various acid concentrations, temperatures and times. It is well known that lower contact angle corresponds to higher wetting

effect and hence higher degree of coating. Figure 7.11(b) shows a plot of contact angle as a function of coating time. From Figure 7.11(b), it is clear that contact angle decreases with increasing coating time.

7.2.2.4 I – V and C – V characteristics

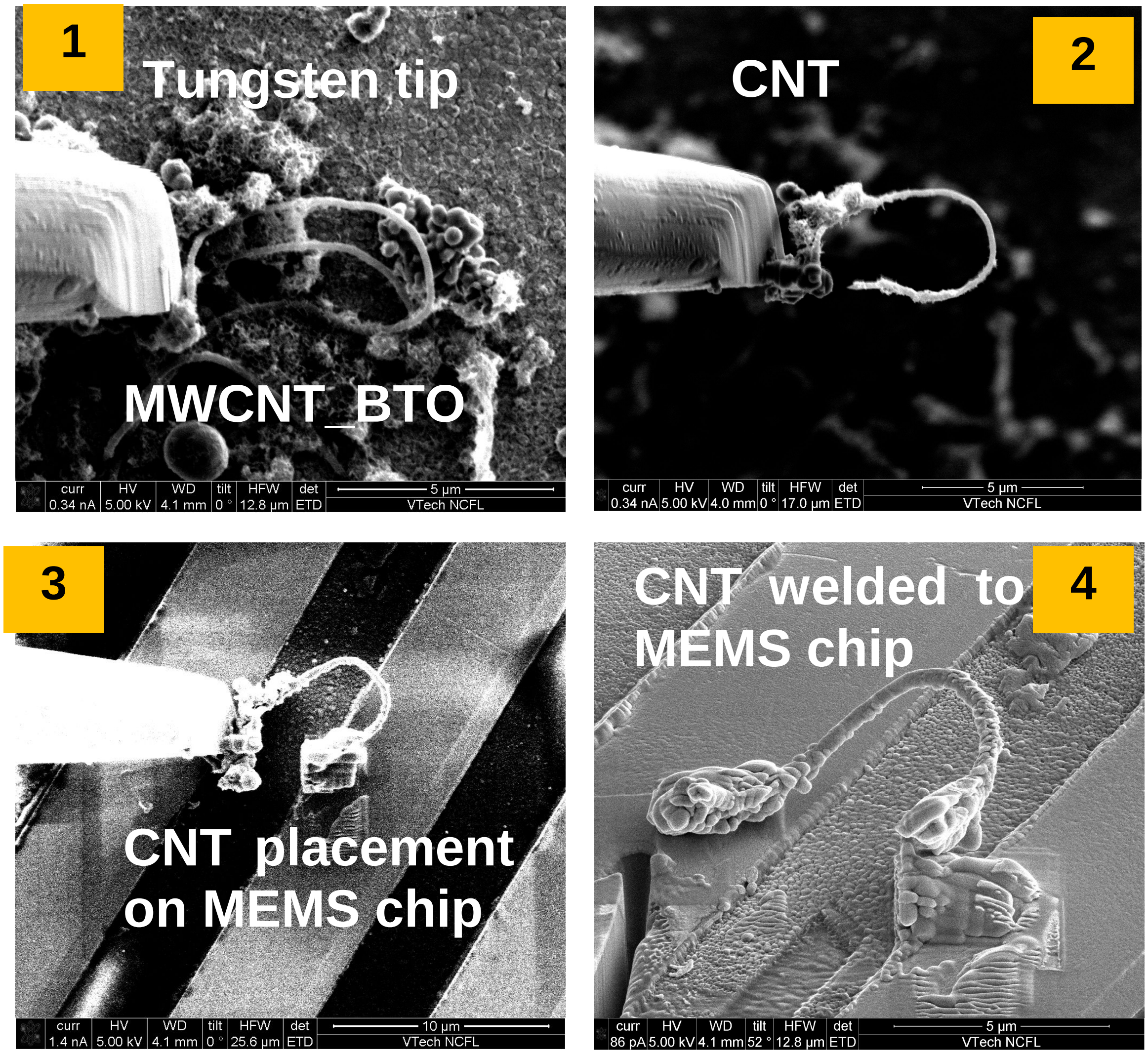

Figure 7.12 Sequential extraction of fully coated single nanotube using focused ion beam microscope.

Extraction of single BTO coated MWCNT from the forest:

MWCNTs fully coated with BTO were mixed with small amount of isopropanol and then ultrasonicated for 5 – 10 mins. Using a dropper, the nanotubes were dispersed on a Si/SiO2/Ti/Pt substrate forming a monolayer. A tungsten tip manipulator inside the focused ion beam microscope was brought in contact with the fully coated nanotube and welded to the probe tip by using electron beam induced deposition (EBID) with platinum at the joint. The attached nanotube was then carefully pulled out from the substrate by retracting the probe to its original position. The manipulator movement was controlled by a high precision 12 bit microprocessor controller. The MEMS chip with gold electrode lines was then brought to a known position. The extracted single nanotubes was placed between the chosen lines on the MEMS chip and welded to the gold electrode lines using platinum deposition. The probe was then retracted back to its position. The process of extracting single nanotubes is shown in Figure 7.12. [95]

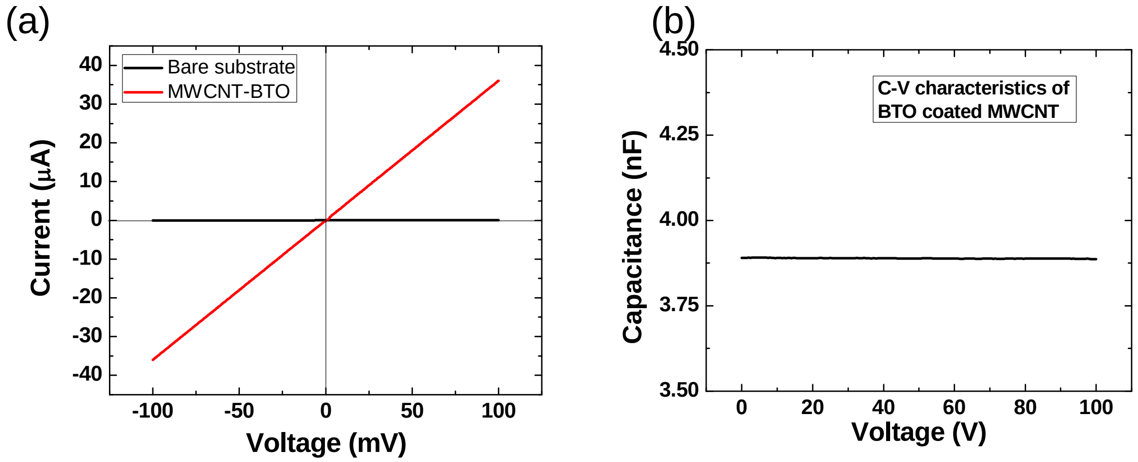

Figure 7.13 (a) I – V characteristics of single fully coated extracted nanotubes (b) C – V characteristics of single fully coated extracted nanotubes.

The I – V and C – V characteristics were measured using Semiconductor Characterization System (Model 4200-SCS) from Keithley Instruments, Inc. Figure 7.13 (a) shows the I – V characteristics of a single BTO coated MWCNT. From this figure, the resistance of the MWCNT-BTO nanotube was calculated to 2786.57 Ω. The applied voltage range was kept in the range of -100 mV to 100 mV. Figure 7.13(b) shows the C – V characteristics of a single BTO coated MWCNT. The capacitance value remained constant on the order of 3.889 nF for the entire applied voltage range of 0 – 100 mV. In order to address the difficulties in electrical characterization of the synthesized nanotubes due to the conductivity of the MWCNTs, we propose following two schemes. In Figure 7.14, the MWCNTs are first fully coated with a monolayer of an insulator material such as silicon carbon nitride (SiCN), silicon dioxide (SiO_2) or aluminum oxide (Al_2O_3). After formation of insulation layer, barium titanate (BTO) is coated on the nanotubes. Electrodes can be made at the ends of the tube by depositing platinum for electrical measurements.

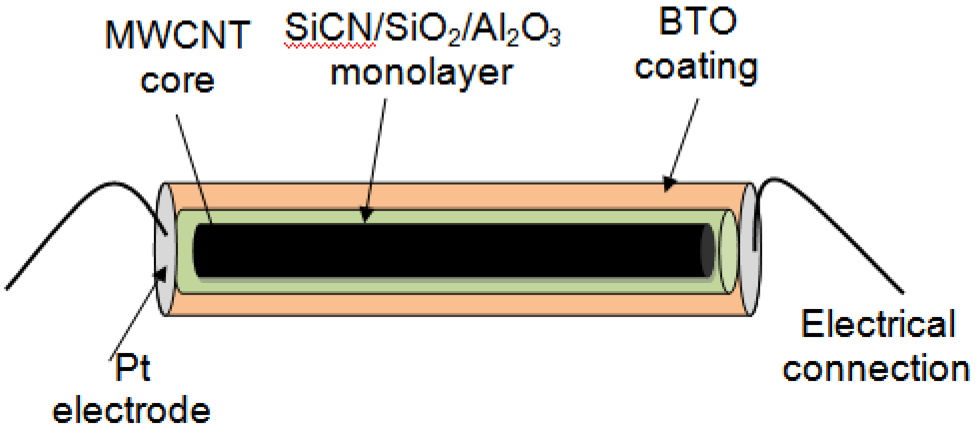

Figure 7.14 Proposed design for electrical characterization of BTO coated MWCNTs

In Figure 7.15, a fully coated MWCNT is assembled on a MEMS chip. In this design, the CNT core acts as ground electrode and platinum can be deposited on top of the BTO coating acting as the positive electrode.

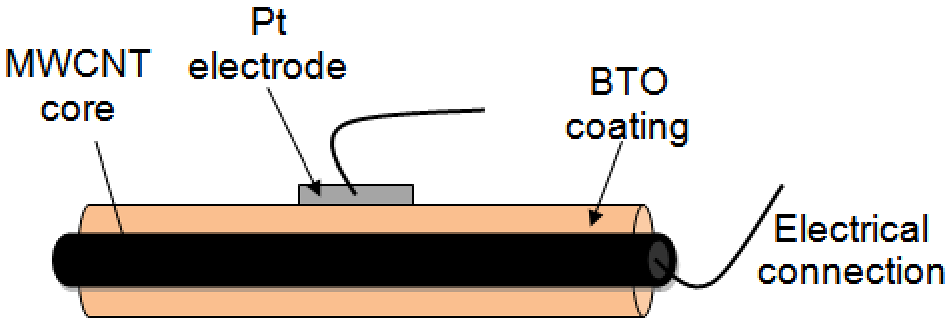

Figure 7.15 Proposed design 2 for electrical characterization of BTO coated MWCNTs.

7.3 Magnetoelectric nanowires

Magnetoelectric nanowires were synthesized by pyrolysis of polyurea (methylvinyl) silazane (Ceraset^{TM} Kion Specialty Polymers, Charlotte, NC), barium titanium ethylhexano-isopropoxide, Iron(III) ethylhexano-isopropoxide, 10%w/v in isopropanol metal organic precursors and Cobalt(II) 2-ethylhexanoate solution 65 wt% in mineral spirits on the surfaces of MWCNTs. Commercially available liquid ceraset, barium titanium ethylhexano-isopropoxide (Alfa Aesar ^{TM}), Iron(III) ethylhexano-isopropoxide, 10%w/v in isopropanol (Alfa Aesar ^{TM}) and Cobalt(II) 2-ethylhexanoate solution 65 wt% in mineral spirits (Sigma Aldreich) were used as precursors for SiCN, barium titanate (BTO) and cobalt ferrite (CFO) respectively. The first step consists of wetting of carbon nanotubes with ceraset: 50 vol % of CNTs in 5 vol % solution of ceraset and propanol. The solution was ultrasonicated for 15 min in order to obtain uniform coating of ceraset on nanotubes. The next step involved addition of 10 vol% BTO precursor to the ceraset-CNT solution and it was ultrasonicated for 30 min. The third step involved addition of 5 vol% each of cobalt and iron precursor to the solution followed by ultrasonication for 30 min. The solution was then dried in air at ~80℃ to allo w evaporation of propanol. Dried powder was then cross-linked and pyrolyzed in an alumina tube furnace using two-step annealing profile under high purity nitrogen atmosphere. The annealing process consisted of heating the powder to 400℃ and holding for 2 hrs for cross linking of ceraset followed by heating at 900℃ for 4 hrs for converting polymer into ceramic and ferrite.

Figure 7.16 (a) and (b) shows the microstructure of BTO-CFO decorated nanowires. The nanowires with diameters in the range of 100 ~ 200 nm were found to be fully coated with nanoparticles whereas nanowires with relatively smaller diameters (20 ~ 50 nm) were partially coated with nanoparticles. The nanoparticles were found to be in the range of 10 ~ 30 nm in diameter.

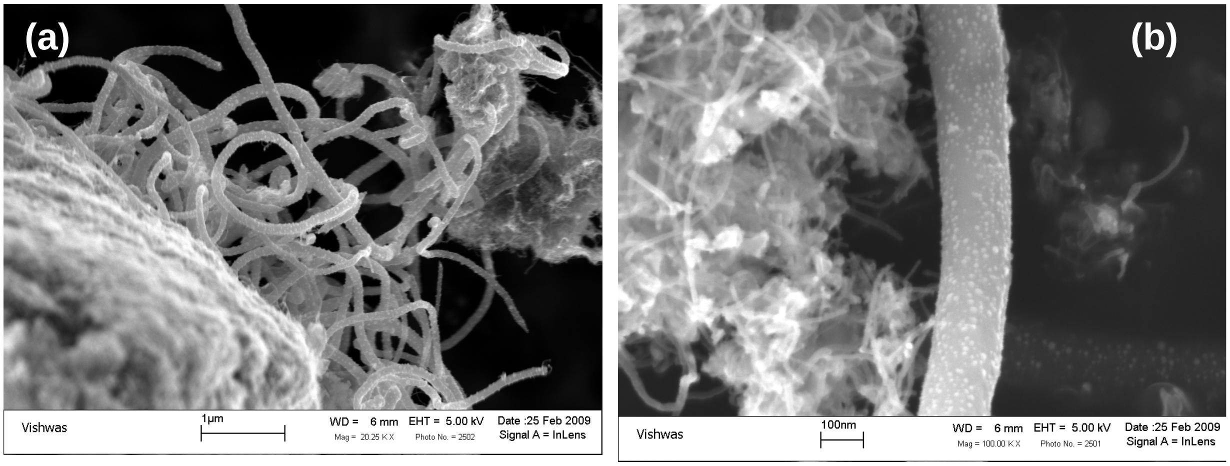

Figure 7.16 Microstructure of magnetoelectric nanowires.

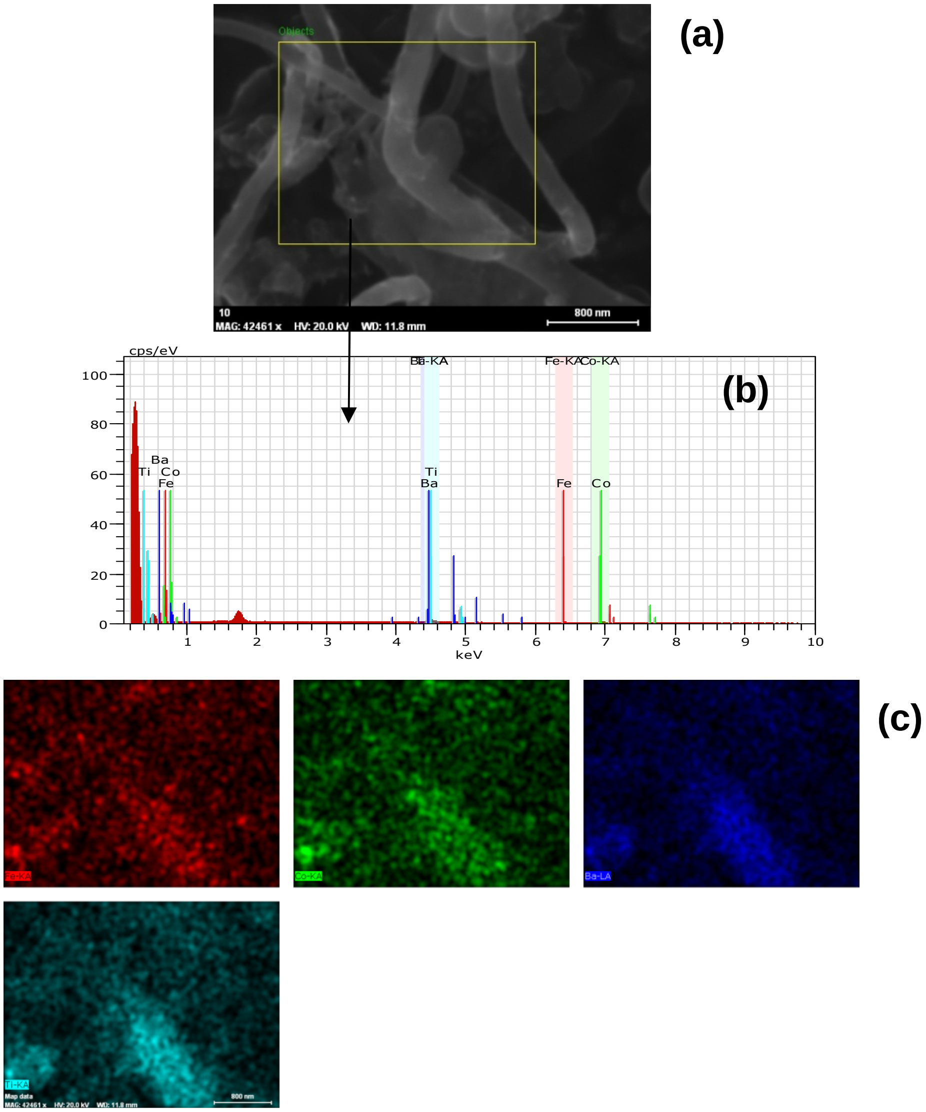

Figure 7.17 (a) shows the selected area for SEM elemental mapping analysis (Bruker^{TM} EDX with a silicon drifted detector). The corresponding elemental spectra and elemental mapping are shown in (b) and (c) respectively.

Elemental mapping reveals presence of Ba, Ti, Co and Fe on the surface of the sample. In order to further confirm the presence of nanoparticles on CNTs, HRTEM (FEI Titan 300) analysis was conducted. Figure 7.18 (a) and (b) shows the BF and HAADF image of the nanowires. Figure 7.18 (c) shows the HRTEM image of nanotube and single nanoparticles. The contrast clearly reveals presence of nanoparticles attached to the nanotube. Spot EDS analysis (Figure 7.18 (d)) in HAADF image shows presence of Ba,Ti, Co, Fe and O elements

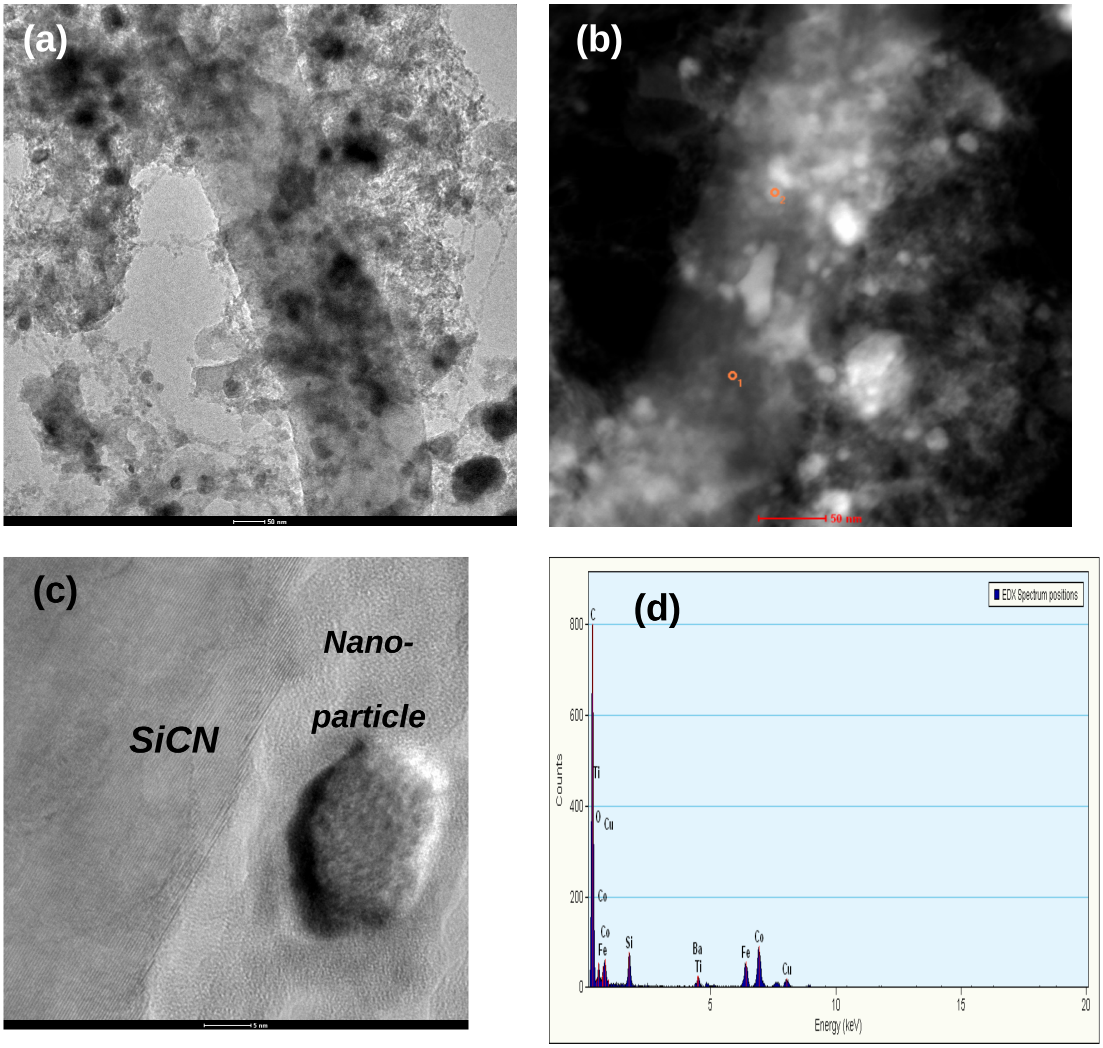

Figure 7.18 TEM (a) Bright field and (b) Dark field image of ME nanowires; (c) HRTEM image of nanoparticle on ME nanowire (d) EDS spectrum from spot 2.

X-ray Photoelectron Spectroscopy (XPS, PHI Quantera SXM with CasaXPS software) was conducted in order to confirm the presence of elements and nature of bonding. High resolution XPS spectrum (longer exposure time) indicated a binding energy of 457.4 eV and 531.5 eV. This indicated presence of TiO_2 and $BaTiO_3$ types of bonding arrangement. Binding energy of 778.2 eV corresponds to Co_3O_4 kind of bonding. The yield of magnetoelectric nanowires could be improved by tailoring the surface characteristics and size of nanoparticles. There is an optimum size ratio above which the nanowires would be fully coated with nanoparticles. The size of nanoparticles can be controlled by controlling the precursor concentration and initial treatments. It can be summarized from HRTEM, SEM and XPS analysis that the nanowires are coated with BTO and CFO. We were able to measure magnetic properties of synthesized nanotubes using VSM measurements as shown in Figure 7.19.

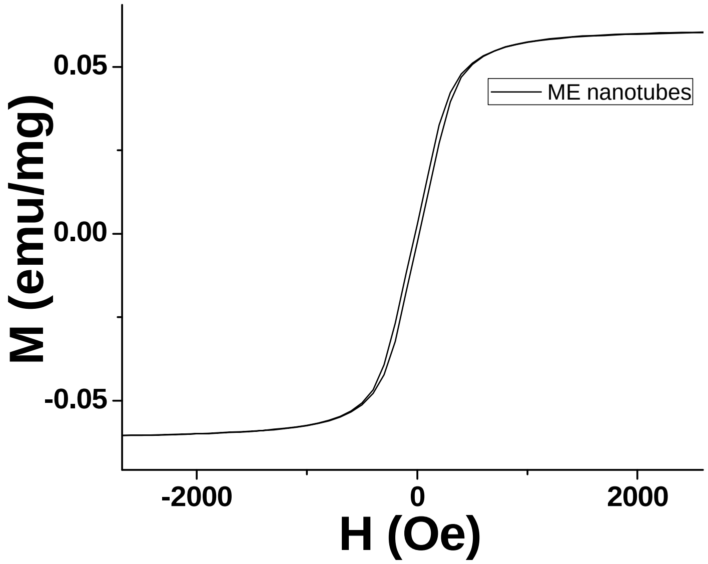

Figure 7.19 M-H curve of ME (SiCN-NT_BTO_CFO) nanotubes

7.4 Improved magnetoelectric properties of piezoelectric– magnetostrictive nanocomposites synthesized using high-pressure compaction technique

7.4.1 Introduction

Magnetoelectric (ME) effect results in polarization of material with applied magnetic field and magnetic field induction with an applied electric field. ME composites with particulate structure show lower magnitude of ME coefficient as compared to that of laminate composites

[96-105]. However, the advantages of particulate composites are simpler and cheaper synthesis technique, availability of wide range of compositions, scalability, and presence of both direct and converse ME effect. Thus, there has been continuous emphasis on enhancing the magnitude of particulate composites [106, 107]. In this section, we report the properties of particulate composites synthesized using: (1) high-pressure compaction sintering technique and (2) conventional technique. The results clearly show that highpressure sintering technique results in improved ME coefficient. We also study the effect of ratio of piezoelectric and magnetostrictive phase in the core-shell nanoparticles which are used to synthesize high-pressure sintered composites. The advantage of using core-shell particles in comparison to individual piezoelectric and magnetostrictive particles for synthesizing composite is that it results in controlled distribution of one phase with respect to other. This preserves the individual electrical and magnetic properties of each phase.

7.4.2 Experimental procedure

The synthesis of nickel ferrite (NFO) nanoparticles was performed by standard airless chemical synthesis technique in a nitrogen atmosphere. The reagents were obtained from commercial sources (Sigma-Aldrich, Inc.) and used without further purification. In a typical synthesis of 18-nm NFO nanoparticles, a mixture of 1 mmol of Ni-II (acetyl acetonate) and 2 mmol of 1,2-hexadecanediol (HDD) was added to a 125-mL European flask containing a magnetic stir bar. Benzyl ether (BE, 20 mL) was then transferred to the flask and the contents were stirred while purging with N2 for 20 min at room temperature. The flask was heated to 120 ℃ for 20 min and 1.5 mmol of iron pentacarbonyl [$Fe(CO)_5$] was injected into the flask while continuing the N_2 purge. After 3 min, 5 mmol each of oleic acid and oleylamine were injected and the mixture was maintained under N_2 blanket and heated to 160 ℃ at a rate of 5 ℃/min for 10 min. Next, the flask was heated to the refluxing temperature of 295 ℃ for 30 min before cooling down to room temperature under the N_2 blanket. Size of the $NiFe_2O_4$ (NFO) nanoparticles was controlled well by varying the solvents, amount of surfactants, and heating rates. For example, when BE was replaced by phenyl ether while keeping other reaction parameters unchanged, particles size was reduced from 18 to 6 nm. If BE was used as solvent and amount of both the surfactants were increased from 5 to 10 mmol, the size of the particles was increased from 18 to 22 nm. TEM images and X-ray diffraction patterns of the as-synthesized particles are shown in Figure 7.20 (a–d).

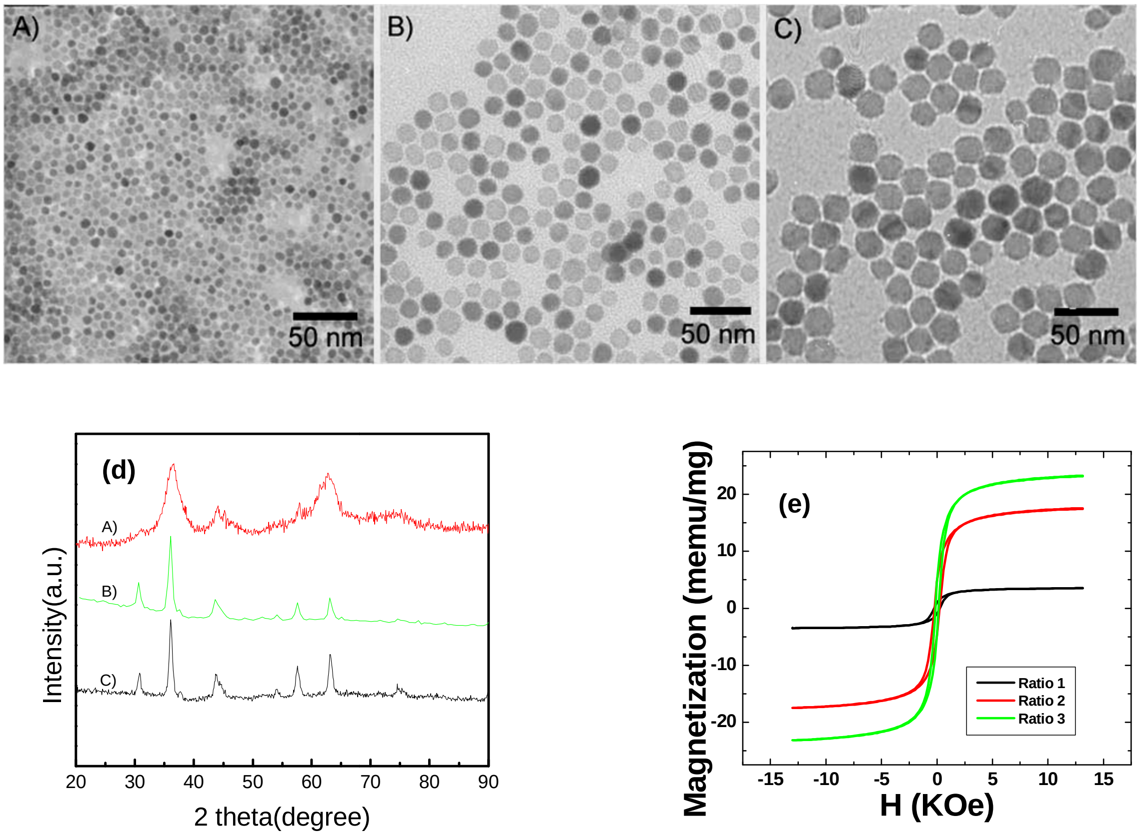

Figure 7.20 (a), (b) and (c) TEM image of the NFO particles with varying particle size, (d) X-ray diffraction pattern of the nanoparticles, and (e) magnetic properties of PZT/NFO nano-particles.

Piezoelectric particles were synthesized corresponding to formulation $0.8[Pb(Zr_{0.52}Ti_{0.48})O_3]–0.2[Pb(Zn_{1/3}Nb_{2/3})O_3]$ (PZT) using conventional mixed oxide route. Coating of NFO nanoparticles on PZT was performed by chemical synthesis method following the procedure described above with addition of PZT particles, as seeds, that were coated after the procedure. Keeping the PZT concentration constant at 6.1 mmol, NFO concentration was increased twice and thrice to obtain Schemes 2 and 3, respectively. Hence, molar ratios of PZT to NFO precursors are 2.44:1, 1.22:1, and 0.81:1 for Schemes 1, 2, and 3, respectively. Table 7.3 shows the three different schemes of NFO/PZT solution used to synthesize the composite particles.

Table 7.3 Variation of PZT to NFO coating in the composite nanoparticles

	PZT	Ni (II) (acetyl acetonate)	1,2 Hexadecanediol (HDD)	Benzyl ether (BE)	Iron pentacarbonyl $Fe(CO)_5$	Oleic acid	Oleyl amine
Scheme 1	6.1 mmol	1 mmol	1 mmol	20 ml	1.5 mmol	5 mmol	5 mmol
Scheme 2	6.1 mmol	2 mmol	2 mmol	50 ml	3 mmol	10 mmol	10 mmol
Scheme 3	6.1 mmol	3 mmol	3 mmol	60 ml	4.5 mmol	15 mmol	15 mmol

The particle size of NFO was 22 nm for all the schemes. Magnetic properties of as-synthesized particles with Schemes 1, 2, and 3 are shown in Figure 7.20 (e). As the amount of magnetic phase increases, the magnetic moment and magnetization increases from 3.50 memu/mg for Scheme 1 to 17.40 memu/mg for Scheme 2 and 23.13 memu/mg for Scheme 3.

7.4.3 Results and discussion

To investigate the effect of NFO–PZT ratio, the coated particles were used to synthesize the particulate composite structure. Pellets of three different schemes were pressed in a 0.25-in. die under hydraulic pressure of 2 kpsi followed by cold isostatic pressure of 30 kpsi. Thin layers of PZT were pressed on top of the pellets to increase the resistivity. The samples were then sintered at 1040 ℃ for 3 h under a 150 g weight. A ll the recovered samples were bi-layered, with one layer each of PZT and PZT–NFO with thickness 0.4 mm. The grain size was found to reduce with increasing NFO concentration in the composite. Figure 7.21 (a–c) shows microstructure of sintered samples with schemes 1, 2 and 3 respectively. The composite with Scheme 1 was found to exhibit uniform and dense microstructure while composites with Schemes 2 and 3 had presence of porosity. Thus, composite nanoparticles of Scheme 1 were used for high-pressure sintering experiments.

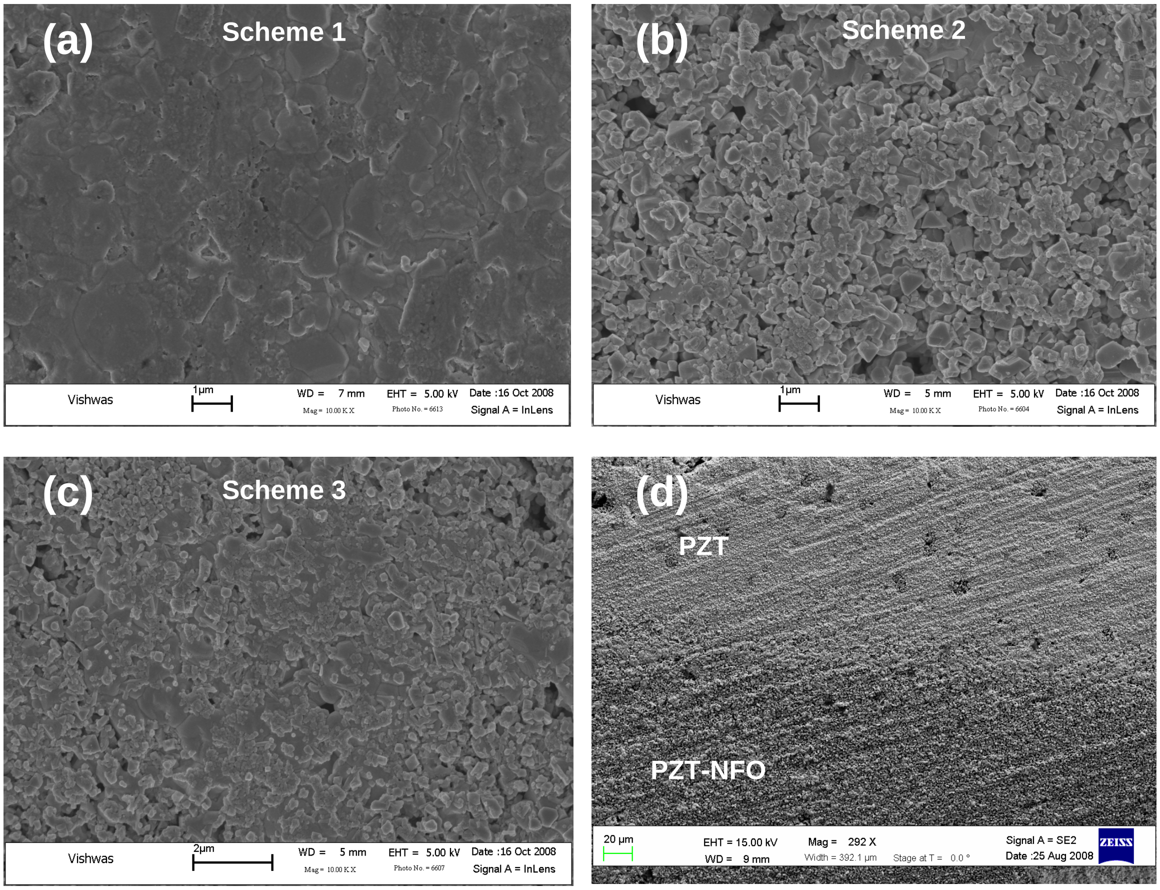

Figure 7.21 Microstructure of sintered magnetoelectric composite samples using different schemes (a) Scheme 1 (b) Scheme 2 (c) Scheme 3; (d) Cross – section image of bilayer sample consisting of PZT and PZT-NFO phases.

The composite with Scheme 1 was found to exhibit uniform and dense microstructure while composites with Schemes 2 and 3 had presence of porosity. Figure 7.22 shows the variation of ME coefficient as a function of DC bias field for three different schemes. Sample with Scheme 1 shows the highest ME coefficient of the order of 105 mV/cm Oe at 500 Oe DC bias field. Thus, composite nanoparticles of Scheme 1 were used for high-pressure sintering experiments.

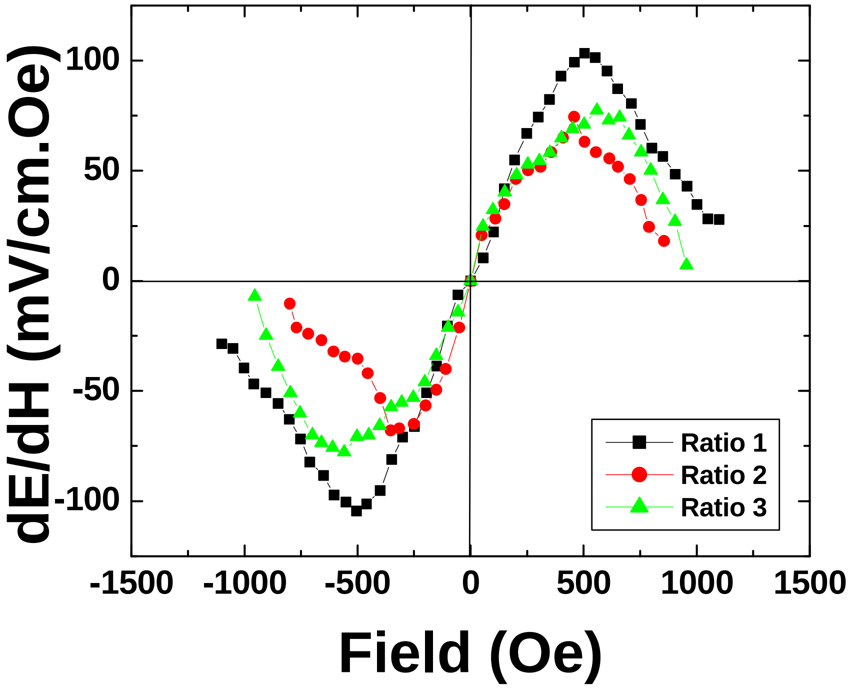

Figure 7.22 Magnetoelectric coefficient of the composites with three different schemes as shown in Table 7.3. The ratio of PZT to NFO decreases from Scheme 1 to 3.

High-pressure sintering was conducted to achieve homogenous microstructure with ordered distribution of NFO phase. PZT–NFO composite particles were pressed using a 0.25-in. disc-shaped die at 2 kpsi and sintered at 1 GPa and 600℃ for 30 min using Rockland SV-TC high compaction machine. After sintering, the bi-layer sample was removed from the metal die using a coarse file. The thickness of PZT–NFO layer in this bi-layer composite was 0.2 mm. The sample was then annealed at 1040℃ for 3 h, electro ded, and, subsequently, poled at 2.5 kV/mm in silicon oil bath at 120℃ for 30 min. This sample was measured to have a longitudinal piezoelectric coefficient of 164 pC/N, dielectric constant of 880, and dielectric loss factor of 1.4%.

Figure 7.23 (a and b) shows the TEM bright-field (BF) and darkfield (DF) image of PZT–NFO-sintered composite. The contrast clearly shows the presence of NFO phase (dark spots at BF) on the bigger PZT grains. SAED pattern indicates the presence of NFO (111) phase with some arc formation in the ring diffraction pattern. The arcs suggest minor texturing effect of NFO phase for some of the grains in the area under investigation. These NFO fragments are fully crystallized after the sintering and annealing process. Based upon the TEM analysis, the microstructure of the composite is schematically depicted in Figure 7.23 (c).

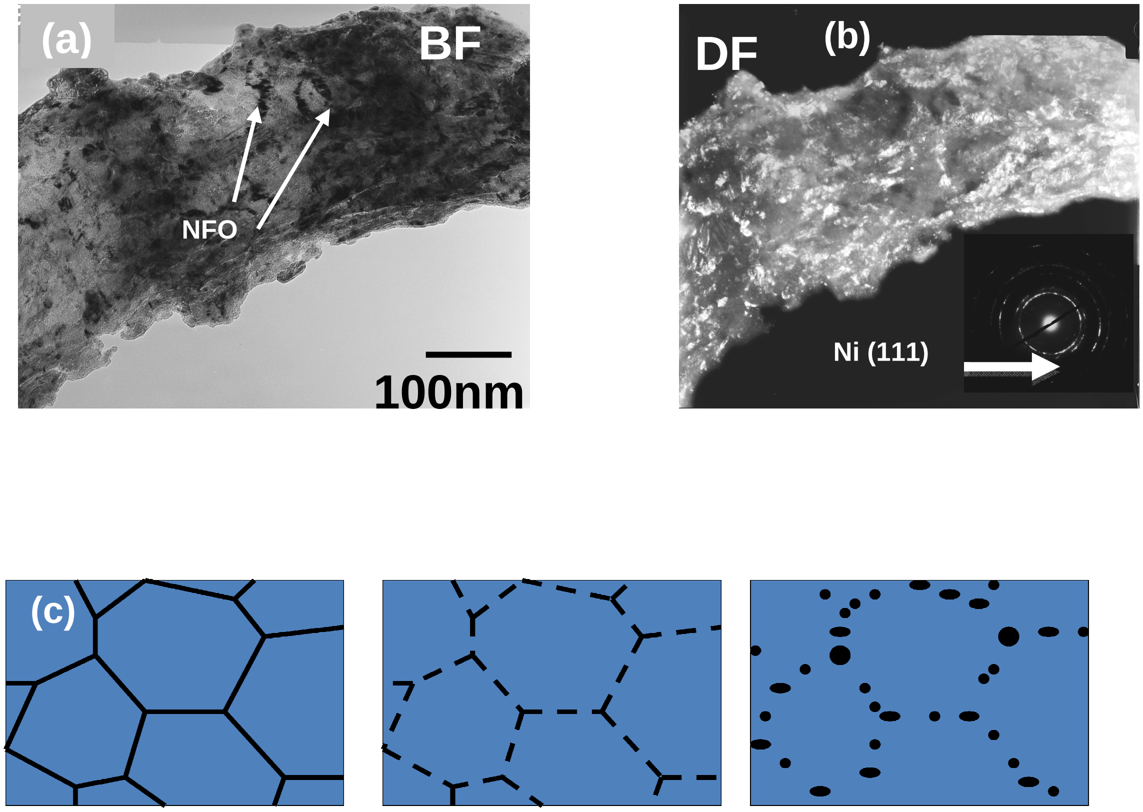

before anneal or before compaction:
Shell layer exists as continuous coating

After compaction or during sintering:
Shell layer break-up and inter particle diffusion becomes possible

After sintering:
NiFe islands coarsens while PZT gets sintered.

Figure 7.23 TEM analysis of the high pressure compacted nanocomposite (a) bright-field image, (b) dark-field image, and (c) schematic illustration of the microstructure under high pressure compaction.

The microstructure reveals well-grown PZT grains with NFO clusters dispersed along the initial grain boundary formed during high-pressure compaction. These NFO clusters migrate from the initial location resulting in mixed orientation of NFO phase at the initial grain boundaries of PZT grains as well as randomly dispersed NFO islands on PZT grains.

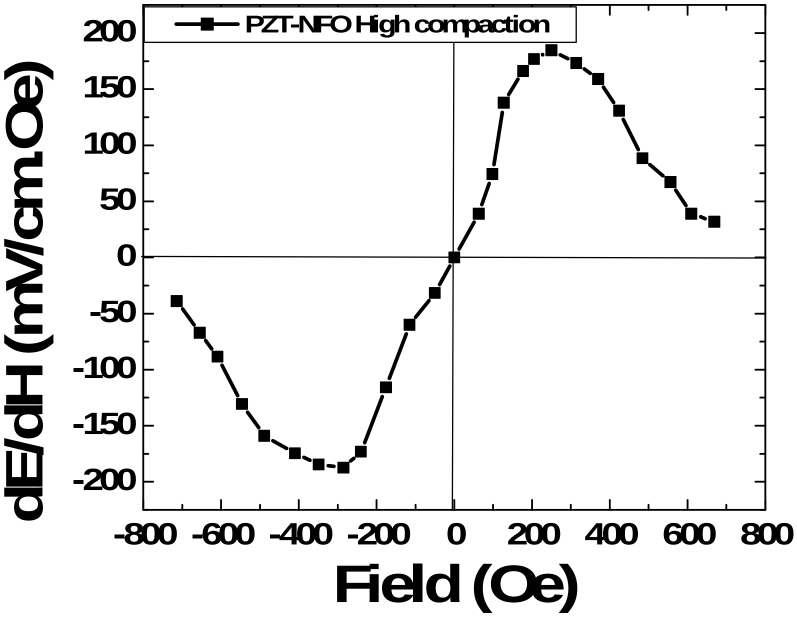

Figure 7.24 Magnetoelectric coefficient as a function of DC bias field for the high-pressure compaction-sintered sample

Figure 7.24 shows the variation of ME coefficient as a function of DC bias field for the composite sample synthesized by high-pressure compaction sintering technique. The peak ME coefficient of 187 mV/cm Oe was found at 285 Oe DC bias field. The result clearly shows that highpressure compaction results in enhanced ME coefficient compared to the conventionally sintered samples. This enhancement may be correlated to partially ordered distribution of NFO particles with specific orientation along the PZT grains as shown in Figure 7.23 (c). Piezoelectric grains in this microstructure are expected to be under finite compressive strain due to difference in volume of unit cell between spinel and perovskite phase. The lattice parameter of PZT in particulate-sintered composite sample of Mn modified NFO (NFM) and PZT was measured to be a^{s}_{pzt} = 3.87 A °and c^{s}_{pzt} = 4.07 A °with c/a = 1.052 while NFM as a_{NFM} = 8.42 A °, resulting in a ~

8% lattice mismatch between the two structures [108]. However, by synthesizing those in composite form such that the phase separation occurs at grain boundaries may accommodate this strain through the creation of misfit dislocations which will provide improved bonding. Dislocations' lifting the incoherency relieves the total internal strain through partially ordered distribution of the NFO phase along the boundary whose width will be determined by the change in free energy of the system with and without ordering of NFO and its shape factor. In conventional particulate-sintered composites consisting of magnetostrictive and piezoelectric grains, the interfacial defects are distributed throughout the microstructure resulting in porosity and heterogeneity. This drawback can be overcome by synthesizing the microstructure shown in Figure 7.23. In addition, the ordered distribution of NFO phase will preserve the physical properties of piezoelectric and magnetostrictive phase. In particulate-sintered composites consisting of random distribution of magnetostrictive particles, there is excessive cross-diffusion of ions across the interface. Recently, it was shown in Cu-modified nickel zinc ferrite (NCZF)–PZNT composites that Cu ions diffuse into PZNT while Pb ions diffuse into NCZF [109]. This cross-diffusion lowers the magnitude of magnetostrictive constant and piezoelectric voltage constant. Another drawback of particulate-sintered composites is connectivity of the ferrite particles which lowers the overall resistivity and reduces the poling voltage. However, by confining the distribution of NFO along the grain boundaries and controlling the fraction of such boundaries, higher poling voltage can be applied. Recent results by Gro¨ssinger et al. on composite consisting of 50% cobalt ferrite–50% barium titanate in ''coreshell'' structure shows 20 times larger Magnetoelectric coefficient as compared to randomly dispersed composites [110]. The results were analyzed in terms of coupling coefficient k, given as $k_{par} = \lambda_{par} d\lambda_{par}/dH$, where λ_{par} represents the longitudinal magnetostriction, H is the applied magnetic field, and d is the effective sample thickness. It was shown that magnitude of ME coefficient increases with k which is higher for core-shell structure. These results are consistent with our own data which shows that core-shell $Pb(Zr,Ti)O_3$ (PZT)–$NiFe_2O_4$ (NF) particulate nanocomposites provide higher magnitude of ME coefficient [111]. In this case, core-shell composite resulted in good interface bonding and effective strain transfer across the interface. These prior results further indicate that the microstructure in Figure 7.23, which has a resemblance to core-shell structure, can provide effective elastic coupling between the magnetostrictive and piezoelectric phases. The magnitude of magnetostriction coefficient, λ_{par}, and k will be higher for the NFO-ordered phase distribution along the grain boundaries due to texturing and phase separation.

7.5 Chapter summary

In summary, we have successfully demonstrated the synthesis of BTO nanoparticles-decorated SiCN-multiwalled carbon nanotubes – "nanoNecklace". Structural characterization performed using SEM and TEM revealed the presence of BTO nanoparticles in the size range of 10-40 nm while XPS analysis confirmed the perovskite phase. Next, functionalized MWCNTs fully coated with barium titanate were synthesized and characterized using techniques such as FTIR, SEM, HR-TEM, EDS. The wetting characteristics were studied to optimize coating parameters. SiCN-NT coated with BTO nanoparticles were further coated with magnetic material CFO. Partially and fully coated SiCN-NTs covered with BTO and CFO nanoparticles were observed under SEM and TEM. EDS and XPS characterization confirmed the bonding states of the respective compounds.

In order to study and understand magnetoelectric phenomenon we synthesized core-shell nanoparticles based macro-scale ME composites. Synthesis process involved the high-compaction sintering of PZT–NFO nano core-shell structure to form a dense ME particulate composite. The results show that high-compaction sintering technique can provide large magnetoelectric coupling. In addition, it was shown that composites corresponding to formulation 1:1 (Scheme 1) have the highest magnetoelectric coefficient which could be related to higher resistivity and dense microstructure for equivalent fraction of piezoelectric and magnetostrictive particles.

In order to study and understand magnetoelectric phenomenon we synthesized core-shell nanoparticles based macro-scale ME composites. Synthesis process involved the high-compaction sintering of PZT–NFO nano core-shell structure to form a dense ME particulate composite. The results show that high-compaction sintering technique can provide large magnetoelectric coupling. In addition, it was shown that composites corresponding to formulation 1:1 (Scheme 1) have the highest magnetoelectric coefficient which could be related to higher resistivity and dense microstructure for equivalent fraction of piezoelectric and magnetostrictive particles.

CHAPTER 8

PIEZOELECTRIC ENERGY HARVESTING

8.1 Introduction

Recent advancements in power electronics have created the opportunity for developing energy harvesting devices that can meet the needs of wireless sensor nodes in a distributed network. Vibration energy harvesting is one of the important mechanisms which is being explored for this purpose. There are four different methods for harvesting the vibration energy, namely piezoelectric, electromagnetic, electrets, and electrostatic. Depending upon the scenario, all these methods have certain advantages and disadvantages. Our research focus in on improving the power density of piezoelectric energy harvesters which mostly utilizes bimorph transducers mounted as fixed – free cantilever. There are three important parameters that should be addressed for improving the efficiency of bimorph transducers: (i) piezoelectric coefficient of material (ii) analytical model for optimizing dimensions of bimorph to tune the working frequency, and (iii) fabrication process for simple manufacturing.

The primary criterion for selection of piezoelectric material for high energy density depends on the piezoelectric charge constant (d) and piezoelectric voltage constant (g) [112]. Islam et al. have showed that material parameter “n” is correlated with “g”, and the magnitude of g increases as the magnitude of n decreases [113]. At the same time, several studies have proposed models for predicting the static behavior of piezoelectric bimorphs [114-116]. Recently, Wu et. al. have proposed a method for calculating the tip deflection at resonance incorporating the damping ratio of the structure [116]. Roundy (2004) [117], and Erturk and Inman (2009) [118] have modeled and experimentally validated the electrical output power of a piezoelectric bimorph energy harvester using two different electromechanical approaches, single degree of freedom and distributed parameter model. In this study, we utilize these prior results to develop piezoelectric bimorph with optimum material and structural performance.

8.2 Experimental procedure

Piezoelectric ceramic composition was synthesized using conventional mixed oxide ceramic processing route. Reagent-grade powders of PbO, ZrO_2, ZnO, NiO, Nb_2O_5, MnO_2, and TiO_2 were obtained from Alfa Aesar Co. (Ward Hill, MA). Stoichiometric ratios of powders corresponding to the composition $0.9Pb(Zr_{0.56}Ti_{0.44})O_3 – 0.1Pb[(Zn_{0.8/3}Ni_{0.2/3})Nb_{2/3}]O_3$ + 2 mol% MnO_2 (PZTZNN) and $0.8[Pb(Zr_{0.52}Ti_{0.48})O_3]–0.2[Pb(Zn_{1/3}Nb_{2/3})O_3]$ (PZTPZN) were ball milled with ethyl alcohol and YSZ grinding media (5 mm diameter, Tosoh Co. Tokyo, Japan) in a polyethylene jar for 24 h. After drying, the powders were calcined at 800℃ for 3 h. Calcined powder was crushed, sieved and then ball milled separately with alcohol and grinding media for 30 ~ 48 h. After ball milling, the powders were dried at 80℃ and sieved. Sieved powders were pressed in to discs of dimension 12.7 mm x 1 mm using a hardened steel die and hydraulic press under a pressure of 1.5 ksi. The green body was next treated in cold isostatic press (CIP) operating at 20 ksi for 10 min for schemes 1 and 2 whereas for 30 min for scheme 3 and 4 in order to improve the density. Schemes 1, 2 and 3 were used to synthesize PZTZNN composition and scheme 4 was used to synthesize PZTPZN composition. Different sintering profiles were used corresponding to: single step sintering profile (scheme 1 for PZTZNN and scheme 4 for PZTPZN) and two step sintering profile (scheme 2 and scheme 3 for PZTZNN). The samples were sintered in air atmosphere using a Sentrotech furnace at 1050℃ – 2h in scheme 1 and 1100℃ – 3 h in scheme 4. In scheme 2, samples were held at 1100℃ for 5 min and then rapidly cooled to 1000℃ and held for 4 h. In scheme 3, samples were heated to 1050℃ and held for 5 min followed by rapid cooling to 950℃ and holding for 4 h. It has been shown that two step sintering profile results in smaller grain size and higher density.

The sintered samples were then polished and electroded using Ag-Pd electrode with firing temperature of 650℃. The samples were poled at 3-4 kV/mm using a high voltage supply in an oil bath maintained at 120℃. The piezoelectric charge constant of poled samples was measured by APC YE 2730A d_{33} meter. Resonance characteristics were determined by HP 4194A impedance analyzer (Hewlett Packard, USA). Table 8.1 summarizes the piezoelectric properties of materials synthesized using schemes 1, 2, 3 and 4. In order to fabricate the bimorphs, rectangular plates were pressed and sintered and then polished along the thickness to 0.4 mm. The final dimensions of the fabricated bimorphs were 25 x 7 x 0.5 mm^3 for scheme 1 and 25 x 5.5 x 0.4 mm^3 for schemes 2, 3 and 4. Two polished plates were electroded, poled and attached to brass foil in sandwich configuration as shown in Figure 8.1(a).

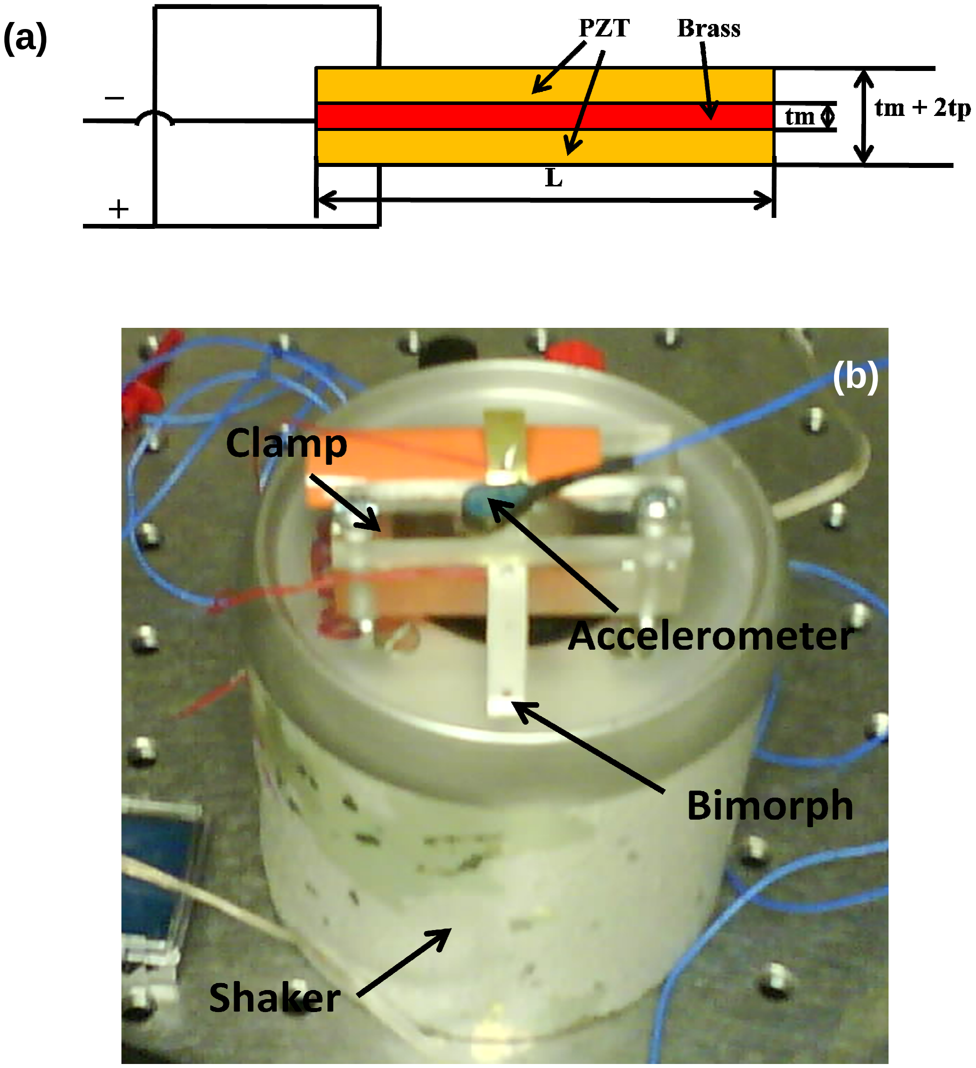

Figure 8.1 (a) Schematic diagram of the bimorph transducer, and (b) Picture of the experimental setup for characterizing output voltage and power.

Fabricated bimorph was mounted on a Ling dynamic shaker as shown in Figure 8.1(b) using a custom clamp. A tip mass of 2.36 grams was attached at the free end of bimorph for dynamic force excitation at the mechanical resonance as shown in Figure 8.1(b). Acceleration measurements were taken on the base of the structure and tip mass by using a shear accelerometer (Piezotronics, Inc.), PDV 100 Laser vibrometer (Polytech, Inc.) and a spectral analyzer (Siglab Model 20-42). The output from the accelerometer was sent through a sensor signal conditioner (Piezotronics Inc. Series 481). The output from laser vibrometer was recorded using Siglab. A small breadboard was used to vary the load resistors across the output of bimorph electrical terminals. The Siglab analyzer was used for collecting the time traces, power spectrums of acceleration and output voltage, and the transfer function from base acceleration to tip mass acceleration.

8.3 Results and discussion

8.3.1 Microstructure and material properties

Piezoelectric plates fabricated using two step sintering profile were found to show higher densities. The density for PZTPZNN was found to increase from 7.41 g/cm^3 in single step sintered sample to 7.89 gm/cm^3 for two step sintering using scheme 2 and to 7.95 gm/cm^3 for scheme 3. The density for PZTPZN was found to be 7.88 gm/cm^3 synthesized using scheme 4. Figure 8.2 (a) – (c) shows the microstructure of PZTZNN plates observed using LEO (Carl Zeiss SMT, Inc.) 1550 high-performance Schottky field-emission SEM. Figure 8.2 (d) shows the microstructure of PZTPZN plates. Chen et al. have shown that rapid grain growth occurs during the final stage of single step sintering resulting in larger grain sizes. On the other hand, two step sintering process results in smaller grain size and higher density. The grain size was found to decrease for PZTZNN plates from 3.3 µm for scheme 1 to 2.29 µm for scheme 2 to1.43 µm for scheme 3 and for PZTPZN plates sintered with one step sintering profile the grain size was found to be 1.306 µm [119]. All the grain sizes were determined from the SEM micrographs by using linear intercept method. It is known that Zn doping enhances the density of ceramics by promoting solid state sintering where Zn occupies the Zr and Ti sites resulting in oxygen vacancies [120].

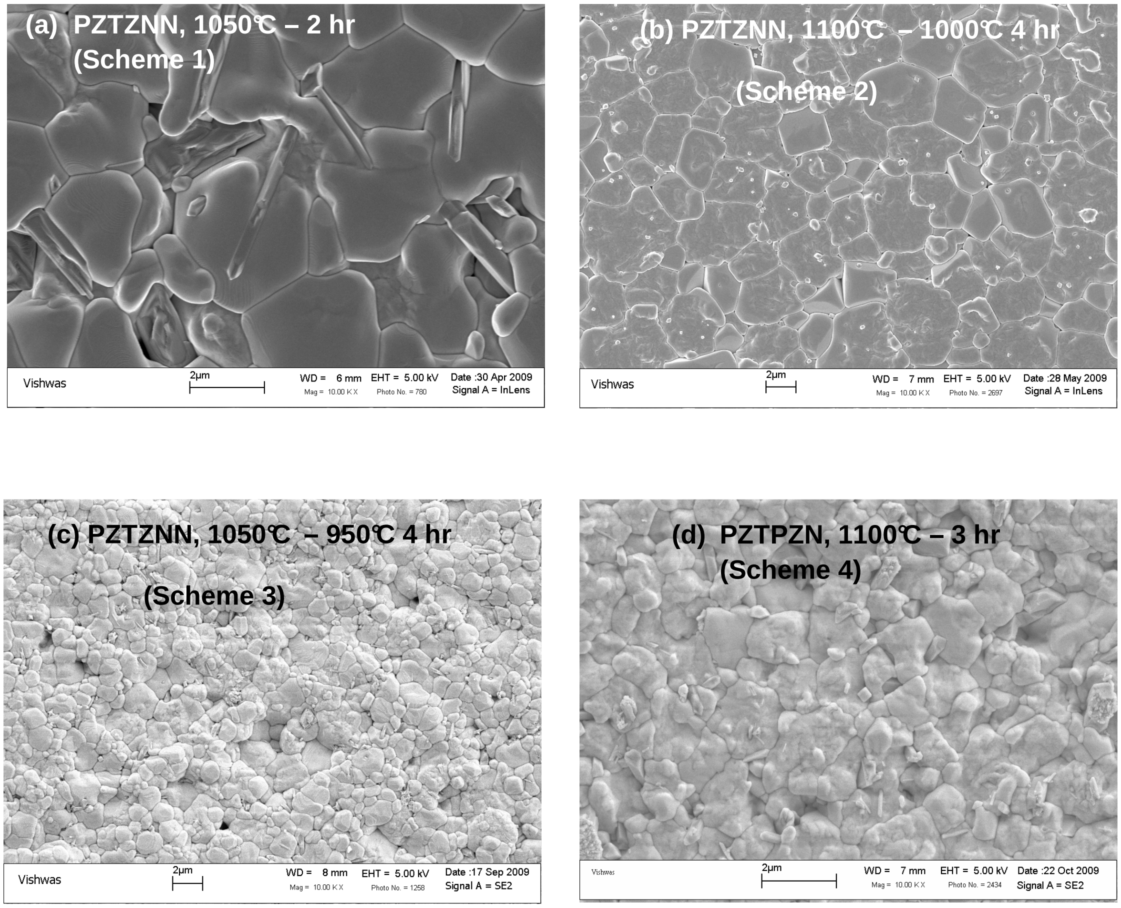

Figure 8.2 Microstructure of sintered PZTZNN plates (a) scheme 1, (b) scheme 2, (c) scheme 3 and (d) Microstructure of sintered PZTPZN plates (scheme 4).

Figure 8.3 (a) – (c) shows the cross – sectional SEM images of sintered PZTZNN plates for schemes 1 – 3 respectively whereas Figure 8.3 (d) shows the cross – sectional SEM images of sintered PZTPZN plates. It can be noted from Figure 8.3 that dense microstructure was obtained with two step sintering. EDX analysis was performed using Oxford INCA Energy E2H X-ray Energy Dispersive Spectrometer (EDS) system with silicon drifted detector. Figure 8.4 (a) – (c) shows the SEM – EDX analysis of various elements for PZTZNN plates sintered in schemes 1 – 3. The concentration of Zn as detected in EDX was found to increase from scheme

1 to scheme 3. This may be due to the segregation effect along the grain boundaries during nucleation and grain growth [121]. Although, schemes 1, 2 and 3 have same composition (i. e. PZTZNN), the variation in the sintering procedure results in different defect concentration and distribution, homogeneity, grain size and apparent density resulting in the difference in piezoelectric and dielectric properties [122, 123]. For example, Priya et al. have shown the effect of Mn doping on the piezoelectric and dielectric properties of PZNT single crystals demonstrating the systematic changes in properties with dopant concentration [124].

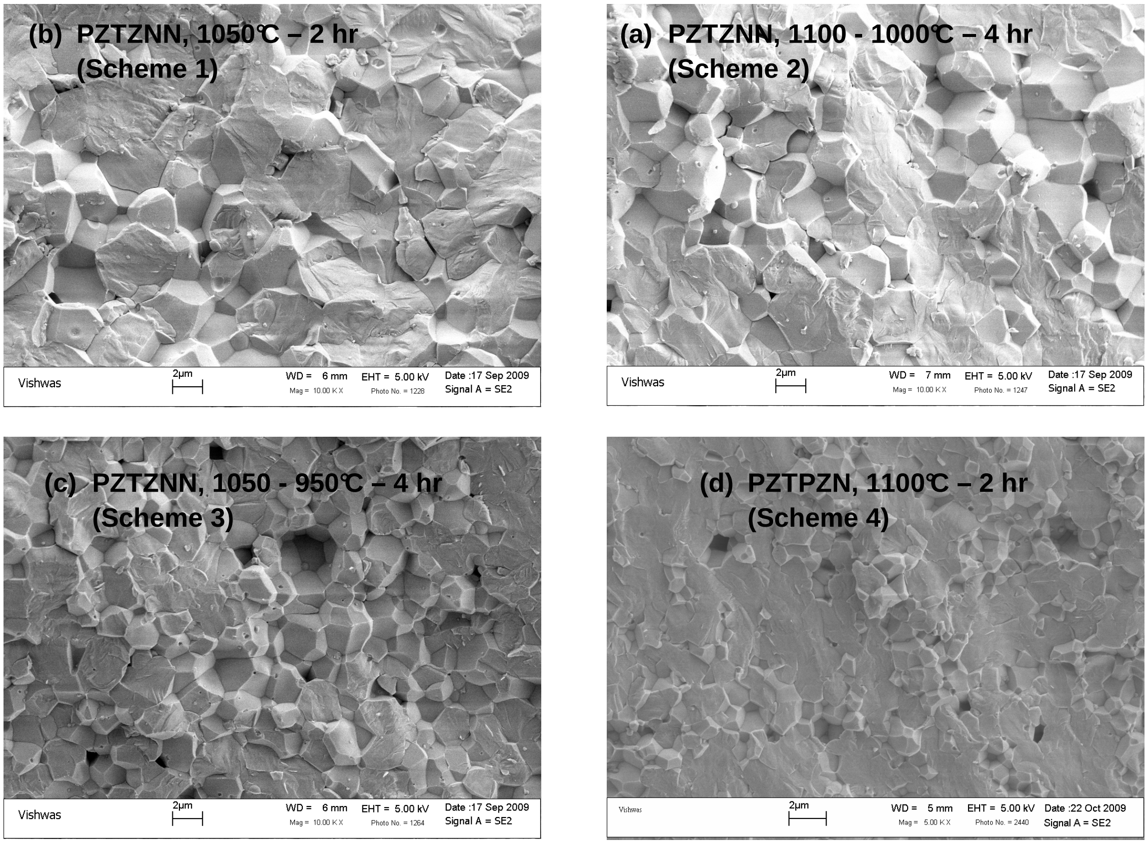

Figure 8.3 Cross-sectional SEM images of the sintered PZTZNN plates (a) scheme 1, (b) scheme 2, (c) scheme 3, and (d) Cross – sectional SEM of sintered PZTPZN plates (scheme 4)

(a)

Element	Weight%	Atomic%
O K	14.87	58.55
Ti K	6.54	8.60
Mn K	0.75	0.86
Ni K	0.21	0.22
Zn K	0.49	0.47
Zr L	15.70	10.84
Nb L	4.72	3.20
Pb M	56.73	17.25
Total:	**100**	

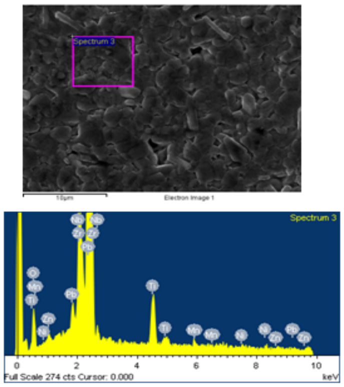

(b)

Element	Weight%	Atomic%
O K	15.57	60.69
Ti K	5.70	7.42
Mn K	0.42	0.48
Ni K	0.19	0.21
Zn K	0.66	0.63
Zr L	14.53	9.93
Nb L	4.60	3.09
Pb M	58.33	17.56
Total:	**100**	

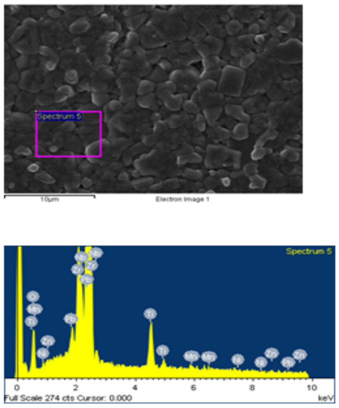

(c)

Element	Weight%	Atomic%
O K	12.96	54.92
Ti K	6.24	8.83
Mn K	0.67	0.83
Ni K	0.16	0.18
Zn K	0.70	0.73
Zr L	14.25	10.59
Nb L	6.22	4.72
Pb M	58.67	19.20
Total:	**100**	

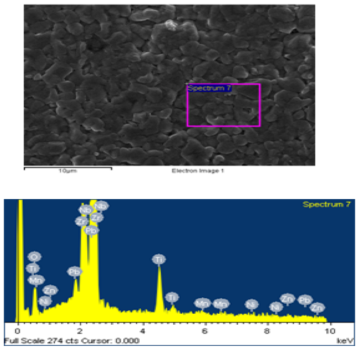

Figure 8.4 SEM EDX analysis for elements Ni and Zn in the PZTZNN sintered plates (a) scheme 1, (b) scheme 2, and (c) scheme 3.

The piezoelectric and dielectric properties were found to improve in two step sintering. Table 8.1 and 8.2 list the relevant dielectric and piezoelectric constants for samples synthesized using four different schemes. The dielectric constant of PZTZNN plates reduced from 538 for scheme 1 to 375 for scheme 3 whereas the dielectric constant of PZTPZN plates (scheme 4) was found to be as high as 1588. The coupling coefficient of PZTZNN plates improved from 0.25 for scheme 1 and 2 to 0.27 for scheme 3 and was found to be 0.57 for PZTPZN plates (scheme 4). The product (d.g) was found to increase with decreasing grain size. Figure 5 shows the variation of product (d.g) as a function of grain size for schemes 1 – 3 (PZTZNN plates) and scheme 4 (PZTPZN plates).

Table 8.1 Dielectric and electromechanical properties of synthesized compositions.

Scheme / Composition	**$\varepsilon_{33}^T/\varepsilon_o$**	**k_p**	**Q_m**	**d_{33} (pC/N)**	**g_{33} (10^{-3}V.(m.N)$^{-1}$)**	**$d_{33}.g_{33}$ (10^{-15} m^2/N)**	**n**
1 / PZTZNN	538	0.44	704	153	32	4922	1.179
2 / PZTZNN	475	0.45	673	167	39	6646	1.167
3 / PZTZNN	375	0.47	780	165	44	8205	1.155
4 / PZTPZN	1588	0.59	78.7	400	28	11406	1.197

Table 8.2 3-1mode piezoelectric properties.

Scheme/Composition	**k_{31}**	**d_{31} (pC/N)**	**g_{31} (10^{-3} mV/N)**
1 / PZTZNN	0.25	56	11
2 / PZTZNN	0.25	53	12
3 / PZTZNN	0.27	50	15
4 / PZTPZN	0.32	153.73	11

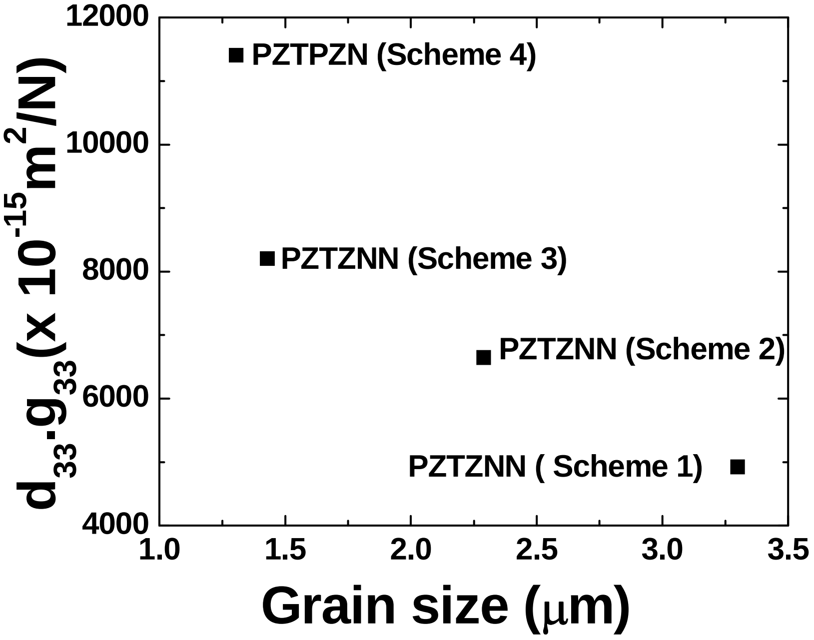

Figure 8.5 Product (d.g) as a function of grain size for PZTZNN plates (schemes 1, 2 and 3) and PZTPZN (scheme 4).

8.3.2 Theoretical analysis of output power from bimorph transducer

The bimorph transducer consists of one metal plate (substructure) sandwiched between the two PZTZNN or PZTPZN plates as shown in Figure 8.1 (a). The effective moment of inertia (M.I.) of the composite beam can be defined as [116]:

$$I_{eff} = 2I_p + \left(\frac{E_s}{E_p}\right) I_s \tag{1}$$

$$I_p = \frac{bh_p \left(h_p/2 - y\right)^2}{12} \tag{2}$$

$$I_s = \frac{bh_s^3}{12} \tag{3}$$

where I_s is the moment of inertia of substructure plate, I_p is the moment of inertia of piezoelectric plate, *b* is the width of bimorph, E_s are E_p are Young's modulus of metal (substructure) and PZT respectively, and h_s, and h_p are thickness of metal substructure and PZT respectively. The centroid position of beam is given by Eq. (4) as:

$$y = \frac{\int y dA}{\int dA} \tag{4}$$

where, *y* is the distance of centroid from the base reference plane, and A is the cross sectional area of the plate. Figure 8.6 schematically shows the neutral axis position. Due to the symmetric geometry of bimorph, centroid is located at the center of total thickness of beam and neutral plane passes through the centroid. Therefore *y* = 0 for this study.

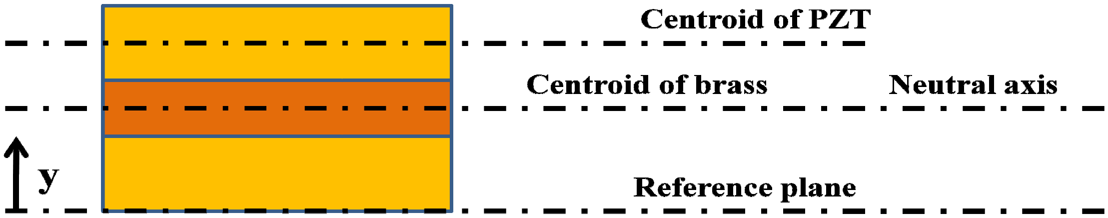

Figure 8.6 Depiction of neutral axis position.

Wang and Cross [125] have proposed the analytical solution for resonance frequency of bimorph as following:

$$f_r = \frac{3.52t}{4\pi L^2}\sqrt{\frac{E_p}{3\rho_p}}\sqrt{\frac{1+3(1+3B)^2+4AB^3}{4(1+B)^2(BC+1)}} \qquad (5)$$

For bimorphs fabricated with scheme 2 and 3; A = E_m/E_p = 1.667, B = $h_s/2h_p$ = 0.0625, C = $\frac{\rho_m}{\rho_p}$ = 1.114, t = $h_s + 2h_p$ = 8.5 x 10^{-4} m and L = 25 x 10^{-3} m. The analytical resonance frequency for PZTZNN bimorph fabricated by scheme 1 was calculated to be 780 Hz. The analytical natural frequency for bimorph was calculated to be 631 Hz. For a clamped-free beam with a tip mass of M_t, and length L, the fundamental natural frequency is given as [126]:

$$f_1 = \frac{1}{2\pi}\left(\frac{3EI}{L^3(M_t + 0.24M_b)}\right) \qquad (6)$$

where M_b is the mass of the beam. The mass of beam can be calculated as follows: density of PZT = 7900 kg /m^3, volume of PZT = $2Lwt_p \times 10^{-9}$ m^3, density of brass = 8800 kg /m^3, volume of brass = $Lwt_m \times 10^{-9}$ m^3, and hence; $M_b = \rho_p V_p + \rho_m V_m$ = 0.935 gm. Thus, using Eq. (6) the analytical resonance frequency of clamped – free bimorphs for PZTZNN plates synthesized using scheme 1 was calculated to be 282 Hz and for PZTZNN plates synthesized using scheme 2 and 3 and PZTPZN plates synthesized using scheme 4 was calculated to be 187 Hz.

Various piezoelectric vibration energy harvesters utilize cantilever beam architecture due to the simplicity in tuning the resonance frequency to a desired range. Alteration of the beam resonant frequency is performed by changing the dimensions of the beam or by increasing/decreasing the seismic mass. Distributed parameter correction factors to the SDOF model provides accurate results around the resonant frequency. Distributed parameter correction factors are especially useful when the electrode sees a spatially varying velocity/displacement field. A distributed parameter model of a piezoelectric bimorph cantilever beam has been developed by Erturk and Inman [118]. This model was further modified by Oliver and Priya and for a single vibration mode was formulated into a block diagram form [127]. Based on the Euler-Bernoulli beam model, the coupled equations of motion (in modal coordinates) and electrical circuit equation for a piezoelectric bimorph bender are given for the rth mode as [118]:

$$\begin{aligned} &\frac{d^2\eta_r^s(t)}{dt^2} + 2\zeta_r\omega_r\frac{d\eta_r^s(t)}{dt} + \omega_r^2\eta_r^s(t) + \chi_r^s U(t) = -\frac{M_b}{L}\frac{d^2y(t)}{dt^2}\int_0^L \Phi_r(x)dx \\ &-M_t\Phi_r(L)\frac{d^2y(t)}{dt^2} \end{aligned} \tag{7}$$

$$\frac{C_p}{a}\frac{dU(t)}{dt} + \frac{aU(t)}{2R_L} = i_p(t) = \kappa_r\frac{d\eta_r^s(t)}{dt} \tag{8}$$

where the following is a list and description of parameters:

x - distance along beam

$\Phi_r(x)$ - modeshape of the cantilever beam as a function of distance along beam

$\eta_r(t)$ - modal displacement

M_b - mass of beam

M_t - tip mass of cantilever

ζ_r - modal damping coefficient

ω_r - modal natural frequency

L - total length of the cantilever beam

χ_r - backward modal coupling term piezoelectric system for rth mode

κ_r - forward modal coupling term piezoelectric system for rth mode

h_{pc} - distance from the ceramic centerline to the neutral axis

h_p - thickness of piezoceramic

h_s - thickness of substructure

b - width of beam

C_p - capacitance of bimorph layer

d_{31} - piezoelectric constant

s_{11}^{E} - elastic compliance of the piezoelectric layer at constant electric field

a – Constant, for parallel connection of layers = 1, for series connection of layers =2

i_p - total current production in system

U - voltage across the load resistance

R_L - load resistance

Additional details on derivation of Eq.(7) and (8) can be found in Ref. 118. The capacitance of bimorph is given as:

$$C_p = \frac{\varepsilon b L}{h_p} \tag{9}$$

The backward modal coupling creates the electrical damping on the mechanical structure given as:

$$\chi_r = \frac{1}{s_{11}^{E}} \frac{d_{31} b}{a h_p} \left(\frac{h_s^2}{4} - \left(h_p + \frac{h_s}{2} \right)^2 \right) \frac{d\Phi_r(x)}{dx} \Big|_{x=L} \tag{10}$$

where h_s and h_p are the thicknesses of the piezoceramic and substructure layers, s_{11}^{E} is the modulus of elasticity for the ceramic, d_{31} is the piezoelectric constant, b is the width of the beam [145]. The modal coupling term transducing modal velocity to current in the electrical equation is given by:

$$\kappa_r = \frac{d_{31} h_{pc} b}{s_{11}^E} \int_0^L \frac{d^2 \Phi_r(x)}{dx^2} dx = \frac{d_{31} h_{pc} b}{s_{11}^E} \frac{d\Phi_r(x)}{dx} \Big|_{x=L} \tag{11}$$

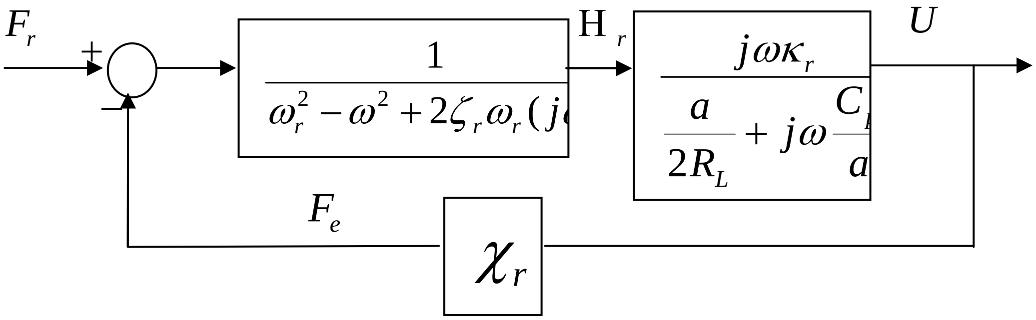

Figure 8.7 Block diagram for energy generation from parallel (a=1) and series (a =2) connected piezoelectric bimorph transducer.

The equations of motion above can be easily rearranged into the block diagram form shown in Figure 8.7 to show the effect of the mechanical system on the electrical output and the feedback term with which the electrical system effects the mechanical vibration of the system. $\mathrm{H}_r(s)$, $F_r(s)$ and $U(s)$ are the Laplace transforms of the modal forcing, modal displacement, and output voltage. The output voltage and power for a series (a=2) and parallel (a =1) connected bimorph operating around the r^{th} mode can be reduced to the following equations:

$$U(t) = \left(\frac{j\omega\kappa_r \left(\frac{M_b}{L} \int_0^L \Phi_r(x) dx + M_t \Phi_r(L) \right)}{\left(\frac{a}{2R_L} + \frac{C_p}{a}\right)(\omega_r^2 - \omega^2 + j2\zeta_r \omega_r \omega) + j\omega\kappa_r \chi_r} \right) \left(\omega^2 \mathrm{Y}_0 e^{j\omega t} \right) \tag{12}$$

$$P_{avg}(t) = \frac{U^2}{2R_L} \tag{13}$$

Figure 8.8 shows the transfer function between base acceleration and seismic mass acceleration measured using an accelerometer mounted on the structure and a laser vibrometer focused on the tip of cantilever beam. For calculation of experimental damping ratio, the half power bandwidth method was employed [128]. Note that the random noise excitation and the sine wave excitations do not match, indicating that the response is a function of excitation levels. For the purposes of the model, the damping ratios were estimated using sine wave excitation at the levels used in the experiment. The maximum electrical power ($P_{e,max}$) can then be calculated by using Eq. (11) as:

$$P_{e,\max} = \frac{mY^2\omega_n^3}{16\zeta_m} \tag{15}$$

It can be noted in Eq. (15) that power is inversely proportional to the damping ratio (ζ_m) and directly proportional to the square of acceleration (α). The damping ratio of system can be reduced by optimizing the material properties and structural support of the cantilever, in order to maximize the available energy.

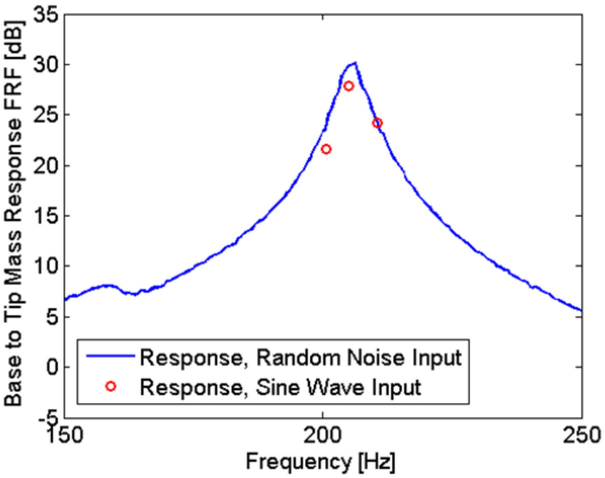

Figure 8.8 Base to tip-mass transfer function used to calculate the damping ratio

The system parameters for the PZTZNN and PZTPZN bimorphs have been summarized in Table 8.3.

Table 8.3 System parameters for Piezoelectric bimorph schemes

Parameters	**Piezoceramic Bimorph Scheme1/** **PZTZNN**	**Piezoceramic bimorph Scheme2/** **PZTZNN**	**Piezoceramic bimorph Scheme3/** **PZTZNN**	**Piezoceramic bimorph Scheme4/** **PZTPZN**
Length, L [mm]	25	25	25	22
Width, b [mm]	5.3	5.3	5.3	5.5
Thickness, h [mm]	0.53 (piezo) 0.05(brass)	0.4 (piezo) 0.05(brass)	0.4 (piezo) 0.05(brass)	0.4 (piezo) 0.05(brass)
Mass density [kg/m^3]	7800 (piezo) 8800 (brass)	7800 (piezo) 8800 (brass)	7800 (piezo) 8800 (brass)	7879(piezo) 8800 (brass)
Young's Modulus [GPa]	66 (piezo), 110(brass)	66 (piezo), 110(brass)	66 (piezo), 110(brass)	66 (piezo), 110(brass)
Piezo. Constant, d_{31} [pm/V]	56.2	53.3	50.0	153.73
Permittivity, ε (nF/m)	$538.5\varepsilon_0$	$475\varepsilon_0$	$376\varepsilon_0$	$1587.93\ \varepsilon_0$
Mechanical Damping Ratio	0.025	0.025	0.025	0.025
Tip Mass [kg]	0.00236	0.00236	0.00236	0.00236

The analytical model was used in order to predict the power output of fabrication schemes 2, 3, and 4 producing a reasonable match to the measured results, as shown in Figure 8.9, Figure 8.10 and Figure 8.11. Bimorphs fabricated with PZTPZN plates (scheme 4) was found to generate the highest power output of the three devices. In this case, the generated output power was found to be 49.5 µW across a load of 90 kΩ at $0.2g_{rms}$ base excitation at frequency of 193.1 Hz with a mechanical damping ratio of 0.025. It should be noted here that due to the more compliant piezoelectric material, the length of beam was shortened to 22 mm in order to produce a resonant frequency on the order of 190 Hz. Bimorph fabricated with two step sintered PZTZNN (Scheme 3) was found to generate a power output of 49.1 µW across a load of 178 kΩ at $0.2g_{rms}$ base excitation, frequency of 197.25 Hz, and mechanical damping ratio of 0.025. The model provides accuracy in order of magnitude and frequency location, and is beneficial in seeing the general impact of several parameters on the output power. For single step sintered PZTZNN bimorph (scheme 1), the generated output power was found to be 7.5 µW across a load of 178 kΩ with tip mass of 2.36 gm and a base excitation of $0.2g_{rms}$. Using the fabrication techniques of two step sintering PZTZNN bimorph (scheme 2), with a tip mass of 2.36 gm the resonance frequency was found to be 184.4 Hz. At this frequency, the bimorph was found to generate output power of 42.9 µW across a load of 90 kΩ at $0.2g_{rms}$ base excitation.

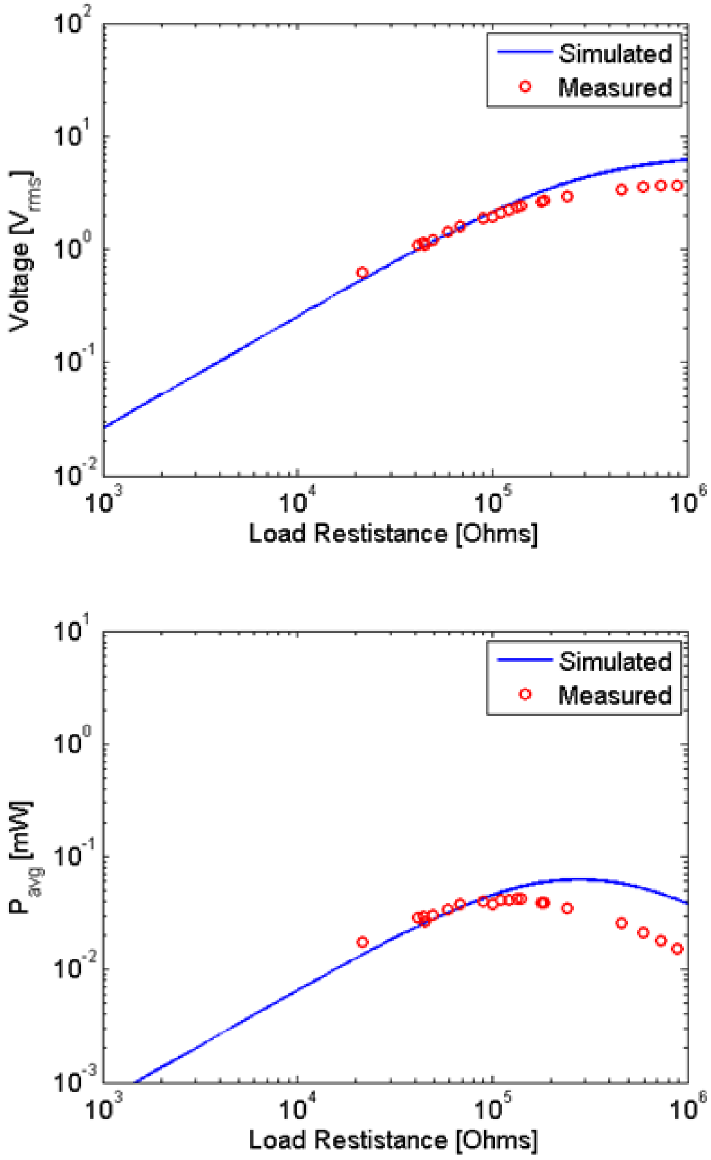

Figure 8.9 Theoretical and experimental output voltage and power characteristics of PZTZNN bimorph transducer fabricated by scheme 2. Operating frequency of the transducers was 184.4 Hz with base acceleration of $0.2g_{rms}$ and damping ratio of 0.025.

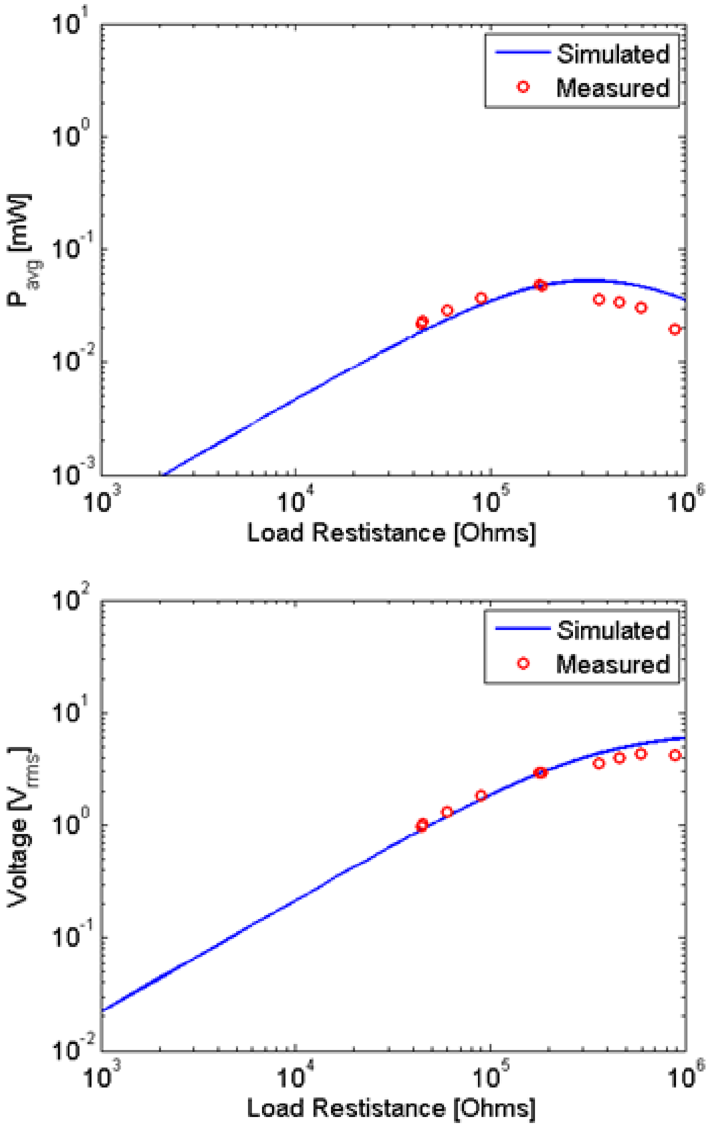

Figure 8.10 Theoretical and experimental output voltage and power characteristics of PZTZNN bimorph transducer fabricated by scheme 3. Operating frequency of the transducers was 197.25 Hz with base acceleration of $0.2g_{rms}$ and damping ratio of 0.025.

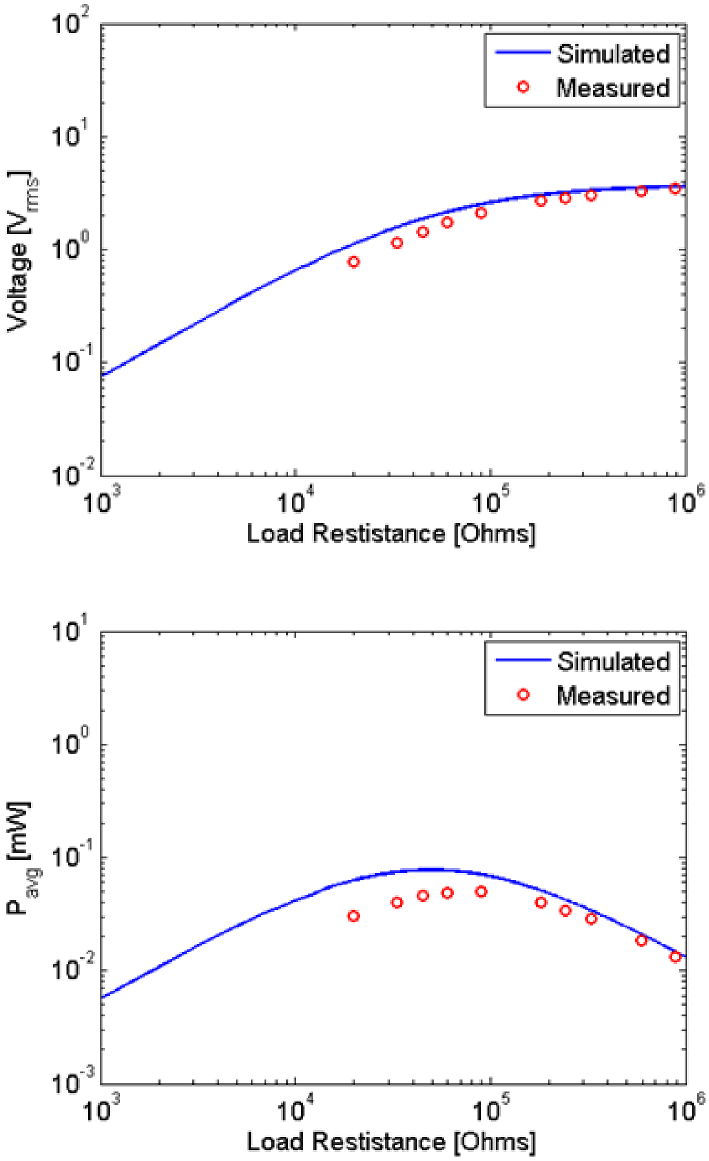

Figure 8.11 Theoretical and experimental output voltage and power characteristics of PZTPZN bimorph transducer fabricated by scheme 4. Operating frequency of the transducers was 193.1 Hz with base acceleration of $0.2g_{rms}$ and damping ratio of 0.025.

As shown in Figure 8.9, Figure 8.10 and Figure 8.11; the modeled and measured output voltage and power had a slight mismatch which can be linked to the approximation in the calculation of coupling factors and estimation of damping factors. Also, bonding layer between the piezoelectric plates and brass was not considered in this model which can affect the prediction of fundamental resonance frequency of structure and coupling factors. Table 8.4 summarizes the predicted and measured power densities for schemes 2, 3 and 4 considering the total volume of the system and piezoelectric bimorph volume alone. The measured power density for the structure and bimorph alone improved with the improvement of the product property (d.g) of the material.

Table 8.4 Comparison of Measured and Predicted Power densities for bimorphs

	Power Output, 0.2 g_{rms}, 190 Hz; (μW)		**Power Density of Structure (μW/mm^3)**		**Power Density of Piezo Element (μW/mm^3)**	
	Measured	Predicted	Predicted	Measured	Predicted	Measured
Scheme2/ PZTZNN	42.9	62.7	0.2071	0.1418	0.5564	0.381
Scheme3/ PZTZNN	49.1	52.8	0.1746	0.1624	0.4692	0.4363
scheme4/ PZTPZN	49.5	77.4	0.2676	0.1713	0.7806	0.4996

8.4 Chapter Summary

This chapter reports the theoretical and experimental results on vibration energy harvesting using the piezoelectric bimorph transducers synthesized using compositions $0.9Pb(Zr_{0.56}Ti_{0.44})O_3 - 0.1Pb[(Zn_{0.8/3}Ni_{0.2/3})Nb_{2/3}]O_3$ + 2 mol% MnO_2 (PZTZNN) and $0.8Pb(Zr_{0.52}Ti_{0.48})O_3$-$0.2Pb(Zn_{1/3}Nb_{2/3})O_3$ (PZTPZN). The results show a direct correlation between the output power and material properties in terms of product (d.g), where d is piezoelectric strain constant and g is piezoelectric voltage constant. Theoretical modeling was conducted to optimize the dimensions of bimorph and predicts its performance. Further improvements in the product (d.g) will lead to higher power densities.

CHAPTER 9

INDUCTIVE ENERGY HARVESTING

9.1 Introduction

In recent years, there has been rapid development in the area of micro-sensors for various applications such as remote structural health monitoring, automotive pressure and gas sensors and biomedical sensors [129]. In many of these applications, power has been provided by batteries which have very small shelf life and are non-biodegradable [130-132]. Thus, the demand for portable on-demand energy harvesting devices has been constantly increasing. The requirements for energy harvester are low cost, high efficiency and high durability; much similar to that of batteries.

There has been significant effort in developing small scale power generators using electromagnetic, piezoelectric, and thermoelectric conversion principles. With regards to human body, vibration and temperature gradient become the important sources. Glynne-Jones et. al. have demonstrated a electromagnetic generator producing 157 μW average power when tested on an engine block [133]. Goto et. al. reported an automatic power-generating system (AGS) which generated 13 μJ per heart beat. In a fully recharged state, it could pace a mongrel dog’s heart at 140 beats per minute for one hour [134]. However, most of the proposed devices in literature are either bulky or do not generate enough power to meet the requirements of external sensor attached to human body. It should also be noted here that the energy harvester for human body should be in conformal shape and size such that it can be integrated with common utilities.

Our focus in this study is to develop a power source for pulse rate sensors. We propose to integrate this power source with pen commonly carried by humans in the pocket close to the heart. Thus, pen is naturally in close vicinity of the sensor. Table 9.1 lists the power requirements for various heart beat or pulse rate sensors available commercially. From this table it can be seen that power required for pulse rate sensors is of the order of 0.3 ~ 0.5 mW. Thus, a vibration energy harvester should be able to generate at least 0.3 mW of average power from human action, e.g. jogging at low speed of the order of 2 steps per second. In that case, this harvester can power a pulse rate sensor while the human body is performing its daily activities.

Table 9.1 Power requirements of commercially available pulse rate sensors.

Example	**Device name**	**Approximate dimensions**	**Power requirement**
1	Piezo film sensor [135]	64 mm x 97 mm	0.36~0.45 mW
2	Nonin Onyx 9500 pulse oxymeter [136]	75 mm x 30 mm	~0.3 mW
3	BCI Digit 3420 Finger Pulse Oximeter [137]	72 mm x 30 mm	~0.3 mW
4	Probasics digit-ox finger pulse oximeter (model no. ISG8600) [138]	43 mm x 57 mm	~0.3 mW

Integrated electronics could be included to send a text message or alarm signal if any kind of abnormal heart rate is measured (typically over range of ±10%).

Our harvester design is based on Faraday's law of electromagnetic induction where a magnet oscillates inside a wound coil [139]. The displacement of the magnet through the coil results in a change of magnetic flux inducing current through the circuit. Higher magnet velocity generates higher electromotive force and thus higher output voltage. This design was primarily selected to meet the shape and size requirement of "Pen" and still generate 0.3mW of power. Most of the other vibration conversion mechanisms based on piezoelectric and electrostatic will not be able to generate this large amount of power at such low frequencies. In the case of a "Pen", thermoelectric harvesting will not be as effective, as there is no direct contact with a sizeable temperature gradient.

9.2 Experimental

Figure 9.1 (a) shows the schematic cross section of the pen harvester prototype. The total length and diameter of the harvester were 70 mm and 12.5 mm respectively. The harvester consists of a permanent magnet which moves inside a coil wound on the middle section of harvester. The diameter and length of the coil were 10.5 mm and 20 mm respectively. The electromagnetic coil consisted of 500 turns of 30AWG wire with an inner diameter of 8.5 mm and outer diameter of 10.5 mm. The magnetic field on the top surface of the disc magnet was measured using a DTM – 141D Group 3 Digital Teslameter (GMW Associates Ltd.) and was found to be of the order of 0.3 T. Two designs have been tested: A design with no springs allowing maximum exertion of the magnet, and a design with two low stiffness springs attached to the two ends of the magnet. The springs allow the magnet to be in the coil region for low input acceleration test conditions. Figure 9.1 (b) shows the picture of fully assembled pen harvester. The right half of the pen was a harvester with electrical connections while the left end was for regular writing purposes. This design of harvester is based on a commercially available shake flashlight power harvester shown in Figure 9.1 (c).

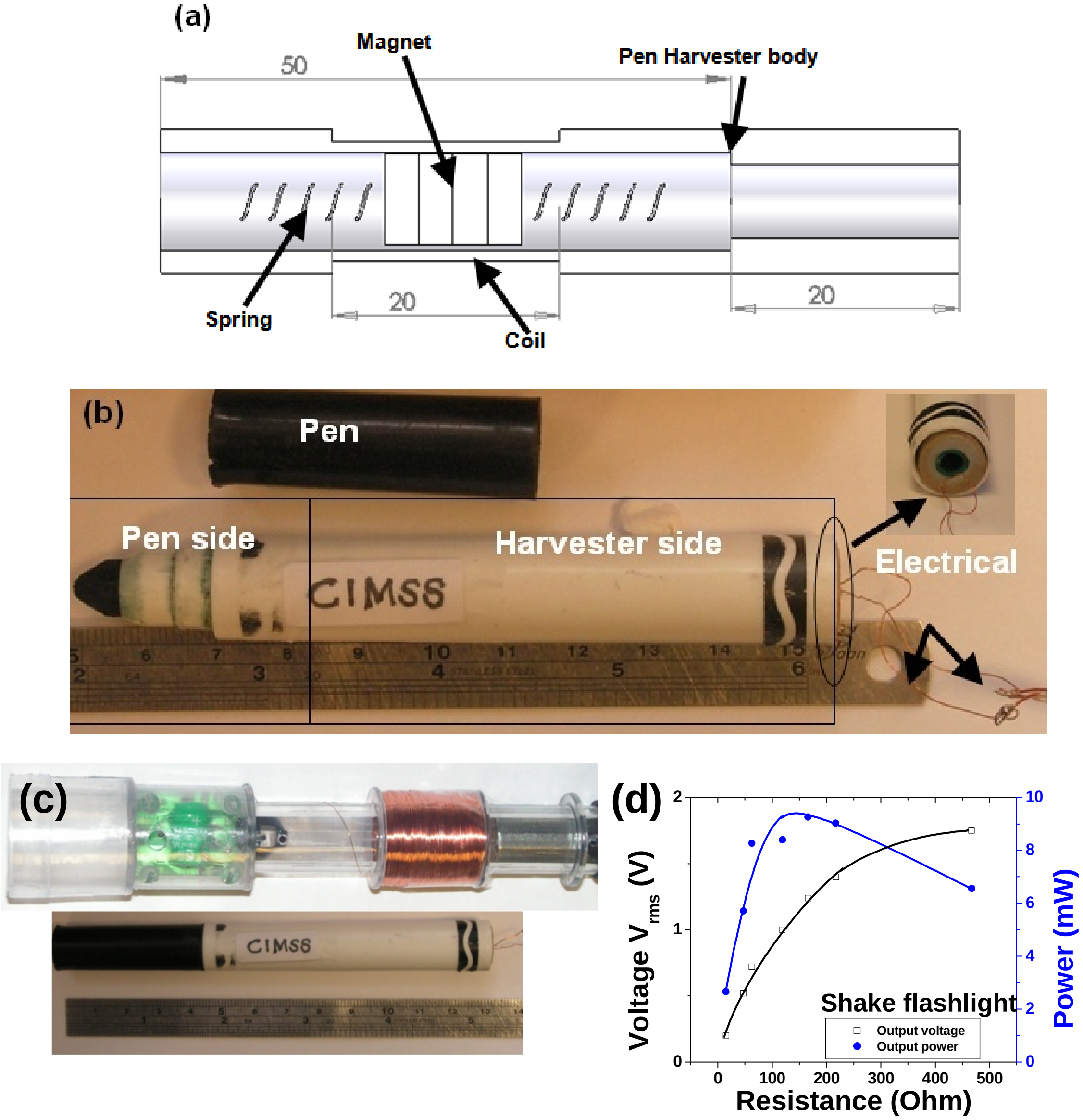

Figure 9.1 (a)Cross-section and front view of pen harvester, and (b) Picture of the fabricated electromagnetic (EM) pen harvester prototype (c) Comparison of the size of shake flashlight and pen harvester prototype, (d) Voltage and power characteristics of shake flashlight at 3.5 Hz used for bench-marking the response of fabricated pen harvester.

The harvester was characterized at various frequencies and output was recorded using a BK Precision 5492 5 ½ Digital Multimeter. A small breadboard from Radio shack, Inc. was used to vary the load resistors across the coil terminals. Our pen harvester was 1/6 times smaller in volume of that of conventional shake flashlight. The shake flashlight we used for benchmarking our harvester consisted of 500 turns of 30AWG copper coil with 19.5 mm diameter and 25 mm length. Figure 9.1 (d) shows the voltage and power output measured on the shake flashlight at 3.5 Hz frequency. The shake flashlight was found to produce a peak power of 9 mW across a load of 166 Ω.

9.3 Theoretical analysis

9.3.1 Vibration Harvesting Theory

Several authors in the literature have presented different ways of predicting the power output of inertial vibration harvesters. It is well agreed upon in the literature that a vibrating mass-spring-damper system has an available amount of power which depends on the stiffness of the spring, k, the total amount of mechanical damping, c_m, and the seismic mass, m as shown in the Figure 9.2.

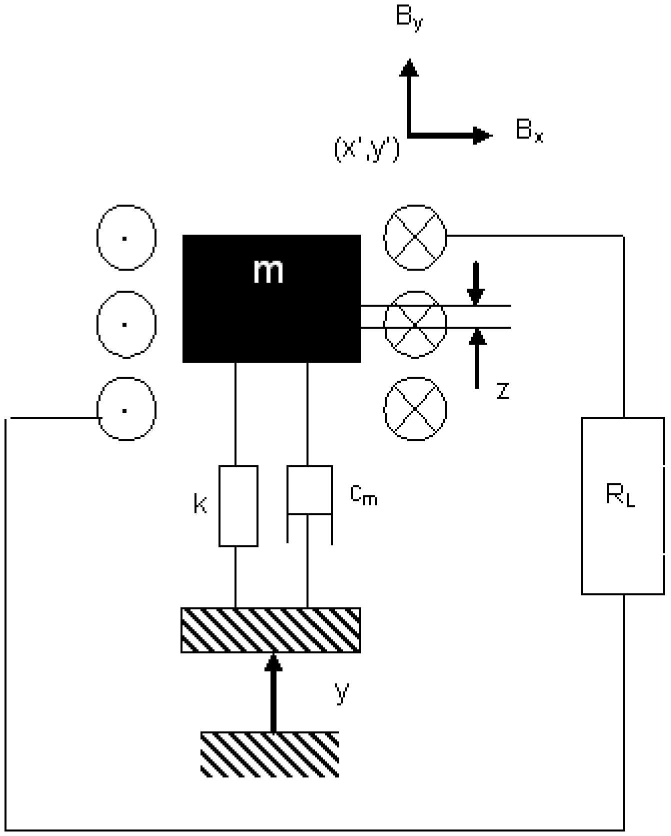

Figure 9.2 Schematic of vibrating spring-mass-damper system

The displacement of the base is given by *y* , the displacement of the seismic mass is given by *x* and the relative displacement of the mass with respect to the housing is given by *z*. The equation of motion for the mass is given by:

$$m\ddot{x}(t) + c_T[\dot{x}(t) - \dot{y}(t)] + k[x(t) - y(t)] = 0 \qquad (1)$$

Equation (1) can be rearranged in order to find a differential equation (2) for the relative motion, *z(t)*, as a function of the base acceleration:

$$m\ddot{z}(t) + c_T \dot{z}(t) + kz(t) = -m\ddot{y}(t) \tag{2}$$

where *z(t)* is the relative motion of the seismic mass with respect to the housing. In this case, the total power dissipated in the damper under sinusoidal forcing is given by:

$$P_T(\omega) = \frac{m\varsigma_T Y^2 \left(\frac{\omega}{\omega_n}\right)^3 \omega^3}{\left[1 - \left(\frac{\omega}{\omega_n}\right)^2\right]^2 + \left[2\varsigma_T \left(\frac{\omega}{\omega_n}\right)\right]^2} \tag{3}$$

where ς_T is the total damping ratio of the damper given by:

$$\varsigma_T = \frac{c_T}{2\sqrt{mk}} = \varsigma_e + \varsigma_m = \frac{c_e}{2\sqrt{mk}} + \frac{c_m}{2\sqrt{mk}} \tag{4}$$

where ς_e and ς_m are the electrical and mechanical damping ratios respectively of the harvester. The total power in the system can be split into sum of the mechanical power and electrical power dissipated across the load as:

$$P_T(\omega) = P_m(\omega) + P_e(\omega) = \frac{m\varsigma_m Y^2 \left(\frac{\omega}{\omega_n}\right)^3 \omega^3}{\left[1 - \left(\frac{\omega}{\omega_n}\right)^2\right]^2 + \left[2(\varsigma_m + \varsigma_e)\left(\frac{\omega}{\omega_n}\right)\right]^2} + \frac{m\varsigma_e Y^2 \left(\frac{\omega}{\omega_n}\right)^3 \omega^3}{\left[1 - \left(\frac{\omega}{\omega_n}\right)^2\right]^2 + \left[2(\varsigma_m + \varsigma_e)\left(\frac{\omega}{\omega_n}\right)\right]^2} \tag{5}$$

where the electrical power generated is equal to $P_e(\omega)$ and the mechanical power dissipated is given by $P_m(\omega)$. At resonance, the amount of electrical power generated reduces to Eq. (6):

$$P_e(\omega_n) = \frac{m\varsigma_e Y^2 {\omega_n}^3}{4(\varsigma_m + \varsigma_e)^2} \tag{6}$$

It is well known now that the maximum power generated by the electrical power takeoff system occurs when the electrical damping on the harvester is equal to the mechanical damping on the harvester. That is, the condition for maximum power take-off occurs when:

$$\varsigma_e = \varsigma_m \tag{7}$$

Therefore the maximum electrical power which can be generated is given by Eq. (8) [140, 141]:

$$P_{e,\max}(\omega_n) = \frac{mY^2 {\omega_n}^3}{16\varsigma_m} \tag{8}$$

9.3.2 Generalized Inductive Energy Harvesting Theory

In section A, we derived the maximum magnitude of electrical energy which can be harvested from a vibrating spring-mass system. Now we will present the theory of inductive energy harvesting, and generalized expressions for conditions under which the magnetic field is not constant across the coil at all times.

The theory for transducing the mechanical energy into electrical energy is described in detail by Poulin [141] and Nakano [142]. Nakano's fundamental equations of motion which couple the movement of seismic mass to a voltage and current in load impedance are given by:

$$\begin{bmatrix} F \\ U \end{bmatrix} = \begin{bmatrix} Z_m & \Phi \\ \Phi & -Z_e \end{bmatrix} \begin{bmatrix} \dot{z} \\ i \end{bmatrix} \tag{9}$$

where *f* is the forcing function on the seismic mass given by ($F=m.d^2y/dt^2$), *U* is the voltage across the load resistance (R_L), Φ is the transduction coefficient, Z_m is the mechanical impedance of the harvester, Z_e is the electrical impedance of the coil, and $\dot{z}$ is the velocity of the coil with respect to the magnetic field. The mechanical and electrical impedances are given by Eqn. (10):

$$\begin{aligned} Z_m &= mj\omega + c_m + \frac{k}{j\omega} \\ Z_e &= R_{coil} + L_{coil}\, j\omega \end{aligned} \tag{10}$$

where R_{coil} and L_{coil} are the resistance and self-inductance of the coil. The transduction coefficient Φ can be determined by investigating the force on a current conducting element inside a magnetic field [143]:

$$\begin{aligned} d\overset{\varpi}{F}_e &= id\overset{\rho}{l}\, x\overset{\varpi}{B} \\ F_e &= i\oint lx\overset{\varpi}{B} \end{aligned} \tag{11}$$

If the magnetic field B is constant within the gap, and the length of coil l is perpendicular to the magnetic field, then the electrical force on the conductor will be given as:

$$F_e = Bli \tag{12}$$

and the transduction coefficient is given by Eqn. (13):

$$\Phi = Bl \tag{13}$$

where l is the total length of the coil inside the magnetic field. This is typically the case in transducers such as voice-coil loudspeakers where the coil sees a constant magnetic field. However, in the case of pen harvester where the magnet has large relative displacement with respect to the coil, the coil will see a time varying magnetic field along its length. Therefore, the sum of the forces (mechanical plus electrical) on the conductor will be given by Eqn. (14):

$$F = F_m + F_e = Z_m \dot{z} + i\oint d\vec{l} \times \vec{B} \tag{14}$$

In addition, the induced EMF on the coil due to the movement of coil within the gap can be determined from an investigation of the motion of a conductor in a magnetic field as shown in Eqn. (15): [142]

$$\begin{aligned} dU_v &= (\vec{\dot{z}} \times \vec{B}) \cdot d\vec{l} \\ U_v &= \oint (\vec{\dot{z}} \times \vec{B}) \cdot d\vec{l} \end{aligned} \tag{15}$$

where U_v is the induced voltage due to the motion of the conductor in the magnetic field, and v is the velocity of the conductor with respect to the magnetic field (= $\dot{z}$). If velocity is perpendicular to the direction of the magnetic field, then the induced voltage is given by:

$$U_v = Bl\dot{z} \tag{16}$$

Note however that in the case of pen harvester there will be certain regions of the displacement of the magnet where the velocity and magnetic field will not be perpendicular. Using KVL around the circuit the potential across the load impedance is equal to:

$$U = \oint (\vec{\dot{z}} \times \vec{B}) \cdot d\vec{l} - Z_e i \tag{17}$$

The coupled equations (under the linearizing assumption of constant magnetic field) are given by Eqn. (18):

$$\begin{aligned} F &= Z_m \dot{z} + Bli \\ U &= Bl\dot{z} - Z_e i \end{aligned} \tag{18}$$

For the case of the pen harvester, the generalized nonlinear equations are summarized in Eqn. (19):

$$\begin{aligned} F &= Z_m \vec{\dot{z}} + i\oint \vec{dl} \times \vec{B}(x',y') \\ U &= \oint (\vec{\dot{z}} \times \vec{B}(x',y')) \cdot \vec{dl} - Z_e i \end{aligned} \qquad (19)$$

where *B(x’,y’)* is the magnetic field vector in a coordinate system relative to the magnet. Due to the nature of the integral equations above, the transduction coefficient will vary with the position of the magnet.

9.3.3 Evaluating Position Dependant Transduction Coefficient

This section presents the evaluation of the position dependant transduction coefficient and the simulation of the expected voltage and power output.

Evaluating the cross products in Eqn. (19) for our geometry we find that only the spatially dependant magnetic field in the direction perpendicular to the magnet movement (B_x) contributes to the induced voltage and the electrical force on the magnet.

$$dF_e = i\left(\vec{dl} \times \vec{B}(x',y')\right) = \det\begin{pmatrix} \hat{i} & \hat{j} & \hat{k} \\ 0 & 0 & -i\vec{l} \\ B_x(x',y') & B_y(x',y') & 0 \end{pmatrix} \qquad (20)$$

$$dF_{e,y} = B_x(x',y')(dl)i$$

$$dU_v = (\vec{\dot{z}} \times \vec{B}(x',y')) \cdot \vec{dl} = \left(\det\begin{pmatrix} \hat{i} & \hat{j} & \hat{k} \\ 0 & \dot{z} & 0 \\ B_x(x',y') & B_y(x',y') & 0 \end{pmatrix}\right) \cdot \vec{dl}$$

$$dU_v = B_x(x',y')(dl)\dot{z}$$

In order to determine the magnetic field in the x-direction, ANSYS 2D- electromagnetic modeling has been compared against the measured magnetic field in the x-direction as a function of the position along the length of the coil. Figure 9.3 (a) shows the ANSYS 2D axisymmetric prediction of magnetic flux density B. Figure 9.3 (b) shows the ANSYS magnetic flux density B along coil location.

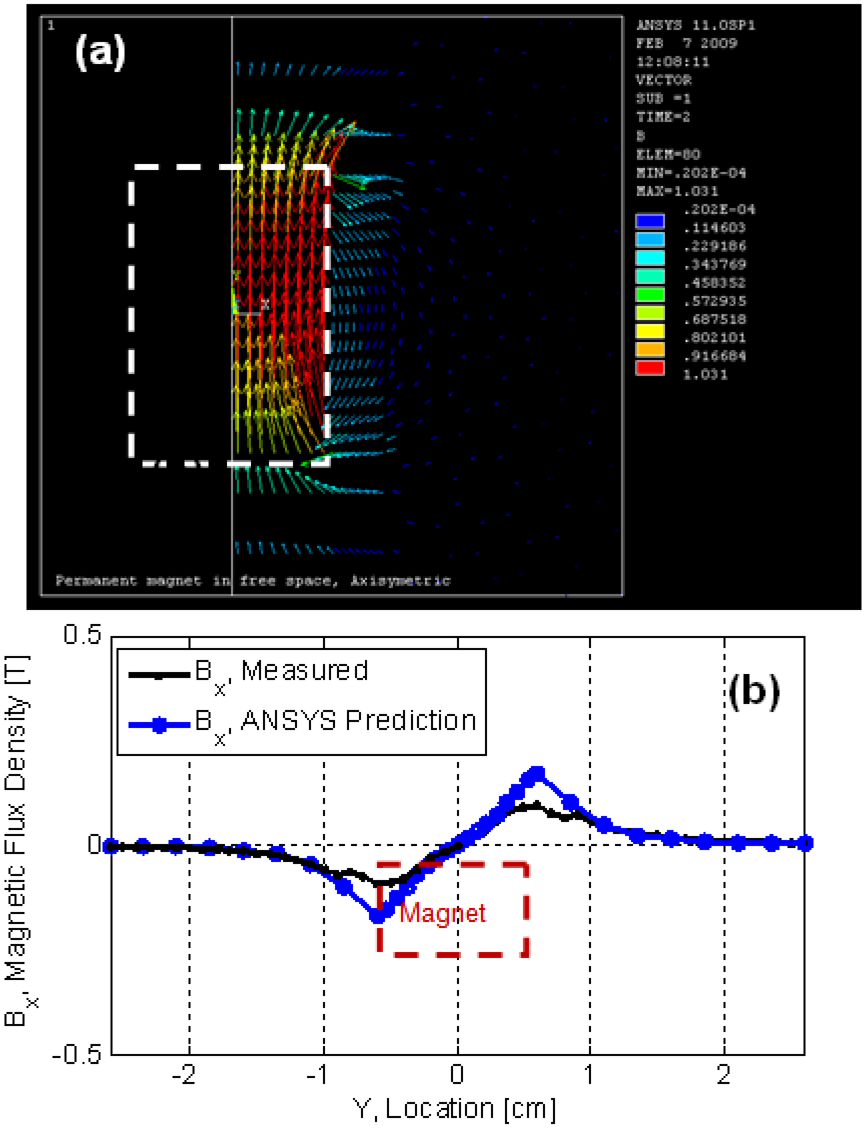

Figure 9.3 (a) ANSYS 2D Axisymmetric prediction of Magnetic flux density B and (b) ANSYS Magnetic flux density B along coil location.

Once the magnetic flux density in the x-direction was measured and modeled in ANSYS, we determined the transduction coefficient as a function of the magnet position (y) in the coil by evaluating the integral in Eqn. (21):

$$\Phi(z) = \oint \vec{dl} \times \vec{B}(x', y') = \oint B_x(x', y')dl \tag{21}$$

Figure 9.4 (a) represents a visual representation of how B_x must be integrated along the length of the coil. Figure 9.4 (b) represents the transduction coefficient calculated from the measured flux density as a function of magnet centroid position. It is clear from Figure 9.4 (b) that the transduction coefficient drops to zero as the magnet passes through the center of the coil.

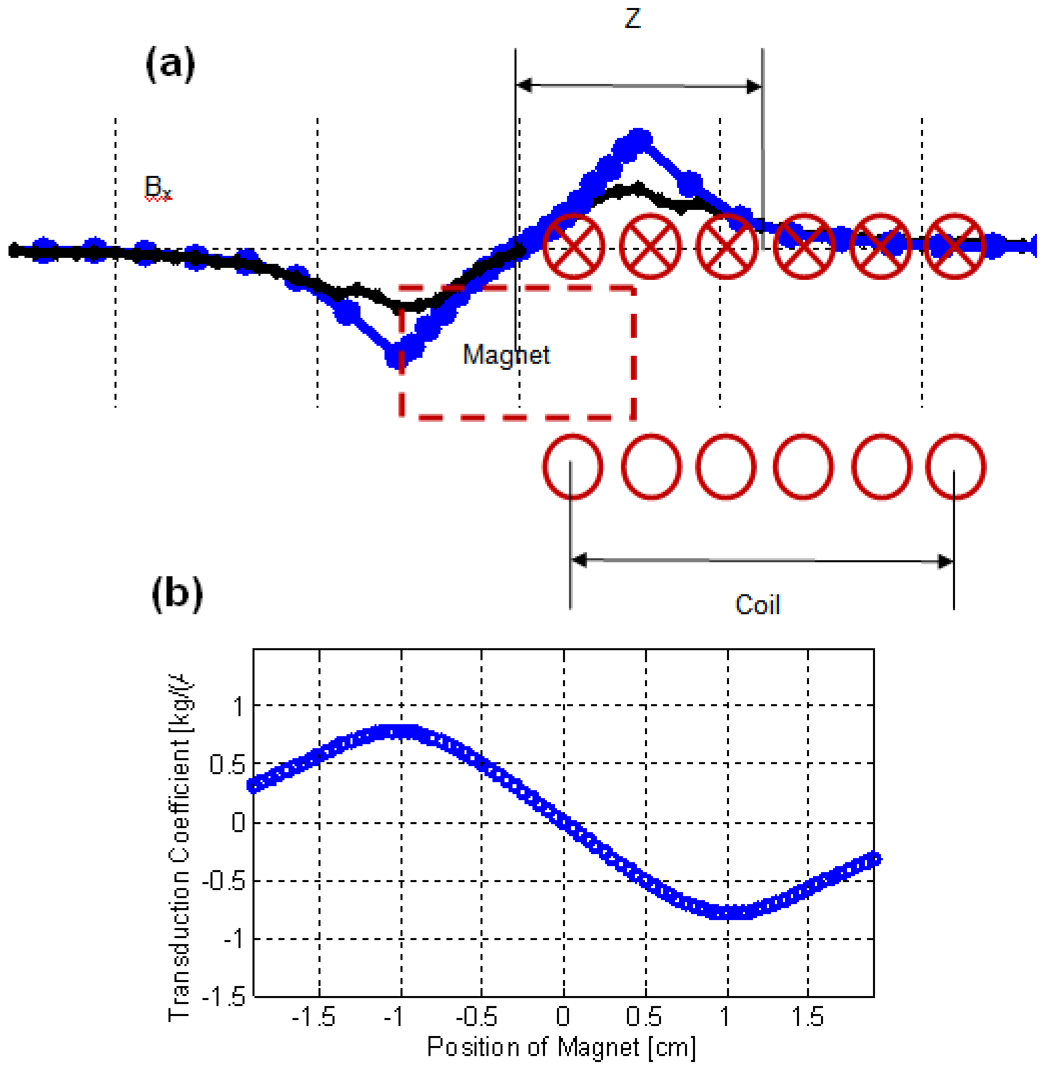

Figure 9.4 (a) Visual representation of integration of B_x along length of the coil and (b) Transduction coefficient calculated from the measured flux density as a function of magnet centroid position.

9.3.4 Simulation

This section presents the simulation results performed in Matlab using numerical integration in order to capture the nonlinear dynamics using the calculated transduction coefficient. In order to simulate the power output, the coupled equations can be put into state-space form (where the derivative of the state vector is a nonlinear function):

$$\dot{\vec{x}} = f(\vec{x},t) \tag{22}$$

The equations in state-space form include the spatially varying transduction coefficient, which produces the nonlinearity:

$$\begin{pmatrix} \dot{z} \\ \ddot{z} \\ \dot{i} \end{pmatrix} = \begin{bmatrix} 0 & 1 & 0 \\ -\frac{k}{m} & -\frac{c}{m} & -\frac{\Phi(z)}{m} \\ 0 & \frac{\Phi(z)}{L_e} & -\frac{R_e + R_L}{L_e} \end{bmatrix} \begin{bmatrix} z \\ \dot{z} \\ i \end{bmatrix} + \begin{bmatrix} 0 \\ \frac{F}{m} \\ 0 \end{bmatrix} \tag{23}$$

9.3.5 Simulation of Inductive Harvester with No Spring

Owing to the softness of spring used in the design, the spring is highly nonlinear in its response. Therefore, we have only modeled the power generation for the harvester without the spring and damping. In the absence of the spring, we have chosen to simplify the dynamics by assuming that the position (z) of the magnet takes the form of a triangle wave. Figure 9.5 (a) presents the predicted position and voltage output of the harvester as a function of time across a load of R_L = 15Ω, frequency f = 3.5Hz and position |z| = 16 mm. The position and velocity wave forms are varying with a period of T = 0.2857 sec. However, the voltage output is varying with a period of 0.1429 sec, indicating nonlinearity. Figure 9.5 (b) presents a comparison between the measured voltage output and the predicted voltage output across a load of R_L = 15Ω, frequency f = 3.5Hz and position |z| = 16mm.

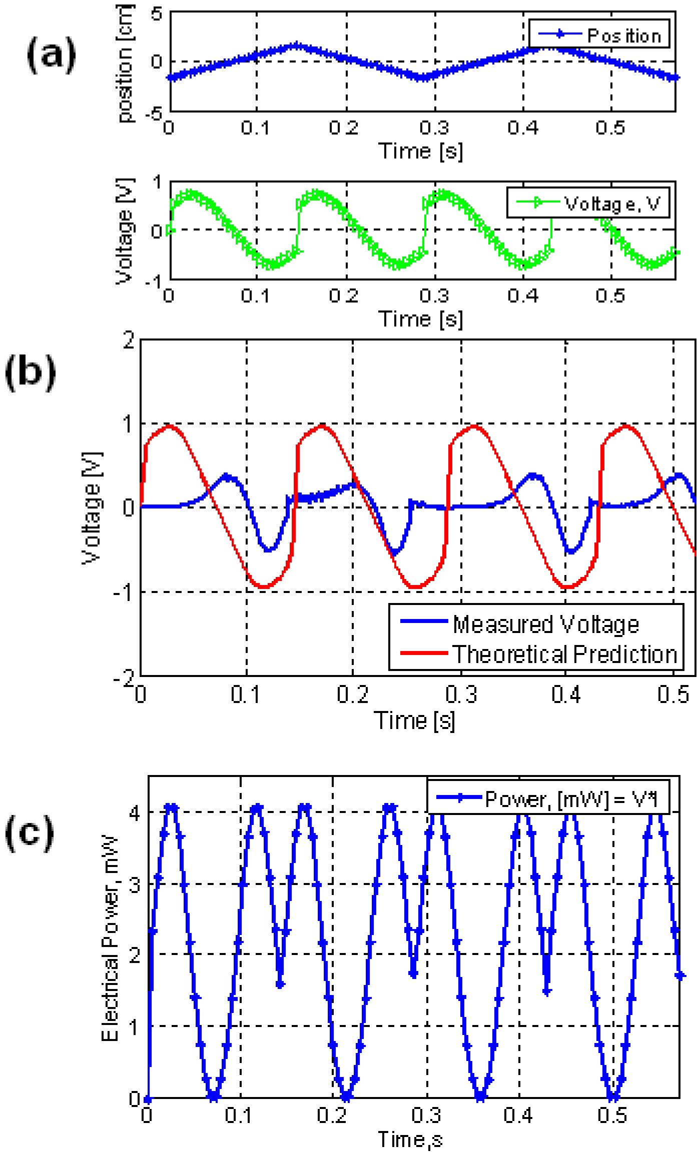

Figure 9.5 (a) Position and Voltage output across R_L = 15 Ω (f = 3.5 Hz, |z| = 1.6 cm), (b) Comparison of Measured and predicted voltage output across R_L = 15 Ω (f = 3.5 Hz, |z| = 1.6 cm), (c) Predicted power output as a function of time across R_L = 15 Ω.

9.4 Experimental results and discussion

It can be noted from Figure 9.5 (b) that the theoretical prediction does not line up with the measured voltage under the stated test conditions. Several factors / assumptions may be responsible for the disagreement as following:

1. It is assumed that the movement of magnet inside the coil does not impact the magnetic flux density, B_x. This is typically assumed in loudspeaker design.
2. The position waveform is assumed to be a triangle wave due to the absence of the spring. This is not an exact assumption, especially when the magnet hits the boundary and reverses directions.
3. Due to the relatively small size of the coil, it is assumed that the velocity of the magnet is not affected by the coil.
4. It is assumed that because of the high amplitude excitation, the friction inside the tube has a negligible impact on the velocity of the magnet.

Figure 9.5 (c) represents the predicted power output as a function of time across R_L = 15Ω. Hence, the predicted average power output across the load resistance is equal to:

$$P_{avg} = 2.32\,\mathrm{mW}$$

Figure 9.6 (a) and (b) shows the voltage and power characteristics of the pen harvester at testing frequencies 3.5 and 5Hz respectively with a 16mm displacement amplitude. The device generated 0.96 mW of power at 3.5 Hz with a load resistance of 15 Ω. The output power increased to ~3 mW at 5 Hz. Figure 9.6 (c) and (d) shows the measurements at 3.5 and 5 Hz after attaching springs on each side of the oscillating magnet. For the test scenario with springs, the pen harvester generated 0.37 mW at 3.5 Hz, and 1.17 mW power at 5 Hz across the load of 22 Ω.

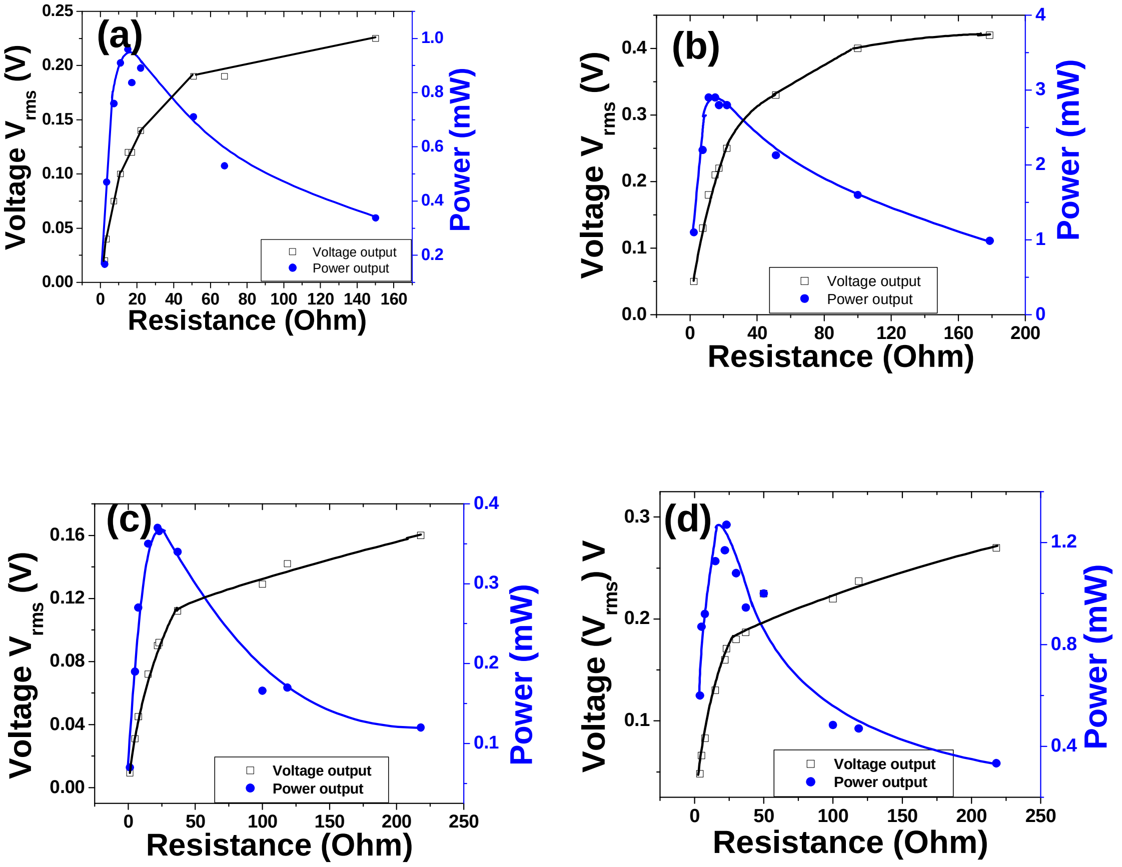

Figure 9.6 (a) Voltage and power output at 3.5 Hz frequency and 50 mm displacement, (b) Voltage and power characteristics at 5 Hz frequency and 50 mm displacement, (c)Voltage and power characteristics with springs attached to the oscillating magnet limiting the maximum displacement to 25 mm at 3.5 Hz frequency, and (d) at 5 Hz frequency.

In order to investigate the feasibility of power generation to power a pulse rate sensor, the pen harvester was tested for various human activities such as walking, jogging and jumping. Figure 9.7 shows the experimental setup used for recording the response, consisting of a National Instrument (NI) – C DAQ 9172 (data acquisition) system with a Labview program interface. The pen harvester was connected across an optimum load of 22 Ω, and placed in the test subject's pocket.

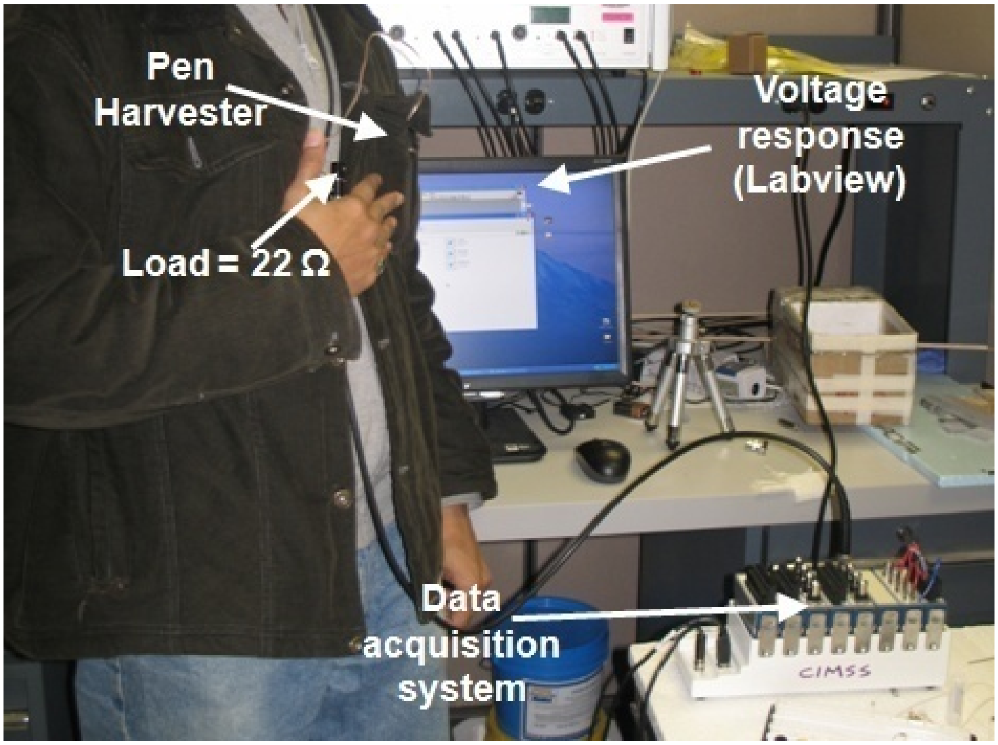

Figure 9.7 Data acquisition setup for recording response of human activities.

Figure 9.8 (a) ~ (d) shows the output response as a function of time for various human activities. Regular walking generated 3.7 μW of power, while jumping generated a power output of 0.46 mW. Jumping frequency was calculated to be 2 jumps/ second (i.e. 2 Hz). Jogging generated a peak average power output of 0.66 mW, which is significantly higher than the corresponding piezoelectric devices demonstrated at this volume.

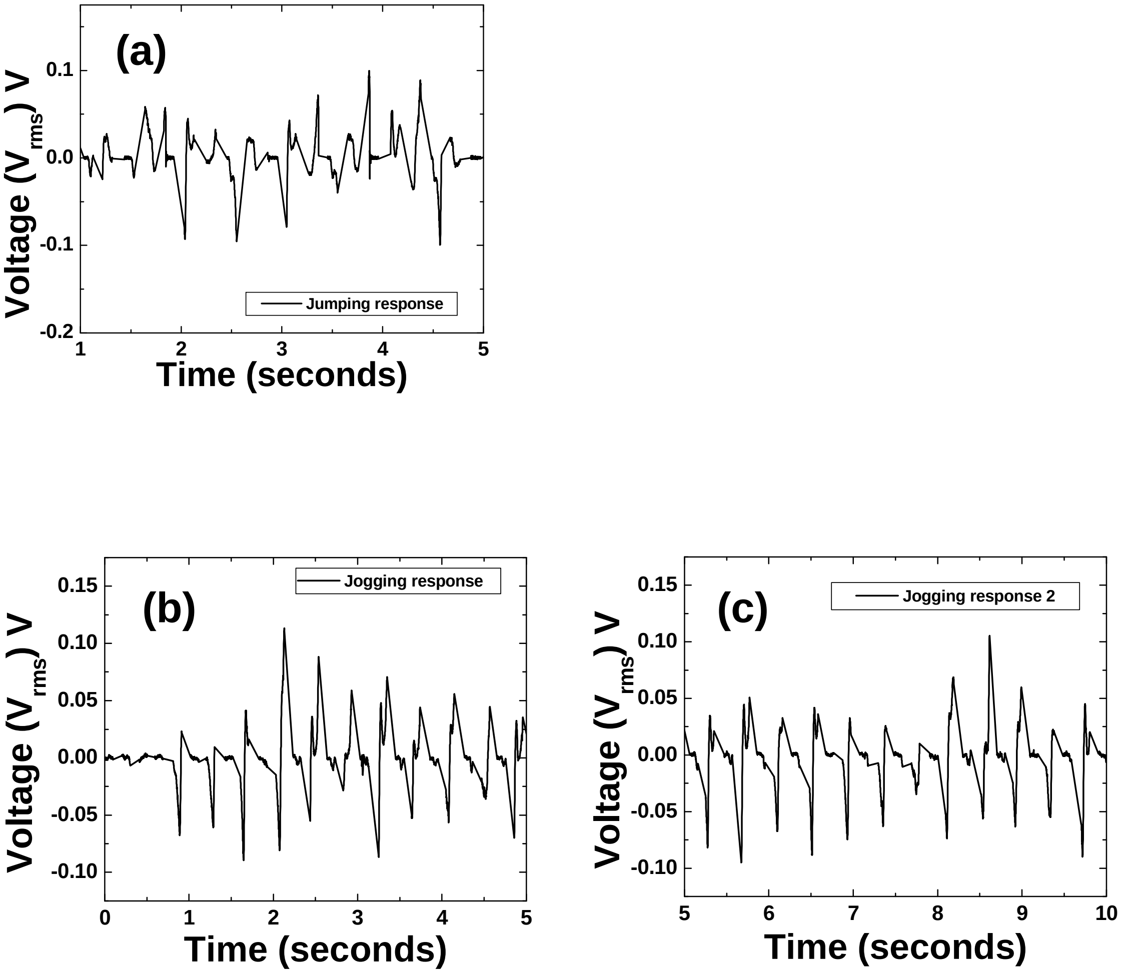

Figure 9.8 Waveform for (a) Jumping (b) Jogging for t = 0 to t = 5 sec, and (c) Jogging for t = 5 to t = 10 sec.

9.5 Chapter Summary

This study reports a prototype of inductive energy harvester generating power on the order of 3 mW at 5 Hz and 1 mW at 3.5Hz operating under a displacement amplitude of 16mm. The displacement amplitude corresponds to an acceleration of approximately 1.14 g_{rms} (5 Hz) nd 0.56 g_{rms} (3.5Hz) respectively. The theoretical prediction was found to be higher than the experimental measurement which could be explained with the help of several factors and assumptions. The prototype was found to generate 0.46 ~ 0.66 mW power under normal human actions such as jumping and jogging which is enough to power a small scale pulse rate sensor.

CHAPTER 10

CONCLUSIONS

The goals of this study were (i) to develop novel sensor architectures for structural health monitoring and magnetic field gradient detection with emphasis on enhancing the functionality while reducing the power consumption, and (ii) to develop vibration and magnetic field energy harvesting techniques for self-powering the sensors. The summary of the accomplishments achieved in this thesis are listed below.

1. Technique for structural health monitoring using impedance spectroscopy was developed with focus on design of piezoelectric sensors. Sensors were fabricated from piezoelectric composition PZTZNN. Using these sensors, experiments were conducted to detect fatigue damage, delamination type of defects in rocket motors and corrosion damage. Sensor location was optimized in order to detect the corrosion with higher sensitivity. Analysis for selection of frequency band and methodology for automated identification of the damage developed. Experiments on characterization of sensitivity of the sensors was conducted clearly delineating the effect of electrode areas.
2. Novel magnetoelectric gradiometers were designed, characterized and analyzed. The results show that the transformer-based gradiometers can provide large detection capability and can be easily scaled to provide on-chip measurements. We demonstrated large ME output voltage from a multilayered PZT – Terfenol D architecture at low frequencies far from EMR, thereby allowing this design to be used as a magnetic field sensor. For laminated ceramic – ceramic gradiometer, a significant change in resonance frequency and amplitude of output

voltage with applied magnetic field was found in the vicinity of EMR. A detailed theoretical model was developed and was found to match with the experimental results.

3. Metal – ceramic gradiometer consisting of PZT and Ni was fabricated and characterized to detect gradient in magnetic field. Metal – ceramic gradiometers worked in frequency ranges of 230 - 250 kHz and maintained high sensitivity near EMR frequency. They require lower magnetic bias field for operation as compared to the ceramic – ceramic gradiometer and are more cost-effective.

4. Barium titanate nanoparticles decorated onto SiCN – MWCNT nanotubes "nanoNecklace" was successfully synthesized and characterized. Structural characterization was performed using SEM and TEM to confirm the presence of BTO nanoparticles in the size range of 10-40 nm and XPS analysis confirmed the formation of perovskite phase. Surface characteristics were optimized by modifying the chemistry and low temperature deposition processes to achieve continuous coating of barium titanate on the nanotubes. nanoNecklace was further modified to realize magnetoelectric (ME) nanotubes using cobalt ferrite as the magnetic layer decorated on the SiCN-MWCNT-BaTiO3 surface.

5. Core – shell ME nanocomposites were synthesized for improving the magnetic field sensitivity by using high pressure compaction technique and high ME coefficient of 187 mV/cm Oe was measured at 285Oe DC bias field. The result clearly shows that high pressure compaction results in enhanced ME coefficient compared to the conventionally sintered samples. Further, 3 – 1 ME composite was designed, synthesized and characterized using pressure assisted co-firing technique in order to understand the effect of connectivity on the elasto-electric coupling.

6. Piezoelectric bimorph transducers were synthesized using compositions 0.9Pb(Zr0.56Ti0.44)O3 – 0.1Pb[(Zn0.8/3Ni0.2/3)Nb2/3]O3 + 2 mol% MnO2 (PZTZNN) and 0.8Pb(Zr0.52Ti0.48)O3-0.2Pb(Zn1/3Nb2/3)O3 (PZTPZN) for vibration energy harvesting. A

detailed theoretical model was developed and compared with the experimental results. The results show a direct correlation between the output power and material properties in terms of product (d.g), where d is the piezoelectric strain constant and g is the piezoelectric voltage constant. The predicted and experimentally measured output power density for PZTPZN bimorph were found to be 0.7806 µW/mm3 and 0.4996 µW/mm3 respectively at 0.2 grms base excitation and base frequency of 190 Hz.

7. Inductive energy harvester design was fabricated and characterized for vibration energy harvesting. The prototype harvester generated power on the order of 3mW at 5 Hz and 1 mW at 3.5Hz operating under a displacement amplitude of 16mm. The displacement amplitude corresponds to an acceleration of approximately 1.14 grms (5 Hz) and 0.56 grms (3.5Hz) respectively. The theoretical prediction was found to be higher than the experimental measurement which could be explained with the help of several factors and assumptions. The prototype was found to generate 0.46 ~ 0.66 mW power under normal human actions such as jumping and jogging which is enough to power a small scale sensor.

CHAPTER 11

FUTURE WORK

Based on the study, this thesis recommends following future works.

1. Structural health monitoring sensors can be further optimized to differentiate types of damages and provide quantitative estimate on location of damage.

2. Magnetic field sensing can be further improved by adopting thin film technology for the fabricated bulk sensor designs. In this case, one needs to fabricate ceramic films on the metallic substrate imparting large flexibility.

3. High aspect ratio 3 -1 composites can result in high magnetoelectric response coupled with low DC bias field which will improve sensing performance and reduce power consumption.

4. Nanotube architectures using piezoresistive effect can be further optimized for obtaining higher yields. In this technique, anodic aluminum oxide (AAO) templates can be used to grow CNTs in a controlled manner to obtain desired dimensions of the nanotube templates. These templates can be coated with various ceramics in order to enhance the sensitivity of the nanomaterials.

APPENDIX A

PUBLICATION RECORD RELATED TO THIS RESEARCH

Published

- V. Bedekar and S. Priya, “Detection of Corrosion using Impedance spectroscopy”, Ferroelectric letters, Vol. 35, Issue: 1-2, pp. 7-16, 2008.
- V. Bedekar, N. Poudyal, C. B. Rong, J. P. Liu, C. Kim and S. Priya, “Improved Magnetoelectric Properties of Piezoelectric - Magnetostrictive Nanocomposites Synthesized Using High Pressure Compaction Technique”, J. of Materials Science, Vol. 44, Issue:8, 2162-2166, Apr 2009.
- V. Bedekar, J. Oliver and S. Priya, “Pen harvester for powering a pulse rate sensor”, J. of Physics D: App. Physics, Vol:42, Issue:10, 105105, May 2009.
- V. Bedekar, R. A. Islam, H. Kim, M. I. Bichurin, S.N. Ivanov, Y.J. Pukinski and S. Priya, “Magnetoelectric Gradiometer”, EPJ B, Aug 2009.
- V. Bedekar, J. Oliver, S. Zhang and S. Priya, “Comparative study of energy harvesting from high temperature piezoelectric single crystals”, JJAP, 2009.
- V. Bedekar, D. Inman and S. Priya, “Design of Impedance Spectroscopy based Structural Health Monitoring Sensors for Damage Detection in Rocket Motors”, submitted to Ferroelectrics letters, 2008.
- R. Islam, V. Bedekar, N. Poudyal, J. P. Liu and S. Priya, “Magnetoelectric properties of core-shell particulate nanocomposites”, J. Appl. Phys. 104, 104111, 2008.
- H. Kim, V. Bedekar, R. Islam, W. Lee, D. Leo, S. Priya, “Laser-machined piezoelectric cantilevers for mechanical energy harvesting”, Ultrasonics, Ferroelectrics and Frequency Control, IEEE Transactions on, Vol. 55, Issue 9, pp. 1900 – 1905, 2008.

Accepted:

- ♦ V. Bedekar, G. Singh, R. Mahajan and S. Priya, "Synthesis and Microstructural Chracterization of Barium Titanate nanoparticles SiCN-MWCNT nanotubes - nanoNecklace", accepted in Ferroelectrics, 2009.

Conference Publications:

- V. Bedekar, S. Karajgikar, D. Agonafer, M. Iyengar, R. Schmidt, "Effect of CRAC Location on Fixed Rack Layout",ITherm, San Diego, CA, May 30 – June 2, 2006.
- V. Bedekar and S. Priya, "Structural Health Monitoring using Impedance Spectroscopy", Materials Science and Technology, Detroit, MI, Sept 2007.
- V. Bedekar, R. Islam, H. Kim, M. I. Bichurin, S. N. Ivanov, Y. J. Pukinski and S. Priya, "Magnetoelectric Gradiometer", Poster presentation, Magnetoelectric Interaction Phenomenon In Crystals (MEIPIC) 6, Santa Barbara, Jan 26 – 29 2009.
- V. Bedekar, G. Singh, R. Mahajan and S. Priya, "Barium Titanate Nano-Particles Decorated SiCN/MWCNT Nanotubes: Synthesis and Microstructural Characterization", Materials Science and Technology, Pittsburg, PA, Oct 2009.
- V. Bedekar, Y. Pukinskii, M. I. Bichurin, D. Viehland and S. Priya, "Metal – Ceramic Magnetoelectric Composite Gradiometer", accepted in ACerS 2010 Electronic Materials and Applications Conference, Jan 2010.
- V. Bedekar, M. I. Bichurin, V. M. Petrov, D. Viehland and S. Priya, "Dual magnetic field and mechanical vibrations energy harvesting system for human health monitoring", accepted in ACerS 2010 Electronic Materials and Applications Conference, Jan 2010.

REFERENCES

1. Doebling S. W, Farrar C.R, Prime M.B, Shevitz D.W. (1998) "A summary review of vibration-based damage identification methods", The Shock and Vibration Digest 30, 91-105.

2. G. Vachtsevanos, F. L. Lewis, M. Roemer, A. Hess, and B. Wu, *Intelligent Fault Diagnosis and Prognosis for Engineering Systems"*, Wiley, NY (2006).

3. G. Vachtsevanos, F. Rufus, J. V. R. Prasad, I. Yavrucuk, D. Schrage, B. Heck, and L. Wills, "An Intelligent Methodology for Real-time Adaptive Mode Transitioning and Limit Avoidance of Unmanned Aerial Vehicles", Software_enabled Control: Information Technologies for Dynamical Systems, (T. Samad and G. Balas, Eds.), IEEE Press, pp. 225 – 252 (2003).

4. F. L. Lewis, *Intelligent Fault Diagnosis and Prognosis*, presentation available at http://arri.uta.edu/acs.

5. Park, G., Cudney, H., and Inman, D., 1999, "Impedance based health monitoring for civil structures", 2nd International workshop on Structural Health Monitoring, September 8-10 Stanford, CA, pp 523-532.

6. C. Liang, F. Sun, C. A. Rogers, "Electro-mechanical impedance modeling of active material systems", Smart Mater. Struct. 5, 171-186, 1996.

7. Chaudhry, Z., Joseph, T., Sun, F., and Rogers, C., 1995, "Local-Area Health Monitoring of Aircraft via Piezoelectric Actuator/Sensor Patches," in Smart Structures and Integrated Systems, SPIE Conference, San Diego, CA, Proceedings of the SPIE, Vol. 2443.

8. Chaudhry, Z., Lalande, F., Ganino, A., and Rogers, C., 1996, "Monitoring the Integrity of Composite Patch Structural Repair via Piezoelectric Actuators/Sensors," AIAA-1996-1074-CP.

9. Park, G., Kabeya, K., Cudney, H. H., and Inman, D. J., 1999a, “Impedance- Based Structural Health Monitoring for Temperature Varying Applications,” JSME International Journal, Series A, Vol. 42, No. 2, 249–258.

10. Park, G., Cudney, H., and Inman, D., 1999b, “Impedance-Based Health Monitoring Technique for Massive Structures and High-Temperature Structures,” in Smart Structures and Materials 1999: Sensory Phenomena and Measurement Instrumentation for Smart Structures and Materials, Proceedings of the SPIE, Vol. 3670, 461–469.

11. Park, G., Cudney, H., and Inman, D. J., 2000a, “Impedance-Based Health Monitoring of Civil Structural Components,” ASCE Journal of Infrastructure Systems, Vol. 6, No. 4, 153–160.

12. Park, G., Cudney, H., and Inman, D.J., 2000b, “An Integrated Health Monitoring Technique Using Structural Impedance Sensors,” Journal of Intelligent Material Systems and Structures, Vol. 11, No. 6, 448–455.

13. Park, G.,Cudney, H., and Inman, D.J., 2001, “Feasibility of Using Impedance-Based Damage Assessment for Pipeline Systems,” Earthquake Engineering and Structural Dynamics Journal, Vol. 30, No. 10, 1463–1474.

14. Park G., Sohn H., Farrar C. R. and Inman D. J. (2003) “Overview of Piezoelectric Impedance-Based Health Monitoring and Path Forward” The Shock and Vibration Digest 35; 451-463.

15. Giurgiutiu V. and Rogers C. A, Recent Advancements in the Electro-Mechanical (E/M) Impedance Method for Structural Health Monitoring and NDE, SPIE’s 5th annual international symposium on smart structures and materials, paper # 3329-53, 1-5 March, CA, (1998).

16. Giurgiutiu V., “Current issues in Vibration based fault diagnostics & prognostics”, SPIE’s Annual International Symposium on smart structures & materials & 7th Annual International Symposium on NDE for health monitoring & diagnostics, paper # 4702-15, San Diego, CA. 17-21 March, (2002).

17. Giurgiutiu V., Bao J., and Zhao W., "Active Sensor Wave Propagation Health Monitoring of Beam and Plate Structures", Proceedings of the SPIE's 8th International Symposium on Smart Structures and Materials, Newport Beach, CA, 4-8 March (2001).

18. Bhalla, S., Naidu, A. S. K., and Soh, C. K., 2002a, "Influence of Structure– Actuator Interactions and Temperature on Piezoelectric Mechatronic Signatures for NDE," in Proceedings of ISSS-SPIE 2002 International Conference on Smart Materials Structures and Systems, December 12–14, Bangalore, India (paper no ISSS-SA-502).

19. Bhalla, S., Naidu, A.S.K, Ong, C.W., and Soh, C.K., 2002b, "Practical Issues in the Implementation of Electromechanical Impedance Technique for NDE," in Proceedings of the SPIE International Symposium on Smart Materials, Nano-, and Micro-Smart Systems, December 16–18, Melbourne, Australia (paper no 4935-77).

20. Naidu, A., and Bhalla, S., 2002, "Damage Detection in Concrete Structures with Smart Piezoceramic Transducers," in Proceedings of ISSSSPIE2002, International Conference on Smart Materials Structures and Systems, July 17–19, Bangalore, India, ISSS2002/SA-538.

21. Abe, M., Park, G., and Inman, D.J., 2000, "Impedance-Based Monitoring of Stress in Thin Structural Members," in Proceedings of the 11th International Conference on Adaptive Structures and Technologies, October 23–26, Nagoya, Japan, 285–292

22. S. Iijima, *Nature*, 354: 56-58, (1991).

23. Andrews R, Jacques D, Qian D and Rantell T 2002 *Acc. Chem.Res.* 35 1008

24. Rao A M, Jacques D, Haddon R C, Zhu W, Bower C and Jin S 2000 *Appl. Phys. Lett.* 76 3813

25. Vivien L, Lancon P, Riehl D, Hache F and Anglaret E 2002 *Carbon* 40 1789

26. YangW R, Thordarson P, Gooding J J, Ringer S P and Braet F 2007 *Nanotechnology* 18 412001.

27. http://en.wikipedia.org/wiki/Carbon_nanotube#Single-walled

28. http://www.crystalsoftcorp.com/Gallery/mwcnt3.jpg.html

29. Liu Z F, Shen Z Y, Zhu T, Hou S F, Ying L Z, Shi Z J and Gu Z N 2000 *Langmuir* **16** 3569

30. Star A, Stoddart J F, Steuerman D, Diehl M, Boukai A, Wong E W, Yang X, Chung S W, Choi H and Heath J R 2001 *Angew. Chem. Int. Edn* **40** 1721

31. Balasubramanian K and Burghard M 2005 *Small* **1** 180

32. Tasis D, Tagmatarc his N, Bianco A and Prato M 2006 *Chem. Rev.* **106** 1105

33. Hu X G and Dong S J 2008 *J. Mater. Chem.* **18** 1279

34. Correa-DuarteM A and Liz-Marzan L M 2006 *J. Mater. Chem.* **16** 22

35. C. S. Smith, “Piezoresistance effect in germanium and silicon”, Phys. Rev., Vol. 94, 42-49 (1954).

36. J. Bryzek, K. Petersen, J. R. Mallon, L. Christel, and F. Pourahmadi, Silicon Sensors and Microstructures, Novasensor (1990).

37. J. C. Sanchez, “Semiconductor strain-gauge pressure sensors”, Instr. Contrl. Syst., 117 – 120 (1963).

38. H. Guckel, D. W. Burns, H. H. Busta, and J. F. Detry, “Laser-recrystallized piezoresistive micro-diaphragm pressure sensor”, in Technical Digest, 1985 International Conference on Solid State Sensors and Actuators, Transducers ’85, 182 – 185 (1985).

39. S. Sugiyama, T. Suzuki, K. Kawahata, K. Shimaoka, M. Takigawa, and I. Igarashi, “Micro-diaphragm pressure sensor”, in Technical Digest, 1986 International Electron Devices Meeting, IEDM ’86, 184 – 187 (1986).

40. W. P. Eaton and J. H. Smith, “A CMOS-compatible surface-micromachined pressure sensor for aqueous ultrasonic application”, Proceedings of Smart Structures 1995, SPIE Vol. 2448, 258 – 265 (1986).

41. H. Makino, M. Asai, S.Tajima, N. Kamiya, “Piezoresistive ceramic composite for miniature force sensor”, R&D Review of Toyota CRDL 37(3), (2002), 67-70.

42. J.L. Davidson, W.P. Kang, Y. Gurbuz, K.C. Holmes, L.G. Davis, A. Wisitsora-at, D.V. Kerns, R.L. Eidson, and T. Henderson, “ Diamond as an active sensor material,” *Diamond Related Mater*. 8, (1999), 1741-1747.

43. H. Kim, Y. Tadesse, and S. Priya, “Piezoelectric Energy Harvesting”, in the book *Energy Harvesting Technologies*, Ed. S. Priya and D. Inman, Springer, 2009.

44. H. Kim, V. Bedekar, R. Islam, W. Lee, D. Leo, and S. Priya, “Laser micro-machined piezoelectric cantilevers for mechanical energy harvesting”, IEEE Ultrason. Freq. Ferroelect. Cntrl. 55, 1900-1905 (2008).

45. S. Priya, “Advances in Energy Harvesting Using Low Profile Piezoelectric Transducers”, J. Electroceram. 19, 165 – 182 (2007).

46. H. Kim, S. Priya, H. Stephanou, and K. Uchino, “Consideration of impedance matching techniques for efficient piezoelectric energy harvesting”, IEEE Trans. Ultrason. Ferroelec. Freq. Cntrl. 54, 1851 – 1859 (2007).

47. S. Dong, J. Zhai, J. F. Li, D. Viehland, and S. Priya, “Multimodal system for harvesting magnetic and mechanical energy”, Appl. Phys. Lett. 93, 103511 (2008).

48. Y. Tadesse, S. Zhang, and S. Priya, “Multimodal energy harvesting system: Piezoelectric and Electromagnetic”, J. Intell. Mater. Sys. 20, 625-632 **(**2009)**.**

49. American National Standard Institute, IEEE Standard on Piezoelectricity (1987).

50. www.discountrocketry.com; Discount Rocketry Rouse-Tech 38/120 Reloadable Rocket Motor System (RT-38120M) Manufactured by Rouse-Tech Monster Motors.

51. Stokes, J. P., and Cloud, G. L., 1993, “The Application of Interferometric Techniques to the Nondestructive Inspection of Fiber-Reinforced Materials,” Experimental Mechanics, Vol. 33, 314–319.

52. G. Park and D. J. Inman, Impedance based structural health monitoring, report, LA-UR-04-5721.

53. http://www.matweb.com, Matweb, material property data by Automation Creations, Inc.

54. A. A. Panova, P. Pantano, and D. R. Walt, “In situ fluorescence imaging of localized corrosion with a pH-sensitive imaging fiber,” Anal. Chem. 69, 1635–1641 (1997).

55. www.ndt-ed.org

56. M. Pourbaix, Atlas of electrochemical equilibria in aqueous solutions, NACE Cebelcor, Huston, 1974.

57. K. Shimizu, R. C. Furneaux, G. E. Thompson, G. C. Wood, A. Gotoh, and K. Kobayashi, “On the nature of “easy paths” for the diffusion of oxygen in thermal oxide films on aluminium, Oxidation Aluminum 35, 427 – 439 (1991).

58. Inman, D. J., Farrar, C.R. , Steffan, V. and Lopes, V., eds., 2005. Damage Prognosis - For Aerospace, Civil and Mechanical Systems, John Wiley & Sons, Ltd., Chichester, UK

59. Giurgiutiu V. 2001. “Active Sensor Wave Propagation Health Monitoring of Beam and Plate Structures”, Proceedings of the SPIE’s 8th International Symposium on Smart Structures and Materials, Newport Beach, CA 4-8 March (2001).

60. K. Nisancioglu, Corrosion of aluminum alloys, Proc. ICAA3, Vol. 3, Trondheim, 239 – 259 (1992).

61. ASM metal handbook vol. 7, (Atlas microstructure for Aluminum alloys)

62. J. Ryu, S. Priya, and K. Uchino: *J. Electroceram*. 8, 107 (2002).

63. S.X. Dong, J.F. Li, and D. Viehland: *IEEE Trans. Ultra. Ferroelec. Freq. Contl*. 50, 1253 (2003).

64. G. Srinivasan, E. Rasmussen, B. Levin, and R. Hayes: *Phys. Rev. B* 65, 134402 (2002).

65. G. Srinivasan, C. P. DeVreugd, C. S. Flattery, Appl. Phys. Lett. 85, 2550 (2004).

66. M. I. Bichurin, V. M. Petrov and G. Srinivasan, Phy. Rev. B 68, 054402 (2003).

67. R. Islam, H. Kim, S. Priya, H. Stephanou, Appl. Phys. Lett. 89, 152908 (2006).

68. H. Kim, R. Islam, and S. Priya, Appl. Phys. Lett. 90, 012909 (2007).

69. S. Priya, S. Ural, H. Kim, K. Uchino, and T. Ezaki, Jpn. J. Appl. Phys. 43, 3503 (2004).

70. M. I. Bichurin, D. A. Filippov, V. M. Petrov, V. M. Laletsin N. Paddubnaya, G. Srinivasan, Phy. Rev. B 68, 132408 (2003)

71. G. Srinivasan, C. P. De Vreugd, V. M. Laletin, N. Paddubnaya, M. I. Bichurin, V. M. Petrov, D. A. Filippov, Phy. Rev. B 71, 184423 (2005)

72. S. Priya, R. Islam, S. Dong and D. Vieland, J. Electroceramics, 19: 147 -164, (2007).

73. C. W. Nan, M. I. Bichurin, S. Dong, D. Vieland and G. Srinivasan, J. App. Phy. 103, 031101, (2008).

74. M. Fiebig, J. Phys. D: Appl. Phys. 38, R123-R152, (2005).

75. V. Bedekar, R.A. Islam, H. Kim, M.I. Bichurin, S.N. Ivanov, Y.J. Pukinski, S. Priya, Eur. Phys. J. B, DOI: 10.1140/epjb/e2009-00275-3 (2009).

76. Source website: http://www.sei.co.jp/news_e/press/01/01_22.html

77. R. E. Newnham, “Properties of Materials: Anisotropy, Symmetry, Structure”, Oxford University Press, USA (2005).

78. R. Islam, H. Kim, S. Priya, H. Stephanou, Appl. Phys. Lett. 89, 152908 (2006).

79. H. Kim, R. Islam, S. Priya, Appl. Phys. Lett. 90, 012909 (2007).

80. S. Priya, S. Ural, H. Kim, K. Uchino, T. Ezaki, Jpn J.Appl. Phys. 43, 3503 (2004).

81. M.I. Bichurin, V.M. Petrov, G. Srinivasan, Phy. Rev. B 68, 054402 (2003).

82. M.I. Bichurin, D.A. Filippov, V.M. Petrov, V.M. Laletsin, N. Paddubnaya, G. Srinivasan, Phys. Rev. B 68, 132408 (2003).

83. G. Srinivasan, C.P. De Vreugd, V.M. Laletin, N.Paddubnaya, M.I. Bichurin, V.M. Petrov, D.A. Filippov, Phys. Rev. B 71, 184423 (2005).

84. S R Shah and R Raj, *J. European Ceram. Soc.,* (2005), 25 243–249

85. 2. R. Riedel, A. Kienzle, W. Dressler, L. Ruwisch, J. Bill, and F. Aldinger, *Nature*, (1996), 382 796–8.

86. S. Trassl, H. J. Kleebe, H. Stormer, G. Motz, E. Rossler, and G. Ziegler, *J. Amer. Ceram. Soc.,* (2002), 85,1268.

87. 4. G. Arlt, D. Hennings, G de. With, *J. Appl. Phys.*, 58, 1619 – 1625 (1985).

88. 5. K. Uchino, E. Sadanaga, and T. Hirose, *J. Amer. Ceram. Soc.*, 72, 1555 – 1558 (1989).

89. 6. W. L. Zhong, Y. G. Wang, P. L. Zhang, and B. D. Qu, *Phys. Rev. B*, 50, 698 – 703 (1994).

90. G. Singh, S. Priya, M. R. Hossu, S. R. Shah, S. Grover, A. R. Koymen and R. L. Mahajan, *Jpn. J. Appl. Phys.*, (2009) submitted.

91. A. H. Barber, S. R. Cohen, and H. D. Wagner, *Phys. Rev. B,* (2005), 71, 115443.

92. H. Ago, T. Kugler, F. Cacialli, W.R. Salaneck, M.S.P. Shaffer, A. H. Windle and R. H. Friend, J. Phys. Chem. B 103: 8116, (1999).

93. S. L. Kim, S. R. Jang, R. Vittal, J. Lee and K. J. Kim, J. of Appl. Electrochemistry, 36: 1433-1439, (2006).

94. M. Mohl, Z. Konya, A. Kukovecz and I. Kiricsi, *NATO Science for Peace and Security Series B: Physics and Biophysics*, Springer Netherlands, Book chapter, part II, pp.365-368, (2008). Web: http://www.springerlink.com/content/u386547867812257

95. K. Balasubramanian and M. Burghard, *Small* 1 180, (2005).

96. Suchetelene JV (1972) Philips Res Rep 27:28

97. Harshe GR (1991) Magnetoelectric effect in piezoelectric–magnetostrictive composite. Ph.D. Dissertation, Pennsylvania State University, University Park, PA

98. Srinivasan G, Rasmussen E, Levin B, Hayes R (2002) Phys Rev B 65:134402

99. Lalestin U, Padubnaya N, Srinivasan G, Devreugd CP (2004) Appl Phys A Mater Sci Process 78(1):33

100. Dong SX, Zhai J, Li JF, Viehland D (2006) J Appl Phys 88:082907

101. Dong SX, Li JF, Viehland D (2003) IEEE Trans Ultrason Ferroelectr Freq Control 50:1253

102. Dong SX, Li JF, Viehland D (2004) J Appl Phys 96:3382

103. Dong SX, Cheng J, Li JF, Viehland D (2003) Appl Phys Lett 83:4812

104. Dong SX, Li JF, Viehland D (2004) Appl Phys Lett 85:3534

105. Ryu J, Priya S, Uchino K (2002) J Electroceram 8:107

106. Islam RA, Priya S (2008) J Mater Sci 43:3560. doi:10.1007/ s10853-008-2562-9

107. Islam RA, Viehland D, Priya S (2008) J Mater Sci Lett 43:1497

108. Islam R, Jiang J, Bai F, Viehland D, Priya S (2007) Appl Phys Lett 9:162905

109. Islam R, Rong C, Liu JP, Priya S (2008) J Mater Sci Lett 43:6337

110. Gro¨ssinger R, Duong GV, Sato-Turtelli R (2008) J Magn Magn Mater 320:1972

111. Islam RA, Bedekar V, Poudyal N, Liu JP, Priya S (2008) J Appl Phys 104:104111

112. R. A. Islam and S. Priya, "High Energy Density Ceramic Composition in the System Pb(Zr,Ti)O3 ─ Pb[(Zn,Ni)1/3Nb2/3]O3", J of Am. Ceram. Soc., 89 (10), pp. 3147 – 3156, 2006.

113. Z. Chaudhey and C. A. Rogers, The pin-force model revisited *J. Intell. Mater. Syst. Struct.* **5** 347–54, 1994.

114. E. F. Crawley and E. H. Anderson "Detailed models of piezoceramic actuation of beams", *J. Intell. Mater. Syst. Struct.* **1** 4–25, 1990.

115. T. Wu and P. Ro, "Dynamic peak amplitude analysis and bonding layer effects of piezoelectric bimorph cantilevers", Smart Mater. Struct. 13 pp. 203-210, 2004.

116. S. Roundy, "On the Effectiveness of Vibration-based Energy Harvesting" *Journal of Intelligent Material Systems and Structures*, Vol. 16, 2005.

117. A. Erturk and D.J. Inman, "An Experimentally Validated Bimorph Cantilever Model for Piezoelectric Energy Harvesting from Cantilevered Beams," *Smart Materials and Structures* 18 2009)

118. I. W. Chen and X. H. Wang, Nature (London), 404, 168, 2002.

119. S. Priya, K. Uchino, J. Ryu, C. W. Ahn and S, Nahm, "Induction of combinatory characteristics by relaxor modification of Pb.Zr0.5Ti0.5.O3" , App. Phy. Lett. vol. 83, no. 24, 2003.

120. K. Matsui, N. Ohmichi, M. Ohgai, H. Yoshida and Y. Ikuhara "Effect of alumina-doping on grain boundary segregation-induced phase transformation in yttria-stabilized tetragonal zirconia polycrystal", J. of Mat. Res. Vol. 21 no. 9, 2006.

121. R. Islam and S. Priya, "Realization of high-energy density polycrystalline piezoelectric ceramics, App. Phy. Lett. 88, 032903, 2006.

122. S. Priya, PhD Dissertation, Pennsylvania State University, University Park, PA, 2003.

123. S. Priya and K. Uchino, "Dielectric and piezoelectric properties of the Mn-substituted Pb.Zn1Õ3Nb2Õ3.O3–PbTiO3 single crystal", J. of App. Phy. Vol. 91, no. 7, 2002.

124. Q. M. Wang and L. E. Cross, "Performance analysis of piezoelectric cantilever bending actuators *Ferroelectrics* **215** 187–213, 1998.

125. R. Blevins, "Formulas for natural frequency and mode shape", Litton Educational Publishing, Inc., 1979.

126. J. Oliver and S. Priya, "unpublished work", submitted to a book being edited by S. Bharadwaja and D. Sinclair.

127. http://www.mfg.mtu.edu/cyberman/machtool/machtool/vibration/damping.html

128. C-Y Chong, S. P. Kumar and B. A. Hamilton, "Sensor networks: evolution, opportunities and challenges," proceedings of IEEE, vol. 91, no. 8, pp. 1247-1256, 2003.

129. C. B. Williams and R. B. Yates, "Analysis of a micro-electric generator for microsystems," Sensors and Actuators A 52, pp. 8-11, 1996.

130. M. El-hami, P. Glynne-Jones, N. M. White, M. Hill, S. P. Beeby, E. James, A. D. Brown and J. N. Ross, "Design and fabrication of a new vibration-based electromechanical power generator", Sensors and Actuators A 92, pp. 335-342, 2001.

131. T. Starner, "Human-power waerable computing", IBM Systems Journal, vol 35, pp. 618-629, 1996.

132. P. Glynne-Jones, M. J. Tudor, S. P. Beeby and N. M. White, “An electromagnetic, vibration-powered generator for intelligent sensor systems,” Sensors and Actuators A 97, pp. 685-690, 2002.

133. H. Goto, T. Sugiura, Y. Harada and T. Kazui, “Feasibility of using the automatic power generating system for quartz watches as a leadless pacemaker power source”, Medical and Biological Engineering and Computing vol. 37, pp. 377-380, 1999.

134. http://www.phoenix.tc-ieee.org/004_Piezo_Film_Blood_Flow_Sensor/Phoenix_PiezoPulse.htm

135. http://www.concordcoinc.com/index.aspx?Command=GroupInfo&GroupID=1404394974

136. http://www.worldwidesurgical.com/bp/v3/bci3420/bci-digit-finger-pulse-ox.html

137. http://www.alltimemedical.com/products/Home_Diagnostics/Pulse_Oximeter/DigitOx_Finger_Pulse_Oximeter.html#specs

138. M. N. O. Sadiku, “Elements of Electromagnetics (Fourth Edition ed.)” NY/Oxford UK: Oxford University Press. p. §9.2 pp. 386 ff. ISBN 0-19-530048-3, 2007.

139. S. P. Beeby, R. N. Torah, M. J. Tudor, P. Glynne-Jones, T. O’Donnell, C. R. Saha and S. Roy, “A micro electromagnetic generator for vibration energy harvesting”, Journal of Micromechanics and Microengineering, 17, 1257-1265, 2007.

140. G. Poulin, E. Sarraute, F. Costa, “Generation of electric energy for portable devices Comparitive study of an electromagnetic and a piezoelectric system”, Sensors and Actuators A, 116, pp. 461-471, 2004.

141. K. Nakano, S. J. Elliott and E. Rustighi, “A unified approach to optimal conditions of power harvesting using electromagnetic and piezoelectric transducers”, *Smart Mater. Struct.* 16, pp. 948–958, 2007.

142. S. Gartenhaus, Physics: Basic Principles (vol II), Holt, Rinehart & Winston, 1975, New York, Sec 26.5, 27.4, ISBN 0030880807, 1975.

BIOGRAPHICAL INFORMATION

Vishwas Bedekar received his Bachelors degree in Mechanical Engineering from University of Mumbai, Bombay, India in 2002. After completing BE, he was employed with a construction firm for 6 months as Quality control engineer and then as an IT professional in a reputed business organization for a year. He received his Masters degree in Mechanical Engineering from University of Texas Arlington in August 2006. He is recipient of EMNSPC graduate scholarship for the year 2005 – 2006 and Deans Doctoral Fellowship 2006 – present. His current research is related to Energy Harvesting, Magnetoelectric Materials, Structural Health Monitoring and synthesis and characterization of novel nanomaterials. He is an active member of ASM International since fall 2006. Mr. Vishwas was one of the attendees at the Magnetoelectric Interaction Phenomenon in Crystals workshop (MEIPIC 6) held at University of California Santa Barbara (UCSB) in January 2009. He was a Visiting Scholar Student at Virginia Polytechnic and State University from October 2008 – December 2009. After completing his degree Doctor of Philosophy in Materials Science and Engineering from University of Texas Arlington he will be joining Virginia Polytechnic and State University as a Post – doctoral fellow beginning the year 2010.